TECHNISCHE UNIVERSITÄT ILMENAU

Fakultät für Elektrotechnik und Informationstechnik
der Technischen Universität Ilmenau

Quasi-Deterministic Channel Modeling and Experimental Validation in Cooperative and Massive MIMO Deployment Topologies

Stephan Jaeckel

Dissertation zur Erlangung des akademischen Grades Doktor-Ingenieur (Dr.-Ing.)

Anfertigung im:	Fachgebiet Elektronische Messtechnik Institut für Informationstechnik Fakultät für Elektrotechnik und Informationstechnik
Gutachter:	Prof. Dr.-Ing. habil. Reiner S. Thomä (TU Ilmenau) Priv.-Doz. Dr. rer. nat. Volker Jungnickel (Fraunhofer Heinrich Hertz Institute, Berlin) Prof. Dr. Claude Oestges (Ecole Polytechnique de Louvain)
Vorgelegt am:	09.09.2016
Verteidigt am:	22.05.2017

urn:nbn:de:gbv:ilm1-2017000330

Abstract

The tremendous growth of mobile data traffic will lead to substantial architectural changes in wireless networks. New wireless systems need to exploit all available degrees of freedom in the wireless channel such as wider bandwidth, multi-carrier operation, large antenna arrays, polarization, and cooperation between base stations, in order to maximize the performance. The wireless industry needs channel models that reproduce the true behavior of the radio channel in all these use cases. However, many state-of-the-art models only support parts of the required functionality and have not been thoroughly validated against measurements in relevant propagations scenarios. It is therefore unclear if the performance predictions made by these models are realistic.

This thesis introduces a new geometry-based stochastic channel model that creates accurate results for two important use cases: massive multiple-input multiple-output (MIMO) and joint transmission (JT) coordinated multi-point (CoMP). For this, the popular WINNER channel model was extended to incorporate 3-D propagation, spherical wave propagation, spatial consistency, temporal evolution of channels, and a new model for the polarization. This model was introduced under the acronym "QuaDRiGa" - quasi deterministic radio channel generator. To validate the model, measurements were done in downtown Dresden, Germany, and downtown Berlin, Germany. Those were used to derive the model parameters. Then, the measurements were resimulated with the new channel model and benchmarked against the Rayleigh i.i.d. model and the 3GPP-3D channel model. Essential performance indicators such as path gain, shadow fading, delay spread, angular spreads, geometry factor, single-link capacity, and the dirty-paper coding capacity were computed from both the measured and resimulated data.

In Dresden, the resimulated channels produce almost identical results as the measured channels. When using the resimulated channels to derive the model parameters, the same results can be obtained as when using the measurement data. Such a direct comparison was not possible with the previous models because they cannot produce sufficiently long sequences of channel data. The performance predictions from the new model are more than 90% accurate whereas only 80% accuracy could be achieved with the 3GPP-3D model. In Berlin, accurate performance predictions could also be made in a multi-cellular environment where the mutual interference between the base stations could be studied. This confirms that it is generally sufficient to use single-link measurements to parameterize channel models that are then used to predict the achievable performance in wireless networks. The new model can generate channel traces with similar characteristics as measured data. This might speed up the evaluation of new algorithms because it is now possible to obtain realistic performance results already in an early stage of development.

Kurzfassung

Das enorme Wachstum des mobilen Datenaufkommens wird zu substantiellen Veränderungen in mobilen Netzwerken führen. Neue drahtlose Funksysteme müssen alle verfügbaren Freiheitsgrade des Übertragungskanals ausnutzen um die Kapazität zu maximieren. Dies beinhaltet die Nutzung größerer Bandbreiten, getrennter Übertragungskanäle, Antennenarrays, Polarisation und Kooperation zwischen Basisstationen. Dafür benötigt die Funkindustrie Kanalmodelle, welche das wirkliche Verhalten des Übertragungskanals in all diesen Fällen abbilden. Viele aktuelle Kanalmodelle unterstützen jedoch nur einen Teil der benötigten Funktionalität und wurden nicht ausreichend durch Messungen in relevanten Ausbreitungsszenarien validiert. Es ist somit unklar, ob die Kapazitätsvorhersagen, welche mit diesen Modellen gemacht werden, realistisch sind.

In der vorliegenden Arbeit wird ein neuen Kanalmodell eingeführt, welches korrekte Ergebnisse für zwei wichtige Anwendungsfälle erzeugt: Massive MIMO und Joint-Transmission (JT) Coordinated Multi-Point (CoMP). Dafür wurde das häufig verwendete WINNER Kanalmodell um neue Funktionen erweitert. Dazu zählen 3-D Ausbreitungseffekte, sphärische Wellenausbreitung, räumliche Konsistenz, die zeitliche Entwicklung von Kanälen sowie ein neues Modell für die Polarisation. Das neue Kanalmodell wurde unter dem Akronym „QuaDRiGa“ (**Qua**si **D**eterministic **R**ad**i**o Channel **G**ener**a**tor, dt.: quasideterministischer Funkkanalgenerator) eingeführt. Um das Modell zu validieren wurden Messungen in Dresden und Berlin durchgeführt. Die Messdaten wurden zunächst verwendet um die Modellparameter abzuleiten. Danach wurden die Messkampagnen im Modell nachgestellt um die Reproduzierbarkeit der Ergebnisse nachzuweisen. Essentielle Leistungsindikatoren wie z.B. der Pfadverlust, die Laufzeitstreuung, die Winkelstreuung, der Geometriefaktor, die MIMO Kapazität und die Dirty-Paper-Coding Kapazität wurden für beide Datensätze berechnet. Diese wurden dann miteinander sowie mit Ergebnissen aus dem Rayleigh i.i.d. Modell und dem 3GPP-3D Kanalmodell verglichen.

Für die Messungen in Dresden erzeugt das neue Modell nahezu identische Ergebnisse wenn die nachsimulierten Kanäle anstatt der Messdaten für die Bestimmung der Modellparameter verwendet werden. Solch ein direkter Vergleich war bisher nicht möglich, da die vorherigen Modelle keine ausreichend langen Kanalsequenzen erzeugen können. Die Kapazitätsvorhersagen des neuen Modells sind zu über 90% korrekt. Im Vergleich dazu konnte das 3GPP-3D Model nur etwa 80% Genauigkeit aufweisen. Diese Vorhersagen konnten auch für das Messszenario in Berlin gemacht werden, wo mehrere Basisstationen zeitgleich vermessen wurden. Dadurch konnten die gegenseitigen Störungen mit in die Bewertung eingeschlossen werden. Die Ergebnisse bestätigen die generelle Annahme, dass es möglich ist den Ausbreitungskanal sequenziell für einzelne Basisstationen zu vermessen und danach Kapazitätsvorhersagen für ganze Netzwerke mit der Hilfe von Modellen zu machen. Das neue Modell erzeugt Kanalkoeffizienten welche ähnliche Eigenschaften wie Messdaten haben. Somit können neue Algorithmen in Funksystemen schneller bewertet werden, da es nun möglich ist realistische Ergebnisse in einem frühen Entwicklungsstadium zu erhalten.

Acknowledgements

This thesis would not have been possible without the support and encouragement of many people. First, I would like to thank Dr. Volker Jungnickel for his continuous support and encouragement, both as a supervisor and as a colleague. I would further like to thank Prof. Dr. Reiner S. Thomä for his support and for giving me the opportunity to do my PhD at the Technische Universität Ilmenau, and Claude Oestges for his time and effort to to review the thesis.

While working at the Fraunhofer HHI, I had the privilege to work with Dr. Lars Thiele. As the leader of the system level innovations group he always found the funding for me to continue working on the QuaDRiGa model and my thesis. Many thanks for that. I also would like to thank my colleagues Leszek Raschkowski, Martin Kurras, Kai Börner and Johannes Dommel for the valuable discussions and their support. It was a pleasure for me to work in this group.

My gratitude extends to Frank Burkhardt and Ernst Eberlein from the Fraunhofer IIS and Gerd Sommerkorn, Christian Schneider and Martin Kaeske from the Technische Universität Ilmenau for their fruitful discussions during the MIMOSA project which initiated the work on the channel model. I also would like to thank all the colleagues that helped throughout the measurements.

Finally, my deepest gratitude goes to my wife, Valeria, for her support and her patience throughout the past years.

Berlin, Germany, August 2016
Stephan Jaeckel

Contents

Contents IX
List of Figures . . . XI
List of Tables . . . XIII
List of Acronyms . . . XIV
List of Symbols . . . XVI
Glossary . . . XIX

1 Introduction 1
1.1 MIMO Wireless Communications . . . 2
1.2 Characterization of the MIMO Channel . . . 4
1.2.1 Channel Measurements . . . 4
1.2.2 Correlation-based Stochastic Channel Models . . . 5
1.2.3 Geometry-based Stochastic Channel Models . . . 7
1.3 Objectives and Contributions . . . 13

2 A 3-D Multi-Cell Channel Model with Time Evolution for Virtual Field Trials 15
2.1 Correlated Large-Scale Parameter Maps . . . 18
2.2 Initial Delays and Normalized Path Powers . . . 21
2.3 Departure and Arrival Angles . . . 23
2.4 Drifting . . . 26
2.5 Antennas and Polarization . . . 31
2.5.1 Relation between the Polarization Model and the Jones Calculus . . . 33
2.5.2 Changing the Orientation of Antennas . . . 33
2.5.3 Constructing the Polarization Transfer Matrix . . . 36
2.6 Combining Sub-Paths into Paths . . . 39
2.7 Path Gain, Shadow Fading and K-Factor . . . 40
2.8 Transitions between Segments . . . 41
2.9 Summary . . . 42

3 Channel Model Parameterization and Validation Methodology 45
3.1 Estimation of Path Parameters . . . 48
3.1.1 Data Model . . . 48
3.1.2 Detection of Multipath Components in the Delay Domain . . . 49
3.1.3 Detection of Multipath Components in the Spatial Domain . . . 53
3.2 Estimation of Large-Scale Parameters . . . 59
3.2.1 Path Gain and Shadow Fading . . . 60
3.2.2 Ricean K-Factor . . . 60
3.2.3 Delay Spread . . . 61
3.2.4 Angular Spread . . . 61
3.2.5 Cross-Polarization Ratio . . . 62
3.2.6 Large-Scale Parameter Correlations . . . 63
3.3 Estimation of Performance Metrics . . . 64

3.3.1 Single-User Capacity at a Fixed SNR . . . 65
3.3.2 Geometry Factor . . . 66
3.3.3 Multi-User Singular Value Spread . . . 66
3.3.4 Dirty-Paper Coding Capacity . . . 68
3.3.5 Dirty-Paper Coding Capacity with Inter-Cell Interference . . . 71
3.4 Summary . . . 73

4 Validation of the Model for Massive MIMO **75**
4.1 Massive MIMO Measurements in Dresden, Germany . . . 75
4.2 Resimulation of the Measurement Campaign . . . 79
4.3 Large-Scale Parameters . . . 84
4.3.1 Effective Path Gain . . . 84
4.3.2 Ricean K-Factor . . . 86
4.3.3 RMS Delay Spread . . . 88
4.3.4 Azimuth of Departure Angular Spread . . . 89
4.3.5 Azimuth of Arrival Angular Spread . . . 89
4.3.6 Elevation of Arrival Angular Spread . . . 91
4.3.7 Cross-Polarization Ratio . . . 91
4.4 Inter-Parameter Correlation Values . . . 92
4.5 Decorrelation Distances . . . 98
4.6 Performance Metrics . . . 100
4.6.1 Signal to Noise Ratio . . . 100
4.6.2 Single-User Capacity at a Fixed SNR . . . 102
4.6.3 Multi-User Singular Value Spread . . . 103
4.6.4 Dirty-Paper Coding Capacity . . . 105
4.7 Summary . . . 111

5 Validation of the Model for Multi-Cell Transmission **113**
5.1 Multi-cell Measurements in Berlin, Germany . . . 114
5.2 Resimulation of the Measurement Campaign . . . 116
5.3 Large-Scale Parameters . . . 117
5.3.1 Effective Path Gain . . . 118
5.3.2 Ricean K-Factor . . . 119
5.3.3 RMS Delay Spread . . . 120
5.4 Inter-Parameter Correlation Values and Decorrelation Distances . . . 121
5.5 Performance Metrics . . . 123
5.5.1 Geometry Factor . . . 123
5.5.2 Single-User Capacity at a Fixed SNR . . . 123
5.5.3 Multi-User Singular Value Spread . . . 125
5.5.4 Dirty-Paper Coding Capacity . . . 126
5.5.5 Dirty-Paper Coding Capacity with Inter-Cell Interference . . . 128

6 Conclusions **135**

A Appendix **137**
A.1 Departure and Arrival Angles (Adopted WINNER Method) . . . 137
A.2 Model of the Transmit Antenna in Berlin . . . 140

Bibliography **141**

List of Figures

1.1 Simplified overview of the modeling approach used by GSCMs 8
1.2 Evolution of GSCMs 9

2.1 Steps for the calculation of time-evolving channel coefficients 16
2.2 Principle of the generation of channel coefficients based on correlated LSPs . . . 19
2.3 Map-based 2-D autocorrelation shaping using FIR filters 20
2.4 Maximal achievable angular spread depending on the K-factor 25
2.5 Scatterer positions and arrival angles (single-bounce model) 27
2.6 Scatterer positions and arrival angles (multi-bounce model) 29
2.7 Example patterns for a dipole antenna 34
2.8 Illustration of overlapping segments and variable MT speeds 42

3.1 Flow chart of the data analysis and model parameterization procedure 47
3.2 Iterative detection of multipath components from MIMO channels 50
3.3 Example output of the iterative tap estimation 53
3.4 Illustration of the arrival angle estimation using an ULA 54

4.1 Transmit antenna for the Dresden measurements 77
4.2 Receiver configuration for the Dresden measurements 77
4.3 Receive antenna schematics for the Dresden measurements 77
4.4 Map of the measurement area in Dresden, Germany 79
4.5 Illustration of the user placement methods 80
4.6 Effective path gain distributions in Dresden, Germany 85
4.7 Regression fit of the measured path-gain values 85
4.8 Ricean K-factor distributions in Dresden, Germany 87
4.9 Illustration of the effect caused by using a Gaussian power angular spectrum . . 87
4.10 Illustration of the effect of the new angular mapping method 87
4.11 RMS delay spread distributions in Dresden, Germany 88
4.12 Azimuth spread of departure distributions in Dresden, Germany 89
4.13 Azimuth spread of arrival distributions in Dresden, Germany 90
4.14 Elevation spread of arrival distributions in Dresden, Germany 91
4.15 Cross-Polarization Ratio in Dresden, Germany 92
4.16 Inter-parameter correlation values in Dresden (part 1) 93
4.17 Inter-parameter correlation values in Dresden (part 2) 94
4.18 Inter-parameter correlation values extracted from the 3GPP-3D model (part 1) . 96
4.19 Inter-parameter correlation values extracted from the 3GPP-3D model (part 2) . 97
4.20 Decorrelation distances in Dresden, Germany 99
4.21 SNR distributions in Dresden, Germany 100
4.22 Number of detected paths vs. SNR in the Dresden measurement data 101
4.23 Capacity distributions in Dresden, Germany 102
4.24 Multi-user singular value spread in Dresden, Germany 104
4.25 DPC capacity for the multi-antenna configuration in Dresden, Germany 106
4.26 DPC capacity for the single-antenna configuration in Dresden, Germany 107

4.27 DPC capacity for different numbers of transmit antennas in Dresden, Germany . 110

5.1 Map of the measurement area in Berlin, Germany 115
5.2 Effective path gain distributions in Berlin, Germany 118
5.3 Ricean K-factor distributions in Berlin, Germany 119
5.4 RMS delay spread distributions in Berlin, Germany 120
5.5 Inter-parameter correlation values in Berlin, Germany 121
5.6 Decorrelation distances in Berlin, Germany 122
5.7 Geometry factor distributions in Berlin, Germany 123
5.8 Capacity at a fixed SNR in Berlin, Germany 124
5.9 Singular value spread in Berlin, Germany 125
5.10 DPC capacity in Berlin, Germany 127
5.11 Massive MIMO antennas for interference mitigation in Berlin, Germany 130
5.12 DPC capacity with different interference mitigation strategies 132
5.13 Interference footprint for different transmission schemes in Berlin, Germany . . . 134

A.1 Visualization of the angular spread correction function $C_\phi(L, K)$ 138
A.2 Synthetic and the measured antenna patterns in Berlin, Germany 140

List of Tables

1.1 Differences between various GSCMs 12

2.1 Offset Angle of the mth Sub-Path from [47] 26

4.1 Measurement parameters for the MIMO measurements in Dresden 76
4.2 Parameters for the Urban Macro-cell (UMa) Scenario 82
4.3 Cross-Correlation Values 83
4.4 DPC capacity in Dresden for a varying number of users at fixed SNR 108
4.5 DPC capacity in Dresden for a varying number of users at the actual SNR 109
4.6 DPC capacity prediction for different numbers of Tx-Antennas 110

5.1 Parameters for the multi-cell measurements in Berlin 114
5.2 Overview of the massive MIMO antenna configurations in Berlin, Germany . . . 130
5.3 DPC capacity prediction for different transmission schemes 131

A.1 Correction values from [47] for different numbers of paths 139
A.2 Comparison of the correction functions 139

List of Acronyms

2-D	two-dimensional
3-D	three-dimensional
3G	third generation
3GPP	3rd generation partnership project
4G	fourth generation
5G	fifth generation
AoA	azimuth angle of arrival
AoD	azimuth angle of departure
AS	angular spread
ASA	azimuth spread of arrival
ASD	azimuth spread of departure
AWGN	additive white Gaussian noise
BC	broadcast channel
BS	base station
CDF	cumulative distribution function
CIR	channel impulse response
CoMP	coordinated multi-point
COST	European Cooperation in Science and Technology
CSI	channel state information
DPC	dirty-paper coding
DS	delay spread
EoA	elevation angle of arrival
EoD	elevation angle of departure
ESA	elevation angle spread of arrival
ESD	elevation angle spread of departure
FBS	first-bounce scatterer
FIR	finite impulse response
FR	frequency response
FR1	frequency reuse 1
FR4	frequency reuse 4
FWHM	full width at half maximum
GCS	global coordinate system
GF	geometry factor
GPS	global positioning system
GSCM	geometry-based stochastic channel model
HHI	Heinrich Hertz Institute
i.i.d.	independent and identically distributed
ISD	inter site distance
ITU	International Telecommunication Union
JT	joint transmission
KF	Ricean K-factor
LBS	last-bounce scatterer

LHCP	left hand circular polarized
LOS	line of sight
LSF	large-scale fading
LSP	large-scale parameter
LTE	long term evolution
MAC	multiple-access channel
MIMO	multiple-input multiple-output
MPC	multipath component
MRT	maximum ratio transmission
MSE	mean square error
MT	mobile terminal
NLOS	non-line of sight
O2I	outdoor-to-indoor
OFDM	orthogonal frequency division multiplexing
PAS	power-angular spectrum
PDP	power delay profile
PG	path gain
QAM	quadrature amplitude modulation
QuaDRiGa	quasi deterministic radio channel generator
RAN	radio access network
RHCP	right hand circular polarized
RMS	root mean square
Rx	receiver
SAGE	space-alternating generalized expectation-maximization
SCM	spatial channel model
SF	shadow fading
SIMO	single input multiple output
SINR	signal to interference and noise ratio
SISO	single input single output
SNR	signal to noise ratio
SSF	small-scale-fading
STD	standard deviation
SV	singular value
SVD	singular value decomposition
TUB	Technische Universität Berlin
Tx	transmitter
ULA	uniform linear array
UMa	urban-macrocell
UMi	urban-microcell
VR	visibility region
WGS	world geodetic system
WINNER	Wireless World Initiative for New Radio
WSS	wide-sense stationary
XPD	cross-polarization discrimination
XPR	cross polarization ratio
ZF	zero-forcing
ZoA	zenith angle of arrival
ZoD	zenith angle of departure
ZSA	zenith angle spread of arrival
ZSD	zenith angle spread of departure

List of Symbols

$(.)^*$	Conjugate of a complex-valued scalar, vector, or matrix	54
$(.)^H$	Conjugate transpose (or Hermitian transpose) of a complex-valued matrix	3
$(.)^T$	Transpose of a matrix	35
α	Amplitude of a path	7
χ_2^2	Chi-squared distribution with 2 degrees of freedom	52
δ	Dirac delta function (is zero everywhere except at zero)	7
ℓ	Water level (for water-filling)	69
η	Array gain	55
γ	Polarization rotation angle for the linear NLOS polarization in [rad]	37
κ	Singular-value spread, also known as condition number	67
λ	Wavelength in units of [m]	18, 29, 53, 59, 66, 132, 142
ν	Sample of additive white Gaussian noise	48, 49, 52
ω	Singular value	67, 69
ϕ	Azimuth angle in [rad]. ϕ can be used for ϕ^d or ϕ^a	23, 24, 32, 110, 139, 140, 142
ϕ^a	Azimuth angle of arrival (AoA) in [rad]	23, 26, 28
ϕ^d	Azimuth angle of departure (AoD) in [rad]	23, 26, 27
$\hat{\phi}$	The offset angle between the path angle ϕ of the mth sub-path in [degree]	26
ψ	Phase of a path in [rad]	7, 29, 39, 49
ρ	Correlation coefficient	21, 63, 96, 97, 99, 124
σ_ν	Standard deviation of noise amplitude	48, 49, 52
σ	Signal to noise ratio (linear scale)	2, 65, 69, 107
σ_{SF}	The shadow fading standard deviation in [dB]	6
σ_ϕ	The RMS angular spread in [rad]	24, 62, 139, 140
σ_τ	The RMS delay spread in units of [s]	19, 22, 61
τ	Delay of a MPC in units of [s]	7, 22, 28, 29, 48, 49, 51
θ	Elevation angle in [rad]. θ can be used for θ^d or θ^a	24, 32, 110, 142
ϑ	Polarization rotation angle in [rad]	35, 36
θ^a	Elevation angle of arrival (EoA) in [rad]	23, 24, 26, 28
θ^d	Elevation angle of departure (EoD) in [rad]	23, 24, 26, 27
ζ	A coefficient describing additional shadowing within a PDP	22
$\mathbf{a}$	Vector pointing from the position of the LBS to the Rx position	28
B	Bandwidth in units of [Hz]	18, 48, 51
$\mathbf{B}$	LSP map represented as a matrix with real-valued coefficients	20
$\mathbf{b}$	Vector pointing from the Tx position to the position of the LBS	28
C	Capacity in [bps/Hz]	2, 65, 66
c	Speed of Light	28, 29
$\mathbf{c}$	Representation of the departure or arrival angle in Cartesian coordinates	34
c_ϕ	The scenario-dependent cluster-wise RMS angular spread in [degree]	26
$\mathcal{CN}$	Complex normal distribution $\mathcal{CN}(\mu, \sigma^2)$ with mean μ and STD σ	6, 48, 49
d	Length of a propagation path in [m]	6, 28, 40, 84, 120
$\mathbf{D}$	Diagonal matrix of singular values; $\mathbf{D}_n = \text{diag}\{\omega_{n,1}, ..., \omega_{n,n_\omega}\}$	67, 69
d_λ	Decorrelation distance in [m] where the autocorrelation falls below e^{-1}	20, 64

$\mathbf{e}_{r,s}$	Vector from the Rx position to Rx antenna element r at snapshot s	28
$\mathbb{E}$	Expected value	6, 52, 63, 66
$\mathbf{F}$	Polarimetric antenna response	32, 35, 38, 54
f_c	Carrier frequency in units of [Hz]	12
f_n	Position of the nth OFDM pilot relative to the beginning of the FR in [Hz]	48, 51, 65
f_S	Sampling Rate in [samples per meter]	18
f_T	Sampling Rate in [samples per second]	18
g	Channel coefficient in time domain	7, 38, 51, 60
$\mathbf{G}$	Matrix of complex-valued channel coefficients in time domain	7, 48, 49, 51
h	Channel coefficient in frequency domain	6, 7, 60
$\mathbf{H}$	Matrix of channel coefficients in frequency domain	2, 6, 7, 48, 49, 65, 71
$\mathbf{h}$	Vector of channel coefficients in frequency domain	6, 52
$\hat{\mathbf{H}}$	Effective reconstructed matrix of channel coefficients in frequency domain	49, 51, 69
$\hat{\mathbf{h}}$	Effective reconstructed vector of channel coefficients	52
$\hat{h}$	Effective reconstructed channel coefficient in frequency domain	51
i	Sector or BS index; $i \in \{1, 2, ..., n_i\}$	67
$\mathbf{I}$	Identity matrix $\mathbf{I}_x$ of size $x \times x$	2, 3, 6, 65, 68, 69, 71
$\mathbf{J}$	Jones vector	33, 55
K	Ricean K-Factor, linear scale	22, 139, 140
k	Filter coefficient index	20, 69
$K^{[\text{dB}]}$	Ricean K-Factor, logarithmic scale	140
L	Number of paths	22, 49, 60, 139, 140
l	Path index, $l \in \{1, 2, ..., L\}$	7, 22, 27, 28, 49, 61
M	Number of sub-paths	57
m	Sub-path index, $m \in \{1, 2, ..., M\}$	7, 26, 27, 57
$\mathbf{M}$	Polarization coupling matrix	49, 58
m_l	Normalized delay of a MPC	49
N	Number of OFDM carriers	48, 49, 60, 65
n	Carrier index; $n \in \{1, 2, ..., N\}$	48, 49, 66
$\mathcal{N}$	Normal distribution $\mathcal{N}(\mu, \sigma^2)$ with mean μ and STD σ	6, 22–25, 37, 139
n_i	Number of BSs or sectors	4, 67, 68
n_ω	Number of singular values	69
n_r	Number of receive antennas	2, 48, 49, 60, 66, 69
n_t	Number of transmit antennas per BS	2, 48, 49, 60, 65, 66, 68
n_u	Number of users	3, 66, 67
P	Power	22, 52, 65, 66, 139, 140
$\mathbf{P}$	Transmit covariance matrix for the BC	3, 71
q	Singular value index	69
$\mathbf{Q}$	Receive covariance matrix for the MAC	68, 71
r	Receive antenna index; $r \in \{1, 2, ..., n_r\}$	6, 27, 49
$\mathbf{R}$	Rotation matrix	34, 35
$\mathbf{r}$	Vector pointing from the Tx position to the Rx position	28, 31
r_τ	Proportionality factor to trade between delays and path powers	22
s	Snapshot index $s \in \{1, 2, ..., S\}$	27
t	Transmit antenna index; $t \in \{1, 2, ..., n_t\}$	6, 27, 49
u	User index; $u \in \{1, 2, ..., n_u\}$	67
$\mathbf{U}$	Correlation matrix	7
$\mathcal{U}$	Continuous uniform distribution $\mathcal{U}(a, b)$ with minimum a and maximum b	22, 32
v	Speed in [m/s]	18
$\mathbf{V}$	Matrix of AWGN samples	48, 49

$\mathbf{v}$	Vector of AWGN samples	2, 71
X	A random variable	22, 38, 139
$\mathbf{X}$	Matrix containing the inter-parameter correlation values	21
$\mathbf{x}$	Vector of transmitted symbols	2, 71
Y	A random variable	139
$\mathbf{Y}$	Matrix of received symbols (e.g. raw channel coefficients from measurements)	48, 49
$\mathbf{y}$	Vector of received symbols	2, 71
$\tilde{\mathbf{Y}}$	Matrix of processed received symbols	51
$\tilde{y}$	Processed received symbol	51
Z	A random variable	22, 32

Glossary

array antenna 4

An array antenna is a set of individual antennas (array antenna elements) connected together in such a way that their individual currents are in a specified amplitude and phase relationship. The individual antenna elements are in rigid arrangement with respect to each other.

base station (BS) 16

The term base station (BS) refers to a fixed transmitter which utilizes one or more transmit antennas to serve one or more MTs. BSs might further use *sectors* to increase the capacity. Usually, BSs operate independent of each other which might lead to inter-BS interference if they use the same time and frequency resource.

cell 71, 115, 116

Synonym for *sector*.

cluster 7, 37, 41

A cluster describes an area where many scattering events occur simultaneously, e.g. at the foliage of trees or at a rough building wall. In the channel model, each scattering cluster is approximated by 20 single reflections. Each of those reflections has the same propagation delay.

cooperation cluster 4, 117, 127, 131

A cooperation cluster is a set of BSs using "*joint transmission*" to serve MTs on the same time and frequency resource.

drifting 27

Drifting occurs within a small area (about 20-30 m diameter) in which a specific "*cluster*" can be seen from the MT. Within this area the cluster position is fixed. Due to the mobility of the terminal the path length (resulting in a path delay) and the arrival angels change slowly, i.e. they "*drift*".

joint transmission 67, 71, 117, 130

Joint transmission denotes a technique where several BSs jointly serve multiple users on the same time and frequency resource. Thus, the antennas of the BSs in the "*cooperation cluster*" appear as a distributed antenna array. This allows for a significant reduction of the inter-cell interference and thus increases the spectral efficiency. However, the joint signal processing requires that CSI and user data are available at each BS. This puts a significant burden on the backhaul.

large-scale parameter (LSP) 18, 59, 84, 119
The term "*large scale parameter*" refers to a set of specific properties of the propagation channel. Those are the "*delay spread*", the "*K-factor*", the "*shadow fading*", the "*cross-polarization ratio*", and four "*angular spread*"-values. Those properties can be extracted from channel sounding data. If a large amount of channel measurements is available for a specific propagation *scenario* and the LSPs can be calculated from those channels, statistics of the LSPs, e.g. their distribution and correlation properties can be obtained. A complete set of such statistical properties forms a "parameter table" that characterizes the *scenario*.

massive MIMO 71, 130
Massive multiple-input multiple-output (MIMO) uses a high number of transmit antennas (several hundred) to multiplex data for several users on a single time-frequency resource. The radiated energy is focussed toward the intended user while minimizing intra and intercell interference.

mobile terminal (MT) 16
Mobile terminals (MTs) are mobile receivers with one or more receive antennas. They are usually assigned to a serving BS which delivers data to the terminal.

multipath component (MPC) 16, 49, 78
Synonym for *path*.

path 7, 23, 28, 39, 41, 86
A path describes the way that a signal takes from the transmitter to the receiver. In the channel model, there is usually a direct, or LOS path, and several indirect, or NLOS paths. Indirect paths involve one or more scattering events which are described by clusters. However, paths do not describe single reflections but combine sub-paths that can not be separated in the delay domain. Usually, the channel model uses 6-25 paths to describe the propagation channel.

scatterer 7, 27, 36
A scatterer describes a single reflection along a NLOS propagation path. Usually, several scatterers with a similar propagation delay and a narrow angular spread are combined into a "*(scattering) cluster*".

scattering cluster 8, 16
Synonym for *cluster*.

scenario 5, 19, 81
In this thesis, the term *scenario* refers to a specific propagation environment such as "Urban macro-cell", "Urban satellite", "Indoor hotspot", etc. Usually, each propagation environment can be further split into LOS and NLOS propagation (e.g. "Urban macro-cell LOS" and "Urban macro-cell NLOS"), both of which might have very different properties. In the channel model, each *scenario* is fully specified by a parameter table.

sector 67, 115, 116, 118

A BS might use directional antennas to separate MTs located in different directions from the BS. The orientations of the sectors are fixed and it is assumed that sectors operate independent of each other. If a BS has only one sector, the terms *sector* and *base station* are synonym.

segment 17, 27, 78, 80, 118

Segments are parts of a user trajectory in which the LSPs do not change considerably and where the channel keeps its WSS properties. Typical segment lengths are 5-30 m. It is assumed that within a segment, the scattering clusters are fixed.

sub-path 8, 26, 39

A sub-path is the exact way that a signal takes from the transmitter to the receiver. It contains at least one reflection. However, normally the channel model uses two scatterers (resulting in two reflections) to create a sub-path. 20 sub-paths are combined to a path. The LOS path has no sub-paths.

time evolution 16, 27

Time evolution describes how the propagation channel changes (or evolves) with time. In the channel model, two effects are used to describe this time-dependency: *drifting* and the birth and death of scattering clusters during the transition between *segments*. The propagation environment is considered static and, thus, the model includes time-evolution only when the receiver is moving.

user 19, 64, 67, 68, 80, 104, 106, 117

Synonym for *mobile terminal*.

1 Introduction

There has been a tremendous growth of mobile data traffic in recent years. This is due to the widespread use of smart phones, tablet computers and other mobile devices which are connected to the internet everywhere and anytime. As a result, worldwide mobile data traffic is expected to grow 10-fold from 2014 to 2019, three times faster than fixed internet traffic, reaching more than 290 exabytes per year by the end of 2019 [42]. As a consequence, the design of future fifth generation (5G) cellular networks will break with the conventional approaches, both on the architectural and the component level [43]. The base station density is increasing rapidly. This is leading to heterogeneous networks where the concept of a *cell* as the fundamental unit of the radio access network starts to disappear. A mobile device will be connected to the network through different nodes simultaneously, each having different transmit powers and coverage areas, operating at different frequencies, and using different protocols and standards. The need for additional spectrum to satisfy the huge data rates leads to the coexistence of radically different propagation characteristics within the same system such as at millimeter wave frequencies above 30 GHz. In order to overcome the huge propagation loss at such high frequencies, and to overcome the tremendous inter-cell interference caused by the high base station density at centimeter wave frequencies, massive multiple-input multiple-output (MIMO) [44, 45] proposes utilizing a very high number of antennas (up to several hundred) to focus the radiated energy toward the intended directions. This leads to major architectural changes and new deployment approaches for the base stations (BSs). The performance of these emerging technologies is highly affected by the wireless propagation channels. Therefore, understanding the properties of wireless channels in time and space is essential in order to assess the performance of these new technologies and guide the development of new communication standards.

There are several approaches to characterize wireless channels. Probably the best way is by measurements. This requires that dedicated transmit and receive equipment (*e.g.*, antennas, channel sounders, *etc.*) needs to be developed. Then, measurement campaigns need to be planned, executed and evaluated in realistic scenarios where the locations of the BSs and the mobile terminals (MTs) match the real network setup later on. Performing such measurements is a complicated process that requires significant financial, manpower and data-processing resources. In addition, the benefit of such early trials is limited from a performance evaluation point of view since it is only possible to characterize a few isolated links. Hence, it is difficult, if not impossible, to correctly predict the achievable data rates for an entire network consisting of thousands of BSs and MTs. Therefore, measurements are usually combined with simulation studies taking the channel and interference characteristics into account. However, these so-called system-level simulations require detailed knowledge of the underlying propagation conditions.

In order to assess the performance of the emerging 5G technologies, continuous research is needed to develop sophisticated channel models that accurately predict the properties of the propagation channel. This includes different propagation scenarios (*e.g.*, indoor, outdoor, outdoor-to-indoor, satellite, *etc.*), a large number of MTs and BSs, heterogeneous deployments (*e.g.*, combinations of conventional macro-cell BSs, micro-cell hotspots, and satellite overlays), massive MIMO antenna configurations with several hundred antennas, various mobility models, and so on. Well-established geometry-based stochastic channel models (GSCMs) such as the 3rd genera-

tion partnership project (3GPP) spatial channel model (SCM) [46], the Wireless World Initiative for New Radio (WINNER) model [47, 48], the 3GPP-3D model [49], and the European Cooperation in Science and Technology (COST) 273/2100 channel model [50, 51] have been reliable tools for system-level studies. However, future wireless systems require a continuous evolution of the current models in order to fulfill the design and planning requirements. According to [45], a realistic performance assessment of massive MIMO systems requires channel models that reflect the true behavior of the radio channel (*i.e.*, the propagation channel including effects of realistic antenna arrangements). State of the art GSCMs allow the separation of antenna and propagation influences. Hence, they are ideal candidates for the evaluation of massive MIMO systems since they are scalable in the spatial domain. However, none of the current publicly available models has been tested against measured data in a representative setup and essential features such as the time evolution of the channel and spherical wave propagation are missing.

In this chapter, a short introduction of MIMO wireless communications is given. Then, some fundamental concepts for channel measurements and the ideas behind existing channel models are presented. Lastly, the objectives and contributions of this thesis are outlined.

1.1 MIMO Wireless Communications

Multiple-input multiple-output (MIMO) involves multiple antennas, both at the transmitter and receiver, to increase the capacity of wireless systems. Initial investigations on the increased performance of multi-antenna systems have been published by J. Winters already in 1984 [52, 53]. Ten years later, spatial multiplexing was introduced by Telatar [54] and Foschini [55]. In these concepts, parallel data streams are transmitted between a multi-antenna transmitter and a multi-antenna receiver on the same time and frequency resource. The huge capacity predictions made by those early findings made MIMO a very popular research area in the following years.

Single-user MIMO MIMO propagation channels are at the core of each MIMO system. Essentially, a MIMO channel is described by a channel matrix $\mathbf{H}$ which contains the complex-valued baseband channel coefficients. The relation between the inputs and the outputs of a MIMO channel with n_r receive and n_t transmit antennas can be expressed as

$$\underbrace{\begin{pmatrix} y_1 \\ y_2 \\ \vdots \\ y_{n_r} \end{pmatrix}}_{\mathbf{y}} = \underbrace{\begin{pmatrix} h_{1,1} & h_{1,2} & \cdots & h_{1,n_t} \\ h_{2,1} & h_{2,2} & \cdots & h_{2,n_t} \\ \vdots & \cdot & \ddots & \vdots \\ h_{n_r,1} & h_{n_r,2} & \cdots & h_{n_r,n_t} \end{pmatrix}}_{\mathbf{H}} \cdot \underbrace{\begin{pmatrix} x_1 \\ x_2 \\ \vdots \\ x_{n_t} \end{pmatrix}}_{\mathbf{x}} + \underbrace{\begin{pmatrix} v_1 \\ v_2 \\ \vdots \\ v_{n_r} \end{pmatrix}}_{\mathbf{v}}, \tag{1.1}$$

where the vector $\mathbf{x}$ contains the transmitted symbols and the vector $\mathbf{y}$ the received symbols. The vector $\mathbf{v}$ contains additive white Gaussian noise (AWGN). The MIMO channel determines the received signal and the performance of a multi-antenna communication system. Provided that the channel matrix $\mathbf{H}$ is properly normalized with respect to the signal to noise ratio (SNR), one can calculate the capacity C measured in units of bps/Hz as [54]

$$C = \log_2 \det \left(\mathbf{I}_{n_r} + \frac{\sigma}{n_t} \mathbf{H}\mathbf{H}^H \right), \tag{1.2}$$

where $\mathbf{I}_{n_r}$ is the identity matrix of size $n_r \times n_r$, σ is the SNR and $\mathbf{H}^H$ is the conjugate transpose (or Hermitian transpose) of $\mathbf{H}$. In this equation, the transmitted power remains constant. Thus, the SNR gets divided by the number of transmit antennas n_t. If the propagation channel has enough degrees of freedom (*i.e.*, if the matrix $\mathbf{H}$ is well conditioned), the capacity scales linearly with $\min(n_t, n_r)$ and logarithmic with σ which can lead to enormous capacity gains when the number of antennas is large. However, the limiting factor is the propagation channel. Again, understanding the channel is essential to bring the theoretic gains into practical systems.

Multi-user MIMO Another ten years later, a paradigm shift was needed when MIMO was applied to multi-user channels [56]. When using spatial multiple access to serve several users on the same time and frequency resource, the additional antennas can be used to suppress multiuser interference. In the downlink broadcast channel (BC) there are n_u multi-antenna users, each having a receive signal

$$\mathbf{y}_u = \underbrace{\mathbf{H}_u \cdot \mathbf{x}_u}_{\text{own signal}} + \underbrace{\sum_{\forall \bar{u}, \bar{u} \neq u}^{n_u} \mathbf{H}_u \cdot \mathbf{x}_{\bar{u}}}_{\text{interference}} + \underbrace{\mathbf{v}_u}_{\text{noise}} . \tag{1.3}$$

The problem is that, unlike in conventional MIMO, each user does not only receive its own signal but also the signals intended for the other users. The optimum transmit strategy involves a theoretical preinterference cancellation technique known as dirty-paper coding (DPC) combined with scheduling and power loading [57]. With DPC, the system capacity is

$$C = \max_{\mathbf{P}_u} \log_2 \det \left(\mathbf{I}_{n_r} + \sum_{u=1}^{n_u} \mathbf{H}_u \cdot \mathbf{P}_u \cdot \mathbf{H}_u^H \right) , \tag{1.4}$$

where $\mathbf{P}_u$ is the covariance matrix of the optimal spatial transmit filter. However, this poses some problems. Although it is possible to calculate the optimal covariance matrices $\mathbf{P}_u$ from the individual user channels [58], it is generally not possible to obtain transmit filters that achieve the DPC capacity. In addition, realizing the theoretic gains in practice requires that the BS has knowledge of the user's channel coefficients. To circumvent this problem and to reduce the feedback overhead, combining simplified precoding methods (such as zero-forcing or maximum ratio transmission) with scheduling is a promising approach. Nevertheless, comparing the performance of the many heuristic approaches requires system-level simulations. As for single-user MIMO, channel models must contain all relevant effects to correctly predict the performance of such systems. Especially, the inter-dependency of the user channels is of importance here. For example, physically closely spaced users often experience very similar propagation conditions. Simple models often fail to include these effects which might lead to wrong predictions of the capacity and system performance.

Joint transmission One problem that is not addressed by multi-user MIMO is inter-cell interference. Inter-cell interference occurs when several neighboring BSs use the same time and frequency resources. The classic approach to circumvent this problem is to use frequency-reuse to prevent neighboring BSs from using the same frequency band. However, this dramatically reduces the spectral efficiently in the network since only a fraction of the spectrum is available to each BS. A frequency-reuse factor of one has been introduced in the third generation (3G) mobile communication systems for effectively allowing all BS to use the full spectrum. On the other hand, this comes at the price of dramatically increased interference levels at the cell-edge.

In order to study the influence of such interference, the additional BSs must be included in the system model. As for multi-user MIMO, there are n_u multi-antenna users. However, in addition to the intra-cell interference introduced in (1.3), there are also n_i BSs operating on the same time-frequency resource. Hence, the receive signal becomes

$$\mathbf{y}_u = \underbrace{\mathbf{H}_{u,i} \cdot \mathbf{x}_{u,i}}_{\text{own signal}} + \underbrace{\sum_{\forall \bar{u}, \bar{u} \neq u}^{n_u} \mathbf{H}_{u,i} \cdot \mathbf{x}_{\bar{u},i}}_{\text{intra-cell interference}} + \underbrace{\sum_{\forall \bar{i}, \bar{i} \neq i}^{n_i} \mathbf{H}_{u,\bar{i}} \cdot \mathbf{x}_{\bar{u},\bar{i}}}_{\text{inter-cell interference}} + \underbrace{\mathbf{v}_u}_{\text{noise}} . \tag{1.5}$$

In this equation the index i indicates the serving BS and the index $\bar{i}$ the interfering ones. When the BSs are allowed to cooperate, they can jointly process the user's signals [59, 60]. Thus, several BSs form a cooperation cluster and serve users on the same time and frequency resource by effectively forming a so-called *distributed antenna system* [61]. In this case, inter-cell interference is transformed into intra-cell (or intra-cluster) interference which can be handled by precoding in the same way as for multi-user MIMO. However, in a full-scale network there will always be out-of-cluster interference that limits the achievable performance of such an approach. Joint transmission adds additional requirements to the channel models, *i.e.*, the inter-dependency of the channels originating from different BSs must be correctly modeled.

Massive MIMO Another way to handle the inter-cell interference that became very popular in the recent years is to scale up the number of antennas per BS [44, 45]. Massive MIMO uses array antennas with an order of magnitude more elements (100 or more) than in conventional MIMO systems. The number of users served by such a system is much smaller than the number of transmit antenna elements. By doing so, it is possible to create narrow beams that direct the transmit power directly to the users. This breaks with the classical MIMO approach of having approximately the same number of transmit and receive antennas in the cell. With massive MIMO, both inter-cell and intra-cell interference will be reduced. However, as for joint transmission, interference is still present and needs to be included in the evaluation.

1.2 Characterization of the MIMO Channel

1.2.1 Channel Measurements

The most straightforward way to characterize the MIMO propagation channels is by channel measurements, also known as channel sounding. A transmitter (the channel sounder) sends out a known signal that is received by a receiver. By comparing the received signal with the known transmit signal, one can calculate the so-called channel impulse response (CIR) which captures the properties of the propagation channel between a single transmit and receive antenna element. For example, one can estimate parameters such as the delay spread (DS) which is caused by reflections of the transmitted signal at objects in the propagation environment from the CIR.

When is comes to MIMO channels, the CIRs of different pairs of transmit and receive antenna elements are different from each other. This is caused by the multiple reflections of the transmitted signal, also known as multipath propagation, and by differences in the orientation and positions of the antenna elements. Multipath propagation is one of the major causes for the capacity increase in MIMO systems since it is possible to use these different propagations paths

to transmit several signals simultaneously. To capture these effects accurately, one needs specially designed array antennas that can resolve signals from all directions. The antenna elements must be arranged in a way that makes it possible to calculate the direction of departure of an outgoing wave at the transmitter and the direction of arrival at the receiver. Thus, antenna design is a major part of planning a MIMO channel measurement campaign.

Due to the large amount of combinations of transmit and receive antenna elements (up to several hundred), it is practically impossible to capture all the CIRs simultaneously. Thus, each antenna pair is measured separately. Fast switches at the transmitter and receiver are used to capture all MIMO subchannels in fast succession. However, this poses restraints on the measurements since switching through several hundred antenna pairs requires time. It must be ensured that the complete MIMO channel remains reasonably static during the measurement time. A complete set of MIMO subchannels, often measured with up to hundreds of MHz bandwidth, is called a *snapshot*. This is similar to a photograph which is also a static image of a changing event. If the transmitter, the receiver or any object in the environment that causes reflections of the transmitted signal is moving too fast, it becomes impossible to resolve its properties (such as the directions of departure and arrival) later on when the recorded data is analyzed. Similarly, a photograph becomes blurry when the exposure time is too long.

Once the channel sounder parameters, the antennas and the allowable speed are fixed, a suitable scenario has to be chosen. The term *scenario* refers to a specific propagation environment such as *urban-macrocell*, *urban satellite*, *indoor hotspot*, *etc.* Usually, each propagation environment can be further split into LOS and NLOS propagation (*e.g.*, *urban-macrocell LOS* and *urban-macrocell NLOS*), both of which might have very different properties. Different scenarios often pose specific requirements on a measurement campaign. For example, characterizing satellite channels requires access to a satellite and suitable interfaces to the channel sounder. Urban-macrocell scenarios require access to the rooftops of buildings in order to put the transmitter or receiver there. Measurements in rural areas require high-power amplifiers and access to transmit towers to cover the large distances common for such scenarios. It is not unusual that the antennas, channel sounders and other equipment such as vans, trolleys, amplifiers, *etc.*, are custom-build for just one specific measurement campaign. This often results in very substantial financial and manpower effort needed for such campaigns.

Once the measurements are finished, a substantial amount of data has been recorded (often up to several terabytes). In the next step, relevant propagation parameters are extracted from the raw data. This requires sophisticated algorithms such as described in [62, 63] to calculate the departure and arrival angles, delays and polarization of individual multipath components (MPCs). Then, these individual measures are analyzed statistically in order to find the characteristic properties for the entire scenario (such as the possible range for the delay spread, *etc.*). In the next step, channel models are derived in order to generalize the findings from the measurements and to enable simulations studies to incorporate multiple transmitters and receivers simultaneously.

1.2.2 Correlation-based Stochastic Channel Models

Correlation-based stochastic channel models describe wireless channels based on statistics of parameters such as path loss, correlation properties between antenna elements, *etc.* They simplify the MIMO channel by using a white Gaussian channel with specific correlation properties at the transmitter and receiver.

Rayleigh i.i.d. model Probably the simplest MIMO channel model is the Rayleigh i.i.d. model which assumes that the entries of the MIMO channel matrix $\mathbf{H}$ are independent and identically distributed (i.i.d.). Hence, a single MIMO channel coefficient between transmit antenna element t and receive element r is modeled as

$$h_{r,t}^{[\text{i.i.d}]} \sim \mathcal{CN}(0,1) \quad \text{and} \quad \mathbb{E}\left(\mathbf{H}\mathbf{H}^H\right) = \mathbf{I} \tag{1.6}$$

A downside of this model is that it is only valid for narrow-band MIMO channels. For wide-band MIMO channels one can use a collection of uncorrelated narrow-band channels. Due to its simplicity, this model is used as a benchmark throughout this thesis.

When using the Rayleigh model, it is important to separate the spatial characteristics (*i.e.*, the effects caused by multipath propagation) from the influence of the received power. The received power is mainly due to the path gain (PG) and the shadow fading (SF). Hata [64] presented a simple model where the PG scales with the logarithm of the distance d (in units of meters) between BS and terminal

$$\text{PG}^{[\text{dB}]} = -A \cdot \log_{10} d_{[\text{m}]} - B + X \quad \text{with} \quad X \sim \mathcal{N}\left(0, {\sigma_{\text{SF}}}^2\right). \tag{1.7}$$

A and B are scenario-specific coefficients that are calculated from the measurements. X is an additional random variable that describes the SF with σ_{SF} as the SF standard deviation. The modified Rayleigh model then follows from

$$h_{r,t} = \sqrt{10^{0.1 \cdot \text{PG}^{[\text{dB}]}}} \cdot h_{r,t}^{[\text{i.i.d}]}. \tag{1.8}$$

The power directly determines the SNR σ since each communication system is limited by a certain noise level at the receiving end. Since the channel capacity scales logarithmic with σ, a 3 dB increase in SNR (which is equivalent to doubling the received power) adds 1 bps/Hz in capacity. On the other side, if the channel matrix is well conditioned, the MIMO capacity (1.2) scales linearly with $\min(n_t, n_r)$ while keeping the total transmit power constant. Thus, doubling the number of antennas at the transmitting and the receiving end also doubles the capacity. However, in reality, there is a tradeoff between the two effects. A high received power often implies a free line of sight (LOS) propagation path in between transmitter and receiver. This might cause the so-called Keyhole effect [65, 66] which reduces the effective rank of the MIMO channel matrix to one (*i.e.*, there is no capacity increase with MIMO).

Keyhole model While the Rayleigh model describes uncorrelated MIMO channels and thus assumes optimal propagation conditions, the Keyhole model does the opposite. The Keyhole effect [65, 66] causes all signals at the receive antennas to be fully correlated. Therefore, no additional capacity can be realized by the additional antennas. Dmitry Chizhik [66] pictures this by placing a screen with a small keyhole punched through it to separate the regions containing the receiving and transmitting array antenna. The MIMO channel matrix of such a model follows from

$$\mathbf{H}^{[\text{keyhole}]} = \sqrt{10^{0.1 \cdot \text{PG}^{[\text{dB}]}}} \cdot \frac{1}{2} \cdot \mathbf{h}_r \cdot \mathbf{h}_t^T \quad \text{with} \quad h = \mathcal{N}(0,1) + j\mathcal{N}(0,1). \tag{1.9}$$

The vector $\mathbf{h}_r$ has n_r elements obtained from a complex-valued normal distribution. Likewise, $\mathbf{h}_t$ has n_t elements. The resulting channel matrix has only one spatial degree of freedom. As for the Rayleigh model, it is important to include the received power (and thus the SNR) in order to obtain meaningful results. This model also serves as a benchmark throughout this thesis since it provides a lower bound on the achievable MIMO capacity.

Kronecker Model Another very popular channel model is the Kronecker model [67] which adds correlation to the transmitter and receiver side. It is thus a simple extension of the Rayleigh i.i.d. model. The channel matrix is obtained by

$$\mathbf{H}^{[\text{kronecker}]} = \left(\mathbf{U}^{[\text{Rx}]}\right)^{1/2} \cdot \mathbf{H}^{[\text{iid}]} \cdot \left(\mathbf{U}^{[\text{Tx}]}\right)^{1/2}, \tag{1.10}$$

where $\mathbf{H}^{[\text{iid}]}$ is the Rayleigh i.i.d. channel matrix from (1.6). The additional correlation matrices $\mathbf{U}$ are estimated from the measured channel matrices with $\mathbf{U}^{[\text{Rx}]} = \mathbb{E}\left(\mathbf{H}\mathbf{H}^H\right)$ and $\mathbf{U}^{[\text{Tx}]} = \mathbb{E}\left(\mathbf{H}^H\mathbf{H}\right)^T$. The Kronecker model is only applicable to narrowband channels, and M. Zhu [68] questions if this simple model can correctly incorporate the correlations effects for large array antennas such as used for massive MIMO. In addition, the correlation-based channel models do not model the propagation process directly but rely on the correlation matrices obtained from measurements. It is thus very difficult, if not impossible, to separate propagation and antenna effects which limits the usability of such models. As a consequence, more complex models that incorporate real-world propagation effects have been developed in the resent years. Those models are knows under the acronym geometry-based stochastic channel models (GSCMs).

1.2.3 Geometry-based Stochastic Channel Models

Cluster Concept Clusters are at the foundation of all GSCMs. The signal that is transmitted by a BS inevitably interacts with objects in the environment. Generally, those objects, *e.g.*, the foliage of trees, rough building walls, office furnishings, *etc.*, do not simply reflect the signal but scatter it in many directions. Hence, these so-called scatterers (the origin of MPCs) appear to be "visible" in a relatively large area, *i.e.*, the scattered signal can be received by a receiver that is located within the visibility area of a scatterer. Another important aspect is that scatterers often appear to be spread out in space [69]. Hence, a MPC does not generally come from a single "scattering"-point but from a confined volume of space. One of the earliest well-known cluster-based channel model that captures this was reported by Saleh-Valenzuela in 1987 [70]. In this model, the time-domain CIR $g(\tau)$ is represented by a series of infinitely short pulses that are described by Dirac delta functions or δ-functions[1].

$$g(\tau) = \sum_{l=0}^{\infty}\sum_{m=0}^{\infty} \alpha_{l,m} \cdot \exp\left(j\psi_{l,m}\right) \cdot \delta(\tau - \tau_l - \tau_{l,m}) \tag{1.11}$$

A MPC (caused by reflections at a scattering cluster) arrives at time τ_l and is split into m subcomponents, each arriving at a later time $\tau_l - \tau_{l,m}$. The parameters α and ψ are the amplitude and phase of the MPC. The parameters of the model are generated randomly such that the resulting CIRs match measured data.

The Saleh-Valenzuela model only considers the arrival times of the MPCs. However, for MIMO channels the departure and arrival directions are also important to correctly predict the channel matrix. Hence, the entire propagation process is included in later models. This is done by introducing *paths* that describe the way that a signal takes from the transmitter to the receiver. In the models, there is usually a direct line of sight (LOS) path and several indirect non-line of sight (NLOS) paths. This is illustrated in Figure 1.1. Indirect paths involve one or more

[1] Geometry-based models usually generate the CIR in the time domain by directly modeling specific aspects of the propagation process. On the other hand, correlation-based models generate the (often narrow-band) CIR in the frequency domain. To distinguish between the two representations, time-domain channels are denoted by the symbol g for scalar channels and $\mathbf{G}$ for matrix channels. Likewise, the symbols h and $\mathbf{H}$ are used for frequency-domain channels. One representation can be transformed into the other by using the Fourier transformation.

scattering events which are described by scattering clusters. As in the Saleh-Valenzuela model, paths do not describe single reflections but are a combination of sub-paths. The main difference is that sub-paths cannot be separated in the delay domain, *i.e.*, they all have the same arrival time τ_l, but different arrival and departure angles.

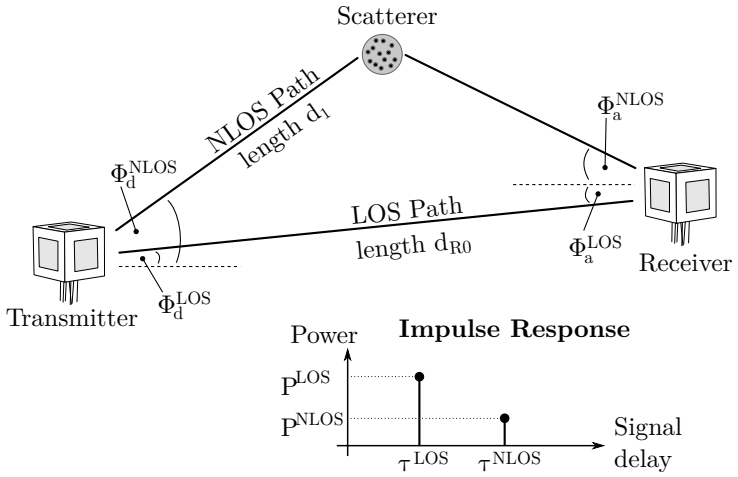

Figure 1.1: Simplified overview of the modeling approach used by GSCMs

SCM(E), WINNER-I/II, and IMT-advanced models Although there were already early studies on geometric channel models, they only became widely used when the 3GPP work on the evolution of the 3G mobile system started. The work on 3GPP-long term evolution (LTE), also known as the fourth generation (4G) of the mobile network, was kicked off with the radio access network (RAN) evolution work shop in November 2004 in Toronto, Canada. Later on, the use of MIMO with up to four antennas at the mobile side and four antennas at the BS side was agreed upon. One important requirement for this work were standardized channel models that can be used to evaluate and compare the different proposals against each other. This was provided with the 3GPP-SCM in 2003 [46]. In this model, BSs, MTs and scattering clusters are in one propagation plane. Hence, the SCM is a two-dimensional (2-D) model. It further supports six paths (each split into 20 sub-paths), 5 MHz bandwidth in the 2 GHz frequency band and three scenarios: Suburban Macro, Urban Macro, and Urban Micro. The Urban Micro scenario is further differentiated in LOS and NLOS propagation.

Parallel to the work in 3GPP, one of the first tasks of the Wireless World Initiative for New Radio (WINNER) project, which started in January 2004, was to provide a reference implementation of the SCM. This model was then extended in order to support larger bandwidths of up to 100 MHz, short-term system-level time-variability, additional parameters for the 5 GHz band, and LOS support for macro-cell scenarios. This model was introduced in 2005 and became widely known under the acronym SCM-E [71].

The WINNER-I model [72] was released shortly after the SCM-E. This model is antenna independent, *i.e.*, different antenna configurations and different element patterns can be used. Parameter tables are provided for indoor office and hotspot scenarios, stationary feeders, and rural macro-cell scenarios. An additional model for the distance-dependent LOS probability was introduced for all supported scenarios. However, the short-term system-level time-variability from the SCM-E was not adopted for the WINNER models.

The WINNER-II model, a further evolution of the WINNER-I model, was released in 2007 [47]. This model supports even more propagation conditions like outdoor-to-indoor and indoor-to-outdoor scenarios, and it supports elevation angles in indoor scenarios. The model sup-

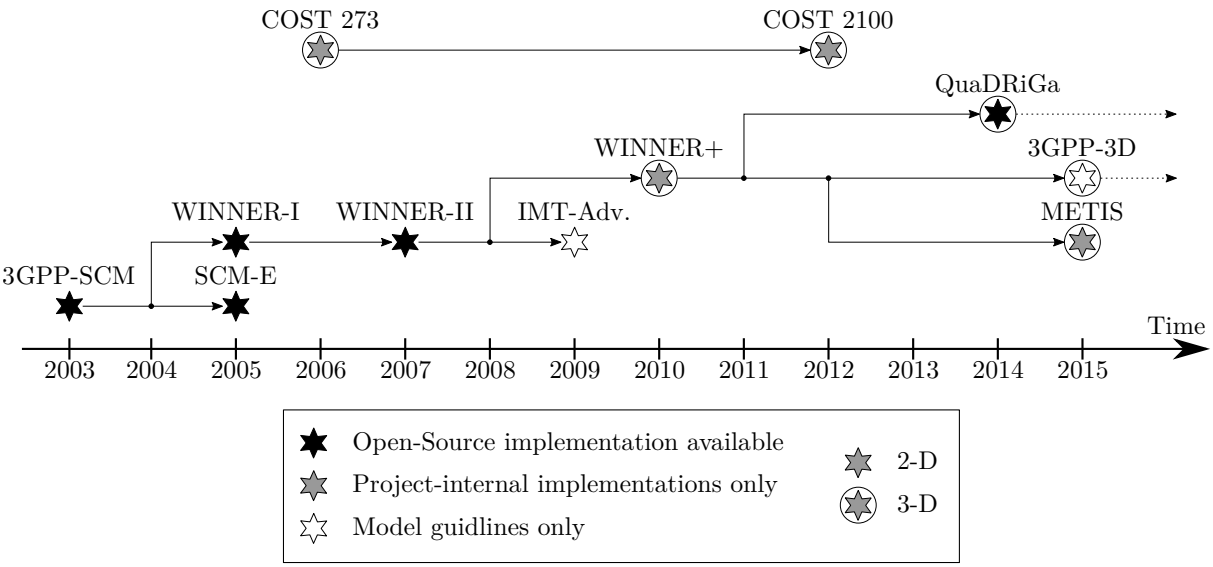

Figure 1.2: Evolution of GSCMs

ports scenario-dependent polarization modeling which improves the accuracy for cross-polarized MIMO antennas. The parameter tables have been reviewed and additional measurements have been done in order to cover the complete 1-6 GHz frequency range. In addition, large-scale parameters (LSPs) now have a spatial correlation which enables to model to be used in multi-user MIMO scenarios.

For a long time, the SCM and WINNER models have been the de-factor standard for geometry-based channel modeling. This is also due to the fact that open-source reference implementations of all the models are available to the general public on the projects website [73]. Therefore, the WINNER-II model was also taken up by the International Telecommunication Union (ITU) as a baseline for the evaluation of radio interface technologies for IMT-Advanced in 2009 [74]. The core part of this so-called IMT-Advanced channel model is identical to the WINNER-II model. An additional extension module enhances the capabilities of the model to support variable BS antenna heights, street widths, and city structures.

WINNER+ model One major limitation of the early GSCMs was that they are only defined for 2-D coordinates. Although this is sufficient for simple MIMO schemes, it was generally not possible to study the effects of larger array antenna structures and beamforming approaches. Hence, another extension of the WINNER project, known as WINNER+, had the aim to extend the existing WINNER-II model in order to support three-dimensional (3-D) propagation effects. This was a major upgrade because everything had to be modeled in 3-D: antennas, scattering clusters, BS and MT positions, *etc.* The new model needed 18 additional parameters (50 compared to 32 for the WINNER-II model). Therefore, a large amount of additional measurements needed to be done to derive the required parameters. The project concluded in 2010 with a report containing the model guidelines and extended parameter tables [48]. However, a publicly available implementation of the channel model was never released.

3GPP-3D channel model The interest in 3-D GSCMs increased significantly when the work on the fifth generation (5G) of the mobile network began. Again, as for the 4G systems, a standardized channel model was needed to compare standardization proposals. New technologies, such as for example massive MIMO, use planar array antennas with several antenna elements

stacked on top of each other. This allows the BSs to steer narrow beams to the positions of the MTs in azimuth and elevation direction. One major requirement to evaluate such systems is a 3-D channel model. Hence, 3GPP worked on a successor of the SCM starting in late 2012 and finishing in mid-2015 with a specification of a 3-D channel model, commonly referred to as the 3GPP-3D model [49]. This model is defined for the 2 GHz band at a relatively narrow bandwidth of 10 MHz. It comes with consolidated parameters for the two most commonly used scenarios: urban-macrocell (UMa) and urban-microcell (UMi). Both scenarios are further split into LOS, NLOS and outdoor-to-indoor (O2I) propagation. The core part of this model, *i.e.*, the small-scale-fading (SSF) model, is in large parts identical to the WINNER+ model. Hence, the same parameter tables can be used and similar functionality is provided. In addition to the small-scale-fading (SSF) model, 3GPP-3D specifies an antenna model, deployment scenarios, as well as path-loss models and parameter tables for UMa and UMi deployments.

METIS models The aim METIS project (acronym for "Mobile and wireless communications Enables for the Twenty-twenty Information Society") was to lay the foundation for the 5G mobile network. Much of the work on channel modeling has been done in parallel to the 3GPP-3D activities. The METIS models [75] consist of a map-based (deterministic) model, a stochastic model, and a hybrid model as a combination of both. The stochastic model is an evolution of the WINNER+ and 3GPP-3D model. It supports 3-D shadowing maps, millimeter-wave parameters, direct sampling of the power angular spectrum, and frequency dependent path loss models. Based on extensive measurement campaigns, channel parameters for below 6 GHz and 50 - 70 GHz bands are available.

COST 273 / 2100 model Parallel to the 3GPP-SCM and WINNER-I models, the European Cooperation in Science and Technology (COST) developed the COST 273 channel model [50] in 2005 as an evolution of the earlier COST 259 channel model by adding support for MIMO technologies. In this model, scattering clusters are geometrically placed in a 2-D propagation environment. MTs are assigned to specific clusters in order to model the interrelationship between the azimuth angles of arrival (AoAs) and azimuth angles of departure (AoDs). This concept is effective to maintain spatial consistency of the small-scale-fading, and it is able to evaluate the performance of MIMO beamforming and multi-cell transmission more accurately. However, the parameterization of the cluster parameters is challenging, and only three scenarios have been parameterized so far.

The COST 2100 channel model [51, 76] is a further evolution of the COST 273 channel model. It introduced the concept of visibility regions to model the scenario-variations. These regions make the evaluation of multi-cell and heterogeneous transmissions more practical by considering the visibility region of BSs from each MT. Although the multipath clusters were extended towards 3-D propagation environments in the COST 2100 channel model, the definition of the visibility regions is still in 2-D. There is also no open source implementation of the COST 2100 channel model until now.

QuaDRiGa model QuaDRiGa (acronym for "QUAsi Deterministic RadIo channel GenerAtor") was developed as an outcome of this thesis to enable the modeling of MIMO radio channels for specific network configurations such as indoor, satellite or heterogeneous configurations. The main concepts were published in [11, 12, 33]. QuaDRiGa contains a collection of features created in the SCM and WINNER channel models along with novel modeling approaches which enable quasi-deterministic multi-link tracking of user movements in changing environments. The

QuaDRiGa channel model has further extended features of spatial consistency to accurately evaluate the performance of massive MIMO and multi-cell transmission systems. All essential parts of the 3GPP-3D model [49] have been implemented in QuaDRiGa as well. Hence, the model can be used to evaluate 3GPP standardization proposals. However, there are some differences between the two models:

- **Coordinate system**
  The 3GPP-3D coordinate system is defined with respect to a spherical coordinate system where the zenith angle $\theta = 0°$ points to the zenith and $\theta = 90°$ points to the horizon. QuaDRiGa uses the geographic coordinate system where the elevation angle $\theta = 90°$ points to the zenith and $\theta = 0°$ points to the horizon. The conversion between the two is straightforward. To avoid confusion between the coordinate systems, 3GPP uses the term *zenith*, *i.e.*, zenith angle of arrival (ZoA), zenith angle of departure (ZoD), zenith angle spread of arrival (ZSA), zenith angle spread of departure (ZSD), while QuaDRiGa uses the term *elevation*, *i.e.*, elevation angle of arrival (EoA), elevation angle of departure (EoD), elevation angle spread of arrival (ESA), elevation angle spread of departure (ESD).

- **Delays and Path Powers**
  3GPP-3D uses a heuristically determined Ricean K-factor dependent scaling constant in order to adjust the delays in LOS scenarios (see [49], pp. 25). QuaDRiGa solves this differently by first assigning delays and path powers, including the Ricean K-factor (KF) power scaling. Then, the resulting DS is calculated and the path delays are scaled to the value from the large-scale fading (LSF) model. This avoids the heuristic scaling. See Section 2.2 for details.

- **Intra-Cluster Delay Spread**
  The 3GPP-3D model splits the two strongest clusters into three sub-clusters (per cluster) with fixed delay offsets. This is not implemented in QuaDRiGa since it adds additional complexity and has no effect on the results obtained from the model.

- **Departure and Arrival Angles**
  3GPP-3D obtains the individual angles from mapping the path powers to a wrapped Gaussian or wrapped Laplacian power-angular spectrum (PAS). Then, heuristically determined scaling factors are used to adjust the angular values for a different number of paths and the Ricean K-factor (see [49], pp. 26, step 7 and 8). However, this approach breaks the input-output consistency of the angular spread, *i.e.*, the angular spread calculated from the channel coefficients for an individual BS-MT link is not equal to the value given to the SSF model. Only the first-order statistics agree with each other. QuaDRiGa solves this by creating random angles, then calculating the resulting angle spread, and finally scaling the angles to obtain the value from the LSF model (see Section 2.3 of this thesis).

- **Polarization Model**
  QuaDRiGa has its own polarization model as described in Section 2.5 of this thesis. The QuaDRiGa polarization model was originally introduced to correctly model ecliptic cross polarization ratios (XPRs) (*e.g.*, for satellite channels) which is not covered well by the existing approach. The 3GPP / WINNER polarization model creates additional random phase shifts which effectively destroy ecliptic polarization in NLOS channels. These effects also change the phase information in the channel coefficients which leads to a different singular-value spread in cross-polarized channels.

Table 1.1: Differences between various GSCMs

Feature	SCM	SCM-E	WINNER-II IMT-Advanced	WINNER+	3GPP-3D	METIS (stochastic)	QuaDRiGa v1.4	METIS (map based)	COST 2100
Year of publication	2003	2005	2007	2010	2015	2015	2016	2015	2012
Literature reference	[46]	[71]	[47, 74]	[48]	[49]	[75]	[12]	[75]	[51]
Frequency range [GHz][a]	2	1-6	1-6	.45-6	2	.45-70	.45-6	.45-100	
Supported scenarios[a]	3[b]	3[b]	13	12[c]	6[d]	30+[e]	24	7[f]	
Bandwidth [MHz]	5	100	100	100	10	100	100	$0.1 f_c$	
No. of parameters	14	14	32	50[g]	50[g]	50[g]	50[g]	8[f]	
Max. no. of paths	6	6	20[h]	20[h]	20[h]	20[h]	∞	∞	
Massive MIMO	✗	✗	✗	✗	✓	✓[v]	✓	✓	
mmWave ($f_c > 6$ GHz)	✗	✗	✗	***O***[a]	✗	✓	✓	✓[a]	
Open-Source	✓	✓	✓	✗	✗	✗	✓	✗	✗
Large-scale fading (LSF)									
Spatial LSP consistency	✗	✗	2-D	2-D	2-D	3-D[t]	2-D	✓	✓
Correlated LSPs[k]	✗	✗	✓[l]	✓[l]	✓[m]	✓	✓[l]	✗[f]	
In/Out LSP consistency[n]	***O***[o]	***O***[o]	***O***[o]	***O***[o]	***O***[o]	***O***[o]	✓	✗[f]	✗
Distance-dependent LSPs	✗	✗	✗	✗	***O***[i]	***O***[i]	***O***[i]	✗[f]	
Spatially consistent LOS	✗	✗	✗	✗	✗	✗	✗	✓[f]	✗
Small-scale-fading (SSF)									
3-D model[u]	✗	✗	✗	✓	✓	✓	✓	✓	✓
Intra-cluster DS	✗	✓	✓	✓	✓	✓	✗	✗	
PAS mapping	R[p1]	R[p1]	G[p2]	G[p2]	G[p2]	G[p2]	SR[p3]	✗	
Spatial consistency[p]	✗	✗	✗	✗	✗	✗	***O***[q]	✓	✓
Geometric polarization	✗	✗	✗	✗	✗	✓	✓	✓	
Diffuse scattering	✗	✗	✗	✗	✗	✗	✗	✓	
Spherical waves	✗	✗	✗	✗	✗	✗	✓	✓	
Time-variability									
SSF time-variability[j]	✗	✓	***O***[r]	***O***[r]	***O***[r]	***O***[r]	✓	✓	
Scenario transitions	✗	✗	✗	✗	✗	✗	✓	✗	
Variable MT speeds	✗	✗	✗	✗	✗	✗	✓	✓	
Dual mobility[s]	✗	✗	✗	✗	✗	✓[t]	✗	✓	

Comments:

[a] This depends on the available parameter tables.
[b] Suburban Macro, Urban Macro, Urban Micro
[c] Indoor, Suburban Macro (LOS/NLOS); Urban Macro, Urban Micro (LOS/NLOS/O2I)
[d] Urban Macro (LOS/NLOS/O2I), Urban Micro (LOS/NLOS/O2I)
[e] See [75], Table 7-1, Page 53
[f] The METIS map-based model is similar to a ray-tracing approach and does not rely on LSPs. However, the model needs detailed geometry information.
[g] The WINNER+, 3GPP-3D, METIS (stochastic), and QuaDRiGa model use the same parameters.
[h] This is limited by the scaling of the arrival and departure angles based on a look-up table.
[i] Elevation angle of departure (EoD) and elevation spread of departure (ESD) only
[j] Dynamic channel (smooth evolution of small-scale-fading and large-scale-fading)
[k] Autocorrelation to obtain the desired decorrelation distance and inter-parameter correlation between LSPs. However, the order of the calculations determines the accuracy of the output.
[l] Autocorrelation by filtered noise, inter-parameter correlation by matrix-square-root
[m] Autocorrelation by filtered noise, inter-parameter correlation by Cholesky decomposition
[n] A model is consistent in the LSPs, when for a set of input parameters (e.g. DS, SF, KF, *etc.*), identical values

can be obtained from the generated channel coefficients (provided that omnidirectional antennas are used).
[o] There are random components, *e.g.*, in the path powers and angles, which will cause differences between the model output and the given parameters (e.g. the DS in the channel coefficients is different from the input DS).
[p] A spatially consistent model produces identical channel coefficients for MTs having the same location. This is also referred to as spatially correlated small-scale fading or spatially correlated fast-fading.
[p1] AoAs are assigned randomly (see [46], pp. 21, step 10)
[p2] AoAs (and AoDs, EoAs, EoDs) are mapped to a wrapped Gaussian distribution (see [47], pp. 39, step 7)
[p3] Arrival and departure angles are created using a random PAS and rescaling the angles to match the given angular spread (AS).
[q] QuaDRiGa is only spatially consistent as long as MTs are located on the same track.
[r] Time-variability is implemented by rotating phasors. This limits the mobility to a few wavelengths.
[s] With dual mobility, both the transmitter and receiver can be mobile.
[t] METIS proposes to use the sum-of-sinusoids method [70, 71] to jointly model correlated LSPs in this case.
[u] Clusters are located in 3-D space, parameters are given for elevation angles, support for 3-D antenna patterns
[v] A different sub-paths mapping is suggested since large arrays could resolve individual sub-paths.

1.3 Objectives and Contributions

This thesis summarizes the author's contributions to the field of geometry-based stochastic channel modeling. The main contributions add 3-D propagation and time-evolution to the popular WINNER channel model [47, 48]. A further extension of the model adds the necessary functionality to study massive MIMO systems, namely a new model for the polarization, a 3-D multi-bounce scattering model, spherical wave propagation, and a new method to derive departure and arrival angles for the multipath components. An outcome of this work is the quasi deterministic radio channel generator (QuaDRiGa) channel model [12] which was developed from 2010 to 2016 at the Fraunhofer Heinrich Hertz Institute (HHI) in Berlin, Germany[2]. The new model has been validated against real-world measurement data. One reason for the lack of validation of the previous channel models is the huge effort that is required to obtain and evaluate measured channel data. Fortunately, measurement data from the German government-funded research project EASY-C (Enabler for Ambient Services and Systems - Part C) [77] could be used to parameterize and validate the new model. Although those campaigns did not utilize hundreds of antennas at the transmitter, they can be used to characterize the channel and to aid the development of the new channel model for two important use cases: massive MIMO and joint transmission (JT) coordinated multi-point (CoMP).

Outline of the Thesis The remainder of this thesis is organized as follows: Chapter 2 provides a detailed description of the channel model. This includes all the changes compared to the WINNER+ and 3GPP-3D channel model that were found to be necessary during the course of the work. Chapter 3 provides detailed descriptions of the methods used to derive parameter tables for the model. This includes a description of the data evaluation algorithms needed to process the measurement data as well as a detailed description of the applied performance metrics. Chapters 4 and 5 present the measurement campaigns in downtown Dresden, Germany and downtown Berlin, Germany, respectively. This includes a discussion of the results and a comparison of the measurement results with results obtained from the channel model. The final Chapter 6 then provides a summary of the work and gives an outlook on future topics.

[2] The QuaDRiGa channel model is available open source at `http://quadriga-channel-model.de`

2 A 3-D Multi-Cell Channel Model with Time Evolution for Virtual Field Trials

Geometry-based stochastic channel models (GSCMs) such as the 3GPP-SCM [78], the WINNER model [47], the COST model [50] and the 3GPP-3D channel model [49] are important tools to validate new concepts in mobile communication systems. Early models such as the 3GPP-SCM [78], its extensions [71, 79], and the WINNER model [47] are based on a 2-D modeling approach. However, Shafi et al. [80] pointed out the importance of a 3-D extension when studying the effects of cross-polarized antennas on the MIMO capacity. This was taken up in the WINNER+ project where the parameter tables were completed with the elevation component [48]. 3-D propagation was also incorporated into other models such as the COST model [51] or mobile-to-mobile propagation models [81]. These later models share similar ideas which are incorporated into the new model outlined in this chapter.

A second aspect of major importance for various propagation environments is polarization. Multiple polarizations can be exploited to increase the number of spatial degrees of freedom especially when using compact antennas with a limited amount of elements [10, 82]. First attempts to include polarization effects into the SCM were made by Shafi *et al.* [80] who extended the simple 2-D antenna pattern of the SCM to a dual-polarized 3-D pattern. This method was then also adopted for the WINNER model [83]. However, Shafi *et al.*'s approach did not include a geometry-based method to calculate the cross-polarization effects. Instead, the XPR was incorporated statistically where the parameters were derived from measurements. This statistical approach leads to correct results for the cross-polarization discrimination (XPD)[1] in case of a well-balanced statistical mixture between LOS and NLOS scenarios in an indoor environment. However, the distribution of singular values, which is a better metric for characterizing the multi-stream capabilities of MIMO channels, was not considered. Zhou *et al.* [85] already indicated that it might be preferable to model the channel XPR by a rotation matrix. Later on, Quitin *et al.* [86] introduced an analytical channel model that correctly takes the antenna orientation into account. However, this method is limited to azimuthal propagation only (*i.e.*, no elevation angles are supported) and it does not support arbitrary antenna characteristics. It is discussed later in this chapter that the WINNER approach, which was adopted by all succeeding models, has great similarities with the Jones calculus, a method for handling polarized electromagnetic waves in the field of optics [87]. A new method to incorporate the polarization effects based on the Jones calculus is proposed in Section 2.5.

Another prerequisite for *virtual field trials* is the continuous time evolution of channel traces. Xiao *et al.* [79] added short-term time evolution to the SCM which was afterwards incorporated into an official SCM extension [71]. The idea is to calculate the position of the last-bounce scatterers (LBSs) based on the arrival angles of individual multipath components. Then, when the MT is moving, the arrival angles, delays and phases are updated using geometrical calculations. However, the WINNER-II model did not incorporate this technique and so did not the

[1] Following the definition in [84], the term cross polarization ratio (XPR) is used for the polarization effects in the channel. Combining the XPR with imperfect antennas yields the cross-polarization discrimination (XPD).

ITU, WINNER+, and 3GPP-3D model. Hence, all those models do not support time evolution beyond the scope of a few milliseconds which restricts the mobility of the MTs to a few meters. The COST model [50] incorporates time evolution by introducing groups of randomly placed scattering clusters that fade in and out depending on the MT position. However, despite the effort that was made to parameterize the model [88, 89], it still lacks sufficient parameters in many interesting scenarios. Czink *et al.* [90] introduced a simplified method that fades the clusters in and out over time. The cluster parameters were extracted from measurements, and the model is well suited for link-level simulations. However, this *random cluster model* cannot be used for system-level scenarios because it does not include geometry-based deployments. Nevertheless, the ideas presented by [90] led to more research on the birth and death probability as well as the lifetime of individual scattering clusters [91]. Wang *et al.* [92] then proposed a model for non-stationary channels that allows the scattering clusters to be mobile.

This chapter describes an extension of the WINNER model [47] where time evolution, geometric polarization and 3-D propagation effects such as spherical waved are incorporated. A reference implementation in MATLAB is available as open source [93]. The modeling approach consists of two steps: a stochastic part generates so-called large-scale parameters (LSPs) (*e.g.*, the delay and angular spreads) and calculates random 3-D positions of scattering clusters. It is assumed that the base station (BS) is fixed and the mobile terminal (MT) is moving. In this case, scattering clusters are fixed as well and the time evolution of the radio channel is deterministic. Different positions of the MT lead to different arrival angles, delays and phases for each multipath component (MPC). Longer sequences are generated by transitions between channel traces from consecutive initializations of the model. This allows the MTs to traverse different scenarios, *e.g.*, when moving from indoors to outdoors.

Figure 2.1 gives an overview of the modeling steps. The network layout (*i.e.*, the positions of the BSs, antenna configurations and downtilts), the positions and trajectories of the MTs, and the propagation scenarios need to be given as input variables. The channel coefficients are then calculated in seven steps which are described in detail in Sections 2.1 to 2.8 of this chapter. A quick summary of the procedure for generating the channel coefficients is given in the following list.

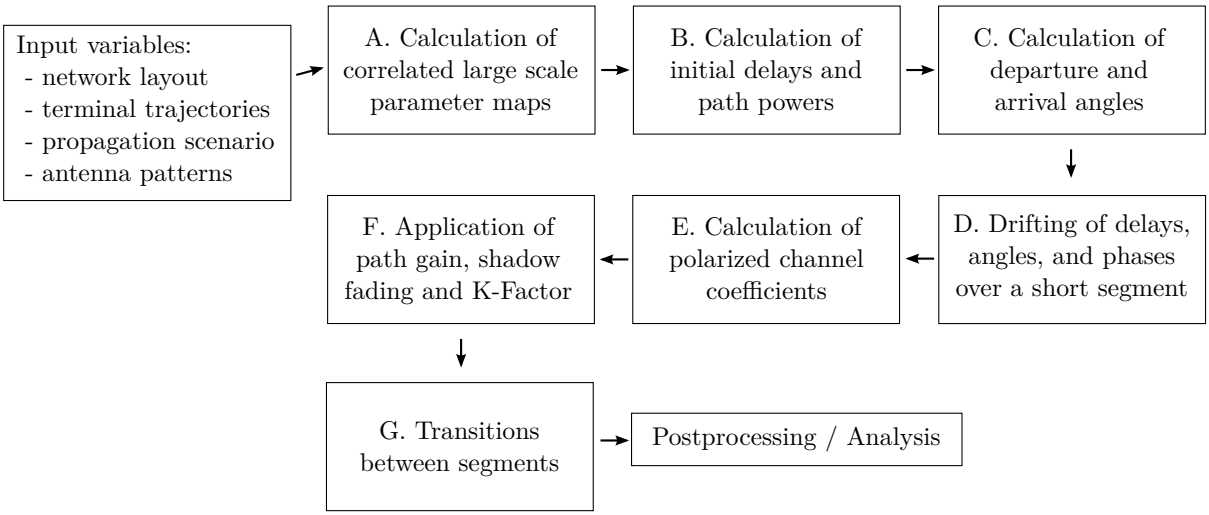

Figure 2.1: Steps for the calculation of time-evolving channel coefficients

A. Calculation of correlated large scale parameter maps
The first step ensures that the LSPs are consistent. As the name implies, these parameters (delay and angular spreads, K-factor and shadow fading) do not change rapidly. Closely spaced MTs will thus experience similar propagation effects. However, their fast-fading channels might be different.

B. Calculation of initial delays and path powers
Once the LSPs are known, the fast-fading channels are calculated for each MT separately. This step takes the specific values of the delay spread and the Ricean K-factor from step A and translates them into a set of multipath components, each having a specific power and delay value.

C. Calculation of departure and arrival angles
Each MPC gets assigned a specific departure direction at the transmitter and an arrival direction at the receiver. The power and delay values from step B remain unchanged during that process. The directions are chosen such that the angular spreads from step A are maintained. It is assumed here, that the propagation path always consists of multiple scatterers and there is no geometric relation between delays and angles.

D. Drifting of delays, angles, and phases over a short segment
This step incorporates mobility and spherical waves at the MT. Given the angles and delays (*i.e.*, the output of steps B and C), it is possible to calculate the exact position of the first-bounce scatterer (FBS) and the last-bounce scatterer (LBS), *i.e.*, the last reflection of a MPC before it reaches the receiver. Then, when the MT moves to a different location, the LBS positions of all MPCs are kept fixed and the delays and arrival directions are updated. This also leads to an update of the phases of the MPCs which reflect the correct Doppler shift when the MT is moving because the length of a propagation path changes in a deterministic manner.

E. Calculation of polarized channel coefficients
This step takes care of the antenna and polarization effects. The antennas are described by their 3-D far field radiation patterns in a polar-spheric representation [94]. However, those patterns are given in an antenna-specific local coordinate system. Thus, this step includes a method to rotate the antennas to match the MT and BS orientations defined in the global coordinate system (GCS) at the input of the model. Then, additional changes in the polarization might occur during scattering of a MPC. The resulting effects are handled by a method inspired by the Jones calculus [87] where successive linear transformations are used to calculate the polarization state of a MPC.

F. Application of path gain, shadow fading and K-Factor
In this step, the remaining LSPs from step A, *i.e.*, the distance-dependent path gain and the shadow fading, are applied to the channel coefficients. When the MT position changes during drifting in step D, the Ricean K-factor at the new location might be different. This is taken into account here as well.

G. Transitions between segments
Longer sequences of channel coefficients need to consider the birth and death of scattering clusters as well as transitions between different propagation environments. This is addressed by splitting the MT trajectory into *segments*. A segment can be seen as an interval in which the LSPs do not change considerably and where the channel maintains its wide sense stationary (WSS) properties. Channel traces are then generated independently for each segment (*i.e.*, steps B-F). Those individual traces are combined into a longer sequence in the last step.

Time evolution requires a more detailed description of the mobility of the terminals compared to previous models. This is done by assigning tracks, *i.e.*, ordered lists of positions, to each MT. In reality, this may include accelerations, decelerations, and MTs with different speeds, *e.g.*, pedestrian and vehicular users. However, to minimize the computational overhead and memory requirements, channel coefficients are calculated at a constant sample rate that fulfills the sampling theorem

$$f_T \geq 2 \cdot B_D = 4 \cdot \max|\Delta f_D| = 4 \cdot \frac{\max|v|}{\lambda_c}, \tag{2.1}$$

where B_D is the width of the Doppler spectrum, Δf_D is the maximum frequency change due to the velocity v, and λ_c is the carrier wavelength. Thus, the appropriate sampling rate is proportional to the maximum speed of the MT. Since it is sometimes useful to examine algorithms at different speeds, it is undesirable to fix the sampling rate in advance as the speed is then fixed as well. To overcome this problem, channel coefficients are calculated at fixed positions with a sampling rate f_S measured in samples per meter. In its normalized form, it is known as sample density (SD). A time-series for arbitrary or varying speeds is then obtained by interpolating the coefficients in a post processing step.

$$f_S = \frac{f_T}{\max|v|} \geq \frac{4}{\lambda_c} \tag{2.2}$$

$$\mathrm{SD} = \frac{f_S}{\lambda_c/2} \geq 2 \tag{2.3}$$

2.1 Correlated Large-Scale Parameter Maps

The first part of the channel model deals with the LSPs. Hence, it can also be considered the large-scale fading (LSF) model (step A in Fig. 2.1). A subsequent small-scale-fading (SSF) model (steps B-F in Fig. 2.1) then generates individual scattering clusters for each MT.

LSPs do not change rapidly. Typically, they are relatively constant for several meters. An example is the shadow fading (SF) which is caused by buildings or trees blocking a significant part of the signal. The so-called decorrelation distance of the SF, *i.e.*, the distance a MT must move to experience a significant change in the SF, is in the same order of magnitude as the size of the objects causing it. Thus, if a MT travels along a trajectory or if multiple MTs are closely spaced together, their LSPs are correlated. The positions of the scattering clusters are based on seven LSPs:

1. RMS delay spread (DS)
2. Ricean K-factor (KF)
3. Shadow fading (SF)
4. Azimuth spread of departure (ASD)
5. Azimuth spread of arrival (ASA)
6. Elevation spread of departure (ESD)
7. Elevation spread of arrival (ESA)

Their distribution properties are directly obtained from measurement data (*e.g.*, [23, 47, 48, 95, 96]). The distance-dependent correlation of the LSPs is modeled by means of 2-D maps as illustrated in Figure 2.2. The method for generating these maps is adopted from [97]. The maps are initialized with values obtained from an i.i.d. zero-mean Gaussian random process with desired variance. The samples are then subsequently filtered to obtain the desired autocorrelation function, *i.e.*, a decaying exponential function with a specific decorrelation distance. In contrast

to [97], the maps are filtered also in the diagonal direction to get a smooth evolution of the values along the MT trajectory. Once the maps are generated, initial LSPs for each segment are obtained by interpolating the maps to match the exact position of the MT. The granularity of each LSP can be described on three levels: the propagation scenario level, the link level, and the path level.

- **Propagation scenario level**
  The magnitude, variance and the correlation of a LSP in a specific scenario, *e.g.*, urban-macrocell, indoor hotspot, or urban satellite, are usually calculated from measurement data. Normally, LSPs are assumed to be log-normal distributed [98]. For example, the median log-normal delay spread DS_μ in an urban cellular scenario is $-6.89\ \log_{10}(\mathrm{s})$ which corresponds to a DS of $\sigma_\tau = 128$ ns[2]. With a standard deviation of $\mathrm{DS}_\sigma = 0.5$, typical values may vary in between 40 and 407 ns. The same principle applies for the other six LSPs. The decorrelation distance (*e.g.*, $\mathrm{DS}_\lambda = 40$ m) describes the distance-dependent correlation of the LSP. If *e.g.*, two mobile terminals in the above example are 40 m apart from each other, their DS is correlated with a correlation coefficient of $e^{-1} = 0.37$. Additionally, all LSPs are cross correlated. A typical example is the dependence of the AS, *e.g.*, the azimuth spread of arrival on the KF. With a large KF (*e.g.*, 10 dB), a significant amount of energy comes from a single direction. Thus, the AS gets smaller which leads to a negative correlation between the DS and the KF.

- **Link level**
  A MT at a specific position (black dot on the map in Figure 2.2) is assigned to a propagation scenario. Depending on the position and the scenario, it experiences a radio channel which is determined by the specific values of the seven LSPs. Due to the autocorrelation

[2]The model parameters are given in logarithmic units. To clearly indicate this, the units are defined in logarithmic scale as well. $\log_{10}(\mathrm{s})$ is the logarithm of seconds and $\log_{10}(^\circ)$ is the logarithm of degrees.

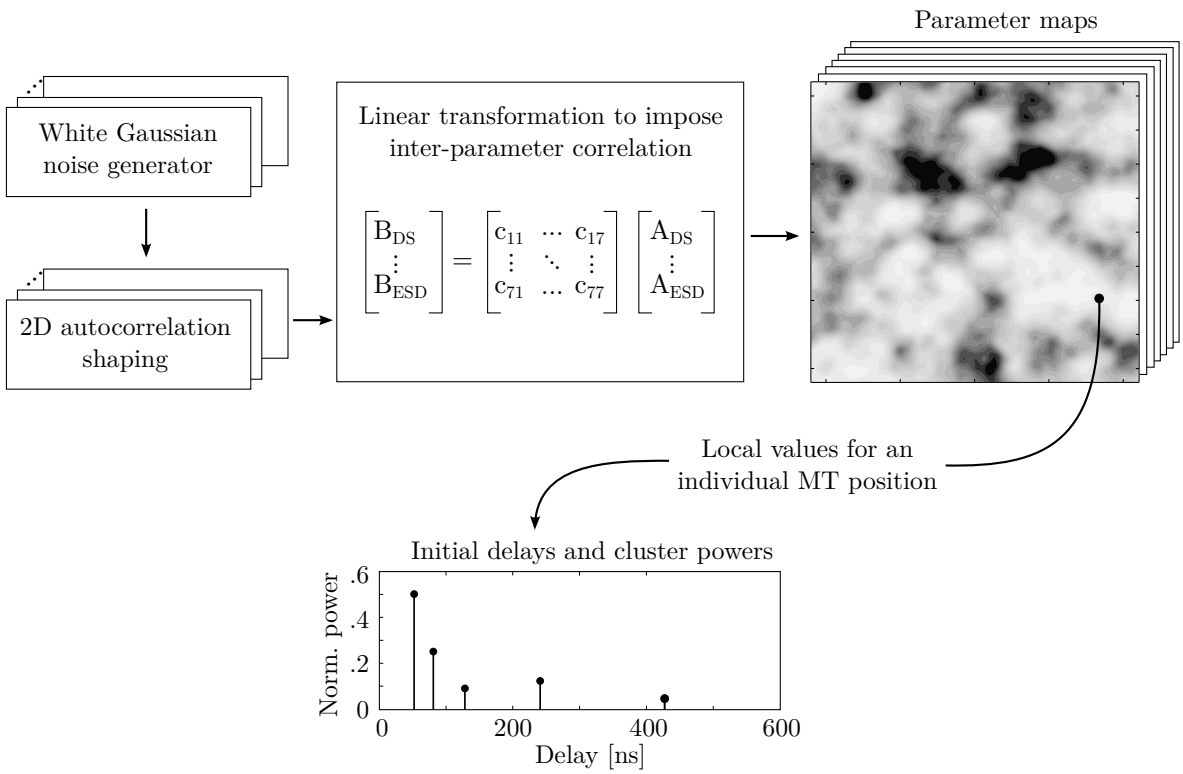

Figure 2.2: Principle of the generation of channel coefficients based on correlated LSPs

properties, small distances between users in the same scenario also lead to high correlations in the channel statistics, *e.g.*, a second terminal right next to the current user will experience a similar DS. The second granularity level thus contains the specific values of the LSPs for each user position. Generating those values can be seen as going from the scenario-wide distribution μ, σ of a LSP to virtual "*measurement*"-values for each MT.

- **Path Level**
  Finally, the individual components of the CIR are calculated. This procedure takes the values of the LSPs into account and calculates the path-powers and the path-delays of the MPCs. The detailed procedure for this is described in the following sections.

The correlation maps are generated for a fixed sampling grid by successively filtering a random, normal distributed sequence of values with a finite impulse response (FIR) filter. The principle is depicted in Figure 2.3. The map is represented by a matrix $\mathbf{B}$ with entries $B_{y,x}$ where y is the row index and x is the column index. The first value $B_{1,1}$ corresponds to the top left (or north-west) corner of the map. The FIR filter coefficients are calculated from the decorrelation distance d_λ (in units of meters). The distance dependent correlation coefficient follows an exponential function

$$\rho(d) = \exp\left(-\frac{d}{d_\lambda}\right), \tag{2.4}$$

with d as the distance between two positions [99]. Two sets of filter coefficients are used: one for the horizontal and vertical direction, and one for the diagonal directions. This is done by taking (2.4) and substituting the distance d by the relative distance d_{px} of two neighboring values.

$$a_k = \frac{1}{\sqrt{d_\lambda}} \cdot \exp\left(-\frac{k \cdot d_{\text{px}}}{d_\lambda}\right) \tag{2.5}$$

$$b_k = \frac{1}{\sqrt{d_\lambda}} \cdot \exp\left(-\frac{k \cdot \sqrt{2} \cdot d_{\text{px}}}{d_\lambda}\right) \tag{2.6}$$

k is the running filter coefficient index. The exponential decay function is cut at a maximum distance of $4 \cdot d_\lambda$ and normalized with $\sqrt{d_\lambda}$. The map size is therefore determined by the distribution of the users in the scenario plus the length of the filter function. This is also illustrated in Figure 2.3 where the user terminals are placed inside the black square. The extension space is needed to avoid filter artifacts at the edges of the map. The map is initialized with random, normal distributed numbers. Then, the filter (2.5) is applied in vertical direction (running from top to bottom) and in horizontal direction (from left to right).

$$B^{[1]}_{y,x} = X \quad \text{with} \quad X \sim N(0,1) \tag{2.7}$$

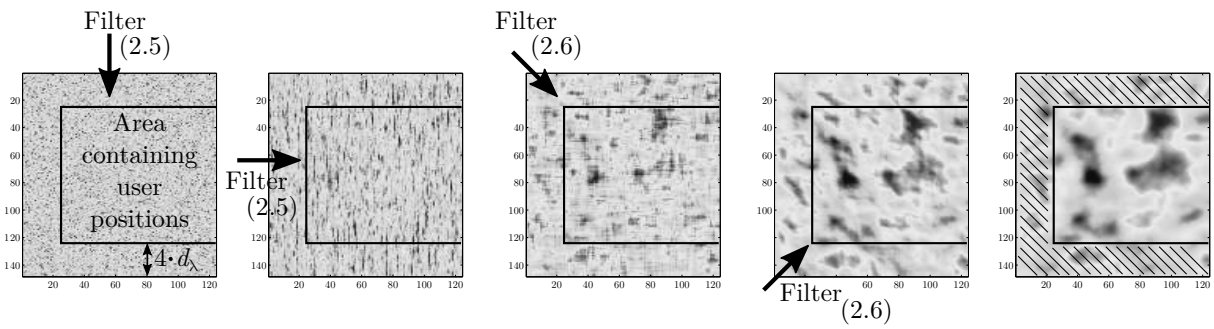

Figure 2.3: Map-based 2-D autocorrelation shaping using FIR filters

$$B^{[2]}_{y,x} = \sum_{k=0}^{\lfloor 4 \cdot d_\lambda / d_{\mathrm{px}} \rfloor} a_k \cdot B_{y-k,x} \tag{2.8}$$

$$B^{[3]}_{y,x} = \sum_{k=0}^{\lfloor 4 \cdot d_\lambda / d_{\mathrm{px}} \rfloor} a_k \cdot B_{y,x-k} \tag{2.9}$$

Next, the second filter (2.6) is applied on the diagonals of the map: at first from the top left to the bottom right, and then from the bottom left to the top right.

$$B^{[4]}_{y,x} = \sum_{k=0}^{\lfloor 4 \cdot d_\lambda / d_{\mathrm{px}} \rfloor} b_k \cdot B_{y-k,x-k} \tag{2.10}$$

$$B^{[5]}_{y,x} = \sum_{k=0}^{\lfloor 4 \cdot d_\lambda / d_{\mathrm{px}} \rfloor} b_k \cdot B_{y+k,x-k} \tag{2.11}$$

After the 2-D autocorrelation shaping is done, the extension space is removed and remaining map are scaled to have the desired distribution μ, σ. The same procedure is repeated for all seven LSPs. However, the decorrelation distance d_λ as well as μ, σ for each LSP can be different.

In order to account for the inter-LSP correlation, a 7×7 matrix $\mathbf{X}$ is assembled containing all cross-correlation values ρ between each two LSPs.

$$\mathbf{X} = \begin{pmatrix} 1 & \rho_{\mathrm{DS,KF}} & \rho_{\mathrm{DS,SF}} & \rho_{\mathrm{DS,ASD}} & \rho_{\mathrm{DS,ASA}} & \rho_{\mathrm{DS,ESD}} & \rho_{\mathrm{DS,ESA}} \\ \rho_{\mathrm{KF,DS}} & 1 & \rho_{\mathrm{KF,SF}} & \rho_{\mathrm{KF,ASD}} & \rho_{\mathrm{KF,ASA}} & \rho_{\mathrm{KF,ESD}} & \rho_{\mathrm{KF,ESA}} \\ \rho_{\mathrm{SF,DS}} & \rho_{\mathrm{SF,KF}} & 1 & \rho_{\mathrm{SF,ASD}} & \rho_{\mathrm{SF,ASA}} & \rho_{\mathrm{SF,ESD}} & \rho_{\mathrm{SF,ESA}} \\ \rho_{\mathrm{ASD,DS}} & \rho_{\mathrm{ASD,KF}} & \rho_{\mathrm{ASD,SF}} & 1 & \rho_{\mathrm{ASD,ASA}} & \rho_{\mathrm{ASD,ESD}} & \rho_{\mathrm{ASD,ESA}} \\ \rho_{\mathrm{ASA,DS}} & \rho_{\mathrm{ASA,KF}} & \rho_{\mathrm{ASA,SF}} & \rho_{\mathrm{ASA,ASD}} & 1 & \rho_{\mathrm{ASA,ESD}} & \rho_{\mathrm{ASA,ESA}} \\ \rho_{\mathrm{ESD,DS}} & \rho_{\mathrm{ESD,KF}} & \rho_{\mathrm{ESD,SF}} & \rho_{\mathrm{ESD,ASD}} & \rho_{\mathrm{ESD,ASA}} & 1 & \rho_{\mathrm{ESD,ESA}} \\ \rho_{\mathrm{ESA,DS}} & \rho_{\mathrm{ESA,KF}} & \rho_{\mathrm{ESA,SF}} & \rho_{\mathrm{ESA,ASD}} & \rho_{\mathrm{ESA,ASA}} & \rho_{\mathrm{ESA,ESD}} & 1 \end{pmatrix} \tag{2.12}$$

Then, the square-root matrix $\mathbf{X}^{1/2}$ is calculated such that $\mathbf{X}^{1/2} \cdot \mathbf{X}^{1/2} = \mathbf{X}$ [100]. In order to calculate the matrix-square-root, $\mathbf{X}$ must be positive definite to get a unique, real-valued solution. The matrix $\mathbf{X}^{1/2}$ is then multiplied with the seven values obtained from the maps at the sample point (y, x).

$$\begin{pmatrix} B_{y,x,DS} \\ \vdots \\ B_{y,x,EsD} \end{pmatrix} = \mathbf{X}^{1/2} \begin{pmatrix} B^{[5]}_{y,x,DS} \\ \vdots \\ B^{[5]}_{y,x,EsD} \end{pmatrix} \tag{2.13}$$

The procedure is repeated for all sample points of the map. Finally, the MTs are placed in the maps and the corresponding LSPs values are obtained by interpolating the surrounding entries of the matrices, *e.g.*, by a 2-D spline interpolation. In this way, initial LSPs for the following steps of the channel model are generated.

2.2 Initial Delays and Normalized Path Powers

Once the LSP maps are generated, the SSF part of the model generates individual scattering clusters for each MT. The next step is to read the delay spread (DS) and the Ricean K-factor

(KF) from the maps at the exact position of the MT. Then, initial delays are drawn randomly from a scenario-dependent delay distribution as

$$\tau_l^{[1]} = -r_\tau \sigma_\tau \ln(X_l), \tag{2.14}$$

where the index l denotes the path number, $X_l \sim \mathcal{U}(0,1)$ is an uniformly distributed random variable having values between 0 and 1, σ_τ is the initial DS from the map, and r_τ is a proportionality factor (see [47]). The term r_τ was introduced in [78] because σ_τ is influenced by both the delays τ_l and the powers P_l; r_τ is usually calculated from measurement data. Next, the delays are adjusted such that the first delay is set to zero and then they are sorted

$$\tau_l^{[2]} = \text{sort}\left\{\tau_l^{[1]} - \min\left(\tau_l^{[1]}\right)\right\}. \tag{2.15}$$

The NLOS path powers are drawn from a single slope exponential power delay profile (PDP) depending on the DS σ_τ and a random component $Z_l \sim \mathcal{N}(0, \zeta^2)$ [47]. The term ζ is a scenario-dependent coefficient emulating an additional shadowing process. It is obtained from measurements.

$$P_l^{[1]} = \exp\left(-\tau_l^{[2]} \cdot \frac{r_\tau - 1}{r_\tau} \cdot \sigma_\tau\right) \cdot 10^{\frac{-Z_l}{10}} \tag{2.16}$$

Here, the power values are given in units of Watts. The power of the first path is further scaled according to the initial KF from the map and the path powers are normalized so that their sum power is one Watt.

$$P_1^{[2]} = K \sum_{l=2}^{L} P_l^{[1]} \tag{2.17}$$

$$P_{2\ldots l}^{[2]} = P_{2\ldots l}^{[1]} \tag{2.18}$$

$$P_l = P_l^{[2]} / \sum_{l=1}^{L} P_l^{[2]} \tag{2.19}$$

The scaling of the powers by the KF changes the DS. Hence, in the last step, this is corrected by calculating the actual delay spread using the scaled powers and normalizing the delays in order to obtain the desired RMS delay spread in the PDP. The DS after applying (2.19) is

$$\sigma_\tau^{[\text{actual}]} = \sqrt{\sum_{l=1}^{L} P_l \cdot \tau_l^2 - \left(\sum_{l=1}^{L} P_l \cdot \tau_l\right)^2}. \tag{2.20}$$

This value differs from the initial value σ_τ that was provided by the parameter map. Hence, the delays (2.15) are scaled such that the correct delay spread can be calculated from the generated path-delay and path-powers.

$$\tau_l = \frac{\sigma_\tau}{\sigma_\tau^{[\text{actual}]}} \cdot \tau_l^{[2]} \tag{2.21}$$

The last step is different from other models. The WINNER [47] and 3GPP-3D model [49] scale the delays with an empiric formula that corrects the delays to reduce the effect of a high KF. However, due to the random variables in (2.14) and (2.16) the resulting DS is always different from the value in the map. The new method ensures that scattering clusters are distributed in a way that the DS calculated from the MPCs is exactly the same as the DS from the maps. In the following section, the departure and arrival directions of each MPC are generated. Those are the combined with the delays in order to calculate the 3-D positions of the scattering clusters.

2.3 Departure and Arrival Angles

Four angles are calculated for each propagation path. The 2-D WINNER model [47] introduced the AoD, ϕ^d, and the AoA, ϕ^a. In 3-D coordinates, the EoD, θ^d, and the EoA, θ^a are also needed[3]. The angles share similar calculation methods but have different angular spreads (ASs) σ_{ϕ^a}, σ_{ϕ^d}, σ_{θ^a}, and σ_{θ^d}. As for the DS, these four values are obtained by reading the values from the LSP maps at the MT position. The individual departure and arrival angles of the MPCs are generated by first assigning random angles to the already known path powers from the previous step. In order to obtain the correct ASs, a scaling operation is used to readjust the angles. This approach is different from the WINNER and 3GPP-3D model where the angles are mapped to the already known powers using a wrapped Gaussian distribution [101][4]. As for the DS, the intention behind the new method is to achieve the best possible match between the ASs that can be calculated from the MPCs and the values from the LSP maps. In this section, the method for generating the azimuth and elevation angles is outlined. Since the angles can only have values between $-\pi$ and π it is not possible to achieve any arbitrary AS. A discussion of the limits of the method is given in a separate paragraph.

Azimuth angles Here, the calculation method for the azimuth angles is described. The same calculation method is used for the AoD and the AoA. Hence, ϕ is used instead of ϕ^d or ϕ^a. Likewise, the corresponding AS is denoted as σ_ϕ.

At first, a random list of angles is created for the NLOS paths from a Gaussian normal distribution with zero-mean and a variance corresponding to the given AS from the LSP maps. The LOS angle is defined to be zero.

$$\phi_1^{[1]} = 0 \qquad \text{and} \qquad \phi_{2\ldots L}^{[1]} \sim \mathcal{N}(0, \sigma_\phi^2) \tag{2.22}$$

The so obtained angles need to be mapped to the interval $[-\pi; \pi]$. This is done by a modulo operation which wraps the angles around the unit circle.

$$\phi_l^{[2]} = \left(\phi_l^{[1]} + \pi \mod 2\pi\right) - \pi. \tag{2.23}$$

The relationship between path powers and angles is random. Hence, the resulting AS is undefined. In the next step, the actual AS is calculated. This requires calculating the power-weighted mean angle $\bar{\phi}$ because the angles are distributed on a sphere and, therefore, the AS depends on the reference angle, *i.e.*, the definition of where 0° is. The angle $\bar{\phi}$ is subtracted from the angles $\phi_l^{[2]}$ to map the mean angle to 0°. Then, the wrapping around the unit circle (modulo operation) is applied a second time. The AS then follows from

$$\bar{\phi} = \arg\left(\sum_{l=1}^{L} P_l \cdot \exp\left(j\phi_l^{[2]}\right)\right), \tag{2.24}$$

$$\phi_l^{[*]} = \left(\phi_l^{[2]} - \bar{\phi} + \pi \mod 2\pi\right) - \pi, \tag{2.25}$$

$$\sigma_\phi^{[\text{actual}]} = \sqrt{\sum_{l=1}^{L} P_l \cdot \left(\phi_l^{[*]}\right)^2 - \left(\sum_{l=1}^{L} P_l \cdot \phi_l^{[*]}\right)^2}. \tag{2.26}$$

[3] The new model uses the geographic coordinate system where the elevation angle $\theta = 90°$ points to the zenith and $\theta = 0°$ points to the horizon.

[4] A summary of the WINNER method together with a description of how it can be used in the new model is given in Appendix A.1.

Now, with σ_ϕ being the initial AS from the map, the angles $\phi_l^{[2]}$ are updated to

$$\phi_l^{[3]} = \frac{\sigma_\phi}{\sigma_\phi^{[\text{actual}]}} \cdot \phi_l^{[2]}. \tag{2.27}$$

If σ_ϕ is larger than $\sigma_\phi^{[\text{actual}]}$, then (2.23) needs to be applied again in order to account for the periodicity of the angles. However, this could lower the AS instead of increasing it as intended by the scaling operation. A solution is to create new angles with a bias to the negative side of the circle.

$$\phi_l^{[4]} = \begin{cases} \phi_l^{[3]}, & \text{if } |\phi_l^{[3]}| < \pi; \\ \mathcal{N}(\pi, \frac{\pi^2}{4}), & \text{otherwise.} \end{cases} \tag{2.28}$$

$$\phi_l^{[5]} = \left(\phi_l^{[4]} + \pi \mod 2\pi\right) - \pi \tag{2.29}$$

However, this changes the AS and the calculations (2.24) to (2.29) need to be repeated iteratively until the actual AS $\sigma_\phi^{[\text{actual}]}$ converges either to the given value σ_ϕ or a maximum value. Finally, the LOS direction is applied.

$$\phi_l = \phi_l^{[5]} + \phi^{LOS} \tag{2.30}$$

Elevation angles Since the elevation angles can only have values in between $-\frac{\pi}{2}$ and $\frac{\pi}{2}$, the calculation method differers from the method used for the azimuth angles. Again, the same method is used for the EoD and the EoA. Hence, θ is used instead of θ^d or θ^a. Likewise, the corresponding AS is denoted as σ_θ.

As for the azimuth angles, a random list of angles is created for the NLOS paths from a Gaussian normal distribution with zero-mean and a variance corresponding to the given AS from the LSP maps. The LOS angle is defined to be 0.

$$\theta_1^{[1]} = 0 \qquad \text{and} \qquad \theta_{2\ldots L}^{[1]} \sim \mathcal{N}(0, \sigma_\theta^2) \tag{2.31}$$

Next, the LOS direction is applied. This makes sure that the elevation angles are spread around the LOS path.

$$\theta_l^{[2]} = \theta_l^{[1]} + \theta^{LOS} \tag{2.32}$$

The so obtained angles need to be mapped to the interval $[-\frac{\pi}{2}; \frac{\pi}{2}]$. This is done by a modulo operation which wraps the angles around the unit circle and an additional operation that mirrors the angles at the poles of the unit sphere, *e.g.*, an elevation angle of 91° is mapped to 89°, 92° to 88°, and so on. This ensures that the previously calculated azimuth angles are not changed.

$$\theta_l^{[3]} = \left(\theta_l^{[2]} + \pi \mod 2\pi\right) - \pi \tag{2.33}$$

$$\theta_l^{[4]} = \begin{cases} \pi - \theta_l^{[3]}, & \text{if } \theta_l^{[3]} > \frac{\pi}{2}; \\ \theta_l^{[3]} - \pi, & \text{if } \theta_l^{[3]} < -\frac{\pi}{2}; \\ \theta_l^{[3]}, & \text{otherwise.} \end{cases} \tag{2.34}$$

As for the azimuth angles, the resulting AS is undefined. Hence, the actual elevation spread $\sigma_\theta^{[\text{actual}]}$ is calculated using equations (2.24), (2.25) and (2.26). Then, with σ_θ being the initial elevation spread from the map, the angles $\theta_l^{[4]}$ are updated. Since the angles should be distributed

around the LOS direction, θ^{LOS} needs to be subtracted before scaling the angles and added again after scaling them.

$$\theta_l^{[5]} = \frac{\sigma_\theta}{\sigma_\theta^{[\text{actual}]}} \cdot \left(\theta_l^{[4]} - \theta^{LOS}\right) + \theta^{LOS} \tag{2.35}$$

However, this update might shift some angles outside the allowed interval, especially if there is already a strong bias due to the LOS path which might happen *e.g.*, in satellite scenarios when the satellite has a high elevation. Hence, angles outside the allowed range are replaced with

$$\theta_l^{[6]} = \begin{cases} \mathcal{N}(\frac{\pi}{2}, \frac{\pi^2}{8}) & \text{if } \theta_l^{[5]} > \frac{\pi}{2}; \\ \mathcal{N}(-\frac{\pi}{2}, \frac{\pi^2}{8}) & \text{if } \theta_l^{[5]} < \frac{\pi}{2}; \\ \theta_l^{[5]} & \text{otherwise.} \end{cases} \tag{2.36}$$

As for the azimuth angles, equations (2.33) to (2.36) must be applied in an iterative fashion until $\sigma_\theta^{[\text{actual}]}$ converges either to the given value σ_θ or a maximum value.

Maximal angular spread The method for generating the angles tries to achieve the AS values from the LSP maps as best as possible. However, the generated angles can only have values between $-\pi$ and π for the azimuth direction and $-\frac{\pi}{2}$ and $\frac{\pi}{2}$ for the elevation direction. As a result, there are upper limits for the ASs. This fact was also acknowledged by the 3GPP-3D model [49] where the azimuth AS is capped at 104° and the elevation AS is capped at 52°. However, with increasing KF, the maximum AS decreases even more since more power is allocated to the LOS path. For example, with a KF of 10 dB the maximum azimuth spread is 57°, provided that all NLOS paths arrive from the opposite direction of the LOS path. If the angles are mapped randomly to the path powers, the realistically achievable AS is even lower (approx. 41°). Figure 2.4 shows the maximum AS for the new method as a function of the KF. For NLOS propagation, the achievable azimuth spread is around 100°, and the elevation spread is around 65°. Those values are close to the limits specified by 3GPP. If the requested AS is larger than the maximum AS, the new method adjusts the angles in a way that the AS at the output of the model is close to the maximum AS. This is illustrated in the right part of Figure 2.4 where the relation between the requested AS from the map and the achieved AS in the generated MPCs is illustrated for three different values of the KF. When the requested AS exceeds the maximal achievable AS, the angles are chosen such that the maximal AS is achieved.

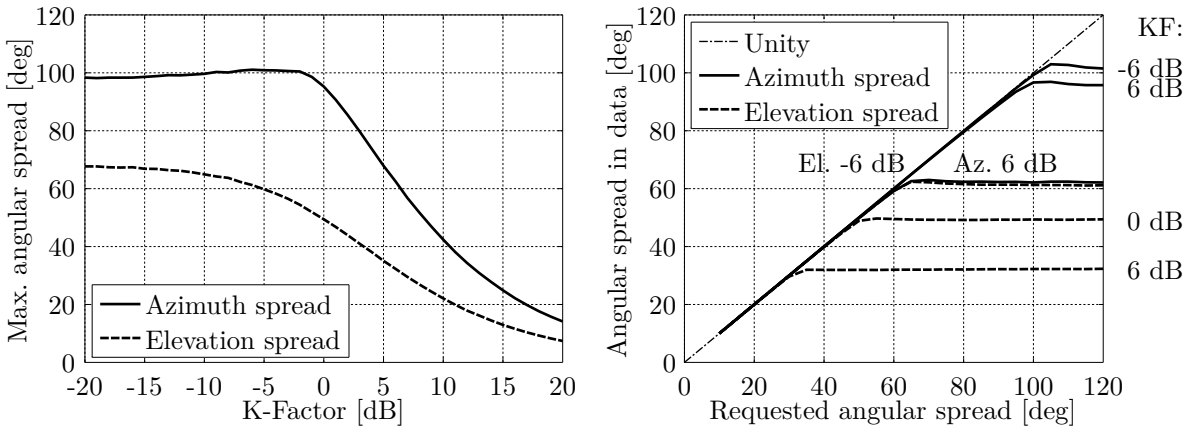

Figure 2.4: Maximal achievable angular spread depending on the K-factor

Subpaths At bandwidths below 100 MHz, closely clustered paths that originate from the same scattering cluster cannot be resolved in the delay domain. However, those unresolvable paths can still arrive from slightly different directions. When the band-limited CIR is observed over time, the power of the *resolved paths* appears to fluctuate as a result of the constructive and destructive interference caused by the superposition of the unresolvable paths. This phenomenon was modeled in the 3GPP-SCM [78] by splitting NLOS paths into 20 sub-paths that arrive from slightly different directions. The LOS path has no sub-paths. The same approach is used in the new model. The azimuth and elevation angles of each sub-paths are calculated as

$$\phi_{l,m} = \phi_l + \frac{\pi \cdot c_\phi \cdot \hat{\phi}_m}{180^\circ}, \quad \text{for } l > 1; \tag{2.37}$$

$$\theta_{l,m} = \theta_l + \frac{\pi \cdot c_\theta \cdot \hat{\phi}_m}{180^\circ}, \quad \text{for } l > 1. \tag{2.38}$$

Here, m is the sub-path index, c_ϕ is the scenario-dependent cluster-wise RMS AS and $\hat{\phi}$ is the offset angle of the mth sub-path from Table 2.1. c_ϕ and $\hat{\phi}$ are given in degrees here. Furthermore, each of the 20 angle pairs $({\theta^d}_{l,m}, {\phi^d}_{l,m})$ at the transmitter (Tx) gets coupled with a random angle pair $({\theta^a}_{l,m}, {\phi^a}_{l,m})$ at the receiver (Rx) (see [47]).

Table 2.1: Offset Angle of the mth Sub-Path from [47]

Sub-path m	Offset angle $\hat{\phi}_m$ (degrees)	Sub-path m	Offset angle $\hat{\phi}_m$ (degrees)
1,2	± 0.0447	11,12	± 0.6797
3,4	± 0.1413	13,14	± 0.8844
5,6	± 0.2492	15,16	± 1.1481
7,8	± 0.3715	17,18	± 1.5195
9,10	± 0.5129	19,20	± 2.1551

At this point, each (sub-)path is described by its delay, power, departure direction, and arrival direction. The next step is to use these values to calculate the exact position of the scatterers. This is needed in order to incorporate mobility at the MT. When the MT moves to a different location, the delays and arrival directions are updated in a deterministic way. One method for doing this was proposed by Baum *et al.* [71] who introduced the term *drifting*.

2.4 Drifting

After the path-delays, powers, and angles are known for the *initial position* of the MT, their values are updated when the MT moves to a different location. This is an essential step to ensure spatial consistency for moving terminals. Without tracking of the delays and directions of a path, the behavior of the channel coefficients at the output of the model does not agree well with the reality. State-of-the-art GSCMs such as the 3GPP-3D model use a simplified approach for the temporal evolution of the CIR. In this approach, each MPC gets assigned a Doppler shift based on the initial arrival angles. However, the angles and and path delays remain unchanged. In these models, there is no way to explicitly describe the movements of a terminal, *e.g.*, pedestrians using mobile phones, people in trains, cars, or other means of transport. This often leads to simplified simulation assumptions such as all MTs having ideal antennas and antenna orientations, moving at a constant speed and in a fixed direction. Conclusions drawn from such simulations might be very different from the achievable performance in real deployments.

In the new model, the MT moves along a trajectory which is divided into segments. Each segment is several meters long and it is assumed that the channel maintains its wide sense stationary (WSS) properties for the time it takes a MT to traverse the segment, *i.e.*, the LSPs don't change significantly. Changes in the orientation of a terminal are treated in Section 2.5 when the antenna characteristics are included. The *birth and death* of MPCs is treated at the edge of a segment when a new segment starts (see Section 2.8). In this section, a method to update the path-parameters (delay, angles, and phase) for each MT position along a segment is presented. Drifting for 2-D propagation was already introduced in an extension of the SCM [71]. However, it was not incorporated into the WINNER and 3GPP-3D models and no evaluation was reported. Here, the idea from [71] is extended towards 3-D propagation to incorporate time evolution into the new model.

The following paragraphs outline the calculations needed to implement drifting in 3-D coordinates which are not part of any of the previous GSCMs. For this, the individual delays and angles for each MPC from the previous sections are needed. In order to obtain correct results for large array antennas, *e.g.*, for massive MIMO, the calculations must be done for each individual element of an array antenna. Thus, the new model inherently supports spherical waves. If the BS array size is small compared to the BS-MT distance, it is sufficient to consider only a single scatterer (the LBS) for the NLOS paths. In this case, all calculations at the BS assume planar waves and the delays, angles and phases are updated for different MT positions with respect to the LBS. This is done in the so-called *single-bounce model*. However, many massive MIMO deployments are done indoors or in so-called micro-cell scenarios where BS and MT are relatively close to each other. At the same time, scattering clusters might be very close to the transmitter which is not the case in macro-cell scenarios when the BS antennas are deployed above the rooftop. For such micro-cell deployments it is essential to calculate the correct phase for each BS antenna element. Thus, in addition to the LBS, it is also necessary to take the position of the FBS into account. This is done in the *multi-bounce model*. Since the single-bounce model is a special case of the multi-bounce model (FBS and LBS are the same), both approaches are used. In the following, the single-bounce model is described first and then extended towards the multi-bounce model. The special LOS case is described last.

Besides the initial delays, path-powers, and angles, drifting requires the exact position of each antenna element. At the MT, element positions need to be updated for each snapshot with respect to the MT orientation. The following calculations are then done element-wise. The indices denote the Rx antenna element (r) and the Tx antenna element (t), the path number (l), the sub-path number (m), and the snapshot number (s) within the current segment, respectively. The scatterer positions are kept fixed for the time it takes a MT to move through a segment. Hence, the angles (θ^d, ϕ^d) seen from the BS do not change except for the LOS angle which is

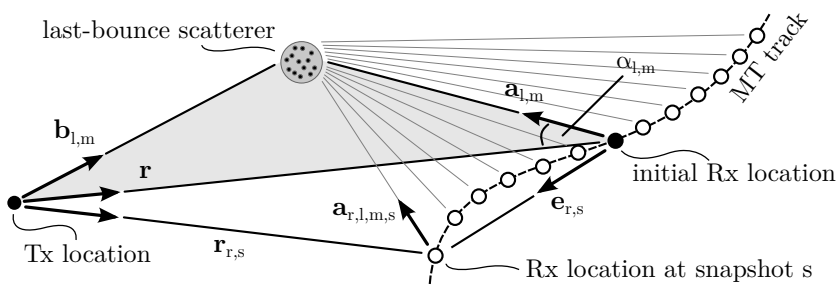

Figure 2.5: Illustration of the calculation of the scatterer positions and updates of the arrival angles in the single-bounce model

treated separately. Based on this assumption, the angles (θ^a, ϕ^a) as well as the path delay only change with respect to the last-bounce scatterer (LBS).

NLOS drifting (single-bounce model) The position of the LBS is calculated based on the initial arrival angles and the path delays. Then, the angles and path lengths between the LBS and the terminal are updated for each snapshot on the track. This is done for each antenna element separately. Figure 2.5 illustrates the angles and their relations. The first delay is always zero due to (2.15). Hence, the total length of the lth path is

$$d_l = \tau_l \cdot c + |\mathbf{r}|\,, \tag{2.39}$$

where $|\mathbf{r}|$ is the distance between the Tx and the initial Rx location and c is the speed of light. All sub-paths have the same delay and thus the same path length. However, each sub-path has different arrival angles ($\theta^a_{l,m}, \phi^a_{l,m}$). Those angles are transformed into Cartesian coordinates to obtain

$$\hat{\mathbf{a}}_{l,m} = \begin{pmatrix} \cos\phi^a_{l,m} \cdot \cos\theta^a_{l,m} \\ \sin\phi^a_{l,m} \cdot \cos\theta^a_{l,m} \\ \sin\theta^a_{l,m} \end{pmatrix} = \frac{\mathbf{a}_{l,m}}{|\mathbf{a}_{l,m}|}. \tag{2.40}$$

This vector has unit length and points from the initial Rx position towards the scatterer. Next, the length of the vector $\mathbf{a}_{l,m}$ is obtained. Since the drifting at the MT is modeled by a single reflection, Tx, Rx, and LBS form a triangle. The values of d_l, $\mathbf{r}$, and $\hat{\mathbf{a}}_{l,m}$ are known. Thus, the cosine theorem can be used to calculate the length $|\mathbf{a}_{l,m}|$ between the Rx and LBS.

$$|\mathbf{b}_{l,m}|^2 = |\mathbf{r}|^2 + |\mathbf{a}_{l,m}|^2 - 2\,|\mathbf{r}|\,|\mathbf{a}_{l,m}| \cos\alpha_{l,m} \tag{2.41}$$

$$(d_l - |\mathbf{a}_{l,m}|)^2 = |\mathbf{r}|^2 + |\mathbf{a}_{l,m}|^2 + 2\,|\mathbf{a}_{l,m}|\,\mathbf{r}^T\hat{\mathbf{a}}_{l,m} \tag{2.42}$$

$$|\mathbf{a}_{l,m}| = \frac{d_l^2 - |\mathbf{r}|^2}{2 \cdot (d_l + \mathbf{r}^T\hat{\mathbf{a}}_{l,m})} \tag{2.43}$$

In (2.42) the term $\cos\alpha_{l,m}$ is substituted with $-\mathbf{r}^T\hat{\mathbf{a}}_{l,m}/|\mathbf{r}|$ since the angle between $\mathbf{a}_{l,m}$ and $-\mathbf{r}$ is needed. Now, the vector $\mathbf{a}_{r,l,m,s}$ is calculated for the Rx antenna element r at snapshot s. The element position includes the orientation of the array antenna with respect to the moving direction of the Rx. Hence, the vector $\mathbf{e}_{r,s}$ points from the initial Rx location to the rth antenna element at snapshot s.

$$\mathbf{a}_{r,l,m,s} = \mathbf{a}_{l,m} - \mathbf{e}_{r,s} \tag{2.44}$$

An update of the arrival angles is obtained by transforming $\mathbf{a}_{r,l,m,s}$ back to spherical coordinates.

$$\phi^a_{r,l,m,s} = \arctan_2\{a_{r,l,m,s,y}, a_{r,l,m,s,x}\} \tag{2.45}$$

$$\theta^a_{r,l,m,s} = \arcsin\left\{\frac{a_{r,l,m,s,z}}{|\mathbf{a}_{r,l,m,s}|}\right\} \tag{2.46}$$

The departure angles ϕ^d and θ^d are identical for all Tx elements in a static scattering environment. However, the phases and path delays depend on the total path length $d_{r,t,l,m,s}$. To obtain this value, the vector $\mathbf{b}_{l,m}$ needs to be calculated from the vectors $\mathbf{r}$ and $\mathbf{a}_{l,m}$ at $r = s = 1$.

$$\mathbf{b}_{l,m} = \mathbf{r} + \mathbf{a}_{l,m} \tag{2.47}$$

$$d_{r,l,m,s} = |\mathbf{b}_{l,m}| + |\mathbf{a}_{r,l,m,s}| \tag{2.48}$$

Finally, the phases ψ and path delays τ are calculated as

$$\psi_{r,l,m,s} = \frac{2\pi}{\lambda} \cdot (d_{r,l,m,s} \bmod \lambda), \tag{2.49}$$

$$\tau_{r,l,s} = \frac{1}{20 \cdot c} \sum_{m=1}^{20} d_{r,l,m,s}. \tag{2.50}$$

The phase always changes with respect to the total path length. Hence, when the MT moves away from the LBS the phase will increase and when the MT moves towards the LBS the phase will decrease. This inherently captures the Doppler shift of single paths and creates a realistic Doppler spread in the channel coefficients at the output of the model.

In the next paragraph, the single-bounce model is extended to include the FBS in order to realistically model the effects caused by large array antennas at the Tx. This is important in scenarios where there is scattering close to the BS, *e.g.*, indoors or in micro-cell deployments with low BS heights.

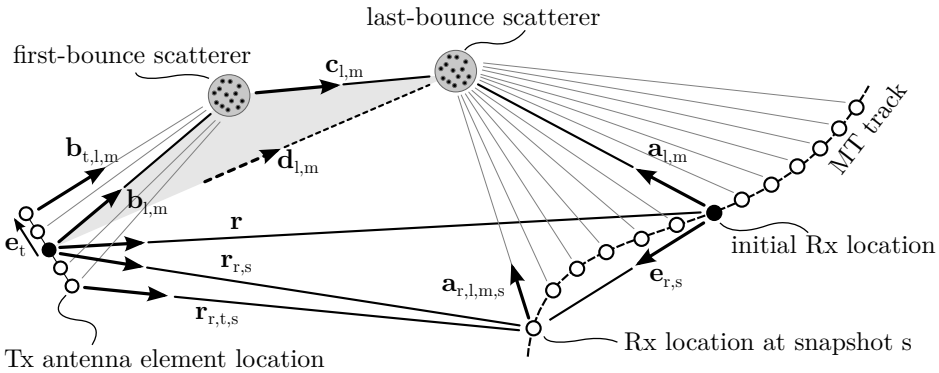

Figure 2.6: Illustration of the calculation of the scatterer positions and updates of the departure and arrival angles in the multi-bounce model

NLOS drifting (multi-bounce model) In the multi-bounce model, the NLOS propagation path consists of three segments as illustrated in Figure 2.6. In the first segment, the vector $\mathbf{b}_{t,l,m}$ points from the position of a Tx-antenna element t to the FBS. The Tx-element position is indicated by the vector $\mathbf{e}_t$. In the second segment, the vector $\mathbf{c}_{l,m}$ points from the FBS to the LBS, and in the third segment, the vector $\mathbf{a}_{r,l,m,s}$ points from the Rx-location to the LBS. The total propagation path length d_l is fixed by (2.39). Hence, the total path lengths is

$$d_l = |\mathbf{b}_{l,m}| + |\mathbf{c}_{l,m}| + |\mathbf{a}_{l,m}|, \tag{2.51}$$

where the vector $\mathbf{b}_{l,m}$ points from the Tx-array center to the FBS, *i.e.*, where $|\mathbf{e}_t| = 0$. The departure and arrival angles are known from the calculations in Section 2.3. Thus, the unit-length vector $\hat{\mathbf{a}}_{l,m}$ can be calculated by converting the departure angles of a path to Cartesian coordinates.

$$\hat{\mathbf{b}}_{l,m} = \begin{pmatrix} \cos\phi^d_{l,m} \cdot \cos\theta^d_{l,m} \\ \sin\phi^d_{l,m} \cdot \cos\theta^d_{l,m} \\ \sin\theta^d_{l,m} \end{pmatrix} = \frac{\mathbf{b}_{l,m}}{|\mathbf{b}_{l,m}|} \tag{2.52}$$

In order to explicitly calculate the positions of the FBS and the LBS, the lengths of the vectors $\mathbf{a}_{l,m}$ and $\mathbf{b}_{l,m}$ are needed. However, (2.51) is ambiguous. One way to fix the additional degree

of freedom is to minimize the length of $\mathbf{c}_{l,m}$. Ideally, $|\mathbf{c}_{l,m}|$ becomes zero and the multi-bounce model collapses to a single-bounce model. In order to obtain realistic results, an additional minimum distance $d_{\min}$ between the phase center of the array antennas and the nearest scatterer is introduced. Then, the lengths $|\mathbf{a}_{l,m}|$ and $|\mathbf{b}_{l,m}|$ can be calculated by solving the following optimization problem

$$\begin{aligned} \underset{|\mathbf{a}_{l,m}|,|\mathbf{b}_{l,m}|}{\text{minimize}} \quad & |\mathbf{c}_{l,m}| = d_l - |\mathbf{b}_{l,m}| - |\mathbf{a}_{l,m}| \\ \text{subject to} \quad & \mathbf{r} = \hat{\mathbf{b}}_{l,m} \cdot |\mathbf{b}_{l,m}| + \hat{\mathbf{c}}_{l,m} \cdot |\mathbf{c}_{l,m}| - \hat{\mathbf{a}}_{l,m} \cdot |\mathbf{a}_{l,m}|\,, \\ & |\mathbf{b}_{l,m}| \geq d_{\min}, \\ & |\mathbf{a}_{l,m}| \geq d_{\min}. \end{aligned}$$

The minimum distance $d_{\min}$ might be fixed according to the scenario and center frequency, *e.g.*, 1 m for outdoor propagation and 0.1 m for indoor propagation. To solve the optimization problem $|\mathbf{a}_{l,m}|$ is set to $d_{\min}$ and $\mathbf{c}_{l,m}$ and $|\mathbf{b}_{l,m}|$ are calculated using the cosine theorem. This is possible since the Tx, the FBS and the LBS form a triangle as indicated in Figure 2.6 by the gray shaded area.

$$d_l^+ = \tau_l \cdot c + |\mathbf{r}| - |\mathbf{a}_{l,m}| \tag{2.53}$$

$$\mathbf{d}_{l,m} = \mathbf{r} + \hat{\mathbf{a}}_{l,m} \cdot |\mathbf{a}_{l,m}| \tag{2.54}$$

$$|\mathbf{b}_{l,m}| = \frac{\left(d_l^+\right)^2 - |\mathbf{d}_{l,m}|^2}{2 \cdot \left(d_l^+ - \mathbf{d}_{l,m}^T \hat{\mathbf{b}}_{l,m}\right)} \tag{2.55}$$

There can be three possible results from this first iteration step that need to be treated separately.

1. The value obtained for $|\mathbf{b}_{l,m}|$ might be smaller than $d_{\min}$ or even smaller than 0. The latter would imply that the departure direction of the path has changed to the other side of the Tx. However, this is not allowed since the departure angles are fixed. In this case, the optimization problem has no solution. This often happens when the propagation delay of a path is very short, *i.e.*, when the path is only a little longer than the LOS path.

This case is treated by setting $|\mathbf{c}_{l,m}| = 0$ and calculating new departure angles using the single-bounce model. This changes the departure angular spread. However, in most cases there will be many paths where the optimization problem has a solution. This is especially true for paths with a longer propagation delay. Hence, it is possible to mitigate the changed departure angular spread by adjusting the departure angles of the multi-bounce paths. The rationale behind this is that many measurements [23, 48] show a rather small departure angular spread of just a few degrees but a large arrival angular spread. This leaves more "room" to adjust the departure angles before they are wrapped around the unit circle. Also, paths with a short propagation delay have more power due to the exponential PDP used in (2.16). From a physical point of view, those paths are more likely to be scattered only once. Later paths have significantly less power and can be the result of multiple scattering events.

2. The value for $|\mathbf{b}_{l,m}|$ is larger than $d_{\min}$ and the optimization problem has a solution. In this case, there will also be an optimal solution, *i.e.*, a minimal distance $|\mathbf{c}_{l,m}|$. This minimum must be in between the start point where $|\mathbf{a}_{l,m}| = d_{\min}$ and the end point where $|\mathbf{b}_{l,m}| = d_{\min}$. For each value $|\mathbf{a}_{l,m}|$ there follows a value for $|\mathbf{b}_{l,m}|$ and a value for $|\mathbf{c}_{l,m}|$ which both can be calculated using the cosine theorem. Hence, it is possible to apply standard numeric methods such as bisection to obtain the optimal solution.

3. The optimization problem has a solution but the solution lies on one of the end points, either at $|\mathbf{a}_{l,m}| = d_{\min}$ or at $|\mathbf{b}_{l,m}| = d_{\min}$. In this case, the LBS or the FBS are very close to either the Tx or the Rx antenna. In this case, the problem is relaxed such that $|\mathbf{c}_{l,m}|$ is allowed to double in order to increase the space between scatterer and array antenna.

Once the positions of the FBS and the LBS are known, the departure angles and the total path length are updated for each antenna element of the Tx array.

$$\mathbf{b}_{t,l,m} = \mathbf{b}_{l,m} - \mathbf{e}_t \tag{2.56}$$

$$\phi^d_{t,l,m} = \arctan_2 \{b_{t,l,m,y}, b_{t,l,m,x}\} \tag{2.57}$$

$$\theta^d_{t,l,m} = \arcsin \left\{ \frac{b_{t,l,m,z}}{|\mathbf{b}_{t,l,m}|} \right\} \tag{2.58}$$

$$d_{r,t,l,m,s} = |\mathbf{b}_{t,l,m}| + |\mathbf{c}_{l,m}| + |\mathbf{a}_{r,l,m,s}| \tag{2.59}$$

The arrival angles are updated using (2.44), (2.45) and (2.46). The phases and delays are calculated using (2.49) and (2.50) where $d_{r,l,m,s}$ is replaced by $d_{r,t,l,m,s}$.

LOS drifting The direct component is handled differently because the angles need to be updated at both sides, the Tx and the Rx. The angles are calculated for each combination of Tx-Rx antenna elements based on the position of the element in 3-D coordinates.

$$\mathbf{r}_{r,t,s} = \mathbf{r} - \mathbf{e}_t + \mathbf{e}_{r,s} \tag{2.60}$$

$$\phi^d_{t,1,s} = \arctan_2 \{r_{r,t,s,y}, r_{r,t,s,x}\} \tag{2.61}$$

$$\theta^d_{t,1,s} = \arcsin \left\{ \frac{r_{r,t,s,z}}{|\mathbf{r}_{r,t,s}|} \right\} \tag{2.62}$$

$$\phi^a_{r,1,s} = \arctan_2 \{-r_{r,t,s,y}, -r_{r,t,s,x}\} \tag{2.63}$$

$$\theta^a_{r,1,s} = \arcsin \left\{ \frac{-r_{r,t,s,z}}{|\mathbf{r}_{r,t,s}|} \right\} \tag{2.64}$$

The vector $\mathbf{r}_{r,t,s}$ points from the location of the Tx element t to the location of the Rx element r at snapshot s. The phases and delays are determined by the length of this vector and are calculated using (2.49) and (2.50) where $d_{r,l,m,s}$ is replaced by $|\mathbf{r}_{r,t,s}|$.

At this point there is a complete description of the propagation path of each MPC, *i.e.*, the departure direction at the Tx, the positions of the scatterers, the arrival direction at the Rx, the phase, as well as the variation of these variables when the MT is moving. In the next Section, the antenna effects are included. This covers the orientation of the antennas at the BS and the MT, as well as the polarization effects which are closely related to the antennas.

2.5 Antennas and Polarization

One major advantage of geometry-based stochastic channel models (GSCMs) is that they allow the separations of propagation and antenna effects. Therefore, it is essential to have a description of the antenna that captures all relevant effects that are needed to accurately calculate the channel coefficients in the model. Antennas do not radiate equally in all directions. Hence,

the radiated power is a function of the angle. The antenna is then defined by its directional response also known as radiation pattern. When the antenna is rotated around a fixed point, an additional variation in the amount of received power can be observed. This variation is due to the polarization of the antenna. There are various so-called polarization bases that can be used to describe this effect. Those different bases arise from the custom to define cross-polarization as "the polarization orthogonal to a reference polarization" [94]. Unfortunately, this leaves the reference polarization undefined and thus is ambiguous.

Of all the different ways to describe polarization (see [94, 102]), the polar spherical polarization basis is the most practical for GSCMs. In the polar spherical basis, the antenna coordinate system has two angles and two poles. The elevation angle θ is measured relative to the pole axis. A complete circle will go through each of the two poles, similar to the longitude coordinate in the world geodetic system (WGS). The azimuth angle ϕ moves around the pole, similar to the latitude in WGS. Thus, the antenna is defined in *geographic* coordinates, the same coordinate system that is used in the channel model. Hence, deriving the antenna response from the previously calculated departure and arrival angles is straightforward. The electric field is resolved onto three vectors which are aligned to each of the three spherical unit vectors $\hat{\mathbf{e}}_\theta$, $\hat{\mathbf{e}}_\phi$ and $\hat{\mathbf{e}}_r$ of the coordinate system. In this representation, $\hat{\mathbf{e}}_r$ is aligned with the propagation direction of a path. In the far-field of an antenna, there is no field in this direction. Thus, the radiation pattern consists of two components, one is aligned with $\hat{\mathbf{e}}_\theta$ and another is aligned with $\hat{\mathbf{e}}_\phi$. It is usually described by a 2-element vector

$$\mathbf{F}(\theta, \phi) = \begin{pmatrix} F^{[\theta]}(\theta, \phi) \\ F^{[\phi]}(\theta, \phi) \end{pmatrix}. \tag{2.65}$$

The complex-valued amplitude g of a path between a transmit antenna and a receive antenna is

$$g = \sqrt{P} \cdot \mathbf{F}_r(\phi^a, \theta^a)^T \cdot \mathbf{M} \cdot \mathbf{F}_t(\phi^d, \theta^d) \cdot e^{-j\frac{2\pi}{\lambda} \cdot d}, \tag{2.66}$$

where $\mathbf{F}_r$ and $\mathbf{F}_t$ describe the polarimetric antenna response at the receiver and the transmitter, respectively. P is the power of the path, λ is the wavelength, d is the length of the path, (ϕ^a, θ^a) are the arrival and (ϕ^d, θ^d) the departure angles that were calculated in the previous steps. $\mathbf{M}$ is the 2×2 polarization coupling matrix. This matrix describes how the polarization changes on the way from the transmitter to the receiver. Many references (e.g. [80, 84, 103–105]) use an approximation of the polarization effects based on the XPR. The XPR quantifies the separation between two polarized channels due to different polarization orientations. $\mathbf{M}$ is then often modeled by using random coefficients ($Z_{\theta\theta}$, $Z_{\theta\phi}$, $Z_{\phi\theta}$, $Z_{\phi\phi}$) as

$$\mathbf{M} = \begin{pmatrix} Z_{\theta\theta} & \sqrt{1/\mathrm{XPR}} \cdot Z_{\theta\phi} \\ \sqrt{1/\mathrm{XPR}} \cdot Z_{\phi\theta} & Z_{\phi\phi} \end{pmatrix}, \tag{2.67}$$

where $Z \sim \exp\{j \cdot \mathcal{U}(-\pi, \pi)\}$ introduces a random phase. However, this does not account for all effects contributing to the polarization state of a radio link. For example, this model does not cover elliptical or circular polarization which depends on the phase difference between the two polarimetric components. With the above model, the phase difference is always random. Hence, the state-of-the-art GSCMs are not well suited for scenarios that rely on circular polarization such as land-mobile satellite scenarios.

A new approach on how to treat polarization in GSCMs is presented in this section. It is shown that the existing framework, *i.e.*, using radiation patterns in a polar spherical basis together with a 2×2 polarization coupling matrix, has great similarities with the Jones calculus, a method

for handling polarized electromagnetic waves in the field of optics [87]. In the Jones calculus, the changes of the polarization of a electromagnetic wave are described by successive linear transformations. The same approach is used for the new channel model.

2.5.1 Relation between the Polarization Model and the Jones Calculus

R. C. Jones invented a simple method to calculate polarization effects in optics [87]. In his work, he described the polarization state of a ray of light by the so-called Jones vector. Any object that changes the polarization of the light is represented by a 2×2 Jones matrix. It was found that the product of the Jones matrix of the optical element and the Jones vector of the incident light accurately describes the polarization state of the resulting ray. Generally, this calculus can be used for any electromagnetic wave. It is especially interesting for the GSCMs such as the SCM and WINNER models where the paths are handled similarly like optical rays.

In the Jones calculus, the Jones vector contains the x and y-polarized components of the amplitude and phase of the electric field traveling along the z-direction.

$$\begin{pmatrix} E_x(t) \\ E_y(t) \end{pmatrix} = e^{j\omega t} \cdot \underbrace{\begin{pmatrix} A_x e^{j\epsilon_x} \\ A_y e^{j\epsilon_y} \end{pmatrix}}_{\text{Jones vector}} = \begin{pmatrix} J^{[\theta]} \\ J^{[\phi]} \end{pmatrix} = \mathbf{J} \tag{2.68}$$

The same expression is found in the antenna pattern (2.65) where the complex value $A_y e^{j\epsilon_y}$ from the Jones vector can be identified with the (generally also complex-valued) component $F^{[\theta]}(\theta, \phi)$ of the antenna pattern. Likewise, $A_x e^{j\epsilon_x}$ can be identified with $F^{[\phi]}(\theta, \phi)$. This implies that the polarization coupling matrix $\mathbf{M}$ in (2.66) is a Jones matrix and that the Jones calculus could be easily integrated into the new channel model.

In general, $\mathbf{M}$ can be seen as a transformation operation that maps the incoming signal on the polarization plane to an outgoing signal. If the coefficients are real-valued, then linear transformations, such as rotation, scaling, shearing, reflection, and orthogonal projection as well as combinations of those operations, are possible. If the coefficients are complex-valued, then the matrix shows characteristics of a Möbius transformation. Such transformations can map straight lines to straight lines or circles and *vice versa*. Since the Jones calculus allows the use of complex-valued coefficients, it can transform linear polarized signals into circular or elliptical polarized signals and elliptical polarized signals into linear polarized signals. This implies that using (2.67) with complex-valued coefficients results in a completely random polarization behavior when the XPR is small, *i.e.*, when the off-diagonal elements are large. When XPR is large (and the off-diagonal elements are close to zero), then (2.67) describes a scaling operation.

In the next section, $\mathbf{M}$ will be calculated explicitly for the LOS and NLOS components also taking the orientation of the antennas into account. For the NLOS components, additional operations are used to convert the XPR value from the parameter tables into Jones matrices for the linear and elliptical polarization component.

2.5.2 Changing the Orientation of Antennas

The antennas are defined in their local coordinate system which is fixed when the radiation patterns are generated either by measurements or by designing the antennas using special software tools. In the channel model, orientation changes of the antennas are desirable in many cases,

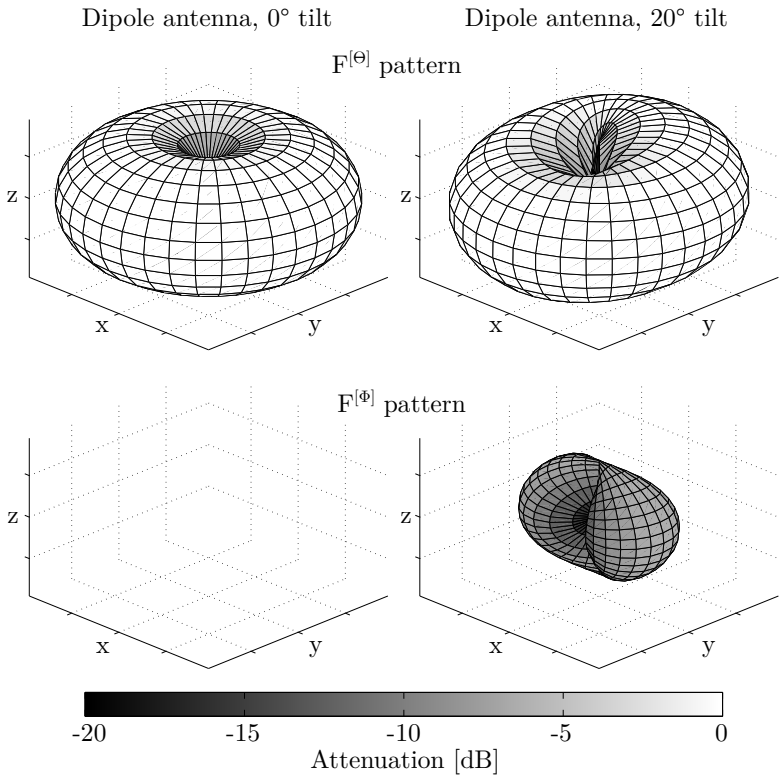

Figure 2.7: Example patterns for a dipole antenna

e.g., when tilting BS arrays or changing the orientation of mobile terminals. However, such orientation changes lead to a different radiation pattern. An example is depicted in Figure 2.7. The left side of the figure shows an ideal dipole radiation pattern that has only an $F^{[\theta]}$ component. When the dipole gets rotated around the x-axis in Cartesian coordinates, the resulting radiation pattern will also have an $F^{[\phi]}$ component and the $F^{[\theta]}$ component is deformed. This is illustrated on the right side of the figure where the dipole is tilted by 20°. The following method shows how an existing antenna pattern can be manipulated in order to change the orientation of the antenna. Such manipulations need to take the polarization into account. It is shown that it is possible to describe this process by a 2×2 linear transformation, *i.e.*, a Jones matrix. Hence, the following method is used in the new channel model to adjust the orientation of the antennas either at the BS or at the MT by using the matrix $\mathbf{M}$ in (2.66). This makes the new model more flexible. For example, it is possible to use realistic radiation patterns at the MT, *e.g.*, the measured patterns from a smartphone. Then, typical orientations of the phone can be incorporated during the runtime of the channel model, *e.g.*, a user holding the phone close to the ear at a 45° angle.

When the orientation of an antenna changes, the radiation pattern has to be read at different angles (Θ, Φ) that include the effect of the orientation change. Rotations in 3-D are easier described in Cartesian coordinates. Therefore, the original angle pair (θ, ϕ) is transformed into a vector $\mathbf{c}$ that describes the arrival or departure angles in Cartesian coordinates. The three vector elements represent the x,y and z-component.

$$\mathbf{c} = \begin{pmatrix} \cos\theta \cdot \cos\phi \\ \cos\theta \cdot \sin\phi \\ \sin\theta \end{pmatrix} \tag{2.69}$$

A 3×3 matrix $\mathbf{R}$ can now be used to describe the orientation change in 3-D space. The example

in Figure 2.7 was tilted by 20° around the x-axis of the coordinate system. The corresponding matrix is

$$\mathbf{R}_x(20°) = \begin{pmatrix} 1 & 0 & 0 \\ 0 & \cos(20°) & -\sin(20°) \\ 0 & \sin(20°) & \cos(20°) \end{pmatrix}. \tag{2.70}$$

The orientation change is included in the vector $\mathbf{c}^+$ by multiplying $\mathbf{R}$ with (2.69).

$$\mathbf{c}^+ = \mathbf{R}^T \cdot \mathbf{c} \tag{2.71}$$

The transformed pattern $\tilde{\mathbf{F}}$ is needed in spherical coordinates. Thus, $\mathbf{c}^+$ is transformed back to spherical coordinates. This results in the new angles

$$\Theta = \arcsin\left[c_z^+\right], \tag{2.72}$$

$$\Phi = \arctan_2\left[c_y^+, c_x^+\right]. \tag{2.73}$$

c_x^+, c_y^+ and c_z^+ are the x, y and z component of $\mathbf{c}^+$, respectively. The coefficients of the rotated pattern are now obtained by reading the original pattern $\mathbf{F}$ at the transformed angles.

$$\hat{\mathbf{F}} = \begin{pmatrix} \hat{F}^{[\theta]} \\ \hat{F}^{[\phi]} \end{pmatrix} = \begin{pmatrix} F^{[\theta]}(\Theta, \Phi) \\ F^{[\phi]}(\Theta, \Phi) \end{pmatrix} \tag{2.74}$$

Since the patterns are usually sampled at a fixed angular grid, *e.g.*, at one degree resolution, interpolation is needed here since the transformed angles (Θ, Φ) will usually not be aligned with the angular grid. Linear interpolation can be used as a standard computationally inexpensive procedure.

The second step takes the polarization into account. The antenna patterns are defined in a polar-spherical polarization basis. However, the rotation is defined in Cartesian coordinates. Thus, the polarization rotation needs to be done in the Cartesian polarization basis as well. The transformation from the polar-spherical polarization basis to the Cartesian polarization basis is given by [94]

$$\begin{pmatrix} \hat{F}^{[x]} \\ \hat{F}^{[y]} \\ \hat{F}^{[z]} \end{pmatrix} = \underbrace{\begin{pmatrix} \sin\Theta\cos\Phi & -\sin\Phi \\ \sin\Theta\sin\Phi & \cos\Phi \\ -\cos\Theta & 0 \end{pmatrix}}_{=\mathbf{T}(\Theta,\Phi)} \cdot \underbrace{\begin{pmatrix} F^{[\theta]}(\Theta, \Phi) \\ F^{[\phi]}(\Theta, \Phi) \end{pmatrix}}_{=\hat{\mathbf{F}}}. \tag{2.75}$$

The transformation matrix $\mathbf{T}(\Theta, \Phi)$ is both orthogonal and normalized to unity. Hence, the inverse transformation matrix is equal to the matrix transpose. The rotated pattern $\tilde{\mathbf{F}}$ is obtained by using the pattern $\hat{\mathbf{F}}$ and transforming it to a Cartesian polarization basis. Then, this pattern is rotated using the rotation matrix $\mathbf{R}$ and the resulting pattern is transformed back to the polar-spherical basis. The inverse transformation needs to be done at the original angles (θ, ϕ) because the rotated antenna pattern $\tilde{\mathbf{F}}$ is aligned with the GCS used in the channel model.

$$\tilde{\mathbf{F}} = \underbrace{\mathbf{T}(\theta, \phi)^T \cdot \mathbf{R} \cdot \mathbf{T}(\Theta, \Phi)}_{=\tilde{\mathbf{M}}} \cdot \hat{\mathbf{F}} \tag{2.76}$$

The entire process can be described by a 2×2 polarization rotation matrix $\tilde{\mathbf{M}}$. The radiated energy in both polarization components remains constant. Hence, this matrix is a rotation matrix having the form

$$\tilde{\mathbf{M}}(\vartheta) = \begin{pmatrix} \cos\vartheta & -\sin\vartheta \\ \sin\vartheta & \cos\vartheta \end{pmatrix}, \tag{2.77}$$

where the polarization rotation angle ϑ follows from

$$\cos\vartheta = \begin{pmatrix} \sin\theta\cos\phi \\ \sin\theta\sin\phi \\ -\cos\theta \end{pmatrix}^T \cdot \mathbf{R} \cdot \begin{pmatrix} \sin\Theta\cos\Phi \\ \sin\Theta\sin\Phi \\ -\cos\Theta \end{pmatrix}, \tag{2.78}$$

$$\sin\vartheta = \begin{pmatrix} -\sin\phi \\ \cos\phi \\ 0 \end{pmatrix}^T \cdot \mathbf{R} \cdot \begin{pmatrix} \sin\Theta\cos\Phi \\ \sin\Theta\sin\Phi \\ -\cos\Theta \end{pmatrix}, \tag{2.79}$$

$$\vartheta = \arctan_2\left[\sin\vartheta, \cos\vartheta\right]. \tag{2.80}$$

This method provides a straightforward way to change the orientation of the antennas by

1. reading the antenna patterns at different angles (Θ, Φ) that include the orientation change,
2. calculating the polarization rotation matrix $\tilde{\mathbf{M}}$, and
3. using both to calculate the channel coefficient g in (2.66).

2.5.3 Constructing the Polarization Transfer Matrix

In this section, the orientation changes for the BS and MT side are combined. For the NLOS components, additional changes of the polarization are caused by scattering. The Jones calculus allows each of these effects to be modeled independently. In the end, the combined Jones matrices are used to calculate the channel coefficients.

Polarization of direct (LOS) path In the LOS polarization model, both the transmitter and the receiver can have different orientations, *e.g.*, due to a downtilt at the BS and a given movement direction at the MT. In addition, a reflection operation is needed to transform the outgoing direction at the transmitter into an incoming direction at the receiver. Thus, a combination of three linear transformations, two rotations and one reflection, is sufficient to construct the polarization transfer matrix of the LOS path.[5]

$$\begin{aligned} \mathbf{M}_{r,t,s}^{[\mathrm{LOS}]} &= \left[\tilde{\mathbf{M}}\left(\vartheta_{r,s}^{[\mathrm{LOS}]}\right)\right]^T \cdot \begin{pmatrix} 1 & 0 \\ 0 & -1 \end{pmatrix} \cdot \tilde{\mathbf{M}}\left(\vartheta_{t,s}^{[\mathrm{LOS}]}\right) \\ &= \begin{pmatrix} \cos\vartheta_{r,s}^{[\mathrm{LOS}]} & -\sin\vartheta_{r,s}^{[\mathrm{LOS}]} \\ -\sin\vartheta_{r,s}^{[\mathrm{LOS}]} & -\cos\vartheta_{r,s}^{[\mathrm{LOS}]} \end{pmatrix} \cdot \begin{pmatrix} \cos\vartheta_{t,s}^{[\mathrm{LOS}]} & -\sin\vartheta_{t,s}^{[\mathrm{LOS}]} \\ \sin\vartheta_{t,s}^{[\mathrm{LOS}]} & \cos\vartheta_{t,s}^{[\mathrm{LOS}]} \end{pmatrix} \end{aligned} \tag{2.81}$$

Model for the indirect (NLOS) paths For the NLOS components, the transmitted signal undergoes some diffraction, reflection or scattering before reaching the receiver. Following the common Fresnel formula in electrodynamics, the polarization direction can be changed at the boundary surface between two dielectric media. T. Svantesson [106] provided a method for modeling the polarization of a reflected wave where the polarization coupling is a function of several geometric parameters such as the orientation of the scatterers. However, these parameters are not generally available in the SCM. In addition to that, only metallic reflections keep the polarization unchanged. Reflections at dielectric media can cause changes of the polarization being a function of the complex-valued dielectric constant of the media and of the angle of

[5] The indices denote the Rx antenna element (r) and the Tx antenna element (t), the path number (l), the sub-path number (m), and the snapshot number (s).

incidence. Hence, not only the polarization angle might change, but also the polarization type. In order to address this issue, studies of the polarizations effects in individual scattering clusters in several outdoor- and indoor scenarios were done [69, 88, 107]. The published results indicate that scattering preserves the polarization in many cases. However, since only the powers of the elements in the polarization coupling matrix were analyzed, no conclusions can be drawn on how elliptic the polarization of the scattered wave will be.

It is possible to use the existing values for the XPR from the parameter tables of state-of-the-art GSCMs and derive additional Jones matrices in order to include the already known effects in the new channel model. The cross polarization ratio (XPR) is calculated from measurement data. A log-normal distribution is fitted to the measurement results having the average XPR_μ and the standard deviation (STD) XPR_σ^2. When those parameters are calculated from measured data, they are usually averaged over different propagations paths. Thus, the XPR value from the parameter tables is a LSP with a scenario-dependent distribution, *i.e.*, it depends on the positions of the MT. However, here, the values $\mathrm{XPR}_{l,m}^{[\mathrm{dB}]}$ for individual MPCs are needed. Those are calculated in two steps. First, a value $\mathrm{XPR}_\mu^{[\mathrm{LSP}]}$ is drawn from

$$\mathrm{XPR}_\mu^{[\mathrm{LSP}]} = \mathcal{N}\left(\mathrm{XPR}_\mu, \mathrm{XPR}_\sigma^2\right). \tag{2.82}$$

This value represents the average XPR over all MPCs at the receiver positions. Then, in a second step, the XPR for the individual MPCs is drawn using $\mathrm{XPR}_\mu^{[\mathrm{LSP}]}$ instead of XPR_μ. This maintains the original spread XPR_σ in the generated channel coefficients.

$$\mathrm{XPR}_{l,m}^{[\mathrm{dB}]} = \mathcal{N}\left(\mathrm{XPR}_\mu^{[\mathrm{LSP}]}, \mathrm{XPR}_\sigma^2\right) \tag{2.83}$$

Following the idea that the polarization coupling matrix $\mathbf{M}$ can be described by a combination of linear transformations, the model for the NLOS polarization maps the XPR to two Jones matrices, one for the linear polarization and one for the elliptic polarization. Additional deterministic components take the antenna orientations into account.

1. **Deterministic part**
   The deterministic component is the same as for the LOS polarization, *i.e.*, the different orientations of the antennas at the transmitter and the receiver are modeled by a rotation matrix as described in Section 2.5.2. A reflection operation is used to change the direction of the path.

2. **Linear component**
   During scattering, the linear polarization of a MPC might change. For example, a transmit antenna sends a *vertically* polarized wave which only oscillates in the $\hat{\mathbf{e}}_\theta$ direction. Then, a receiver might detect a wave that oscillates in both the $\hat{\mathbf{e}}_\theta$ direction and $\hat{\mathbf{e}}_\phi$ direction because scattering changed the *polarization angle* while the phases of the $\hat{\mathbf{e}}_\theta$ and $\hat{\mathbf{e}}_\phi$ components remain unchanged. In other words, a linear polarized wave stays linear polarized. In order to model this polarization change, the XPR of a path (2.83) is mapped to a rotation matrix. This was also suggested by [85].

   $$\mathbf{M}_{l,m}^{[\mathrm{linear}]} = \begin{pmatrix} m_{\theta\theta} & m_{\theta\phi} \\ m_{\phi\theta} & m_{\phi\phi} \end{pmatrix} = \begin{pmatrix} \cos\gamma_{l,m} & -\sin\gamma_{l,m} \\ \sin\gamma_{l,m} & \cos\gamma_{l,m} \end{pmatrix} \tag{2.84}$$

   Following the notations in [84], the rotation angle γ is calculated as

   $$\mathrm{XPR}_{l,m} = \frac{|m_{\theta\theta}|^2}{|m_{\phi\theta}|^2} = \frac{|m_{\phi\phi}|^2}{|m_{\theta\phi}|^2} = \frac{(\cos\gamma_{l,m})^2}{(\sin\gamma_{l,m})^2} = (\cot\gamma_{l,m})^2, \tag{2.85}$$

   $$\gamma_{l,m} = \operatorname{arccot}\left(\sqrt{\mathrm{XPR}_{l,m}}\right). \tag{2.86}$$

3. **Elliptical component**
When channel measurements are done with circular polarized antennas such as in land-mobile satellite scenarios [32], there is a very clear indication that scattering alters the phase between the two polarization components. In other words, a purely left hand circular polarized (LHCP) signal can be received with a right hand circular polarized (RHCP) antenna after scattering. There might also be a transformation from linear to elliptic polarization and *vice versa*. This is not covered well by the existing GSCMs. The commonly used approach in (2.67) creates a random phase difference between the polarization components. As a result, all paths have a (random) elliptic polarization and there is no way to adjust the XPR for circular polarized antennas. This is addressed in the new model by adding elliptic polarization using an additional Jones matrix. The phase difference between the $\hat{\mathbf{e}}_\theta$ and $\hat{\mathbf{e}}_\phi$ component is obtained by a scaling matrix

$$\mathbf{M}_{l,m}^{[\text{elliptic}]} = \begin{pmatrix} \exp(j\kappa_{l,m}) & 0 \\ 0 & \exp(-j\kappa_{l,m}) \end{pmatrix}. \tag{2.87}$$

The phase shift κ is calculated using the XPR from (2.83).

$$\kappa_{l,m} = X_{l,m} \cdot \operatorname{arccot}\left(\sqrt{\text{XPR}_{l,m}}\right) \tag{2.88}$$

$X_{l,m} \sim \{-1, 1\}$ is the positive or negative sign. In this way, the same XPR can be calculated from the channel coefficients at the output of the model when using circular polarized antennas.

The polarization for the NLOS paths is a combination of five linear transformations. First, any change in the transmitter orientation is included by a rotation matrix $\tilde{\mathbf{M}}(\vartheta_{t,l,m,s})$. Then, the influence of the scattering cluster is modeled by a combination of three operations: a scaling operation that introduces a phase shift between the vertical and horizontal component to obtain an elliptic XPR, a reflection operation, and a rotation operation to obtain the desired linear XPR. Last, the change in the receiver orientation is included by a second rotation matrix $\tilde{\mathbf{M}}(\vartheta_{r,l,m,s})$. The complete polarization transfer matrix is

$$\mathbf{M}_{r,t,l,m,s}^{[\text{NLOS}]} = \left[\tilde{\mathbf{M}}(\vartheta_{r,l,m,s})\right]^T \cdot \mathbf{M}_{l,m}^{[\text{linear}]} \cdot \begin{pmatrix} 1 & 0 \\ 0 & -1 \end{pmatrix} \cdot \mathbf{M}_{l,m}^{[\text{elliptic}]} \cdot \tilde{\mathbf{M}}(\vartheta_{t,l,m,s}) \tag{2.89}$$

The equation can be simplified by combining the first three operations into one.

$$\gamma_{l,m}^{+} = \vartheta_{r,l,m,s} - \gamma_{l,m} \tag{2.90}$$

$$\mathbf{M}_{r,t,l,m,s}^{[\text{NLOS}]} = \begin{pmatrix} \cos\gamma_{l,m}^{+} & -\sin\gamma_{l,m}^{+} \\ -\sin\gamma_{l,m}^{+} & -\cos\gamma_{l,m}^{+} \end{pmatrix} \begin{pmatrix} \exp(j\kappa_{l,m}) & 0 \\ 0 & \exp(-j\kappa_{l,m}) \end{pmatrix} \begin{pmatrix} \cos\vartheta_{t,s} & -\sin\vartheta_{t,s} \\ \sin\vartheta_{t,s} & \cos\vartheta_{t,s} \end{pmatrix}$$

In the channel model, the polarization effects and the antenna patterns are combined into a single channel coefficient

$$g_{r,t,l,m,s}^{[1]} = \mathbf{F}_r(\Theta_{r,l,m,s}^a, \Phi_{r,l,m,s}^a)^T \cdot \mathbf{M}_{r,t,l,m,s} \cdot \mathbf{F}_t(\Theta_{t,l,m,s}^d, \Phi_{t,l,m,s}^d), \tag{2.91}$$

where the angle pairs (Θ^d, Φ^d) and (Θ^a, Φ^a) include the orientation of the transmit antenna element t and receive antenna element r, respectively. Contrary to (2.66), the phase ψ (which results from the path length) and the path power P are not included yet. They are handled separately in the next section when the sub-paths were combined into paths.

2.6 Combining Sub-Paths into Paths

Sub-paths were introduced in Section 2.3 in order to emulate fading for the NLOS MPCs over time. Each path is split into (typically 20) sub-paths. The basic assumption is that sub-paths cannot be resolved in the delay domain but have a small angular spread. Each of the sub-paths gets initialized with a random phase ψ^0. In addition, a deterministic phase component $\psi_{r,l,m,s}$ is obtained from the total length of the propagation path using (2.49). Both components are combined to

$$\psi^{+}_{r,t,l,m,s} = \exp\left(-j\psi^{0}_{l,m} - j\psi_{r,t,l,m,s}\right). \tag{2.92}$$

The initial channel coefficients for each sub-path, including the polarization and antenna effects, were calculated in the previous section. Here, the sub-paths are combined again to obtain the channel coefficients for the paths. However, due to the random initial phases, a simple sum will result in a random path power since it is impossible to predict if the phase components add up constructively or destructively. This issue is left open in WINNER and 3GPP-3D channel model. Here, it is solved by defining an average power around which the path power is allowed to fluctuate. This average value is the initial path power P_l that was calculated in Section 2.2.

In the first step, the phase (2.92) is combined with the initial coefficients (2.91) to

$$g^{[2]}_{r,t,l,m,s} = g^{[1]}_{r,t,l,m,s} \cdot \psi^{+}_{r,t,l,m,s}. \tag{2.93}$$

Then, the resulting average power is calculated for each path and each segment. Segments were introduced in Section 2.4 as part of the user trajectory along which the LSPs don't change much and where the scatterer positions remain fixed. In the above equation, the channel coefficients g are given for $s = 1 \ldots S$ positions of a segment. Next, the coefficients of the 20 sub-paths are summed up and the average path powers from Section 2.2 are applied.

$$g^{[3]}_{r,t,l,s} = \sum_{m=1}^{20} g^{[2]}_{r,t,l,m,s} \tag{2.94}$$

$$g^{[4]}_{r,t,l,s} = \sqrt{\frac{P_l}{20} \cdot \frac{\sum_{s=1}^{S}\sum_{m=1}^{20}\left|g^{[2]}_{r,t,l,m,s}\right|^2}{\sum_{s=1}^{S}\left|g^{[3]}_{r,t,l,s}\right|^2}} \cdot g^{[3]}_{r,t,l,s} \tag{2.95}$$

If the resulting paths are observed over time, a characteristic fluctuation of the path power can be observed, similar to measurements with limited bandwidth. If there is only one snapshot in a segment, the scaling operation (2.95) ensures that each path gets assigned the power value from Section 2.2. The new method ensures that the input variables given to the SSF model, *i.e.*, the delay and angular spreads, are correctly mapped to the channel coefficients generated by the model. This is different from the WINNER and 3GPP-3D channel models where the sum over the subpaths produces random path powers. Hence, the new model can also be used to create channels having specific properties, *e.g.*, a predefined DS, to benchmark algorithms. For example, it is possible to evaluate the throughput of a MIMO-orthogonal frequency division multiplexing (OFDM) scheme as a function of the DS. In the next section, the remaining LSPs, *i.e.*, the PG, the SF, and the KF are applied to the channel coefficients.

2.7 Path Gain, Shadow Fading and K-Factor

Hata [64] presented a simple model for macro-cellular settings where the PG scales with the logarithm of the distance d (in units of meters) between BS and terminal

$$\mathrm{PG}^{[\mathrm{dB}]} = -A \cdot \log_{10} d_{[\mathrm{km}]} - B + X, \tag{2.96}$$

where A and B are scenario-specific coefficients that are typically determined by measurements. The path gain exponent A often varies between values of 20 and 40, depending on the propagation conditions, the BS height, and other factors. The shadow fading (SF) is modeled by a random variable X. However, this variable is correlated with the distance between two points, *i.e.*, two closely spaced MTs will experience the same SF. A 2-D correlation model for this effect was introduced in Section 2.1 where the SF, among other parameters, is described by a map. Combining the PG and SF results in the effective path gain

$$\mathrm{PG}_s^{[\mathrm{eff}]} = \sqrt{10^{0.1\left(\mathrm{PG}_s^{[\mathrm{dB}]} + \mathrm{SF}_s^{[\mathrm{dB}]}\right)}}. \tag{2.97}$$

The movement of the MT is described by a trajectory where the index s denotes a specific position on this trajectory. Hence, the effective PG is a vector of $s = 1 \ldots S$ elements. The S values of the SF in (2.97) come from the map. Since the sampling grid of the map is usually different from the positions of the terminal trajectory, an interpolation of the surrounding points of the map is needed. This can be done with standard numeric methods, *e.g.*, by spline interpolation.

The Ricean K-factor (KF) describes the power difference between the LOS and NLOS components. In the previous section, the channel coefficients were scaled by the power values P_l that were calculated in Section 2.2. These power values already include the KF. However, like the SF, the KF is also correlated with the distance which is described by a map as well. The initial power values from Section 2.2 only consider the KF at the beginning of the trajectory. When the MT moves to a different position, its KF changes and so do the power values of the MPCs. Hence, an additional scaling factor for the path powers is needed.

$$\mathrm{KF}_{l,s}^{[\mathrm{scale}]} = \sqrt{1 + P_1 \left(\frac{K_s}{K_0} - 1\right)} \cdot \begin{cases} \sqrt{\frac{K_s}{K_0}} & \text{for } l = 1; \\ 1 & \text{otherwise.} \end{cases} \tag{2.98}$$

The index $l = 1 \ldots L$ is the path number, P_1 is the power of the first path that was calculated in Section 2.2, K_0 is the KF at the beginning of the trajectory, and K_s is the KF at the sth position of the user trajectory. The values for K_s come from the KF map from Section 2.1. The channel coefficients from the previous section (2.95) are then scaled to

$$g_{r,t,l,s} = \mathrm{PG}_s^{[\mathrm{eff}]} \cdot \mathrm{KF}_{l,s}^{[\mathrm{scale}]} \cdot g_{r,t,l,s}^{[4]} \tag{2.99}$$

This is the last step in the small-scale-fading (SSF) model. At this point, the complex-valued amplitude g for each of the L MPCs of the CIR is described for all antenna pairs r, t at S positions of the user trajectory. In addition, there is an equal amount of values for the path delays τ that were calculated in Section 2.4. In the next section, adjacent parts of the user trajectory (*i.e.*, the segments) get merged into an even longer sequence of channel coefficients. With this, channels can be observed over long periods of time which includes transitions between propagation scenarios, *e.g.*, when a MT moves from outdoors to indoors.

2.8 Transitions between Segments

The small-scale-fading (SSF) model, which was laid out in the previous Sections 2.2 to 2.7 is only defined for a short part of a MT trajectory. If the MT traverses larger distances, the LSPs will change when the terminal sees different scattering clusters. Hence, in order to include long terminal trajectories in the model, there needs to be a model for the "birth and death of scattering clusters". One idea on how to include such a process in GSCMs comes from the WINNER II model [47] where paths fade in and out over time. However, [47] does not provide a method to keep the LSPs consistent. For example, if one cluster disappears and a new on appears in its place, the delay and angular spread of the channel changes. However, those values are fixed by LSF model.

In the new model, long terminal trajectories are split into shorter segments where the LSPs are reasonably constant. Then, for each segment the small-scale-fading (SSF) model creates independent scattering clusters, channel coefficients, and path delays. Two adjacent segments are overlapping as depicted in the top of Figure 2.8. The lifetime of scattering clusters is confined within the combined length of two adjacent segments. In the overlapping part, the power of paths from the old segment is ramped down and the power of new paths is ramped up. Hence, this process describes the birth and death of scattering clusters along the trajectory. All paths of the segment are active outside the overlapping region. The overlapping region is further split into sub-intervals to keep the computational and memory overhead of the model low. During each sub-interval, one old path ramps down and one new path ramps up. The power ramps are modeled by a squared sine function

$$w^{[\mathrm{sin}]} = \sin^2\left(\frac{\pi}{2} \cdot w^{[\mathrm{lin}]}\right). \tag{2.100}$$

Here, $w^{[\mathrm{lin}]}$ is the linear ramp ranging from 0 to 1, and $w^{[\mathrm{sin}]}$ is the corresponding sine-shaped ramp with a constant slope at the beginning and the end. This prevents inconsistencies at the edges of the sub-intervals. If both segments have a different number of paths, the ramp is stretched over the whole overlapping area for paths without a partner. For the LOS path, which is present in both segments, only power and phase are adjusted.

Paths need to be carefully matched to minimize the impact of the transition on the instantaneous values of the LSPs. For example, the DS increases if a path with a small delay ramps down and a similarly strong path with a large delay ramps up. Hence, the DS can fluctuate randomly within the overlapping region. To balance this out, paths from both segments are paired in a way that minimizes these fluctuations. This is done by determining the values of the DS before and after the transition. Then, a target DS is calculated for each sub-interval. For example, if the old segment yields a DS of 200 ns and the new segment has 400 ns, then the target DS will be 220 ns for the first sub-interval, 240 ns for the second and so on. Then, a combination of paths is searched that best matches the target DS for each sub-interval.

In the real world, MTs move at arbitrary speeds, including accelerations and decelerations. Provided that the sampling theorem is fulfilled, *i.e.*, that the channel is sampled four times per wavelength, it is possible interpolate the channel coefficients to include such effects. This is illustrated in the bottom part of Figure 2.8. The white dots represent the snapshots at a constant distance. However, the sample points (gray stars) can have unequal spacing, *e.g.*, for an accelerated movement. Each sample point in the time domain (given in units of seconds) has a corresponding position on the MT trajectory (in units of meters). The amplitudes and phases of the channel coefficients are interpolated separately using cubic spline interpolation. The path delays are interpolated with a piecewise cubic hermite interpolating polynomial.

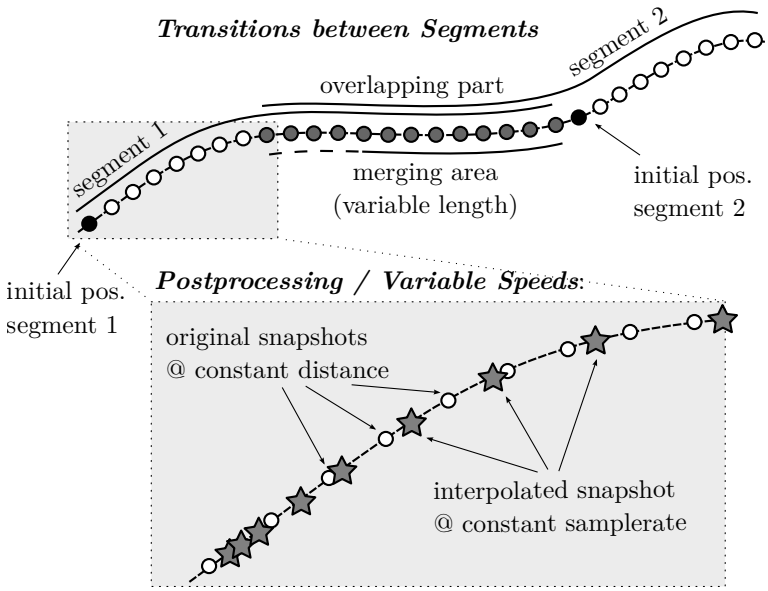

Figure 2.8: Top: illustration of the overlapping area used for calculating the transitions between segments (step G), Bottom: illustration of the interpolation to obtain variable MT speeds (step H).

2.9 Summary

A new channel model has been derived from existing GSCMs such as the WINNER and 3GPP-3D model. The LSF and SSF parts of the model have been extended in several ways in order to overcome some drawbacks and limitations of the state-of-the-art approaches. The main problems that were addressed by these modifications are:

- **Spatial consistency of LSPs**
  3GPP does not specify a method to ensure spatial consistency, neither for the LSF nor SSF model. In the new model, a map-based approach similar to [74] is used to correlate the LSPs with the distance between two pints. Additional filtering steps were introduced in the new model to make the maps "smoother" in order to interpolate them to support extended mobility features.

- **Consistency between LSF and SSF model**
  The WINNER and 3GPP models do not map large-scale parameters to channel coefficients. They are only correct in a statistical sense. This is solved in the new model by additional scaling operations for the delays, angles, and powers after combining the sub-paths. As a result, the correct delay and angular spreads can be calculated from the generated channel coefficients of the model.

- **Mobility of MTs**
  The WINNER and 3GPP models do not allow MTs to move more than a few meters because there is no method to track the delays and directions of a path. Only the Doppler shifts of the MPCs are modeled. The mobility extensions made in the new model are two-fold: First, a concept known as *drifting* [71] was added to the SSF model. Second, a model for the appearing and disappearing of scattering clusters was added. This is done by splitting a user trajectory in short overlapping segments. When the terminal moves from one segment to the next, the scattering clusters from the old segment are smoothly replaced with clusters from the new segment while keeping the LSPs consistent.

- **Polarization**
  The WINNER and 3GPP models do not correctly model elliptical and circular polarization. Therefore, a new model for the polarization was derived from the Jones calculus [87]. In this approach, changes of the polarization during scattering are modeled by successive linear transformations, allowing linear and elliptic polarization to be adjusted independently.

With these updates, it is possible to generate channel coefficients with the same spatial and temporal resolution as measured data. Thus, the output of the channel model can be directly compared to the output of a measurement campaign. This is done in the next chapters. At first, the methods for deriving the model parameters are presented in Chapter 3. Then, two measurement campaigns are evaluated and the results are compared with the model.

3 Channel Model Parameterization and Validation Methodology

Geometry-based stochastic channel models such as the new model outlined in Chapter 2 are used to test and validate new concepts in mobile communications. This requires that the channel coefficients, which are generated by such models, represent the real world accurately. In order to be able to do so, current state-of-the-art models such as the 3GPP-3D model [49] require more than 50 parameters to fully characterize a propagation scenario. All of these parameters need to be obtained from measurements. Unfortunately, there is no straightforward way to perform the measurements, process the data and extract the model parameters. Measurements are often limited by technical or regulatory constraints such as bandwidth, transmit power, number of antennas, access to measurement locations, *etc.* The raw data, which is acquired from the measurement system, needs to be processed in order to calculate the model parameters. However, the data format and the processing techniques are often undefined. Lastly, the calculation methods for the model parameters themselves are ambiguous. They often lack a clear definition, *e.g.*, the exact definition of the angular spread, and they depend on additional variables such as thresholds and resolution limits. Thus, the model parameters do not only depend on the measured scenarios, but also on the evaluation methods. In this chapter, a general framework for the model parameterization is outlined. This covers four aspects: the estimation of path parameters, the estimation of large-scale parameters, the estimation of performance metrics, and the validation of the model.

Estimation of path parameters First, the path parameters, *i.e.*, the path-delays, path-powers, departure and arrival angles, need to be extracted from the raw measurement data. The high-resolution estimation of these parameters has attracted quite a lot of interest in the past years and there are many algorithms for this task. The common approach followed by all estimation algorithms is to fit the parameters of a so-called *data model*, *i.e.*, an ideal representation of how the received signal should look like, to the measured signal. The data model contains the known quantities of the measurements, *e.g.*, the antenna positions, the measurement bandwidth, *etc.*, and the unknown properties of the radio channel, *e.g.*, the number of paths, their delays and angles. In addition, the useful signal is generally hidden in measurement noise which needs to be taken into account by the algorithms.

The algorithms can be divided into two classes: the so-called subspace based class of algorithms and the expectation maximization algorithms. The subspace-based methods, such as MUSIC (MUltiple SIgnal Classification) [108] and ESPRIT (Estimation of Signal Parameters via Rotational Invariance Techniques) [109] try to find the path parameters by separating the signal and noise subspaces. Early work was only focused on estimating the arrival directions. However, Richter *et al.* [110] have shown that the ESPRIT algorithm can be extended to jointly estimate departure and arrival angles as well as the path-delays. Unfortunately, most subspace-based approaches only work well with so-called shift invariant array antennas [63] which limits their practical applicability. The second class of algorithms breaks the multidimensional search for the path parameters into sequential one-dimensional searches. In this way, these algorithms can

take advantage of standard numeric techniques to find the parameters one after the other. A well-known method is the SAGE algorithm (Space Alternating Generalized Expectation Maximization) [111, 112].

A new method similar to the SAGE algorithm is proposed in Section 3.1.2 of this thesis. The idea is to separate the estimation of the delays and angles into separate steps. This makes the delay estimation independent of the antenna patterns. As a result, a time-domain representation of the channel is calculated from the measurement data where the bandwidth limitation and most of the noise have been removed. Hence, identical evaluation techniques can be used for both the measurement data and the channel coefficients which are obtained from the model. If the radiation patterns of the measurement antennas are available, an optional second step of the algorithm detects the angles of the paths.

Estimation of LSPs A second aspect that is left open in current state-of-the-art GSCM is how to derive the model parameters. For example, the 3GPP-3D model [49] provides parameters for several propagation conditions, *e.g.*, urban-macrocell (UMa), urban-microcell (UMi), and outdoor-to-indoor (O2I). For each of the scenarios, there are values for the delay spread, the angular spread, the Ricean K-factor and many other parameters. However, it is not specified anywhere how these parameters are defined and how they can be calculated from measured data. For the new model, the model parameters are defined in Section 3.2. Each of the parameters can be estimated from the paths parameters that were calculated in the previous step, *i.e.*, the delays, powers and angles of the MPCs.

Estimation of performance metrics The main purpose of GSCMs is to provide an antenna and location-independent description of the radio channel. Then, results from single-link measurement campaigns can be generalized and performance predictions can be made for entire networks having hundreds of BSs and MTs. However, it is unclear if the channel models are suitable for this task, *i.e.*, if the performance predictions made by the models are comparable to the real world. Therefore, several performance metrics, *e.g.*, single and multi-user MIMO capacities, are introduced in Section 3.3. These performance metrics can be calculated from both the measured channels and the channel coefficients from the model. Results can then be directly compared and the model can be *validated*.

Validation of the channel model A flow chart of the entire parameterization and validation procedure of the new channel model is depicted in Figure 3.1. The general procedure can be grouped in four main steps:

1. Measurements,
2. Estimation of path parameters,
3. Estimation of LSPs and performance metrics,
4. Resimulation.

In the first step, the wireless channels are measured in a characteristic propagation scenario, *e.g.*, in urban-macrocell or microcell conditions. This requires suitable measurement equipment to derive the required path and model parameters. For example, data with high spatial and temporal resolution is required to accurately derive the delay and angular spreads. It is also mandatory to characterize the antenna patterns for estimating the arrival and departure angles. This is usually done by measuring the antenna radiation patterns in an anechoic chamber.

In the second step, the raw measurement data is processed in order to identify the multipath components, their delays, powers, and angles. The delays and angles are extracted in two separate steps. Path delays and MIMO coefficient matrices are calculated as described in Section 3.1.2. The resulting channel coefficients are then used to estimate the LSPs and the performance metrics. This involves estimating the departure and arrival angles in order to derive the angular spreads as described in Section 3.1.3.

Once the model parameters are known, initial parameter tables are created that can be used in the channel model. However, in the channel model, propagation and antenna effects are treated separately while the antenna effects are always included in the measured data. Hence, the initial parameter tables might not be suitable for the model. To validate the correctness of the parameters, the entire measurement setup is recreated in the channel model and artificial channel coefficients are generated in the resimulation step. Those have the same format as the output of the preprocessing step (MIMO coefficient matrices in delay domain). The same LSPs and the performance metrics are estimated from the resimulated channels. If there are differences between the model output and the measurement results, adjustment are made for the model input parameters. A thorough comparison of the LSPs from the measured data, the LSPs at the input of the channel model, and the LSPs from the resimulated data is then done to confirm that the channel model can recreate all observed phenomena.

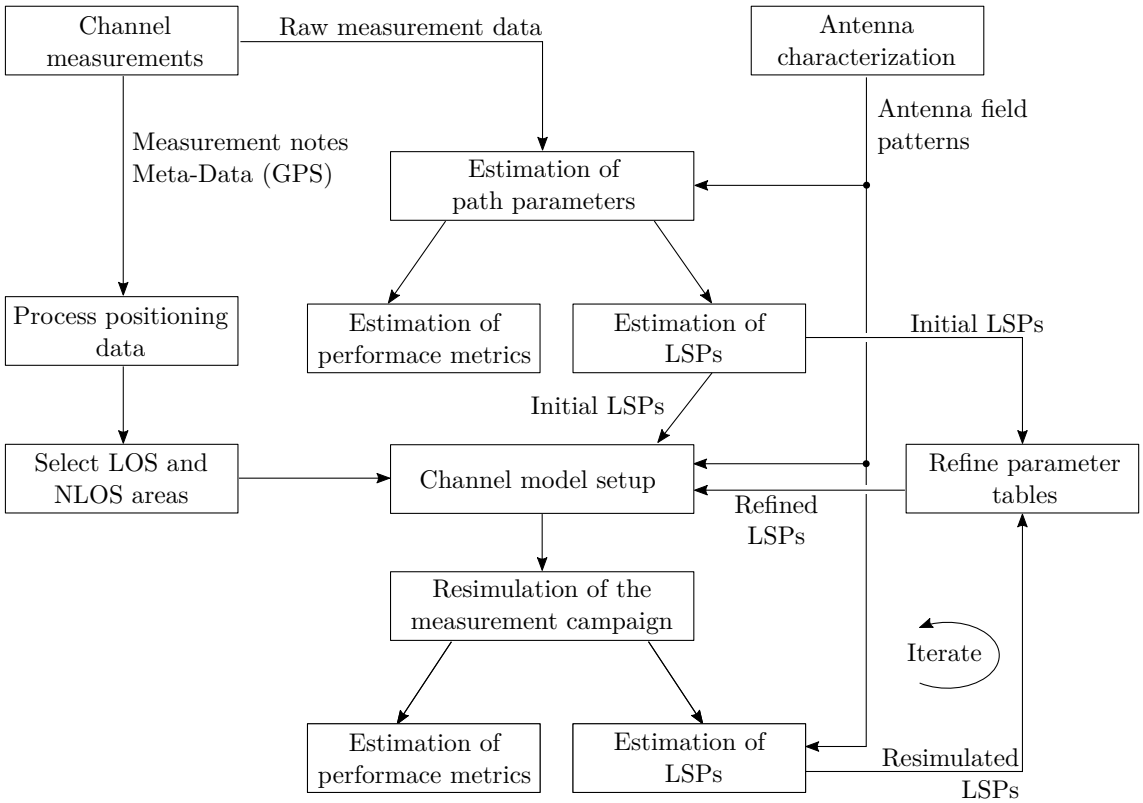

Figure 3.1: Flow chart of the data analysis and model parameterization procedure

3.1 Estimation of Path Parameters

In this section, the path parameters (delay, power, angles, and polarization) are estimated from the raw measurement data. The method presented here is similar to the SAGE algorithm (Space Alternating Generalized Expectation Maximization) [111, 112]. However, the procedure is divided into two steps. First, the path-delay and the MIMO coefficient matrix are calculated for each MPC. This step is independent of the antennas used in the measurement. The output data format is identical to the output format of the channel model from Chapter 2. Then, a second step calculates the departure and arrival angles of the paths.

3.1.1 Data Model

In order to extract the path parameters from the measurement data, it is necessary to define how they are contained in the data. This is done by the so-called *data model*. The data model contains the known quantities, *e.g.*, the antenna positions, the measurement bandwidth, *etc.*, and the unknown properties of the radio channel, *e.g.*, the number of paths, their delays and angles. The estimation algorithms in the following sections then try to find the unknown parameters, *i.e.*, the path parameters.

The wireless channel is characterized by measurements. A transmitter (the channel sounder) sends out a known signal (the sounding sequence) that is received by a receiver. Both the transmitter and the receiver are (generally) equipped with array antennas having n_t transmit antenna elements and n_r receive antenna elements, respectively. Thus, the MIMO channel is composed of $n_t \times n_r$ individual *links*. It is further assumed that the sounding sequence has a bandwidth B and that the measurement system is able to provide the baseband frequency response (FR) for each MIMO link at N sample frequencies f_n spread over the entire bandwidth B. The N sample frequencies do not need to be equally spaced. The observation of the broadband MIMO channel can then be described as

$$\mathbf{Y}_n = \mathbf{H}_n + \mathbf{V}_n, \qquad n \in \{1, 2, ..., N\}, \tag{3.1}$$

where the complex-valued matrix $\mathbf{Y}_n$ is the measured channel matrix with n_r rows and n_t columns. $\mathbf{H}_n$ is the "true" channel matrix and $\mathbf{V}_n$ is a noise matrix. The index n describes the sample frequency. If the data model can describe the real world perfectly, then $\mathbf{V}_n$ is an AWGN matrix with elements $\nu_{r,t,n} \sim \mathcal{CN}(0, {\sigma_\nu}^2)$.

In the data model, each MPC is described by an infinitely short pulse arriving with a delay τ relative to the beginning of the channel impulse response (CIR), *e.g.*, the time when the transmitter starts sending its sounding sequence. In addition, it is assumed that the physical size of the array antennas is small enough so that delay differences caused by different positions of the antenna elements cannot be resolved. Thus, the frequency domain channel $\mathbf{H}$ can be decomposed into

$$\mathbf{H}_n = \sum_{l=1}^{L} \mathbf{G}_l \cdot e^{-2\pi j \cdot f_n \cdot \tau_l}. \tag{3.2}$$

In this equation, the index $l = 1 \ldots L$ denotes the path number and $\mathbf{G}_l$ is the MIMO coefficient matrix. f_n is the nth sample frequency in Hz relative to the beginning the measurement bandwidth and τ_l is the delay of the lth path in seconds. The coefficient matrix $\mathbf{G}_l$ has n_r row and n_t columns. It contains one complex-valued channel coefficient for each antenna pair. The

individual values of the coefficients are a result of the attenuation of a path, the weighting by the antenna radiation patterns, and the polarization. They are described by

$$g_{r,t,l} = \sqrt{P_l} \cdot \mathbf{F}_r(\phi_l^a, \theta_l^a)^T \cdot \mathbf{M}_l \cdot \mathbf{F}_t(\phi_l^d, \theta_l^d) \cdot e^{-j\psi_{r,t,l}}, \tag{3.3}$$

where $r = 1 \dots n_r$ is the receive antenna index and $t = 1 \dots n_t$ is the transmit antenna index. P_l is the power of the lth path and $\psi_{r,t,l}$ is a random phase offset. The 2×2 matrix $\mathbf{M}_l$ describes how the polarization of a path changes during propagation. The antenna radiations patterns for the transmit and receive antenna elements are described by a two 2-element vectors $\mathbf{F}_t$ and $\mathbf{F}_r$, respectively. They are a function of the elevation angles ϕ and azimuth angles θ. Radiation patterns need to be given in a polar spherical polarization basis. A detailed introduction on the antenna and polarization model is given in Section 2.5 of this thesis.

In addition to the so-called *specular* components, *i.e.*, the infinitely short pulses, A. Richter [113] also introduced so-called *dense multipath components* (DMC). These components cannot be described by the above model, but they also do not have AWGN properties, *i.e.*, they are not noise. However, when analyzing the measurement data to validate the new channel model, it was found that the specular components account for more than 90% of the energy in almost all measured CIRs. Thus, the contribution of unresolvable paths is small. Also, there is no model for the DMC in the channel model. For these reasons, DMC is not included in the data model and all unresolvable components are considered to be noise.

The algorithm presented in the next section solves (3.2), *i.e.*, it decomposes the channel tensor $\mathbf{H}$ into L delays τ_l and coefficient matrices $\mathbf{G}_l$. Then, the method from Section 3.1.3 further processes the coefficient matrices to find the angles, polarization states, and path-powers.

3.1.2 Detection of Multipath Components in the Delay Domain

In this section, the number of paths L, the path delays τ_l and the MIMO coefficient matrices $\mathbf{G}_l$ are estimated from the measurement data. During the measurements, the MT obtains the frequency response of the MIMO channel. Thus, it is possible to estimate the MPCs and their complex-valued amplitudes. The basic idea goes back to the space-alternating generalized expectation-maximization (SAGE) algorithm [112] where channel parameters have been estimated in a similar fashion. However, here, calibrated antenna patterns are generally not required. Hence, it is not possible to calculate the arrival and departure angles directly. A coefficient matrix for each MPC is obtained which can then be further processed to obtain the angles and angular spreads.

Problem statement: The observation of the broadband MIMO channel can be described as

$$\mathbf{Y}_n = \mathbf{H}_n + \mathbf{V}_n, \qquad n \in \{1, 2, ..., N\}, \tag{3.4}$$

where the matrix $\mathbf{Y}_n$ is the measured channel matrix with n_r rows and n_t columns. $\mathbf{H}_n$ is the true channel matrix and $\mathbf{V}_n$ is an AWGN matrix with elements $\nu_{r,t,n} \sim \mathcal{CN}(0, {\sigma_\nu}^2)$. The L strongest MPCs are estimated with their normalized delay m_l and their complex-valued coefficient matrix $\mathbf{G}_l$ with $l \in \{1, 2, ..., L\}$ from the observation $\mathbf{Y}$ in an iterative fashion in order to find a representation $\hat{\mathbf{H}}$ of the channel matrix where most of the noise has been removed. In the following, r is the receive antenna index, t is the transmit antenna index, l is the path index and n is the pilot tone index.

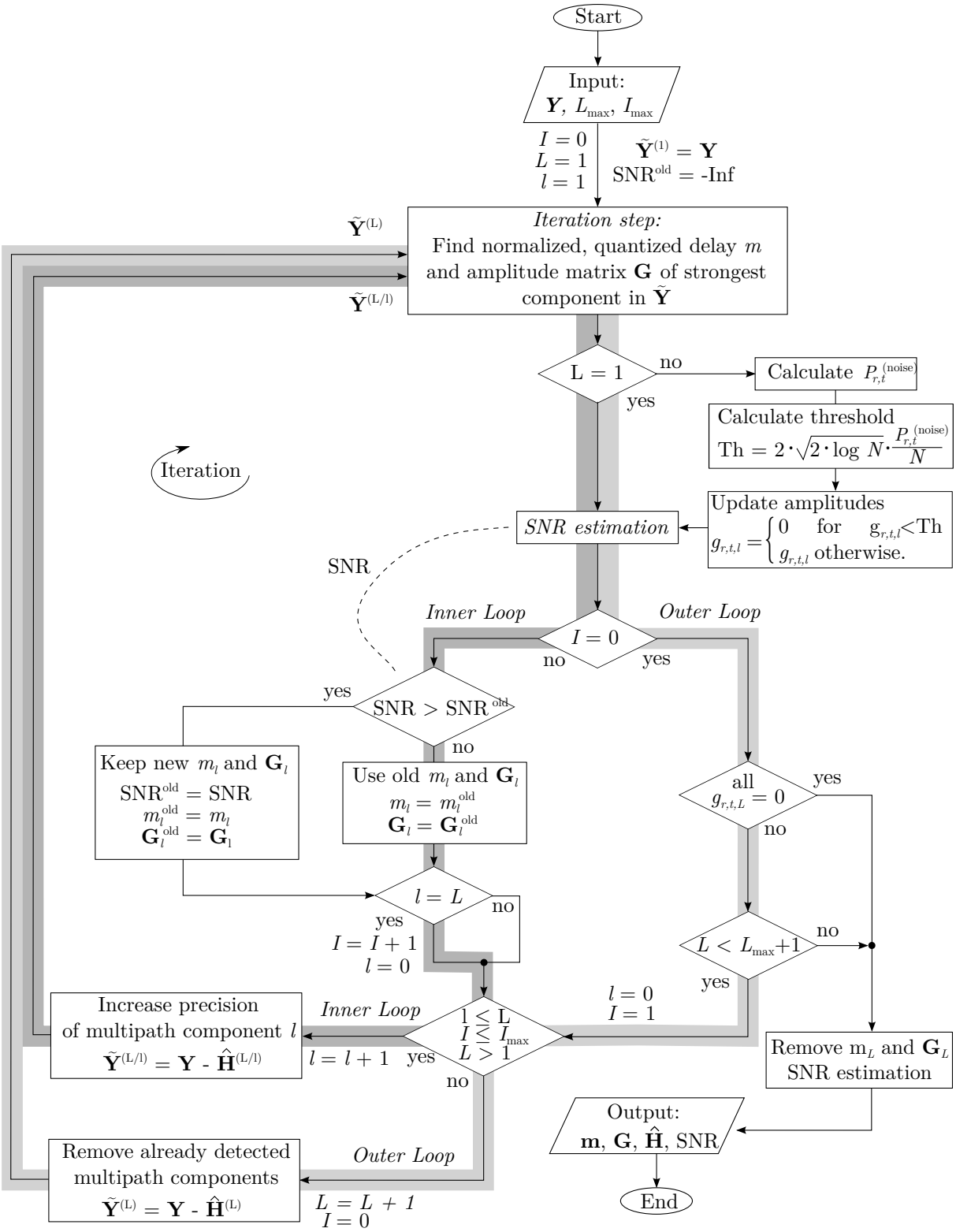

Figure 3.2: Flow chart of the iterative detection of multipath components from MIMO channels. The inner iteration loop can be repeated more than once for each MPC which results in further precision improvements.

Iteration step: In each iteration step, the normalized delay m_l of the lth MPC is estimated by

$$m_l = \arg\max_{m_l} \sum_{r=1}^{n_r} \sum_{t=1}^{n_t} \underbrace{\left| \sum_{n=1}^{N} \tilde{y}_{r,t,n}^{(l)} \cdot e^{2\pi j \cdot m_l \cdot \frac{f_{r,t,n}}{B}} \right|^2}_{\text{Power-Delay Profile}}, \tag{3.5}$$

where the matrix $\tilde{\mathbf{Y}}^{(l)}$ (composed of elements $\tilde{y}_{r,t,n}^{(l)}$) is a representation of $\hat{\mathbf{H}}$ where already detected MPCs have been removed. f_n in the argument of the exponential function is the position of the pilot relative to the beginning of the FR in units of Hz and B is the bandwidth. Each MIMO sublink can have different pilot positions. Hence, the additional indexes t and r are for the transmit and receive antenna element, respectively. In the first step, no MPCs are known yet ($L = 0$). Therefore, l is set to 1 and $\tilde{\mathbf{Y}}^{(1)} = \mathbf{Y}$ from (3.4) is used.

The values m_l are normalized to the bandwidth B. The corresponding path delay in units of seconds is

$$\tau_l = \frac{m_l}{B}. \tag{3.6}$$

The coefficient matrix $\mathbf{G}_l$ has n_r rows and n_t columns since in (3.5) the delay estimation was done on the combined PDP of the channel. The scalar coefficients $g_{r,t,l}$ of the matrix $\mathbf{G}_l$ are

$$g_{r,t,l} = \frac{1}{N} \sum_{n=1}^{N} \tilde{y}_{r,t,n}^{(l)} \cdot e^{2\pi j \cdot m_l \cdot \frac{f_{r,t,n}}{B}}. \tag{3.7}$$

After each iteration step an update of the effective channel matrix $\hat{\mathbf{H}}$ is calculated using

$$\hat{h}_{r,t,n}^{(L)} = \sum_{l=1}^{L} g_{r,t,l} \cdot e^{-2\pi j \cdot m_l \cdot \frac{f_{r,t,n}}{B}}. \tag{3.8}$$

Depending on the state of the iterative detection algorithm, there are two options for setting $\tilde{\mathbf{Y}}^{(l)}$ in (3.5). These are shown in Figure 3.2 as an inner and an outer iteration loop.

1. **Outer loop**
   A new MPC is detected. Therefore, all previously detected MPCs are removed from the observation $\mathbf{Y}$, l is set to $l = L + 1$ and a new delay is detected using (3.5) with

$$\tilde{\mathbf{Y}}^{(L)} = \mathbf{Y} - \hat{\mathbf{H}}^{(L)} \qquad \tilde{y}_{r,t,n}^{(L)} = y_{r,t,n} - \hat{h}_{r,t,n}^{(L)} = y_{r,t,n} - \sum_{l=1}^{L} g_{r,t,l} \cdot e^{-2\pi j \cdot m_l \cdot \frac{f_{r,t,n}}{B}}, \tag{3.9}$$

   where $\hat{\mathbf{H}}^{(L)}$ is the effective reconstructed channel matrix (3.8) using the L already detected MPCs. After this iteration step, L is increased by one.

2. **Inner loop**
   The delays m_l and amplitudes $\mathbf{G}_l$ of each MPC are distorted by interference from the following (still undetected) MPCs and also by approximation errors of the already estimated ones. The precision of an already detected MPC can be increased by repeating the iteration (3.5) for the lth component with

$$\tilde{\mathbf{Y}}^{(l)} = \mathbf{Y} - \hat{\mathbf{H}}^{(L/l)} \qquad \tilde{y}_{r,t,n}^{(l)} = y_{r,t,n} - \hat{h}_{r,t,n}^{(L/l)} = y_{r,t,n} - \sum_{\substack{\forall \tilde{l} \in \{1 \ldots L\} \\ \tilde{l} \neq l}} g_{r,t,\tilde{l}} \cdot e^{-2\pi j \cdot m_{\tilde{l}} \cdot \frac{f_{r,t,n}}{B}}, \tag{3.10}$$

where $\hat{\mathbf{H}}^{(L/l)}$ is the effective channel matrix reconstructed from L MPCs except the lth one. At this point, it might happen that two closely spaced MPCs cancel each other out when the phase differences of strong components in $\mathbf{G}_l$ is close to $\pm\pi$. In this case, the inner iteration loop can lead to erroneous results. Therefore, updates of m_l and $\mathbf{G}_l$ are only applied when the new values improve the detection SNR.

SNR estimation: If all MPCs are detected correctly, then $\mathbf{Y} - \hat{\mathbf{H}}^{(L)}$ contains only noise. The channel estimation SNR can be estimated by

$$P_{r,t}^{(\text{equiv})} = \frac{1}{N}\sum_{n=1}^{N}\left|\hat{h}_{r,t,n}^{(L)}\right|^2, \tag{3.11}$$

$$P_{r,t}^{(\text{noise})} = \frac{1}{N}\sum_{n=1}^{N}\left|y_{r,t,n} - \hat{h}_{r,t,n}^{(L)}\right|^2, \tag{3.12}$$

$$\text{SNR}_{\text{dB}} \approx 10\cdot\log_{10}\left(\sum_{r=1}^{n_r}\sum_{t=1}^{n_t}\frac{P_{r,t}^{(\text{equiv})} - \frac{3\tilde{L}_{r,t}}{2N}\cdot P_{r,t}^{(\text{noise})}}{(1+\frac{3\tilde{L}_{r,t}}{2N})\cdot P_{r,t}^{(\text{noise})}}\right). \tag{3.13}$$

The empirical factor $\frac{3\tilde{L}_{r,t}}{2N}$ accounts for the remaining noise included in $\mathbf{G}_l$ and the jitter in m_l which is proportional to the number of estimated MPCs. $\tilde{L}_{r,t}$ is used instead of L because it might happen that paths are only detected on some MIMO sublinks but not on others. Hence, the number of detected MPCs might differ on each MIMO sublink. As mentioned above, the updates in the inner iteration loop are only carried out if they increase the overall SNR.

Stop criterion: Candes and Tao [114] state that for a sparse channel vector $\mathbf{h}_{r,t}$, which is satisfied when $L \ll N$, it is possible to find a $\hat{\mathbf{h}}_{r,t}$ such that the mean square error (MSE) is within a factor of $\log N$ of the ideal MSE.

$$||\mathbf{y}_{r,t} - \hat{\mathbf{h}}_{r,t}||^2 = O(\log N)\cdot\mathbb{E}\{||\mathbf{y}_{r,t} - \mathbf{h}_{r,t}||^2\} \tag{3.14}$$

Donoho and Johnstone [115] further state that thresholding achieves the ideal MSE with a threshold level at $\sqrt{2\cdot\log N}\cdot{\sigma_\nu}^2$. In general, the exact number of MPCs is unknown. If the exact value σ_ν^2 is also unknown it is possible to set the threshold in an adaptive fashion. However, if N is not large enough compared to L, the detection fails. Therefore, the noise floor can be estimated from the PDP of the measurement data.

Since the estimation of the delays is done on the combined PDP of all MIMO sublinks and (3.14) is only defined for single input single output (SISO) channels, some additional effects need to be taken into account.

1. There are paths that cause a signal on some MIMO sublinks but fall below the threshold on others. Therefore, some values in $\mathbf{G}_l$ might be zero and a different number of paths $\tilde{L}_{r,t}$ might be obtained for each MIMO sublink.

2. The stop criterion is checked independently for each MIMO sublink. When the delays are refined in the inner iteration loop, there might be paths that have been above the threshold in an earlier iteration step but fall below in a later one. Hence, paths can also disappear.

After each iteration step, the noise power $P_{r,t}^{(\text{noise})}$ is calculated on all MIMO sublinks (3.11). Given that all $|\nu|^2 \sim \chi_2^2$, σ_ν^2 can be set to $2\cdot P^{(\text{noise})}$ and the coefficient matrix is updated in

order to remove MPCs that fall below the threshold.

$$\tilde{g}_{r,t,l} = \begin{cases} 0 & \text{for} \quad g_{r,t,l} < 2 \cdot \sqrt{2 \cdot \log N} \cdot P_{r,t}^{(\text{noise})}/N \\ g_{r,t,l} & \text{otherwise.} \end{cases} \tag{3.15}$$

The detection of new MPCs in the outer iteration loop stops when all amplitudes of the last detected path fall below the threshold. An example of the processed output can be seen in Figure 3.3.

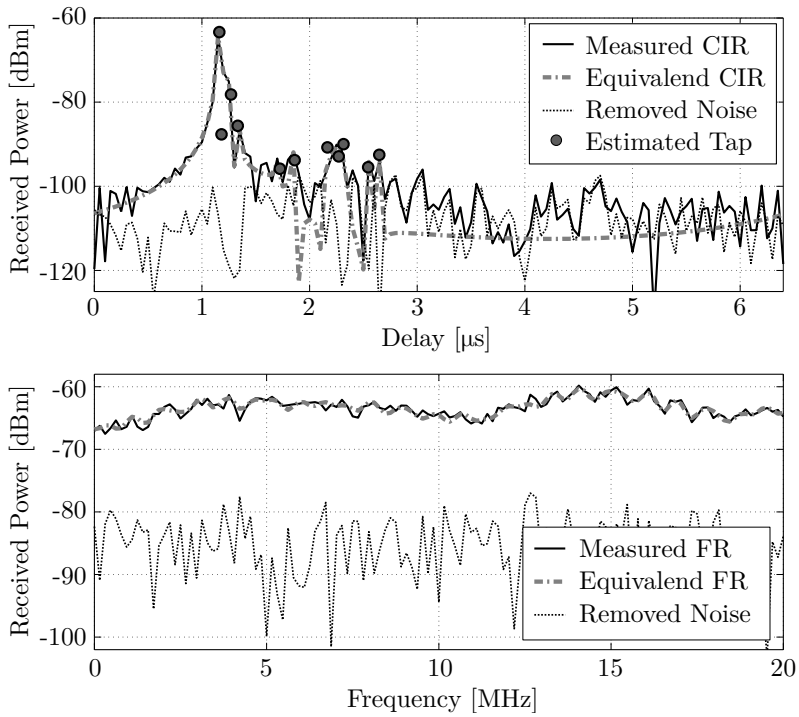

Figure 3.3: Example output of the iterative tap estimation in the time domain (top) and frequency domain (bottom). The measured channel response (black, solid line) is processed by the algorithm and 11 taps are estimated before the threshold is reached. Those taps are used to calculate a noise-reduced equivalent channel.

3.1.3 Detection of Multipath Components in the Spatial Domain

In this section, the previously detected coefficient matrices $\mathbf{G}_l$ are further processed to derive the departure angles at the BS, the arrival angles at the MT, and the polarization effects that occur during propagation. The antenna radiation patterns are de-embedded in this process.

For each MPC (in the time domain) a $n_r \times n_t$ complex-valued channel coefficient matrix is estimated using the algorithm from Section 3.1.2. Each coefficient has an amplitude and a phase value. The amplitudes are mostly determined by the directional gain of the antenna elements. If the array antennas are reasonably compact, *i.e.*, the element spacing is below 2 λ, it can be assumed that the average path length is about the same for all transmit antennas. The resulting average path delay causes the same phase offset at all antenna elements. Since the elements have different positions in the array, the individual path lengths will be slightly different for each antenna element. This results in an individual phase offset for each element which depends on the arrival angle of the path. An example for an uniform linear array (ULA) is shown in Figure 3.4.

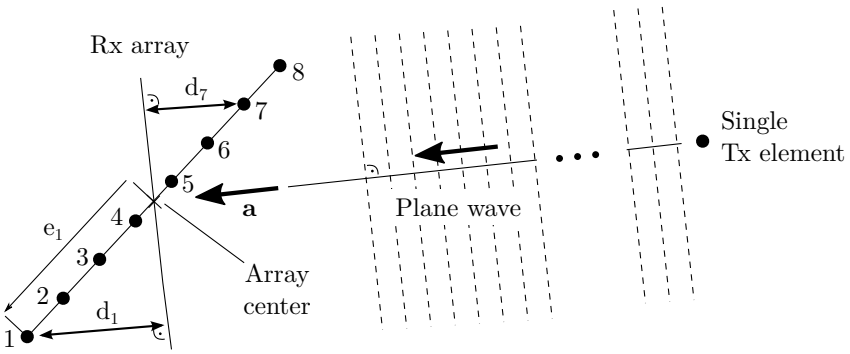

Figure 3.4: Illustration of the arrival angle estimation using an ULA

Each antenna element has an additional initial phase due to different lengths of the feeder cables. It is assumed here that this initial phase offset is the same for all angles. Hence, it is only necessary to determine it once for each element and calibrate it out of the measured channel coefficients. For this purpose, the antenna needs to be calibrated. Assuming a planar wave and linear polarization, it is possible to estimate the departure and arrival angles of a MPC from the phase and amplitude differences between the antenna elements. In this section, a generic approach for the angle estimation is presented. The algorithm takes the polarization into account (see Section 2.5 for an introduction). In general, no assumption on the polarization state of the incoming wave can be made. Hence, the most general approach is to assume that all waves are elliptically polarized, *i.e.*, both components of the Jones vector have an unknown amplitude and phase.

For the sake of clarity, the description of the procedure is done for the arrival angles, *i.e.*, there is a *transmit* array antenna which is the origin of electromagnetic waves and a *receive* array antenna which is used for estimating the *arrival* angles. The same procedure is also used for the departure angles. In this case, the order is reversed, *i.e.*, the *transmit* array antenna is used to estimate the *departure* angles.

Estimating arrival angles The following procedure needs the receive antenna patterns $\mathbf{F}_r$ in a polar spherical polarization basis for each element $r \in \{1 \dots n_r\}$ of the receive array antenna, *i.e.*, the two polarimetric components $F_r^{[\theta]}(\theta, \phi)$ and $F_r^{[\phi]}(\theta, \phi)$ at a sufficient number of sample points for the elevation angles θ and azimuth angles ϕ (*e.g.*, at a grid of 1 degree). Those patterns are typically acquired by characterizing the array antenna in an anechoic chamber. However, tests have shown that good results can also be obtained with an approximate model of the antenna patterns as long as the array geometry is known and the element-specific initial phases can be determined. The arrival angle estimation at the receiver also does not need the transmit antenna patterns. Hence, it can also be used for single input multiple output (SIMO) measurements with only one transmit antenna.

The first step is to calculate the combined receive antenna pattern $\hat{\mathbf{F}}$ by using the conjugate time-domain channel coefficients $g^*_{r,t,l}$ as weights.

$$\hat{\mathbf{F}}_{t,l}(\theta, \phi) = \begin{pmatrix} \hat{F}_{t,l}^{[\theta]}(\theta, \phi) \\ \hat{F}_{t,l}^{[\phi]}(\theta, \phi) \end{pmatrix} = \sum_{r=1}^{n_r} g^*_{r,t,l} \cdot \mathbf{F}_r(\theta, \phi) \tag{3.16}$$

The idea here is that the product of the conjugate coefficients with the matching patterns $\mathbf{F}_r(\theta, \phi)$ sum up constructively for angles where there is a signal coming from and destructively

everywhere else. This approach is similar to beamforming using maximum ratio transmission [57]. However, here the beamforming weights are applied to the receive array.

In order to calculate the arrival angles from $\hat{\mathbf{F}}_{t,l}(\theta,\phi)$, the two polarimetric components must be combined. This needs to take the polarization of the incoming wave into account. For example, a perfectly *vertically* polarized wave would only excite the $F^{[\theta]}$ component of a receive antenna while a *horizontally* polarized wave would only excite the $F^{[\phi]}$ component. Any other polarization (*e.g.*, $\pm 45°$, circular, elliptic) would excite both components. Since the directional amplitudes and phases of the two parts of the antenna pattern can be quite different, incorrect angles might be calculated if the assumptions on the polarization do not match the polarization of the incoming wave. The polarization of the wave is described by the Jones vector $\mathbf{J}$. Since each element of the transmit antenna can have a different polarization, the Jones vectors need to be estimated at the receive array antenna for each transmit antenna element separately since otherwise the polarization effects will interfere with the angle estimation. For this reason, linearly polarized ULAs are generally a bad choice for angle estimation since they will only work well if the polarization of the incoming wave matches the polarization of the array elements. Assuming that the Jones vector is known, the power-angular spectrum (PAS) of the two components of $\hat{F}$ can be calculated as

$$\left|\hat{F}_{t,l}(\theta,\phi)\right|^2 = \left|J_{t,l}^{[\theta]}\right|^2 \cdot \left|\hat{F}_{t,l}^{[\theta]}(\theta,\phi)\right|^2 + \left|J_{t,l}^{[\phi]}\right|^2 \cdot \left|\hat{F}_{t,l}^{[\phi]}(\theta,\phi)\right|^2. \tag{3.17}$$

Depending on the geometry of the array antenna, $\left|\hat{F}_{t,l}(\theta,\phi)\right|^2$ has a maximum at the arrival angles (θ_l^a, ϕ_l^a) of the incoming wave. However, one practical problem is that array antennas do not receive the same energy from all directions. This needs to be taken into account since otherwise the directional array gain shifts the maximum in the PAS to another angle. The array gain η is calculated as

$$\eta_{t,l}(\theta,\phi) = \left|J_{t,l}^{[\theta]}\right|^2 \cdot \sum_{r=1}^{n_r} \left|F_r^{[\theta]}(\theta,\phi)\right|^2 + \left|J_{t,l}^{[\phi]}\right|^2 \cdot \sum_{r=1}^{n_r} \left|F_r^{[\phi]}(\theta,\phi)\right|^2. \tag{3.18}$$

By definition, the Jones vector is already normalized such that $\left|J^{[\theta]}\right|^2 + \left|J^{[\phi]}\right|^2 = 1$. Hence, η contains the sum-power of all antenna patterns at the correct polarization. Now, it is possible to calculate the azimuth and elevation angle of the strongest spatial sub-path as

$$(\theta_l^a, \phi_l^a) = \arg\max_{\theta,\phi} \sum_{t=1}^{n_t} \frac{\left|\hat{F}_{t,l}(\theta,\phi)\right|^2}{\eta_{t,l}(\theta,\phi)}. \tag{3.19}$$

Assuming that the angles of the incoming wave are known, it is possible to estimate the Jones vector for each transmit antenna element $t \in \{1 \dots n_t\}$ by reading the receive antenna patterns at the angles (θ_l^a, ϕ_l^a), assembling them in a $n_r \times 2$ matrix, calculating its pseudoinverse, and multiplying it with the coefficient vector $\mathbf{g}$.

$$\tilde{\mathbf{J}}_{t,l} = \begin{pmatrix} \mathbf{F}_1(\theta_l^a, \phi_l^a)^T \\ \mathbf{F}_2(\theta_l^a, \phi_l^a)^T \\ \vdots \\ \mathbf{F}_r(\theta_l^a, \phi_l^a)^T \end{pmatrix}^{-1} \cdot \mathbf{g}_{t,l} \tag{3.20}$$

$$P_{t,l}^a = \left|\tilde{J}_{t,l}^{[\theta]}\right|^2 + \left|\tilde{J}_{t,l}^{[\phi]}\right|^2 \tag{3.21}$$

$$\mathbf{J}^a_{t,l} = \frac{\tilde{\mathbf{J}}_{t,l}}{\sqrt{P^a_{t,l}}} \tag{3.22}$$

The power values $P^a_{t,l}$ and the Jones vectors $\mathbf{J}^a_{t,l}$ are no longer influenced by the receive antenna patterns. In other words, the inverse operation in (3.20) de-embeds the receive antenna. However, the influence of the transmit antenna patterns is still included. For example, the Jones vectors $\mathbf{J}^a_{t,l}$ include both the polarization of the transmit antenna element t and the polarization changes that occur during propagation.

Another issue is that the Jones vectors are needed to calculate the arrival angles and the arrival angles are needed to calculate the Jones vectors. Fortunately, in order to calculate the angles using (3.17) and (3.18), only a rough estimate of the Jones vectors is required. In order to keep the computational burden acceptable, it is sufficient to calculate the angles (3.19) for a certain number of *test* Jones vectors. Then, the correct Jones vectors can be obtained using (3.20)-(3.22). This has to be done for each transmit antenna element separately since the elements might have different polarizations. As a consequence, different arrival angles might be estimated for each transmit element. However, despite differences in the estimated angles, the estimation of the polarization is reasonably robust. Hence, the obtained *initial* Jones vectors can be used to solve (3.17) and (3.18). Then, the signals from all transmit antennas can be combined using (3.19) and the final Jones vectors are calculated using (3.20)-(3.22). The proposed *test* Jones vectors are

$$\mathbf{J}^{[1]} = \begin{pmatrix} 1 \\ 0 \end{pmatrix}; \quad \mathbf{J}^{[2]} = \begin{pmatrix} 0.8 \\ 0.6 \end{pmatrix}; \quad \mathbf{J}^{[3]} = \begin{pmatrix} 0.6 \\ 0.8 \end{pmatrix}; \quad \mathbf{J}^{[4]} = \begin{pmatrix} 0 \\ 1 \end{pmatrix}.$$

The first vector uses only the $\hat{F}^{[\theta]}$ part of the pattern. The second vector combines 64% of the $\hat{F}^{[\theta]}$ and 36% of the $\hat{F}^{[\phi]}$ pattern. Likewise, the third vector uses 36% of $\hat{F}^{[\theta]}$ and 64% of $\hat{F}^{[\phi]}$. The last vector uses only the $\hat{F}^{[\phi]}$ pattern. For each of the four *test* vectors, the angles and the *correct* Jones vectors are calculated using (3.16)-(3.22). Then, for each of the four vectors, it is tested how well the results match with the original channel coefficients by calculating the MSE by

$$\hat{\mathbf{g}}_{t,l} = \sqrt{P^a_{t,l}} \cdot \begin{pmatrix} \mathbf{F}_1(\theta^a_l, \phi^a_l)^T \\ \mathbf{F}_2(\theta^a_l, \phi^a_l)^T \\ \vdots \\ \mathbf{F}_r(\theta^a_l, \phi^a_l)^T \end{pmatrix} \cdot \mathbf{J}^a_{t,l}, \tag{3.23}$$

$$\mathrm{MSE}_{t,l} = \frac{\sum_{r=1}^{n_r} |g_{r,t,l} - \hat{g}_{r,t,l}|^2}{\sum_{r=1}^{n_r} |g_{r,t,l}|^2}, \tag{3.24}$$

where $\hat{\mathbf{g}}$ is the vector of reconstructed channel coefficients using the estimated path power from (3.21), the antenna response $\mathbf{F}$ at the estimated arrival angles, and the Jones vector $\mathbf{J}$ which is always calculated using (3.22).

At this point, the coefficient matrix $\mathbf{G}_l$ can be described by

$$g_{r,t,l} = \sqrt{P^a_{t,l}} \cdot \mathbf{F}_r(\theta^a_l, \phi^a_l)^T \cdot \mathbf{J}^a_{t,l} + \tilde{g}_{r,t,l}, \tag{3.25}$$

where $P^a_{t,l}$ is the power transmitted by the tth element of the transmit array antenna, $\mathbf{F}_r$ are the radiation patterns of the receive array antenna elements, (θ^a_l, ϕ^a_l) are the arrival angles, and $\mathbf{J}^a_{t,l}$

are the Jones vectors for the t waves arriving at the receiver. The receive antenna has been de-embedded, yet the influence of the transmit antenna is still included in the powers $P^a_{t,l}$ and the Jones vectors $\mathbf{J}^a_{t,l}$. In addition, there is a remainder $\tilde{g}_{r,t,l}$ that cannot be resolved by the above algorithm. This remainder might contain additional spatial sub-paths, *i.e.*, specular paths that could not be detected in the delay domain but that might be identifiable in the spatial domain.

Detecting multiple paths in the spatial domain The coefficients $g^*_{r,t,l}$ in (3.16) might be composed of several spatial sub-paths. This is often the case when the measurement bandwidth is not enough to accurately resolve a specular path in the delay domain. Hence, there are often several local maxima in (3.19). To find additional sub-paths, the above procedure is first executed to find the strongest sub-path. Then, this already detected sub-path (3.23) is removed from the channel coefficients by

$$\tilde{g}_{r,t,l,M_l+1} = g_{r,t,l} - \sum_{m=1}^{M_l} \hat{g}_{r,t,l,m}. \tag{3.26}$$

Here, m is the sub-path index and M_l is the number of already detected sub-paths ($m = M_l = 1$ for the first sub-path). Then, the next sub-path ($M_l + 1$) is detected by using $\tilde{g}_{r,t,l,M_l+1}$ instead if $g_{r,t,l}$ in (3.16). After this, the overall MSE is updated to

$$\mathrm{MSE}_{l,M_l+1} = \frac{\sum_{t=1}^{n_t}\sum_{r=1}^{n_r}\left|g_{r,t,l} - \sum_{m=1}^{M_l+1}\hat{g}_{r,t,l,m}\right|^2}{\sum_{t=1}^{n_t}\sum_{r=1}^{n_r}\left|g_{r,t,l}\right|^2}. \tag{3.27}$$

The detection of new paths stops when $\mathrm{MSE}_{t,l,M_l+1} \leq \mathrm{MSE}_{t,l,M_l}$, *i.e.*, when including the newly detected sub-path leads to a worse or equal MSE than not including it. In this case the newly detected sub-path ($M_l + 1$) gets discarded and M_l sub-paths are used for further processing. The number of detected sub-paths differs for each path. For example, there might be only one sub-path for the LOS path and more than 10 sub-paths for a NLOS path. At the output of the processing, there are $\sum_{l=1}^{L} M_l$ values for the arrival angles $(\theta^a_{l,m}, \phi^a_{l,m})$, and $n_t \cdot \sum_{l=1}^{L} M_l$ values for both the powers $P^a_{t,l,m}$ and the Jones vectors $\mathbf{J}^a_{t,l,m}$. Now, the coefficients from (3.25) are updated to

$$g_{r,t,l} = \sum_{m=1}^{M^a_l}\left\{\sqrt{P^a_{t,l,m}} \cdot \mathbf{F}_r(\theta^a_{l,m}, \phi^a_{l,m})^T \cdot \mathbf{J}^a_{t,l,m}\right\} + \tilde{g}_{r,t,l}, \tag{3.28}$$

where the remainder $\tilde{g}_{r,t,l}$ is treated as noise.

Estimating departure angles As mentioned in the beginning of this section, the departure angles are estimated in an identical fashion. However, now the transmit antenna gets de-embedded and the influence of the receive antenna remains. Thus, a second decomposition of the coefficient matrix can be obtained as

$$g_{r,t,l} = \sum_{m=1}^{M^d_l}\left\{\sqrt{P^d_{r,l,m}} \cdot \left(\mathbf{J}^d_{r,l,m}\right)^T \cdot \mathbf{F}_t(\theta^d_{l,m}, \phi^d_{l,m})\right\} + \tilde{g}_{r,t,l}. \tag{3.29}$$

In this equation, $P^d_{r,l,m}$ is the power received by the rth element of the receive array antenna, $\mathbf{F}_t$ are the radiation patterns of the transmit array antenna elements, and $(\theta^d_{l,m}, \phi^d_{l,m})$ are the departure angles. The transmit antenna has been de-embedded. Thus, the Jones vectors $\mathbf{J}^d_{r,l,m}$ contain the changes of the polarization during scattering and the weighting by the r receive antenna elements. Since the arrival and departure angles are calculated independently, a different number of sub-paths is generally detected in both steps.

Estimating the polarization coupling matrix In the last step, the polarization coupling matrix $\mathbf{M}$ is estimated. This can be done by either de-embedding the transmit antenna from (3.28) or by de-embedding the receive antenna from (3.29). Usually, in UMa and UMi deployments, the angular spread is smaller at the BS side and there is more scattering close to the MT. Therefore, less sub-paths are identified at the BS. In this case, de-embedding the transmit antenna from (3.28) will provide better results. The procedure is as follows:

First, the departure angles at the transmitter (the BS) need to be estimated. In this case, sub-paths can only be considered at the receiver. Additional sub-paths that were detected at the BS are discarded and only the departure angles of the strongest (first) spatial path are used. Then, the 2×2 polarization coupling matrix $\mathbf{M}_{l,m}$ is estimated by assembling a matrix of the received Jones vectors (including transmit antenna and propagation effects) and multiplying it with the pseudoinverse of the transmit antenna patterns.

$$\mathbf{M}^{[1]}_{l,m} = \begin{pmatrix} m_{\theta\theta} & m_{\theta\phi} \\ m_{\phi\theta} & m_{\phi\phi} \end{pmatrix} = \underbrace{\begin{pmatrix} \mathbf{J}^a_{1,l,m} & \mathbf{J}^a_{2,l,m} & \dots & \mathbf{J}^a_{t,l,m} \end{pmatrix}}_{\text{Received Jones vectors}} \cdot \underbrace{\begin{pmatrix} \mathbf{F}_1(\theta^d_l, \phi^d_l)^T \\ \mathbf{F}_2(\theta^d_l, \phi^d_l)^T \\ \vdots \\ \mathbf{F}_t(\theta^d_l, \phi^d_l)^T \end{pmatrix}^{-1}}_{\text{Transmit Antenna Patterns}} \tag{3.30}$$

The transmit antenna patterns include the antenna gain while the received Jones vectors are normalized to $\left|J^{[\theta]}\right|^2 + \left|J^{[\phi]}\right|^2 = 1$. As a consequence, the received Jones vectors get weighted with the antenna directivity, *i.e.*, transmit elements having less gain at the given departure angles influence the result less. Therefore, the Jones matrix needs to be normalized such that its Frobenius norm is equal to one.

$$\mathbf{M}_{l,m} = \frac{\mathbf{M}^{[1]}_{l,m}}{\left|\left|\mathbf{M}^{[1]}_{l,m}\right|\right|_F} \quad \text{with} \quad \left|\left|\mathbf{M}^{[1]}_{l,m}\right|\right|_F = \sqrt{\left|m^{[1]}_{\theta\theta}\right|^2 + \left|m^{[1]}_{\theta\phi}\right|^2 + \left|m^{[1]}_{\phi\theta}\right|^2 + \left|m^{[1]}_{\phi\phi}\right|^2} \tag{3.31}$$

The final decomposition of the coefficient matrix is described by

$$g_{r,t,l} = \sum_{m=1}^{M} \underbrace{\left\{ \sqrt{P_{l,m}} \cdot \mathbf{F}_r(\theta^a_{l,m}, \phi^a_{l,m})^T \cdot \mathbf{M}_{l,m} \cdot \mathbf{F}_t(\theta^d_l, \phi^d_l) \right\}}_{=\hat{g}_{r,t,l,m}} + \tilde{g}_{r,t,l}. \tag{3.32}$$

The path-power $P_{l,m}$ after de-embedding the antenna patterns are updated such that the MSE given by (3.28) is minimized.

At this point, the path parameters are determined. There are L delay-resolvable paths that could be identified by the algorithm in Section 3.1.2. For each of these paths, M sub-paths can be identified in the spatial domain. The derived parameters are the path delays τ_l, the path powers $P_{l,m}$, the departure angles (θ^d_l, ϕ^d_l), the arrival angles $(\theta^a_{l,m}, \phi^a_{l,m})$, and the polarization coupling matrix $\mathbf{M}_{l,m}$. In the next Section, the model parameters are derived from these values.

3.2 Estimation of Large-Scale Parameters

This section describes how the model parameters are calculated. Usually, measurements are done at a limited number of positions for the BS and the MT. For example, the MT might be integrated in a measurement car that moves along some streets in an urban area. Then, the complete MIMO channel, *i.e.*, the broadband channel response of all Tx-Rx antenna pairs, is sampled every few centimeters. One such characterization of the channel is called a *snapshot*. The first processing step is to derive the *path parameters*, *i.e.*, the path powers, delays and angles of the MPCs from the channel snapshot. This was described in the previous section. The next step is to calculate the LSPs from the path parameters. For example, the path powers and the path delays can be used to calculate the delay spread. Likewise, the path powers and the angles are used to calculate the angular spread. The complete list of parameters consists of

- the effective path gain (PG),
- the Ricean Ricean K-factor (KF),
- the root mean square (RMS) delay spread (DS),
- the RMS azimuth spread of arrival (ASA),
- the RMS elevation angle spread of arrival (ESA),
- the RMS azimuth spread of departure (ASD),
- the RMS elevation angle spread of departure (ESD), and
- the cross polarization ratio (XPR).

Small-scale fading, *i.e.*, fast fluctuations of the received power of a MPC, can lead to strong fluctuations of these parameters even in subsequent snapshots. For example, different DS values might be calculated from two successive snapshots, even if they were measured only centimeters away from each other. To reduce this effect, Jalden *et al.* [116] suggested to average the results within a radius of 30 λ. This would correspond to a distance of roughly 3.3 m at a carrier frequency of 2.6 GHz. This distance is called the *averaging interval*. For example, in a typical measurement campaign, the measurement car might move along 10 separate measurement tracks, each having a length of about 300 m. With four snapshots per wavelength, a total amount of roughly 100,000 snapshots is captured. Then, the total track length of 3 km is split into roughly 900 *averaging intervals* of 3.3 m length, each containing 115 snapshots. The above parameters are calculated for each snapshot and are averaged within the interval. Thus, at the output of this processing step, there are 900 values for the DS, the KF, the SF, and so on.

In the last step, the distributions of the LSPs are obtained. Since the direct component has a very dominant impact on the overall propagation conditions, the measurement tracks are usually split into LOS and NLOS parts. Then, the individual values are fitted to a distribution that matches well with the observation. In the above example, 300 *averaging intervals* might be in LOS and 500 intervals in NLOS conditions. It is assumed that the DS is typically log-normal distributed. Thus, from the 300 LOS samples of the DS, a median value DS_μ and a standard deviation DS_σ are calculated that parameterize the log-normal distribution. Those values are summarized in tables and can be used as input to the channel model in Section 2.

In the next section, each of the above LSPs is defined and it is described how they are calculated from the data.

3.2.1 Path Gain and Shadow Fading

The effective PG is defined as the instantaneous propagation loss, *i.e.*, the received power without antenna gain normalized to 0 dB. The transmit power is calibrated out of the measured channel coefficients. If the antenna patterns are de-embedded using the algorithm in Section 3.1.3, the path powers can be used to calculate the PG by summing up the power of all MPCs.

$$P = \sum_{l=1}^{L} \sum_{m=1}^{M} P_{l,m} \tag{3.33}$$

However, de-embedding the antenna patterns is not always possible and there might be unresolvable paths in the spatial domain that still contribute to the received power. In this case, the PG is estimated from the data by summing up the power of all L paths and averaging over the n_t transmit and n_r receive antennas.

$$P = \frac{1}{n_r \cdot n_t} \cdot \sum_{r=1}^{n_r} \sum_{t=1}^{n_t} \sum_{l=1}^{L} |g_{r,t,l}|^2 \tag{3.34}$$

$$\approx \frac{1}{n_r \cdot n_t \cdot N} \cdot \sum_{r=1}^{n_r} \sum_{t=1}^{n_t} \sum_{n=1}^{N} |h_{r,t,n}|^2 \tag{3.35}$$

The variable g denotes the complex-valued amplitude of a single MPC in time domain, h is the channel coefficient in frequency domain, and N is the number of OFDM carriers. It is essential that the power values are corrected by the antenna gain since otherwise the model parameters will be incorrect.

In order to remove the effects of fast fading from the statistics, neighboring values for P within a distance of 3.3 m ($\approx 30\lambda$) are averaged. These values are then used to parameterize a Hata model [64] with parameters A and B

$$\mathrm{PG}_{[dB]} = A \cdot \log_{10}(d_{[km]}) + B + X, \tag{3.36}$$

where $d_{[km]}$ is the distance between BS and MT in kilometers. The SF, *i.e.*, the fluctuation of the instantaneous effective PG around the distance-dependent value $\mathrm{PG}_{[dB]}$, is usually modeled by a random, normal-distributed variable X with zero-mean and standard deviation SF_σ. An additional parameter SF_λ describes how the SF is correlated with the distance. This value is calculated as described in Section 3.2.6.

3.2.2 Ricean K-Factor

The KF is defined as the ratio of the power of the direct path divided by the sum-power of all other paths. Some literature sources (*e.g.*, [117, 118]) define the KF with respect to the strongest path in the CIR which can originate from a dominant scattering cluster. In the channel model, however, the KF is defined as the power ratio between LOS and NLOS paths (see Section 2.2 on Page 21). Hence, to estimate the KF, the LOS path has to be detected.

The empirical detection of the LOS path works in two steps: First, the power delay profiles (PDPs) of all MIMO sublinks are summed up. Then, a peak at the beginning of this sum-PDP, *i.e.*, the first path that exceeds 1% of the total power, is detected. This ensures that small

paths originating from noise at the beginning of the CIR are excluded. In the second step, the LOS delays of successive snapshots within a 3.3 m radius are compared and false detections are removed. From the remaining snapshots, the KF is calculated as

$$K = \frac{P^{[\mathrm{LOS}]}}{P - P^{[\mathrm{LOS}]}}, \quad \text{where} \quad P^{[\mathrm{LOS}]} \approx \sum_{r=1}^{n_r} \sum_{t=1}^{n_t} P_{r,t}^{[\mathrm{LOS}]}. \tag{3.37}$$

The KF is typically given in dB and it is mapped to three parameters: KF_μ and KF_σ (both in [dB]) to parameterize a normal distribution, and KF_λ (given in [m]) to describe how the KF is correlated with the distance.

3.2.3 Delay Spread

The DS measures how the multipath power is spread out over time. For calculating the DS, one needs the path power and the path delay. The delay τ_l is obtained either directly from the channel model (see Section 2.2 on Page 21) or from the MPC extraction in case of measured data (see Section 3.1.2 on Page 49). An estimate of the path power P_l is obtained by de-embedding the antenna patterns or by averaging the power of all MIMO sublinks. The DS is calculated as [118]

$$\sigma_\tau = \sqrt{\frac{1}{P} \cdot \sum_{l=1}^{L} P_l \cdot (\tau_l)^2 - \left(\frac{1}{P} \cdot \sum_{l=1}^{L} P_l \cdot \tau_l\right)^2}, \tag{3.38}$$

$$P_l = \sum_{m=1}^{M} P_{l,m} \approx \frac{1}{n_r \cdot n_t} \sum_{r=1}^{n_r} \sum_{t=1}^{n_t} |g_{r,t,l}|^2, \tag{3.39}$$

where the index l indicates the path number and m is the sub-path index. If multiple sub-paths were detected in the spatial domain, their power is summed up.

Since the number of the detected MPCs depends on the SNR in the channel, it is common to remove weak paths having power values below a threshold relative to the strongest path. In order to make the results comparable, the same threshold is used for low and high SNR channels and it was ensured that there is always enough dynamic range in the CIR to support the chosen threshold. As for the PG, values within a distance of 3.3 m are averaged to reduce the influence of the small-scale fading. Usually, the DS follows a log-normal distribution. Thus, statistics on the DS are presented in the log-domain using units of $\log_{10}(s)$.

3.2.4 Angular Spread

The AS measures how the multipath power is spread out in the spatial domain. This requires that the individual angles of the MPCs can be extracted from the measurement data, *e.g.*, by using the method from Section 3.1.3. Then, each path has four angles, the azimuth angle of departure (AoD), the elevation angle of departure (EoD), the azimuth angle of arrival (AoA), and the elevation angle of arrival (EoA). However, a clear definition of the angular spread does not exist. Durgin and Rappaport [119] define the AS as a measure ranging from 0 to 1, where a value of 0 means that all the multipath power is concentrated on one direction and a value of 1 corresponds to the case of uniform illumination in all directions. Yu *et al.* [120], on the

other side, define the angular spread similar to the DS where the angles get weighted by the path power. However, this measure of the AS is ambiguous since the angles are distributed on a sphere and the resulting value depends on the reference angle, *i.e.*, the definition of where 0° is. A linear shift of the angles $\phi_{l,m} + \Delta_\phi$ then leads to the angular spread being a function of Δ_ϕ. In the 3GPP SCM [46], this was solved by an exhaustive search over $\Delta_\phi \in [-\pi, \pi[$ to find the minimum angular spread

$$\sigma_\phi = \min_{\Delta_\phi} \sigma_\phi(\Delta_\phi). \tag{3.40}$$

A similar approach is used here. The angles are normalized such that the combined power-angular spectrum (PAS) of all paths and sub-paths points to $\theta = \phi = 0$. The individual angles are calculated from the measurement data using the method from Section 3.1.3. In order to calculate azimuth spread of arrival, the angles need to be calculated at the receiver side and the receive array antenna gets de-embedded. However, the influence of the transmit array antenna is still included and might influence the results. The normalization of the AoAs ϕ^a is done by

$$\tilde{\phi}^a_{l,m} = \left(\phi^a_{l,m} - \Delta_\phi + \pi \mod 2\pi\right) - \pi, \tag{3.41}$$

$$\Delta_\phi = \arg\left(\sum_{l=1}^{L}\sum_{m=1}^{M} \exp\left(j\phi^a_{l,m}\right) \cdot \sum_{t=1}^{n_t} P_{t,l,m}\right), \tag{3.42}$$

where $P_{t,l,m}$ are the power values obtained from the $t = 1 \ldots n_t$ transmit antenna elements. l and m are the path and sub-path index, respectively. Then, the ASA is calculated by

$$\sigma_{\mathrm{ASA}} = \sqrt{\frac{1}{P} \cdot \sum_{l=1}^{L}\sum_{m=1}^{M} \left(\tilde{\phi}^a_{l,m}\right)^2 \cdot \sum_{t=1}^{n_t} P_{t,l,m} - \left(\frac{1}{P} \cdot \sum_{l=1}^{L}\sum_{m=1}^{M} \tilde{\phi}^a_{l,m} \cdot \sum_{t=1}^{n_t} P_{t,l,m}\right)^2}, \tag{3.43}$$

with P being the total received power

$$P = \sum_{t=1}^{n_t}\sum_{l=1}^{L}\sum_{m=1}^{M} P_{t,l,m}. \tag{3.44}$$

The same is done for the EoAs $\theta^a_{l,m}$, resulting in the ESA σ_{ESA} and the AoDs $\theta^d_{l,m}$, resulting in the ASD σ_{ASD}. The AS values for the entire measurement scenario get mapped to a log-normal distribution. Thus, the model parameters, *e.g.*, ASA_μ and ASA_σ, are given in units of $\log_{10}(°)$.

3.2.5 Cross-Polarization Ratio

The XPR measures how the polarization of a transmitted electromagnetic wave changes on the way to the receiver. The mechanisms that influence the polarization were introduced in Section 2.5 of this thesis. In this model, the XPR is defined for the NLOS paths only. However, the measurement data includes the LOS component which has a strong influence on the average XPR seen by the MT. The LOS-XPR is only affected by the positions and antenna orientations of the BS and the MT, and it can thus not be considered a property of the propagation channel since it can be calculated deterministically. Hence, in order to extract the NLOS-XPR from the measurement data, one has to detect the LOS path and exclude it from the evaluation. This is done in the same way as for the KF estimation (see Section 3.2.2 on Page 60).

In order to calculate the XPR, the 2×2 polarization coupling matrix

$$\mathbf{M}_{l,m} = \begin{pmatrix} m_{\theta\theta} & m_{\theta\phi} \\ m_{\phi\theta} & m_{\phi\phi} \end{pmatrix} \tag{3.45}$$

needs to be estimated for each path and sub-path. This is done using the method in Section 3.1.3. $\mathbf{M}^a_{l,m}$ does not include any antenna effects. However, only the departure angles of the strongest (first) sub-path are used because sub-paths are obtained from the receiver side only. The XPR for the linear polarization is defined as the power of the main diagonal elements divided by the off-diagonal elements of the matrix. Thus, the XPR can be calculated as

$$\mathrm{XPR}_{l,m} = \frac{1}{4} \cdot \left(\frac{|m_{\theta\theta}|^2}{|m_{\phi\theta}|^2} + \frac{|m_{\theta\theta}|^2}{|m_{\theta\phi}|^2} + \frac{|m_{\phi\phi}|^2}{|m_{\phi\theta}|^2} + \frac{|m_{\phi\phi}|^2}{|m_{\theta\phi}|^2} \right) \tag{3.46}$$

The XPR is usually given in dB and it is mapped to two parameters: XPR_μ and XPR_σ (both in [dB]) to parameterize a normal distribution in the channel model. The values for the LOS path are excluded for this mapping. In the channel model, no correlation with the distance is assumed.

3.2.6 Large-Scale Parameter Correlations

There are two measures of the correlation that are needed in order to parameterize the channel model: the *inter-parameter correlation* and the *decorrelation distance*. The *inter-parameter correlation* describes how the LSPs depend on each other. For example, when the KF is high, a significant part of the multipath power is concentrated on the LOS path. In this case, the DS will be low. As a result, a negative correlation between the DS and KF can be observed.

In the beginning of this section, the concept of the *averaging interval* was introduced. For example, a typical measurement track with a length of 300 m gets divided into 91 such intervals. The distance between two intervals is roughly 3.3 m. For each interval, one value for all LSPs is obtained from the data. The inter-parameter correlation between two LSPs is then calculated using the Pearson product-moment correlation coefficient [121]

$$\begin{aligned} \rho\{\mathbf{a},\mathbf{b}\} &= \frac{\mathbb{E}\{(\mathbf{a}-\mu_\mathbf{a})\cdot(\mathbf{b}-\mu_\mathbf{b})\}}{\sigma_\mathbf{a}\cdot\sigma_\mathbf{b}} \\ &\approx \frac{\frac{1}{K}\sum_{k=1}^{K} a_k \cdot b_k - \frac{1}{K^2}\sum_{k=1}^{K} a_k \cdot \sum_{k=1}^{K} b_k}{\sqrt{\left(\sum_{k=1}^{K}\frac{|a_k|^2}{K} - \left|\sum_{k=1}^{K}\frac{a_k}{K}\right|^2\right)\cdot\left(\sum_{k=1}^{K}\frac{|b_k|^2}{K} - \left|\sum_{k=1}^{K}\frac{b_k}{K}\right|^2\right)}}. \end{aligned} \tag{3.47}$$

In this equation, there are two vectors $\mathbf{a}$ and $\mathbf{b}$, each having K elements. In the numerator, the values are centered by subtracting the mean μ of each vector. The cross-products of the centered values are then summed up. The denominator normalizes the STD of the values in the vectors to unity. Thus, (3.47) describes the centered and standardized sum of the cross-product of two variables. The resulting values $\rho\{\mathbf{a},\mathbf{b}\}$ can only have values between -1 and 1. To calculate the correlation between the DS and the KF ($\rho_{\mathrm{DS,KF}}$) in the above example, $\mathbf{a}$

would contain the 91 values of the DS and $\mathbf{b}$ the 91 values of the KF. In the channel model, all inter-parameter correlation values are defined in the logarithmic domain. Therefore, when calculating the correlation from measured data, the LSPs have to be given in logarithmic units as well, *i.e.*, the KF and SF in [dB], the DS in $[\log_{10}(s)]$ and the ASs in $[\log_{10}(^\circ)]$.

The second correlation measure used in the channel model is the *decorrelation distance* d_λ. This value, which is given in units of meters, describes how a LSP is correlated with itself when the MT moves a certain distance. In order to calculate d_λ, (3.47) is used to obtain $\rho\left\{\mathbf{a}, \mathbf{a}^{(q)}\right\}$ where the superscript (q) denotes a shift of $\mathbf{a}$ by q entries. For example, if $\mathbf{a}$ contains 91 values, then $\rho\left\{\mathbf{a}, \mathbf{a}^{(1)}\right\}$ is the correlation coefficient between the first 90 elements of $\mathbf{a}$ and the last 90 elements of $\mathbf{a}$, *i.e.*, elements 2 to 91. Since the distance between two LSP samples in the above example is 3.3 m, the correlation coefficient at 3.3 m distance is calculated for $q = 1$. For $q = 2$, the correlation coefficient at 6.6 m distance is calculated. The maximum number of shifts depends on the length of the individual measurement tracks, and a value that corresponds to half the average track length is reasonable to have a sufficient number of samples to calculate the correlation coefficient.

In the channel model, the distance dependent correlation coefficient follows an exponential function

$$\rho(d) = \exp\left(-\frac{d}{d_\lambda}\right), \tag{3.48}$$

where both the distance d and the decorrelation distance d_λ are given in units of meters. Thus, d_λ is calculated by fitting this function to the values $\rho\left\{\mathbf{a}, \mathbf{a}^{(q)}\right\}$ from the measurement data.

3.3 Estimation of Performance Metrics

The main purpose of a channel model is to enable realistic performance assessments of wireless communication systems before the standardization and product development stages. For this reason, performance indicators such as throughput, error rate, jitter, interference power, required bandwidth *etc.* are often defined. Those indicators then serve as benchmarks in order to find suitable system configurations, *e.g.*, bandwidth allocation, number of antennas, interleaving and coding schemes. However, the channel properties have a paramount influence on the resulting system performance. If the assumptions made in the channel model are not in line with the reality, unsuitable system configurations might result. Those are then often discovered only during field trials using hardware implementations of the system. If the system performance does not match the predictions, expensive redesigns may be necessary.

This section defines a set of performance metrics that help to assess if the model assumptions are correct. As for the LSPs, those metrics are extracted from both the measured data and the channel model. However, they are not linked directly to the input parameters of the channel model but are influenced by all parameters simultaneously, including the antenna configuration and user placement. For example, it is predicted that the MIMO capacity scales linear with the number of antennas used at the transmitter and the receiver [54]. However, a small angular spread at the transmitter can result in a so called *keyhole channel* [66], a channel that allows only a single independent propagation path. In this case, adding more antennas does not increase the capacity. Simplified channel models, such as the theoretical i.i.d. Gaussian (Rayleigh fading) channel, severely overestimate the performance in this case since they do not resemble the physical propagation conditions sufficiently.

3.3.1 Single-User Capacity at a Fixed SNR

A MIMO communication system uses multiple antennas at both ends of the communication link, the transmitter and the receiver. The achievable data rate of such a system is limited by the propagation channel and the antennas which exploit the spatio-temporal structure of the channel. Ideally, the MIMO capacity scales linearly with $\min(n_t, n_r)$ and logarithmic with the signal to noise ratio (SNR) which can lead to enormous capacity gains when the number of antennas is large. Unfortunately, this is often not the case because there are not enough independent propagation paths to support such a capacity growth. One way to test the correctness of the channel model is to compare the MIMO capacity of the measured channels with predictions made by the model. From the measurements, the coefficient matrices $\mathbf{G}_l$ and path delays τ_l for the $l = 1 \ldots L$ MPCs are used for estimating the capacity. They are extracted from the raw data by using the algorithm from Section 3.1.2. This removes a significant portion of the measurement noise from the raw data which otherwise might lead to inaccurate capacity results. The antenna influence, however, remains in the data. The channel model in Section 2 generates the coefficient matrices $\mathbf{G}_l$ and path delays τ_l directly. However, the model parameters, antenna patterns, BS and MT positions, LOS and NLOS conditions must match with the measurements. The capacity C [54], measured in bps/Hz, is defined as

$$C^{[\text{link}]} = \frac{1}{N} \sum_{n=1}^{N} \log_2 \det \left(\mathbf{I}_{n_r} + \frac{\sigma}{n_t \cdot P} \cdot \mathbf{H}_n \mathbf{H}_n^H \right), \tag{3.49}$$

where $\mathbf{I}_{n_r}$ is the identity matrix of size $n_r \times n_r$. The channel matrix $\mathbf{H}_n$ of size $n_r \times n_t$ describes the broadband fading channel in the baseband at N sample frequencies f_n spread over the bandwidth B. It is calculated from the coefficient matrices of the $l = 1 \ldots L$ multipath components by

$$\mathbf{H}_n = \sum_{l=1}^{L} \mathbf{G}_l \cdot e^{-2\pi j \cdot f_n \cdot \tau_l}, \tag{3.50}$$

where τ_l is the delay of the lth MPC. P is the effective path gain which is calculated by

$$P = \frac{1}{n_r \cdot n_t \cdot N} \cdot \sum_{r=1}^{n_r} \sum_{t=1}^{n_t} \sum_{n=1}^{N} |h_{r,t,n}|^2 . \tag{3.51}$$

Any communication system has a limited transmit power. The combined transmit power at the BS and the PG of the channel leads to a SNR σ that can be achieved at the MT. In (3.49) it is assumed that there is a sum-power budget that gets divided by the number of transmit antenna elements.

There are two ways to look at the capacity. Either the SNR is set according to the received power at the MT or the SNR is kept at a fixed value. In the first case, the power has a huge influence on the results and it is hard to compare different spatial channel models with each other. With a fixed SNR, only the spatial properties (number of antennas, number of MPCs, delay spread, angular spread, *etc.*) have an influence. Thus, the performance of the small-scale-fading part of the model, which is responsible of the correct prediction of the MIMO properties, can be assessed. A lower bound of the capacity is given by the keyhole channel [66] which allows only one spatial degree of freedom. The other extreme is reached when there are $1/\min(n_t, n_r)$ parallel channels. Assuming that the channel is normalized such that each

propagation coefficient is typically equal to one, the bounds of the capacity can be computed by [44]

$$\underbrace{\log_2(1+\sigma\cdot n_r)}_{\text{Keyhole Channel}} \leq C \leq \underbrace{\min(n_t,n_r)\cdot\log_2\left(1+\frac{\sigma}{n_t}\cdot\max(n_t,n_r)\right)}_{\text{Parallel Channels}}. \tag{3.52}$$

Any capacity prediction made by channel models or results obtained from the measurement data have to be in between these bounds. In Chapters 4 and 5, the capacity results are presented for two different measurement campaigns and it is shown that the predictions made by the new channel model are very close to the capacity of the measured channels. In the following sections, the performance measures are extended to include multiple MTs and multiple BSs as well. Thus, it is possible to assess the scalability of the model.

3.3.2 Geometry Factor

When several BS use the same time and frequency resources, they create interference. A MT will not only receive the signal from its serving BS but also signals from other interfering BSs as well. The correct prediction of the signal strength is therefore an important criterion for channel models. The geometry factor (GF) is a lower bound for the actual signal to interference and noise ratio (SINR). It is defined as the power ratio of the serving BS to all interfering BSs plus noise

$$\mathrm{GF} = \frac{\mathbb{E}_{\mathrm{f/t}}\left[P_i\right]}{P^{[\mathrm{noise}]} + \sum\limits_{\forall k, k\neq i}\mathbb{E}_{\mathrm{f/t}}\left[P_k\right]} = \frac{P^{[\mathrm{signal}]}}{P^{[\mathrm{noise}]} + P^{[\mathrm{interference}]}} \leq \mathbb{E}\left[\mathrm{SINR}_{\mathrm{inst.}}\right], \tag{3.53}$$

where $\mathbb{E}_{\mathrm{f/t}}\left[P\right]$ denotes the expectation value of the effective path gain over frequency and over successive snapshots. Thus, the small-scale-fading gets removed by averaging the PG values within a small area within a 30 λ radius. The index i denotes the serving BS and the index k the interfering ones. Due to handover between BSs, the MT is always assigned to the BS with the highest received power. The instantaneous PG is calculated from the coefficient matrices $\mathbf{G}_l$ as

$$P = \frac{1}{n_r\cdot n_t}\cdot\sum_{r=1}^{n_r}\sum_{t=1}^{n_t}\sum_{l=1}^{L}\left|g_{r,t,l}\right|^2, \tag{3.54}$$

where r, t and l are the indices of the receive antenna element, the transmit antenna element, and the MPC, respectively. It is important that the antenna gains are not calibrated out of the data since they have a tremendous influence on the GF. The noise power $P^{[\mathrm{noise}]}$ is limited either by thermal noise or by the sensitivity of the measurement system. These limitations of the measurement system need to be included in the channel model as well in order to make the results comparable. Evaluations of the GF are done in a multi-cell measurement setup in Chapters 5. The results show that the model supports all necessary features to accurately predict the power differences in the channels of different BSs.

3.3.3 Multi-User Singular Value Spread

The signal model of the multi-user MIMO downlink can be considered a combination of several individual single-link MIMO channels, each having n_t transmit antennas per BS and n_r receive antennas per MT. The compound channel matrix $\mathbf{H}_n^{[\mathrm{cmp.}]}$ at subcarrier n consists of $n_r\cdot n_u$ rows

and $n_t \cdot n_i$ columns where $u \in \{1, 2, ..., n_u\}$ is the MT or user index and $i \in \{1, 2, ..., n_i\}$ is the BS or sector index. Likewise, the transmit and receive symbol vectors are also a combination of the individual single-link symbol vectors.

$$\begin{pmatrix} \mathbf{y}_{n,1} \\ \vdots \\ \mathbf{y}_{n,u} \\ \vdots \\ \mathbf{y}_{n,n_u} \end{pmatrix} = \underbrace{\begin{pmatrix} \mathbf{H}_{n,1,1} & \cdots & \mathbf{H}_{n,1,i} & \cdots & \mathbf{H}_{n,1,n_i} \\ \vdots & \ddots & \vdots & \ddots & \vdots \\ \mathbf{H}_{n,u,1} & \cdots & \mathbf{H}_{n,u,i} & \cdots & \mathbf{H}_{n,u,n_i} \\ \vdots & \ddots & \vdots & \ddots & \vdots \\ \mathbf{H}_{n,n_u,1} & \cdots & \mathbf{H}_{n,n_u,i} & \cdots & \mathbf{H}_{n,n_u,n_i} \end{pmatrix}}_{\mathbf{H}_n^{[\text{cmp.}]}} \cdot \begin{pmatrix} \mathbf{x}_{n,1} \\ \vdots \\ \mathbf{x}_{n,u} \\ \vdots \\ \mathbf{x}_{n,n_u} \end{pmatrix} + \mathbf{v} \tag{3.55}$$

In a multi-user system, each MT has only knowledge of its own channels but not the channels of other users. Hence, unlike in single-link MIMO, inverting $\mathbf{H}^{[\text{cmp.}]}$ to obtain the users signals is not possible. Depending on the granularity of the channel knowledge at the transmitter, different precoding schemes such as beamforming or joint transmission can be applied to separate the users' signals. However, this relies on the propagations conditions where, ideally, channel vectors become pairwise orthogonal.

One way of measuring the orthogonality of users' signals can be done by calculating the singular value (SV) spread, also known as condition number, of the joint propagation matrix [122]. For calculating meaningful values for this metric, a normalization of the compound channel matrix is required. This is done by first calculating the average broadband power $P_{u,i}$ for each MT-BS combination over all carriers and antenna pairs using (3.35). Each user terminal has a serving BS, usually the BS providing the strongest signal, and the terminal always performs a handover to this BS. The normalization is thus done by

$$\begin{aligned} \mathbf{H}_{n,u,i}^{[\text{norm}]} &= \sqrt{\frac{1}{P_u}} \cdot \mathbf{H}_{n,u,i} \qquad (3.56) \\ &= \begin{pmatrix} \sqrt{\frac{1}{P_1}} \cdot \mathbf{H}_{n,1,1} & \cdots & \sqrt{\frac{1}{P_1}} \cdot \mathbf{H}_{n,1,i} & \cdots & \sqrt{\frac{1}{P_1}} \cdot \mathbf{H}_{n,1,n_i} \\ \vdots & \ddots & \vdots & \ddots & \vdots \\ \sqrt{\frac{1}{P_u}} \cdot \mathbf{H}_{n,u,1} & \cdots & \sqrt{\frac{1}{P_u}} \cdot \mathbf{H}_{n,u,i} & \cdots & \sqrt{\frac{1}{P_u}} \cdot \mathbf{H}_{n,u,n_i} \\ \vdots & \ddots & \vdots & \ddots & \vdots \\ \sqrt{\frac{1}{P_{n_u}}} \cdot \mathbf{H}_{n,n_u,1} & \cdots & \sqrt{\frac{1}{P_{n_u}}} \cdot \mathbf{H}_{n,n_u,i} & \cdots & \sqrt{\frac{1}{P_{n_u}}} \cdot \mathbf{H}_{n,n_u,n_i} \end{pmatrix} \\ P_u &= \max_i \left(P_{u,i}\right). \end{aligned}$$

Hence, the single-link channel matrix of the serving BS has unit average power over transmit and receive antennas and over frequency. The channel matrices to other BSs preserve their relative power-difference. The compound normalized channel matrix is then composed of those normalized single-link matrices. This normalization removes the path-gain imbalance between the users. The singular value decomposition (SVD) of this normalized compound matrix is

$$\mathbf{H}_n^{[\text{cmp.}]} = \mathbf{U}_n \cdot \mathbf{D}_n \cdot \mathbf{V}_n^H, \tag{3.57}$$

where $\mathbf{U}_n$ and $\mathbf{V}_n$ are unitary matrices. The diagonal matrix $\mathbf{D}_n = \text{diag}\left\{\omega_{n,1}, ..., \omega_{n,n_\omega}\right\}$ contains the ordered singular values of the compound channel at subcarrier n with $\omega_{n,1}$ being the largest and ω_{n,n_ω} being the smallest singular value. The SV spread is then defined as

$$\kappa_n = \frac{\omega_{n,1}}{\omega_{n,n_\omega}} \tag{3.58}$$

User selection One important aspect for the estimation of the SV spread, as well as the DPC capacity (see next section), is the selection of users. Normally, scheduling is performed to improve the overall data rate by transmitting to users when their channels have maximum gain. With non-orthogonal spatial channels, however, it is critical to select spatially compatible users [123]. Such scheduling algorithms can be quiet complex and rely on user feedback that allows the BS to perform the appropriate decisions. Nevertheless, here the goal is to evaluate the correct working of the channel model in a multiuser setup and not obtain the optimal user allocation. Therefore, a simplified scheduling method is applied.

First, the measurement track is divided into pieces of 30 λ length. Each piece corresponds to one user position. A 3 km long measurement track at a carrier frequency of 2.6 GHz would yield approximately 900 user locations. Then, the effective PG (3.34) is calculated for each user location. A first user is picked by chance. The other users, which are served simultaneously on the same time and frequency resource, are required to be in a 6 dB path gain window, *i.e.*, their effective PG can be at most 3 dB higher or lower than the PG of the first user. This ensures that the data rate is distributed fairly among the users. If the difference in received power between the users is too high, *e.g.*, if all users are picked randomly, the user with the highest PG might get the entire data rate and the others get nothing. Grouping users with similar PG also enables the evaluation of the SV spread and the DPC capacity in dependence of the SNR.

Antenna selection Another aspect is the selections of the antennas that are used for the calculations of the multiuser capacity and the SV-spread. This is relevant for the measurements because the used array antennas often have many more elements then in realistic deployments. For example, the measurements in Chapter 4 use 58 antennas at the receiver. Such a large number of antennas will probably not be seen in commercial mobile devices in the near future.

3.3.4 Dirty-Paper Coding Capacity

The DPC capacity is the upper bound of the achievable rates in a multi-user system [124]. The system model is the same as in (3.55) and it is also assumed here that MTs cannot cooperate, *i.e.*, they don't know each other's channel matrices. While the SV spread gives an indication on how well users can be separated in the spatial domain, it does not provide a measure of the overall performance. A large SV spread does not automatically imply a low capacity. The DPC capacity for the multiple-access channel (MAC) [58] is computed as

$$C^{[\mathrm{DPC}]} = \frac{1}{N} \cdot \sum_{n=1}^{N} \max_{\mathbf{Q}_{n,u}} \log_2 \det \left(\mathbf{I}_{n_t} + \sum_{u=1}^{n_u} \mathbf{H}_{n,u}^H \cdot \mathbf{Q}_{n,u} \cdot \mathbf{H}_{n,u} \right), \tag{3.59}$$

$$\mathbf{H}_{n,u} = \sqrt{\frac{1}{P_u^{[\mathrm{norm}]}}} \left(\begin{array}{ccccc} \mathbf{H}_{n,u,1} & \cdots & \mathbf{H}_{n,u,i} & \cdots & \mathbf{H}_{n,u,n_i} \end{array} \right). \tag{3.60}$$

In a joint transmission channel, *i.e.*, when a number of n_i multi-antenna BSs serve the same user simultaneously, the compound channel matrix $\mathbf{H}_{n,u}$ is the composition of the channels from multiple BS seen by the user. It has n_r rows and $n_t \cdot n_i$ columns. The challenge is to find the $n_r \times n_r$ covariance matrices $\mathbf{Q}_{n,u}$ that maximize the capacity. With $n_t \cdot n_i$ transmit antennas and unit power per antenna, the sum transmit power is constrained to

$$\sum_{u=1}^{n_u} \mathrm{tr}\left(\mathbf{Q}_{n,u}\right) = n_t \cdot n_i \tag{3.61}$$

As for the SV spread, a normalization of the channel matrix is required in order to obtain meaningful values of the capacity. In the first approach, each user gets a SNR "budget" σ from its serving BS which is divided by the number of transmit antennas of this BS. Usually, σ is set to a fixed value of 10 dB. Hence, the PG of the serving link is removed from the data. However, the PG differences between the serving link and the interfering links remain in the data. The channel matrix is normalized according to a sum-power constraint where the power $P_u^{[\text{norm}]}$ in (3.60) is set to

$$P_u^{[\text{norm}]} = \frac{\sigma}{n_t} \cdot \max_i \left(P_{u,i}\right). \tag{3.62}$$

In the second normalization, the aim is to preserve the individual power differences between the users. The normalization of the channel matrix is thus done with respect to the individual noise power $P_u^{[\text{noise}]}$ of each user. Hence, the single-link channel matrices $\mathbf{H}_{n,u}$ include the average SNR over the transmit and receive antennas and over the frequency. This also allows us to evaluate different classes of terminal equipment where the MTs might have different noise floors.

A lower bound of the capacity is obtained by assuming equal power per transmit antenna, *i.e.*, by setting $\mathbf{Q}_{n,u} = \frac{n_t \cdot n_i}{n_r \cdot n_u} \cdot \mathbf{I}$. The factor $\frac{n_t \cdot n_i}{n_r \cdot n_u}$ ensures that the constraint (3.61) is still valid.

$$C^{[\text{DPC}]} \geq C^{[\text{EQ}]} = \frac{1}{N} \cdot \sum_{n=1}^{N} \log_2 \det \left(\mathbf{I}_{n_t} + \frac{n_t \cdot n_i}{n_r \cdot n_u} \cdot \sum_{u=1}^{n_u} \mathbf{H}_{n,u}^H \cdot \mathbf{H}_{n,u} \right) \tag{3.63}$$

When the system consists of only one BS and one user, and normalization (3.62) is used, then this lower bound would be identical to the single-user capacity (3.49). The optimal multi-user capacity for a given set of users is found by calculating the covariance matrices $\mathbf{Q}_{n,u}$ that maximize the capacity. This is done by the sum power iterative water-filling algorithm [125]. The algorithm is sketched out as follows:

1. Generate effective channels $\hat{\mathbf{H}}$ for each user

$$\hat{\mathbf{H}}_{n,u}^{(k)} = \mathbf{H}_{n,u} \cdot \left(\mathbf{I}_{n_t} + \sum_{v \neq u} \mathbf{H}_{n,v}^H \cdot \mathbf{Q}_{n,v}^{(k-1)} \cdot \mathbf{H}_{n,v} \right)^{-1/2} \tag{3.64}$$

   The index k is the iteration number. In the first step, *i.e.*, for $k = 0$, the covariance matrices $\mathbf{Q}_{n,u}^{(0)}$ are initialized with zeros. Hence, the effective channels are equal to the real channels. These effective channels are then treated as parallel, noninterfering channels.

2. An update of the covariance matrices is obtained by water-filling the block-diagonal channels with diagonals equal to $\hat{\mathbf{H}}_{n,1}^{(k)} \ldots \hat{\mathbf{H}}_{n,n_u}^{(k)}$. This requires the computation of the SVD

$$\hat{\mathbf{H}}_{n,u}^{(k)} \cdot \left(\hat{\mathbf{H}}_{n,u}^{(k)} \right)^H = \mathbf{U}_{n,u} \cdot \mathbf{D}_{n,u} \cdot \mathbf{U}_{n,u}^H. \tag{3.65}$$

   The diagonal matrix $\mathbf{D}_n = \operatorname{diag}\{\omega_{n,1}, ..., \omega_{n,n_r}\}$ contains the singular values of the uth user, where n_r is the number of receive antennas per user. The block-diagonal channel has $n_\omega = n_r \cdot n_u$ singular values. They represent the effective SNR per data stream due to the normalization. Hence, water-filling can be done assuming unit power per transmit antenna.

3. The noise variance for a singular value ω_q is equal to $\frac{1}{\omega_q}$. If all channels get allocated non-zero power, then the water-level ℓ must be at least equal to the largest noise variance

$$\ell \geq \max_q \left(\frac{1}{\omega_q} \right). \tag{3.66}$$

With $n_t \cdot n_i$ transmit antennas and unit power per antenna, the water level ℓ must be chosen such that

$$n_t \cdot n_i = \sum_{q=1}^{n_\omega} \begin{cases} \ell - \frac{1}{\omega_q}, & \text{for } \ell - \frac{1}{\omega_q} > 0 \; ; \\ 0, & \text{otherwise.} \end{cases} \quad . \tag{3.67}$$

If all data streams get served, the required power might be larger than the available power. In this case, streams with low SNR get allocated zero power, *i.e.*, they are not served. Provided that the singular values of all users are sorted in descending order, the optimal water level is

$$\ell = \frac{1}{n_\omega^{[\text{served}]}} \cdot \left(n_t \cdot n_i + \sum_{q=1}^{n_\omega^{[\text{served}]}} \frac{1}{\omega_q} \right) \tag{3.68}$$

4. The covariance matrix $\mathbf{Q}_{n,v}^{(k)}$ is computed as

$$\mathbf{Q}_{n,u}^{(k)} = \begin{cases} \mathbf{U}_{n,u} \cdot \left(\ell \mathbf{I} - \mathbf{D}_{n,u}^{-1}\right)^+ \cdot \mathbf{U}_{n,u}^H, & \text{for } k \leq 5; \\ \frac{n_u - 1}{n_u} \cdot \mathbf{Q}_{n,u}^{(k-1)} + \frac{1}{n_u} \cdot \mathbf{U}_{n,u} \cdot \left(\ell \mathbf{I} - \mathbf{D}_{n,u}^{-1}\right)^+ \cdot \mathbf{U}_{n,u}^H, & \text{otherwise.} \end{cases} \tag{3.69}$$

The operation $(.)^+$ sets all negative entries to zero, *i.e.*, streams with an effective noise power above the water level get disabled. The two cases are motivated by [125] where the first case leads to a fast convergence towards the optimal solution. However, for more than two users, the algorithm does not always converge. The second case is the modification proposed by [125] which always converges to the optimum but at a much slower rate.

Capacity limits at a fixed SNR It is assumed that the BS serves n_u users, each having n_r receive antennas. When applying the normalization (3.62), the channel to each user is normalized such that the channel coefficients are usually equal to one and the trace $\text{tr}\left(\mathbf{H}^H \mathbf{H}\right) \approx n_t \cdot n_r$. If the users cannot be separated in the spatial domain, *i.e.*, if their channel matrices are fully correlated, then a lower bound can be computed. This might happen, for example, when the users are very close together. If there is no channel knowledge at the BS, the power gets divided equally over all transmit antennas. In this case, the same bound as in (3.52) applies.

$$C^{[\text{EQ}]} \geq \log_2 \left(1 + \sigma \cdot n_r \cdot n_u\right) \tag{3.70}$$

Provided that the channels are known to the BS, optimal precoding can be applied. In this case, all available transmit power gets transmitted towards the users. This intuitively makes sense since with a large amount of transmit antennas, very narrow beams can be formed and less power gets wasted. In this case, the lower bound of the capacity is

$$C^{[\text{DPC}]} \geq \log_2 \left(1 + \sigma \cdot n_t \cdot n_i \cdot n_r\right). \tag{3.71}$$

A special case arises when the single-user channels are represented by a keyhole channel while the channels to different users are mutually orthogonal, *i.e.*, each user can receive one data stream, independent of the number of receive antennas. In reality, however, the orthogonality of the user channels depends on many factors such as the scheduling approach and the propagation conditions. Hence, this case can be used discuss the performance results.

$$C_{n_u}^{[\text{EQ}]} \quad = \quad n_u \cdot \log_2 \left(1 + \sigma \cdot n_r\right) \tag{3.72}$$

$$C_{n_u}^{[\mathrm{DPC}]} = n_u \cdot \log_2\left(1 + \frac{\sigma}{n_u} \cdot n_t \cdot n_i \cdot n_r\right) \tag{3.73}$$

Finally, an upper bound is reached when the number of parallel data streams is maximized. This maximum is determined by $\min(n_t \cdot n_i; n_r \cdot n_u)$.

$$C^{[\mathrm{EQ}]} \leq \min(n_t \cdot n_i; n_r \cdot n_u) \cdot \log_2\left(1 + \frac{\sigma}{n_t} \cdot \max(n_t \cdot n_i; n_r \cdot n_u)\right) \tag{3.74}$$

$$C^{[\mathrm{DPC}]} \leq \min(n_t \cdot n_i; n_r \cdot n_u) \cdot \log_2\left(1 + \frac{\sigma}{n_r \cdot n_u} \cdot \max(n_t \cdot n_i; n_r \cdot n_u)\right). \tag{3.75}$$

With equal power allocation, the capacity does not depend on the number of transmit antennas, *i.e.*, increasing the number of antennas does not increase the achievable rate. However, if there is channel knowledge at the transmitter and an optimal precoder can be calculated, the achievable rate scales with the logarithm of the number of transmit antennas - independent of the total transmit power. Hence, increasing the number of transmit antennas while keeping the sum-power constant will increase the capacity.

3.3.5 Dirty-Paper Coding Capacity with Inter-Cell Interference

The interference-limited downlink channel of a single user can be described by

$$\mathbf{y}_{n,u} = \mathbf{H}_{n,u,i} \cdot \mathbf{x}_{n,u,i} + \underbrace{\sum_{\forall \bar{u}, \bar{u} \neq u}^{n_u} \mathbf{H}_{n,u,i} \cdot \mathbf{x}_{n,\bar{u},i}}_{\text{intra-cell interference}} + \underbrace{\sum_{\forall \bar{i}, \bar{i} \neq i}^{n_i} \mathbf{H}_{n,u,\bar{i}} \cdot \mathbf{x}_{n,u,\bar{i}}}_{\text{inter-cell interference}} + \mathbf{v}, \tag{3.76}$$

where a BS $i \in [1 \ldots n_i]$ transmits to a user $u \in [1 \ldots n_u]$. If there are multiple spatial data streams transmitted from the same BS to different users (*i.e.*, $n_u > 1$), there will be intra-cell interference since the users cannot cooperate with each other. If, in addition, there are other BSs using the same time and frequency resource, there will be inter-cell interference since the BSs can also not cooperate in this case. There are several ways of mitigating this interference in the spatial domain. Two promising ideas are *joint transmission* and *massive MIMO* (see Section 1.1).

The notation for the DPC capacity in (3.59) includes the intra-cell interference between the different users. However, the derivation was done for the multiple-access channel (MAC), *i.e.*, the uplink channel from the users to the BS. To include inter-cell interference, a similar expression is needed for the broadcast channel (BC), *i.e.*, the downlink channel. In other words, the transmit covariance matrices $\mathbf{P}$ are required in order to calculate

$$C^{[\mathrm{DPC}]} = \frac{1}{N} \cdot \sum_{n=1}^{N} \max_{\mathbf{P}_{n,u}} \log_2 \det\left(\mathbf{I}_{n_r} + \sum_{u=1}^{n_u} \mathbf{H}_{n,u} \cdot \mathbf{P}_{n,u} \cdot \mathbf{H}_{n,u}^H\right). \tag{3.77}$$

A method for transforming the receive covariance matrices $\mathbf{Q}_{n,u}$ into the corresponding transmit covariance matrices $\mathbf{P}_{n,u}$ is given in [58]. In the MAC, users are decoded at the BS in a specific order, *i.e.*, user 1 us decoded first, user 2 is decoded second, and so on. Depending on the

decoding order, the users will achieve a different individual rate while the sum-capacity remains the same. The interference experienced by user u in the MAC is

$$\mathbf{B}_{n,u} = \mathbf{I}_{n_t} + \sum_{\bar{u}=u+1}^{n_u} \mathbf{H}_{n,\bar{u}}^H \cdot \mathbf{Q}_{n,\bar{u}} \cdot \mathbf{H}_{n,\bar{u}}. \tag{3.78}$$

In the BC, the opposite encoding order is used, *i.e.*, user 1 is encoded last, user 2 is encoded second to last, *etc.* In this case, the interference experienced by user u is

$$\mathbf{A}_{n,u} = \mathbf{I}_{n_r} + \mathbf{H}_{n,u} \cdot \left(\sum_{\bar{u}=1}^{u-1} \mathbf{P}_{n,\bar{u}} \right) \cdot \mathbf{H}_{n,u}^H \tag{3.79}$$

[58] calculates an effective channel $\hat{\mathbf{H}}$ and its SVD as

$$\hat{\mathbf{H}}_{n,u} = \mathbf{B}_{n,u}^{-1/2} \cdot \mathbf{H}_{n,u}^H \cdot \mathbf{A}_{n,u}^{-1/2} = \mathbf{U}_{n,u} \cdot \mathbf{D}_{n,u} \cdot \mathbf{V}_{n,u}^H. \tag{3.80}$$

The transmit covariance matrix $\mathbf{P}$ is then calculated as

$$\mathbf{P}_{n,u} = \mathbf{B}_{n,u}^{-1/2} \cdot \mathbf{U}_{n,u} \cdot \mathbf{V}_{n,u}^H \cdot \mathbf{A}_{n,u}^{1/2} \cdot \mathbf{Q}_{n,u} \cdot \mathbf{A}_{n,u}^{1/2} \cdot \mathbf{V}_{n,u} \cdot \mathbf{U}_{n,u}^H \cdot \mathbf{B}_{n,u}^{-1/2}. \tag{3.81}$$

The individual user rates can now be calculated as

$$\begin{aligned} R_{n,u} &= \log_2 \det \left(\mathbf{I}_{n_r} + \mathbf{A}_{n,u}^{-1} \cdot \mathbf{H}_{n,u} \cdot \mathbf{P}_{n,u} \cdot \mathbf{H}_{n,u}^H \right) && (3.82) \\ &= \log_2 \det \left(\mathbf{I}_{n_t} + \mathbf{B}_{n,u}^{-1} \cdot \mathbf{H}_{n,u}^H \cdot \mathbf{Q}_{n,u} \cdot \mathbf{H}_{n,u} \right) && (3.83) \\ C^{[\mathrm{DPC}]} &= \frac{1}{N} \cdot \sum_{n=1}^{N} \sum_{u=1}^{n_u} R_{n,u}. && (3.84) \end{aligned}$$

The covariance matrix $\mathbf{A}_{n,u}$ in (3.82) describes the intra-cell interference, *i.e.*, the interference caused by the data streams for the other users within the same cell. In order to include the inter-cell interference, *i.e.*, the interference caused by the other BSs transmitting on the same frequency, their channels need to be included as well. This is done by calculating the interference covariance matrix $\mathbf{Z}_{n,u}$ for the user u including intra and inter-cell-interference as

$$\mathbf{Z}_{n,u} = \mathbf{I}_{n_r} + \underbrace{\mathbf{H}_{n,u,i} \cdot \left(\sum_{\bar{u}=1}^{u-1} \mathbf{P}_{n,\bar{u},i} \right) \cdot \mathbf{H}_{n,u,i}^H}_{\text{intra-cell interference}} + \underbrace{\sum_{\forall \bar{i}, \bar{i} \neq i}^{n_i} \mathbf{H}_{n,u,\bar{i}} \cdot \left(\sum_{\bar{u}_{\bar{i}}=1}^{n_{\bar{u},\bar{i}}} \mathbf{P}_{n,\bar{u}_{\bar{i}},\bar{i}} \right) \cdot \mathbf{H}_{n,u,\bar{i}}^H}_{\text{inter-cell interference}}. \tag{3.85}$$

In this equation, a serving BS i transmits parallel spatial data streams to several users. Thus, there is intra-cell interference, depending on the encoding order of the data streams. In addition, there are $n_i - 1$ interfering BSs $\bar{i}$ having the channel matrix $\mathbf{H}_{n,u,\bar{i}}$. Each of those BSs serves $n_{\bar{u},\bar{i}}$ users. They apply their own specific transmit strategies and it is necessary to consider the transmit covariance matrices $\mathbf{P}_{n,\bar{u}_{\bar{i}},\bar{i}}$ of the interfering BSs $\bar{i}$ transmitting to their own users $\bar{u}_{\bar{i}}$. The multi-user sum-capacity for BS i now is [126]

$$C_i^{[\mathrm{INT}]} = \frac{1}{N} \cdot \sum_{n=1}^{N} \sum_{u=1}^{n_u} \min_{\mathbf{Z}_{n,u}} \max_{\mathbf{P}_{n,u}} \log_2 \det \left(\mathbf{I}_{n_r} + \mathbf{Z}_{n,u}^{-1} \cdot \mathbf{H}_{n,u,i} \cdot \mathbf{P}_{n,u} \cdot \mathbf{H}_{n,u,i}^H \right). \tag{3.86}$$

Finding this capacity is generally a nontrivial problem since it involves finding a global optimum where the sum-capacity over all BSs is maximized. This is generally a nonconvex optimization problem and involves scheduling in order to find the maximum [127]. It has been shown by [128] that finding a globally optimal solution to this so-called interference management problem is generally a NP-hard problem.

Results on the interference-limited capacity for different transmission schemes are presented for the Berlin testbed in Chapter 5 on Page 128 where coherent channel measurement data for several BSs is available.

3.4 Summary

In this chapter, the model parameterization and validation methodology has been introduced. This is done by means of channel measurements during which the wireless channel is characterized in a representative scenario. The measurement data is analyzed in several stages. In the first stage, the multipath components are identified in the recorded channel data and their parameters, *i.e.*, the path delays, departure and arrival angles, polarization properties, and powers are calculated. For this, an algorithm has been developed that estimates the delays and angles in separate steps. This makes the delay estimation independent of the antenna patterns. A time-domain representation of the channel is calculated from the measurement data where the bandwidth limitation and most of the noise is removed. Then, in the second stage, the large-scale parameters, *i.e.*, the path gain, shadow fading, delay spread, Ricean K-factor, cross polarization ratio and four angular spread values are calculated. All of these parameters have been introduced and it was described how they can be calculated from the data. In a third stage, the statistical properties of the large-scale parameters, *i.e.*, their distributions and correlation properties are calculated. These statistics of the channel parameters form the basis of the so-called *parameter tables* that are needed by the channel model from Section 2. In the last stage, the channel model is used to generate "artificial" channel coefficients while taking the parameter tables, base station and mobile terminal positions, and antenna characteristics into account. The results can then be directly compared. This includes a comparison of the achievable performance of a radio communication system. For this, performance metrics, *e.g.*, the single-link and multi-link capacity, have been introduced.

In the next two chapters, the results of the parameterization and validation procedure are presented for two measurement campaigns in urban-macrocell conditions. The first campaign in Dresden, Germany, used a RUSK HyEff channel sounder [129] with 58 receive and 16 transmit antennas. The data was used to derive a complete parameter set. The measurement campaign and the results are described in Chapter 4. A second campaign (Chapter 5) was done in Berlin, Germany using a different measurement setup. This setup was used to validate the model in a multi-cellular environment. Here, only a subset of the model parameters could be derived. However, the additional validation results could be obtained in a system-level environment with multiple base stations. This is important because channel models are often used to predict the performance of transmission schemes in large deployments.

4 Validation of the Model for Massive MIMO

The most straightforward way to gain knowledge of the propagation conditions is by means of measurements. A transmitter (the channel sounder) sends out a known signal that is received by a receiver. By comparing the received signal with the known transmit signal, one can calculate the channel impulse response (CIR) which captures the properties of the propagation channel. Then, relevant propagation parameters can be extracted from the data. However, due to the substantial financial and manpower effort that is needed to perform such measurements, they are often limited to a relatively confined area. Therefore, the so-called *propagation scenario*, *e.g.*, "urban-macrocell" or "indoor office", must be well defined and the measurements must be planned accordingly. One such measurement campaign has been done in downtown Dresden, Germany, with the aim to characterize a typical urban-macrocell (UMa) scenario at a carrier frequency of 2.53 GHz [23]. The measurements have been done within the EASY-C project (Enabler for Ambient Services and Systems Part C - Wide Area Coverage) [77]. The aim of the research in EASY-C was to develop key technologies for the next generation of cellular networks. In order to generalize the findings from such a measurement campaign, the data is used to develop and parameterize channel models that can then be used instead of the measurement data to test and validate new concepts in mobile communications. In Chapter 3, the methodology on how to derive the model parameters has been introduced. In this chapter, the measurement data, which was collected in Dresden, is analyzed again in order to parameterize and validate the new channel.

This Chapter is organized as follows: The measurements are described in Section 4.1. Then, in Section 4.2, the measurement results, the base station (BS) and mobile terminal (MT) positions, and the antenna characteristics are used to parameterize the channel model from Chapter 2. The model is used to *resimulate* the measurement campaign. The *resimulated* channel coefficients are processed in the same way as the raw measurement data and the large-scale parameters (LSPs) are calculated from the two data sets as described in Chapter 3. Such a direct comparison between channel modeling and measurement results has not been done before. So far, it was an open issue if the results from state-of-the-art geometry-based stochastic channel models, such as the WINNER and 3GPP model, are trustworthy. The results in Section 4.3 show that for almost all parameters there is a good agreement between the predictions made by the model and the results from the measurements. The performance metrics, which provide a measure of the achievable data rate of a communication system, are discussed in Section 4.6. Again, there is a good match between model and measurements. It is also shown that predictions can be made for different antenna configurations by replacing the antenna characteristics in the model while keeping the propagation parameters unchanged.

4.1 Massive MIMO Measurements in Dresden, Germany

In order to extract the LSPs from measured data and validate the channel model, measurement data with high spatial and temporal resolution is required. Such measurements have been done in 2009 in downtown Dresden, Germany. A RUSK HyEff channel sounder [129] was used at a center frequency of 2.53 GHz with a bandwidth of 100 MHz. The length of the recorded CIR was

set to 12.8 μs for each MIMO sublink. Thus, the baseband CIR consists of 1,281 complex-valued samples in the frequency domain which, after transformation into time domain, corresponds to a delay resolution of 10 ns. In other words, the delays of the multipath components (MPCs) can be calculated with an accuracy of 10 ns or less.

The array antennas at the transmitter and receiver are made from cross-polarized patches with two points of delivery feeding vertical and horizontal polarization of the same element. The full width at half maximum (FWHM) beam width of a single patch element is roughly 90°, depending of the array geometry. The coupling of the two polarizations measured at broadside in an anechoic chamber is less than -30 dB and does not exceed -25 dB at the 90° FWHM beam width. 40 pieces of those patch antennas were assembled into an uniform linear array (ULA) for the transmitter shown in Figure 4.1, right. The element spacing is 62.5 mm. Furthermore, four elements in each column are coupled by a power divider to reduce the FWHM in elevation direction to 20° which leads to an effective antenna gain of approximately 11 dBi. However, the high-power switch, the power divider, and the cables introduced an additional attenuation of 4.3 dB. The left-most and the right-most column in the array are grounded by 50 Ω resistors to minimize edge effects in the array. Therefore, altogether eight columns of cross-polarized patches at $\lambda/2$ spacing result in 16 transmit elements in the MIMO matrix.

The receive array antenna (see Figure 4.2) consists of 29 cross-polarized patch-elements. This allows for a sufficiently high spatial resolution in order to estimate the receive angles in both azimuth an elevation direction. In total, the array has 58 ports, 29 for vertical polarization and 29 for horizontal polarization. Hence, 928 CIRs were recorded for each snapshot. A schematic view of the antenna is depicted in Figure 4.3. The bottom part is assembled of two rings with a diameter of 150 mm consisting of 12 dual-polarized patch elements, each. On top of the antenna, a so-called MIMO cube was assembled out of 5 patch elements (see Figure 4.1, left). The same terminal antenna configuration was already used in earlier measurements [11, 19]. However, here, the cube is scaled to an edge length of 5 cm to fit the patches for 2.53 GHz. Both the transmit and receive antenna were calibrated in an anechoic chamber where the polarimetric antenna patterns (see Section 2.5 on Page 31) were measured. Those patterns can be directly used in the channel model without further processing.

To extract the statistics of the LSPs and other metrics, a significant number of measurement locations is required. Therefore, the entire receiver chain, consisting of the array antenna, the receiving part of the channel sounder, hard disk storage, control computers, a global positioning system (GPS) logger, a camera, and the power supply, was mounted into a measurement van (see Figure 4.2, right). This setup was then used to collect samples of the wireless channel along a street grid around the campus of the Technische Universität Dresden. The total measurement track had a length of 2.9 km, along which 60.000 channel snapshots were recorded. This corresponds to one snapshot every 5 cm. In addition to that, three different locations for the transmitter were measured sequentially. The total recorded raw data volume was roughly

Table 4.1: Measurement parameters for the MIMO measurements in Dresden

Parameter	Value
Frequency Range	2.53 GHz (center freq.) ; 100 MHz (bandwidth) ; 1281 carriers
CIR length	12.8 μs ; update every 25.6 ms
Link Budget	36 dBm Tx power per antenna; -90.2 dBm noise floor
Max. MT speed	10 km/h
Measurement Track	$3 \cdot 2.9$ km
Tx antenna configuration	16 elements, XPOL H/V, 11 dBi gain, 100° azimuth, 24° elevation
Rx antenna configuration	58 patch antennas, XPOL H/V, 5 dBi gain, 135° azimuth, 75° elevation

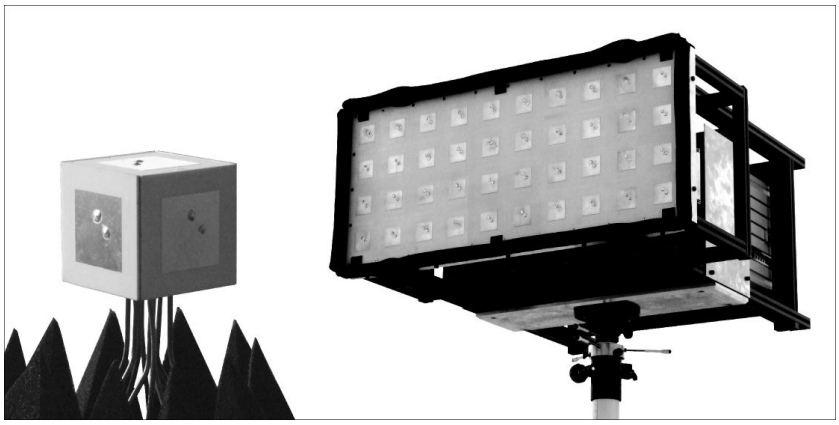

Figure 4.1: Transmit antenna for the Dresden measurements: An ULA assembled from 40 elements was used at the transmitter (right). The elements in vertical direction were coupled by a power divider in order to achieve an higher elevation gain. Left: Top part of the receive antenna.

Figure 4.2: Receiver configuration for the Dresden measurements: The receive array antenna (left) is assembled from 29 dual-polarized patch elements. This antenna is mounted on the roof of a measurement car (right). The absorption material around the antenna reduces reflections of the radio signal.

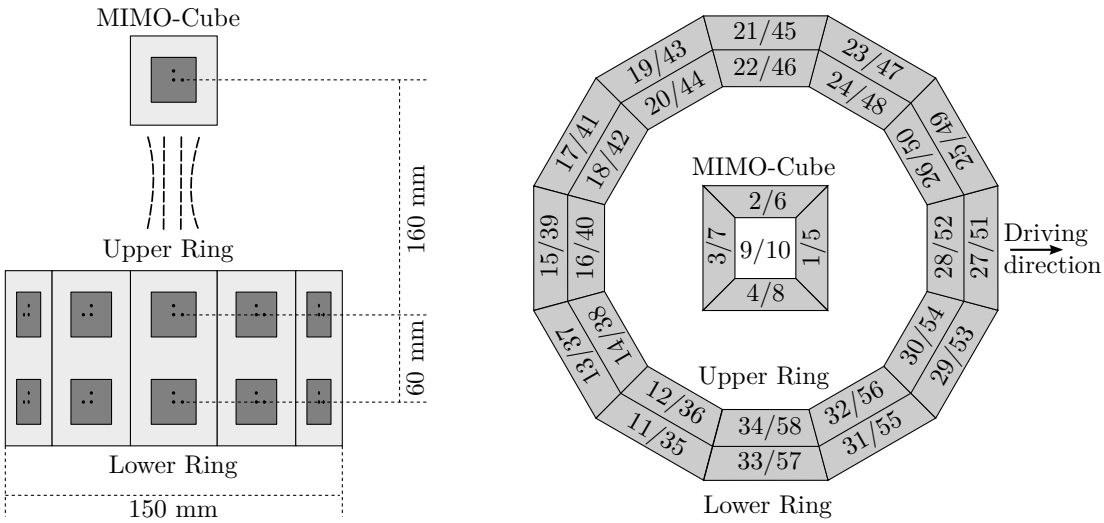

Figure 4.3: Receive antenna schematics for the Dresden measurements. Left: Lateral view of the antenna with array dimensions. Right: Schematic top view of the array. The numbers correspond to the row in the recorded channel matrix. The first number is for the vertical port and the second for the horizontal port.

one terabyte. One of the measurements locations was sampled twice in order to evaluate the stationarity of the outdoor environment between repeated measurements [22]. It was found that a multi-run measurement procedure causes decorrelation of the estimated delay and azimuth spreads lower than 9%. The low decorrelation levels indicate that large-scale characterization of multi-link configuration can be performed sequentially with a single sounding device.

An overview of the measurement site is given in Figure 4.4. The figure shows the transmitter positions and transmit antenna orientations (black ellipse with white arrow) as well as the measurement tracks (thick black line). Start and end points are numbered are marked by a black dot. The start point has an arrow indicating the driving direction. The coordinates of the measurement area are 51°2'8.88"N and 13°44'9.96"E. An overview of the measurement parameters is given in Table 4.1.

In order extract the LSPs and performance metrics for the channel model, and validate the model assumptions, further processing steps are needed. Those steps are:

1. The GPS positioning data was aligned with the measurement track and the recording time for each snapshot. In this way, the position of each snapshot could be calculated.

2. The individual MPCs were extracted from the raw measurement data using the algorithm in Section 3.1.2. This processing step reduced the data volume from 1 terabyte (raw data) down to 36 GB (extracted MPCs). After the extraction, the format of the processed measurement data is identical to the output data format of the channel model. Hence, the following processing steps can be applied to both the measured data and the resimulated data.

3. The LSPs and the performance metrics were extracted from the processed measurement data. The distributions of those parameters serve as a reference. In order to validate the model, the same distributions must be created by the channel model. The procedures for extracting the LSPs are described in Section 3.2 (Page 59) and the performance metrics are described in Section 3.3 (Page 64).

4. The transmitter and receiver positions were imported into the channel model and a classification into LOS and NLOS segments was done based on the received power and a 3-D model of the measurement environment. In addition, a model of the antennas was created using data from a calibration measurement in an anechoic chamber. This allows recreating channels with the same properties as the measured data. The same procedures for extracting the LSPs and performance metrics can be used and the outputs can be directly compared to the measurement results.

5. The LSPs extracted from the measurement data (step 3) are often different from the values in the parameter tables which are needed as an input of the channel model. The reason is that the model parameters do not include the antenna influence whereas measurements can only be done with antennas. Therefore, a parameter table for the channel model has to be derived where the antenna influence is removed.

6. Finally, the results of the measurement and the channel model results are compared and discussed.

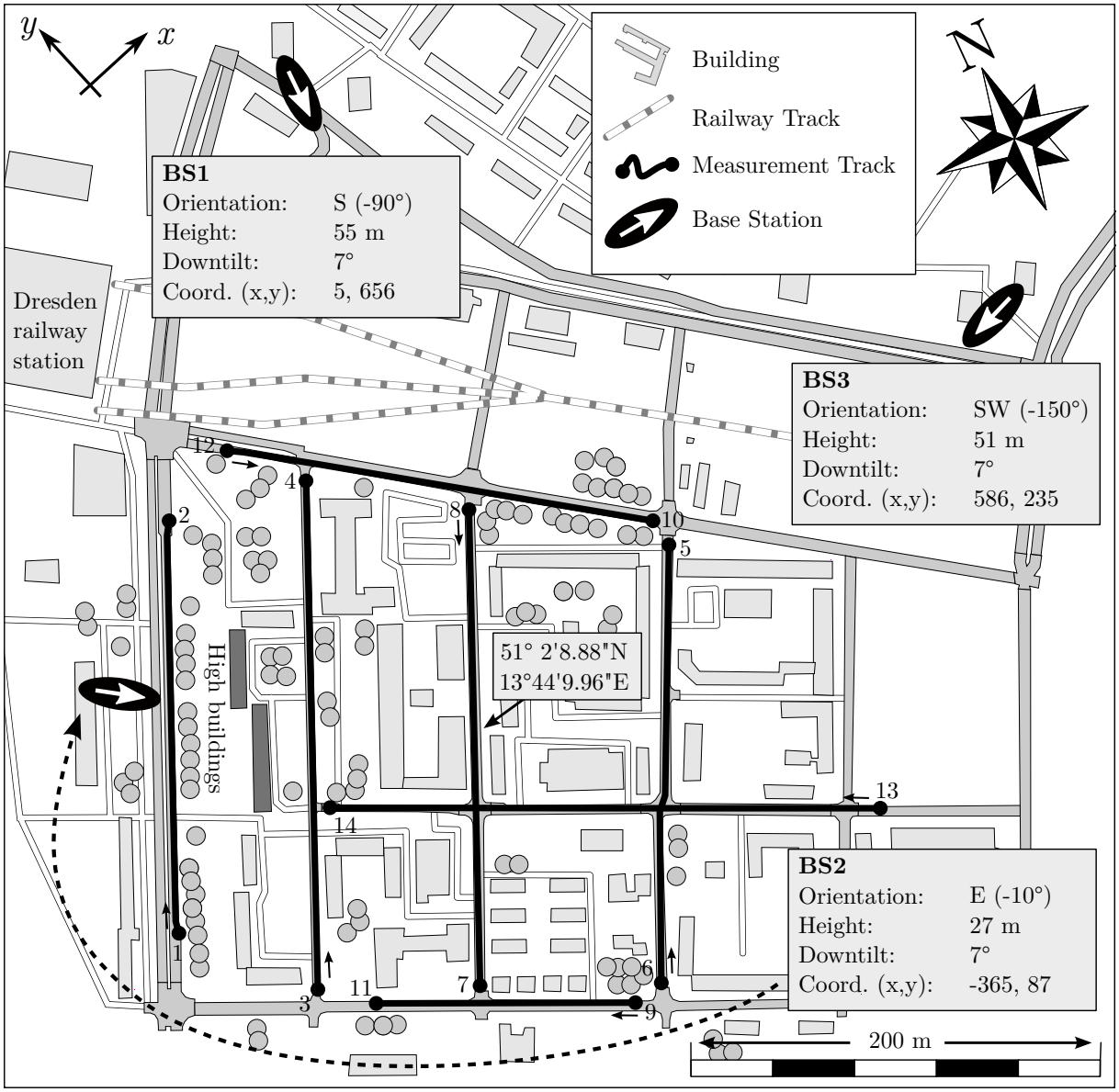

Figure 4.4: Map of the measurement area in Dresden, Germany, showing the transmitter and receiver positions and the orientations of the antennas.

4.2 Resimulation of the Measurement Campaign

As already discussed earlier, the channel model separates the antenna influence from the propagation effects and thus requires "ideal" parameters as input. Since such parameters cannot be extracted directly from the measurements, an iterative fitting method was used to adjust the input parameters of the model such that the LSP calculated from the model output (with antennas) matched the LSP calculated from the measured data. A reference parameter table was extracted from the same data but with a different method by [23]. However, some values are different from the current evaluation. The performance metrics from Section 3.3 are not linked directly to the input parameters of the model but are influenced by all parameters simultaneously. Thus, comparing the results gives an indication for the accuracy and limitations of the assumptions made in the channel model. This is done in Section 4.6 on Page 100.

Channel Model Setup At first, the Tx-positions, sector orientations and Rx-tracks (see Figure 4.4) were imported into the channel model. The Rx-tracks were then split into 94 segments with an average length of 31 m. The standard deviation of the segment length was 13 m. A segment can be seen as an interval in which the LSPs do not change considerably and where the channel maintains its wide sense stationary (WSS) properties. It is important not to confuse *segments*, which are used in the channel model, with the *averaging intervals*, which are used during the data analysis in order to suppress small-scale-fading effects. Usually, the *averaging intervals* are much shorter than the *segments*. A classification into LOS and NLOS segments was done based on the received power and a 3-D model of the measurement environment. In total, 22% of the measurement tracks were classified as LOS. However, there are significant differences between the BSs where BS1 had a LOS coverage of 42%, BS2 had 17% and BS3 had only 7%. The low value for BS3 is due to an high building close to the transmitter that blocked the LOS for a large part of the measurement area. Then, a model of the antennas was created using data from a calibration measurement in an anechoic chamber.

Reference Simulations for the 3GPP-3D Model The 3GPP-3D channel model [49] is the state-of-the-art geometry-based stochastic channel model. It serves as a well-established reference for both urban-macrocell and urban-microcell channel simulations. However, an open-source implementation of the 3GPP-3D model is not available. The curves were therefore generated using the QuaDRiGa channel model with some modifications that implement all the core functions of the 3GPP-3D model. First, the algorithm for generating the parameter maps (see Section 2.1 on Page 18) was replaced with the method from [97] which essentially removed the filtering over the map diagonals. Second, the departure and arrival angles were generated based on the description in [47], page 39. However, some modifications were necessary to apply the method also in 3-D coordinates. Those are described in Appendix A.1 of this thesis. Time evolution, drifting, and scenario transitions are not supported by the 3GPP-3D model. Those features were therefore disabled and rotating phasors were used to emulate Doppler spreads. MT positions were chosen randomly by *dropping* users in the same area that was used for the measurements (see Figure 4.5). Then, random propagations conditions were assigned with a LOS probability of 22%. Last, the new polarization model from Section 2.5 was disabled and the NLOS polarization

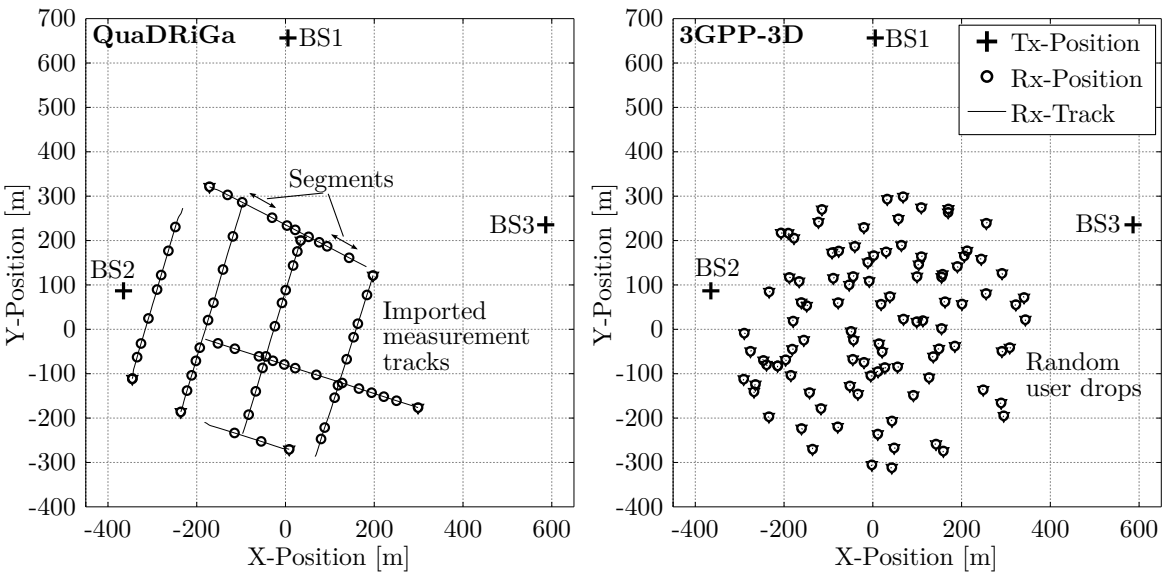

Figure 4.5: Illustration of the user placement methods: The new model (left) uses the imported measurement tracks which are divided into segments. The 3GPP-3D model (right) uses *drops*. Each drop represents one independent user position.

was modeled by (2.67). The antenna model remains the same. It has been shown that these modifications are well in line with the 3GPP guidelines by calibrating the model as described in [49]. The calibration results can be found in [14]. The generated channel coefficients were then evaluated in the same way as the measured data and the coefficients from the new model.

Parameterization of the Model In a first attempt, the LSPs extracted from the measured channels were used as input to the model. However, the results did not match well because of the influence of the random LSP maps and the antennas. The random LSP maps from Section 2.1 on Page 18 do not exactly match the Dresden measurement setup. Hence, there might be differences in the obtained results due to this randomness. However, when the simulations are repeated several times, it is possible to determine a validity range for the model which may or may not include the measurement results. Thus, 16 sets of channel coefficients were generated. A complete parameter table was then calculated from both the measured and the resimulated data. This includes the empirical cumulative distribution functions (CDFs) of all LSPs, the performance metrics, decorrelation distances, and the inter-parameter correlations. However, a comparison of the results still showed differences between model and measurement results. Those deviations can have two reasons: either the model or the input parameters do not agree with the reality.

The model requires "ideal" input parameters that are not altered by the antennas. A solution was to iteratively adjust the input parameters until the results obtained from the resimulated data match the results from the measured data. However, this method might mask some "mistakes" made in the model, either in the conceptual part or in the implementation. For example, if there is an error in the implementation that reduces the delay spread in the output data, the iterative parameter fitting would compensate for this by increasing the DS at the input of the model. In this case, the input parameter would only be valid for this specific implementation of the model. Thus, generally, it is only possible to draw conclusions on the combination of both the channel model itself and the input parameters. In order to minimize such effects, extensive testing and debugging was done to make sure that for each input parameter the reference implementation of the model produces exactly the same value in the output channel coefficients (assuming ideal onmi-directional antennas). The input parameters can then be discussed in the light of other published findings.

Parameter Tables The input parameters of the model are listed in Tables 4.2 and 4.3. Table 4.2 provides the LSPs for the urban-macrocell scenario, both for LOS and NLOS propagation. Each of the eight columns represents one parameter set that can be used to generate channel coefficients. The first and fifth column contain the parameters for the 3GPP-3D model [49]. Several measurement campaigns in different cities were done to obtain those tables. The second and sixth column list the findings from [23] that were extracted from the Dresden measurement data using a different evaluation method. The third and seventh column then contain the results from the iterative parameter fitting. Finally, the last columns contain the input parameters for the Berlin scenario. Those parameters will be discussed in Section 5.1.

Table 4.3 lists the inter-parameter correlation values. Again, there are four values for each parameter - one for the 3GPP-3D model, one from [23], one obtained from the iterative fitting of the Dresden scenario, and one for the Berlin scenario. The upper left part of the table contains the values for LOS propagations and the lower right part for NLOS propagation. These values are used in the correlation matrix (2.12). The cross-correlation matrix must be positive definite to create correlated sequences, *e.g.*, by Cholesky factorization.

Table 4.2: Parameters for the Urban Macro-cell (UMa) Scenario

Parameter		LOS				NLOS			
		3GPP	[23]	Dresden	Berlin	3GPP	[23]	Dresden	Berlin
No. Clusters	L	12	*N/A*	*12*	*15*	20	*N/A*	*20*	*25*
Path Gain	A	22.0	14.9	24.0	21.0	40.0	10.3	46.0	28.5
	B	102.1	126.3	114.0	110.5	137.6	134.2	136.5	123.5
SF (dB)	σ	4.0	8.3	6.1	3.7	8.0	6.0	3.0	4.0
decorr. [m]	λ	37	129	275	90	50	3	170	100
Delay Spread	μ	-7.03	-7.45	-7.05	-6.69	-6.44	-6.88	-6.54	-6.47
($\log_{10}$s)	σ	0.66	0.56	0.35	0.30	0.39	0.44	0.27	0.20
(ns)	μ	93	36	89	204	363	132	288	339
decorr. [m]	λ	30	131	200	130	40	38	70	100
Delay factor	r_τ	2.5	*N/A*	*2.5*[a]	*2.5*[a]	2.3	*N/A*	*2.0*[b]	*2.0*[b]
K-factor	μ	9.0	9.8	4.0	2.7	*-100*[c]	*N/A*	-10.4	-6.3
(dB)	σ	3.5	7.8	6.9	2.3	*0*[c]	*N/A*	5.5	3.7
decorr. [m]	λ	12	31	100	23	*40*[c]	*N/A*	21	40
ASD	μ	1.15	0.67	0.83	*0.65*[d]	1.41	0.67	1.11	*0.65*[d]
($\log_{10}$°)	σ	0.28	0.08	0.27	*0.23*[d]	0.28	0.08	0.18	*0.22*[d]
(°)	μ	14.1	4.7	6.8	*4.5*[d]	25.7	4.7	12.9	*4.5*[d]
decorr. [m]	λ	18	2	150	*8*[e]	50	2	70	*25*[e]
per cluster	c_ϕ	5.0	*N/A*	*0.7*[f]	*2.0*[f]	2.0	*N/A*	*1.3*[f]	*2.0*[f]
ESD	μ	N/A[g]	*N/A*	*0.12*[h]	*0.70*[a]	N/A[i]	*N/A*	*0.27*[h]	*0.90*[a]
($\log_{10}$°)	σ	0.40	*N/A*	*0.20*[h]	*0.20*[a]	0.20	*N/A*	*0.20*[h]	*0.20*[a]
(°)	μ	N/A	*N/A*	*1.3*[h]	*5.0*[a]	7.9	*N/A*	*1.9*[h]	*7.9*[a]
decorr. [m]	λ	15	*N/A*	*130*[j]	*15*[a]	50	*N/A*	*70*[h]	*50*[a]
per cluster	c_ϕ	3.0	*N/A*	*0.1*[h]	*3.0*[a]	3.0	*N/A*	*0.2*[h]	*3.0*[a]
ASA	μ	1.81	1.55	1.74	*1.61*[d]	1.87	1.55	1.83	*1.50*[k]
($\log_{10}$°)	σ	0.20	0.12	0.14	*0.17*[d]	0.11	0.12	0.13	*0.16*[d]
(°)	μ	65	35	55	*41*[d]	74	35	68	*32*[d]
decorr. [m]	λ	15	6	120	*11*[e]	50	5	130	*45*[l]
per cluster	c_ϕ	11	*N/A*	*6*[f]	*12*[a]	15	*N/A*	*7*[f]	*15*[a]
ESA	μ	0.95	1.19	1.05	*1.16*[m]	1.26	1.19	1.10	*1.25*[m]
($\log_{10}$°)	σ	0.16	0.11	0.12	*0.14*[m]	0.16	0.11	0.18	*0.14*[m]
(°)	μ	8.9	15.5	11.5	*14.5*[m]	18.2	15.5	12.6	*17.8*[m]
decorr. [m]	λ	15	2	80	*11*[n]	50	2	105	*25*[n]
per cluster	c_ϕ	7.0	*N/A*	*1.1*[f]	*3.0*[a]	7.0	*N/A*	*1.3*[f]	*7.0*[a]
XPR	μ	8.0	9.7	23.5	*9.0*[o]	7.0	7.0	20.5	*7.8*[o]
(dB)	σ	4.0	3.6	3.0	*4.3*[o]	3.0	4.1	2.5	*4.3*[o]

[a] This is taken from the WINER model [47, 48].
[b] This is the average of the values from the WINNER model [47] and the 3GPP SCM [130].
[c] The WINNER model supports no NLOS-KF. Those settings effectively disable the LOS component.
[d] This is a combination of the results from [23, 47, 96].
[e] This is a combination of the results from [23, 47].
[f] It seems to be unlikely that the per-cluster angular spread exceeds the total angular spread. This can be seen in all WINNER results where the per-cluster spread is at most around half the total angular spread.
[g] 3GPP defines the ESD as $\sigma_{\theta^d} = \max\{-0.5; -2.1 \cdot (d/1000) + 0.75\}$.
[h] It is assumed that the ESD values are small in Dresden due to the above-rooftop deployment.
[i] 3GPP defines the ESD as $\sigma_{\theta^d} = \max\{-0.5; -2.1 \cdot (d/1000) + 0.9\}$.
[j] ESD decorrelation distance is assumed to be the average of the other decorrelation distances.
[k] This is a combination of the results from [23, 47, 95, 96]
[l] This is a combination of the results from [23, 47, 95]
[m] This is a combination of the results from [23, 48, 96].
[n] This is a combination of the results from [23, 48].
[o] This is a combination of the results from [23, 47, 69].

Table 4.3: Cross-Correlation Values

Cross-correlation			LOS DS	KF	SF	ASD	ASA	ESD	ESA
	DS	3GPP	1	-0.4	-0.4	0.4	0.8	-0.2	0
		[23]	1	-0.5	-0.5	-0.1	0.1	*N/A*	0
		Dresden	1	-0.8	-0.8	0.65	0.8	*0.6*[a]	0.6
		Berlin	1	-0.35	-0.62	*0*[b]	*0.2*[b]	*-0.4*[b]	*0*[b]
	KF	3GPP	*0*[c]	1	0	0	-0.2	0	0
		[23]	*N/A*	1	0.7	-0.1	-0.1	*N/A*	-0.3
		Dresden	0	1	0.85	-0.65	-0.85	*-0.6*[a]	-0.6
		Berlin	-0.1	1	0.6	*0*[b]	*-0.2*[b]	*0*[b]	*-0.3*[d]
	SF	3GPP	-0.4	*0*[c]	1	-0.5	-0.5	0	-0.8
		[23]	-0.3	*N/A*	1	-0.1	-0.1	*N/A*	-0.4
		Dresden	-0.4	0.2	1	-0.65	-0.75	*-0.45*[a]	-0.45
		Berlin	-0.65	0.12	1	*-0.2*[b]	*-0.4*[b]	*0*[b]	*-0.6*[b]
N	ASD	3GPP	0.4	*0*[c]	-0.6	1	0	0.5	0
L		[23]	-0.1	*N/A*	0.1	1	0.4	*N/A*	0
O		Dresden	0.45	-0.2	-0.65	1	0.6	*0.6*[a]	0.5
S		Berlin	*0.1*[b]	*0*[f]	*0*[b]	1	*0.5*	*0.5*	*-0.3*
	ASA	3GPP	0.6	*0*[c]	0	0.4	1	-0.3	0.4
		[23]	-0.2	*N/A*	0.1	0.4	1	*N/A*	0.2
		Dresden	-0.25	0	0.25	-0.2	1	*0.6*[a]	0.65
		Berlin	*0*[b]	*-0.2*[b]	*-0.2*	*0.5*	1	*0*[e]	*0.3*[b]
	ESD	3GPP	-0.5	*0*[c]	0	0.5	0	1	0
		[23]	*N/A*	*N/A*	*N/A*	*N/A*	*N/A*	1	*N/A*
		Dresden	*0.4*[a]	*0*[f]	*-0.3*[a]	*0.5*[e]	*0*[e]	1	*0.6*[a]
		Berlin	*-0.4*[b]	*0*[f]	*0*[e]	*0.5*[e]	*0*[e]	1	*0*[e]
	ESA	3GPP	0	*0*[c]	-0.4	-0.1	0	0	1
		[23]	-0.3	*N/A*	-0.3	0	0.3	*0*[e]	1
		Dresden	-0.4	0	0.2	0	0.7	*0*[e]	1
		Berlin	*-0.2*[b]	*-0.2*	*-0.5*[b]	*-0.3*[b]	*0.3*[d]	*0*[e]	1

[a] A similar correlation as for the ASD is assumed.
[b] This is a combination of the results from WINNER [47, 48] and other measurements [23, 96].
[c] 3GPP-3D supports no NLOS-KF and the median KF is set to -100 dB in Table 4.2.
[d] This is taken from [23].
[e] This is taken from the WINER model [47, 48].
[f] There is no measurement reference available.

4.3 Large-Scale Parameters

In this section, the results for the LSPs are presented and discussed. The first order statistics of each parameter are shown in two figures (see for example Figure 4.6), one for the LOS scenario (on the left) and one for the NLOS scenario (on the right). Each plot contains up to four empirical CDF curves. The thick solid line shows the results for the measured data. The thin solid line shows the results for the channel model. Since the simulations were repeated 16 times, there are 16 CDFs and 16 median values (2-quantile) for each parameter. The average of those values is plotted in the point where the ordinate shows a value of 0.5. The STD above and below the mean of those 16 samples determines the width of the errorbars. The third, dashed and dotted, thin line represents the input of the channel model, *i.e.*, the CDF calculated from μ and σ in Table 4.2. Ideally, those three lines would be identical. However, this is not always the case since several effects, *e.g.*, the antenna or the noise, alter the distributions. A fourth, thick dotted curve shows the results for the 3GPP-3D model using the default parameters for the urban-macrocell (UMa) scenario [49].

4.3.1 Effective Path Gain

The effective PG combines the directional antenna gain, the SF, and the distance-dependent PG. The results are shown in Figure 4.6. The measured power levels were fitted to the Hata model [64] by

$$\mathrm{PG}^{[\mathrm{LOS}]} = -24 \cdot \log_{10} d_{[\mathrm{km}]} - 114 \tag{4.1}$$

$$\mathrm{PG}^{[\mathrm{NLOS}]} = -46 \cdot \log_{10} d_{[\mathrm{km}]} - 136.5 \tag{4.2}$$

The results agree well with findings from the WINNER project [47] where similar values were reported. The SF was estimated to 6.1 dB for LOS propagations and 3 dB for NLOS. With this parameterization, the results from the measurements, the input parameters of the model, and the results extracted from the output of the model agree well. However, the LOS channels in the 3GPP-3D model have roughly 10 dB more power compared to the measurement results.

Narandzic *et al.* [23] reported a NLOS-PG exponent of only 10.3 for the Dresden measurement data which indicates that there is almost no relationship between the received power and the distance to the BS. The given explanation by [23] was that there is a "strong guiding effect of the radiated energy along the streets". However, a closer look at the data indicates a different reason that is specific to the measurement setup in Dresden. Directly in front of BS2 were two high buildings (approx. 35 m high) at a distance of 90 m from the transmitter (see Figure 4.4). Those building were higher than the transmitter itself (27 m) and they blocked a significant part of the signal. Hence, very little power was received along the street directly behind those buildings, only 160 m away from BS2. If BS2 is included in the analysis, a very low path gain exponent of 7.9 is estimated. This is illustrated in Figure 4.7 where the dashed curve includes BS2 and the solid curve does not include it.

A different picture arises when BS2 is excluded from the regression fit. In this case, the fit to the Hata model indicates a very high PG exponent of 44 (including antenna effects). This is not unusual for heavily shaded areas. In the absence of a LOS connection, the received power decreases rapidly with the distance. Using those parameters in the channel model seems to produce accurate results which can be seen in Figure 4.6, on the right side. In most cases, the CDFs for the measured and resimulated channels agree well. However, the power in the resimulated channels gets too large above a PG of 120 dB. The corresponding positions are those on the street behind the high buildings.

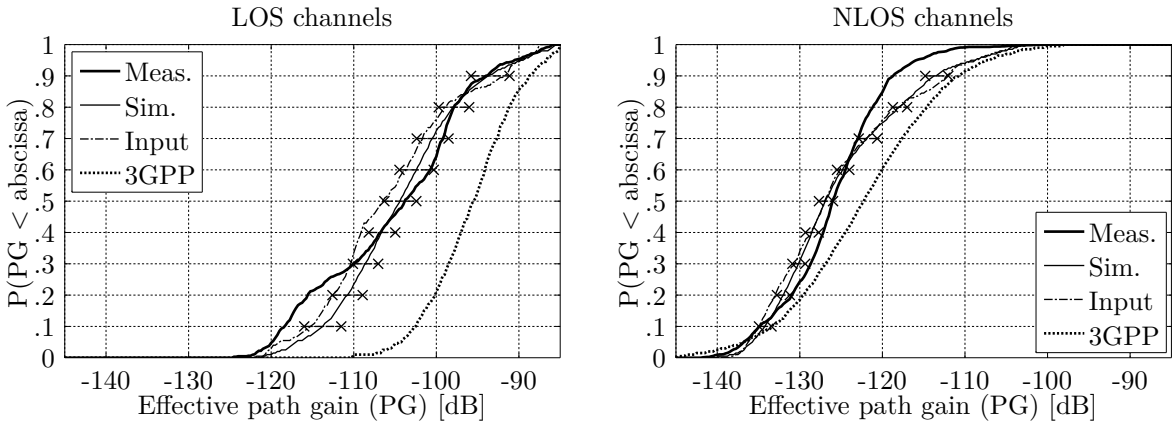

	LOS		NLOS	
	μ [dB]	σ [dB]	μ [dB]	σ [dB]
Meas. Results	-103.7	9.1	-125.9	6.3
QuaDRiGa In	-106.5	8.6	-127.0	8.5
QuaDRiGa Out	-104.4	7.9	-126.8	8.1
3GPP-3D In	-96.4	5.2	-121.8	8.2
3GPP-3D Out	-95.5	5.4	-122.2	9.0

Figure 4.6: Effective path gain distributions in Dresden, Germany

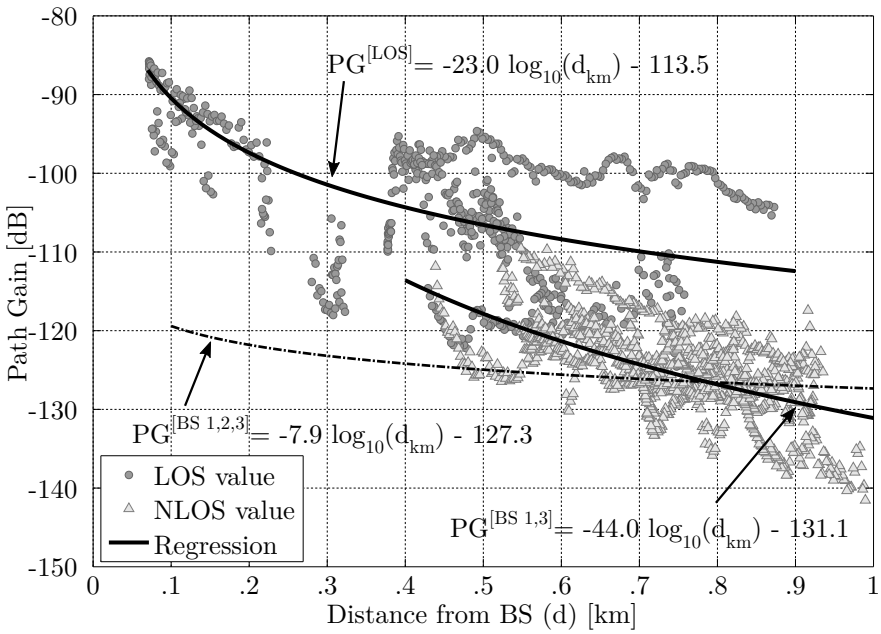

Figure 4.7: Regression fit of the measured path-gain values

4.3.2 Ricean K-Factor

The results for the KF can be seen in Figure 4.8. Results from the measurements and the model are in good agreement. The LOS-KF in the measured data is on average 5.7 dB with a STD of 7.3 dB. 25% of the LOS tracks have a KF smaller than 0 dB. This indicates that there are some channels that were classified as LOS but where the LOS component is very weak.

The NLOS measurement results show an average KF of -6.1 dB. However, this is not the true value since the LOS detection might falsely identify a strong indirect path as the LOS path. This becomes obvious when looking at the 3GPP-NLOS results. Here, the direct component was removed by setting the KF at the input of the model to -100 dB. However, at the model output a KF of -4.4 dB was calculated since a random NLOS path at the beginning of the CIR was taken as the direct component. With the new model and the new parameter set, a weak LOS component was added by setting KF_{μ} to -10.4 dB. With this setting, the model output agrees well with the measured results. This indicates that in some NLOS channels, the LOS component is present but is has a minor effect on the generated channel statistics.

The most interesting observation, however, is the large offset between the model input and output in case of the 3GPP-LOS results. With an average input value of 9 dB, an output of 12.5 dB is predicted. The STD also roughly triples. The reason for this is possibly an anomaly in the angular mapping function which is most evident at high KF values and when using directional antennas. An illustration of this effect is given in Figure 4.9.

The 3GPP-3D model maps the departure and arrival angles to a wrapped Gaussian distribution as shown on the left side of the Figure (see also Appendix A.1, Page 137). The strongest path has unit power and lies in the center of this distribution. All other paths get relative departure and arrival angles depending on their power. However, if the KF is high (12 dB in the figure), the sum-power of the indirect components is at roughly $\frac{1}{15}$ of the power of the direct component. This power is further divided by the number of paths. Mapping the path powers to the Gaussian distribution results in an 11° gap between the LOS angle and the first NLOS angle. Additionally, all LOS angles are clustered relatively close to each other due to the shape of the Gaussian curve. With omnidirectional antennas, this mapping does not affect the angular spread calculated at the output of the model. However, when directional antennas are used, the NLOS paths are further attenuated by the pattern. This is illustrated in the right side of Figure 4.9. The gray shaded area represents the directional antenna gain of the transmit array antenna. The dots represent the departure angles of the MPCs. There are four clusters of NLOS angles due to using the same mapping function for azimuth and elevation angles. The typical cross-shape always appears for KF value greater than 0 dB. In the example, the LOS path has an additional attenuation of 1 dB. However, the NLOS paths with positive elevation angles are attenuated heavily by the pattern. The cross gets bigger either with increasing KF or with increasing angular spread. Thus, high KF values at the input of the model result in even higher values at the output. This explains the results obtained with the 3GPP-3D model. This effect was also the main reason for replacing the WINNER mapping function with the one described in Section 2.3. To illustrate the difference, an identical plot for the new angular mapping method is shown in Figure 4.10. The resulting angles are distributed randomly and there is only a small increase of the KF (1 dB) due to the effect of the antenna pattern at the output of the model.

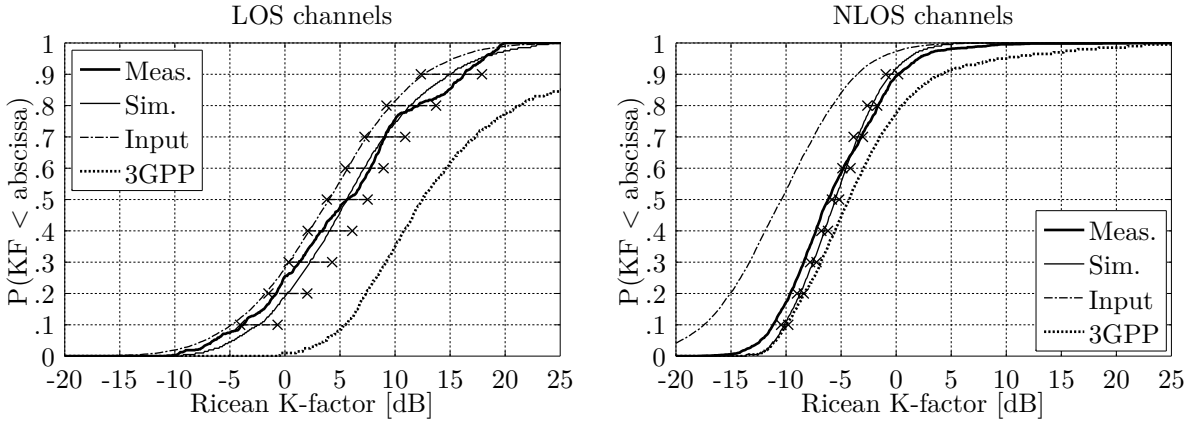

	LOS		NLOS	
	μ [dB]	σ [dB]	μ [dB]	σ [dB]
Meas. Results	5.7	7.3	-6.1	4.6
QuaDRiGa In	4.0	6.9	-10.4	5.5
QuaDRiGa Out	5.7	6.7	-5.5	3.7
3GPP-3D In	9.0	3.5	-100.0	0.0
3GPP-3D Out	12.5	10.6	-4.3	6.7

Figure 4.8: Ricean K-factor distributions in Dresden, Germany

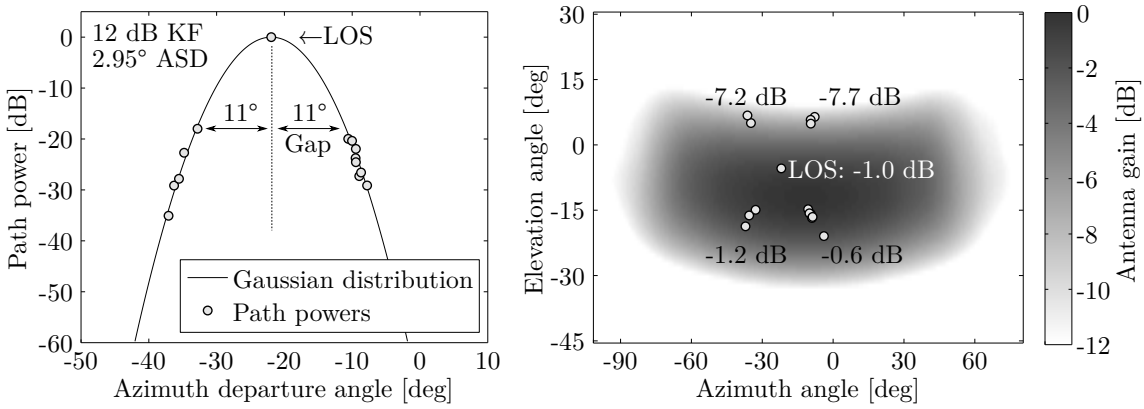

Figure 4.9: Illustration of the effect caused by using a Gaussian power angular spectrum

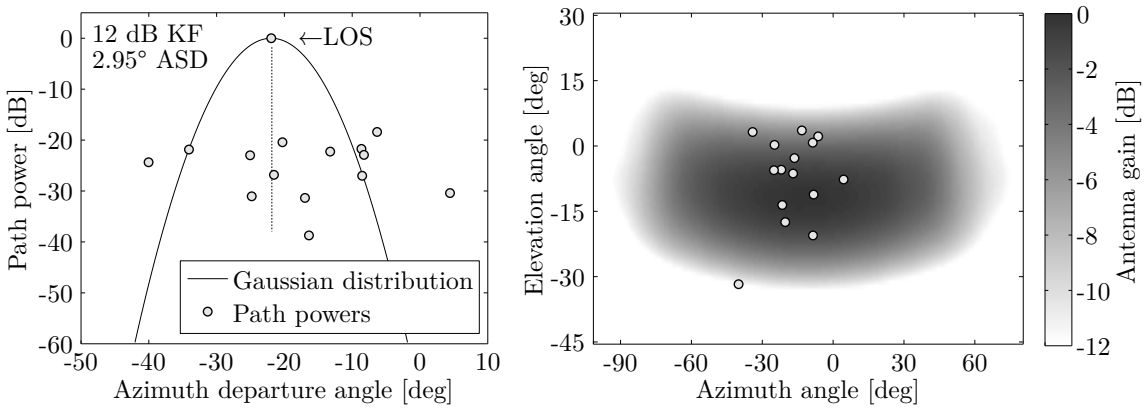

Figure 4.10: Illustration of the effect of the new angular mapping method

4.3.3 RMS Delay Spread

The results for the DS are presented in Figure 4.11. The minimum dynamic range in all the measured CIRs was 37.9 dB. Therefore, a threshold of 30 dB was used to calculate the DS, *i.e.*, paths having less than -30 dB of the power of the strongest path in a CIR were not used for calculating the DS. The same threshold was used for the resimulated channels. The measurement results indicate an average DS of 92 ns for LOS channels and 282 ns for NLOS channels. The iterative fitting of the input parameters of the channel model obtained almost identical values (89 and 288 ns, respectively). This indicates that the antennas have almost no influence on the DS.

Results reported in [23], however, indicate a much shorter DS of only 36 ns for the LOS scenarios and 132 ns for the NLOS channels. Those values were obtained from the same measurement data but with a different estimation method. The reason for this difference is unclear. Comparing the findings with results from the literature indicates even longer delay spreads in similar environments. Algans *et al.* [95], for example, reported DSs having average values of around 900 ns. This was obtained from measurements at 1.8 GHz with approximately 25 m BS height. In [7], average DS values of 330 ns were obtained from two measurement campaigns in Dresden, Germany and Berlin, Germany at 2.6 GHz using the same channel sounder as in the current campaign. However, different antennas and measurement tracks were used. The 3GPP SCM, a predecessor of the WINNER model, suggested using a DS of 660 ns for the urban-macrocell scenario (NLOS propagation). Thus, the current results seem to be reasonable.

Another observation is that the DS gets shortened at the output of the 3GPP-3D simulations. In the LOS case, the average input value of 93 ns gets further reduced to 39 ns. Likewise, the 363 ns for the NLOS channels get reduced to 228 ns. In contrary to the new model, where the antenna has only a minor effect on the DS, the 3GPP-3D simulations show a larger influence. This can be explained by the same phenomena responsible for the differences in the KF results. Due to the angular mapping function NLOS paths are attenuated more strongly by the directional antenna pattern. Less NLOS power then also leads to a shorter DS.

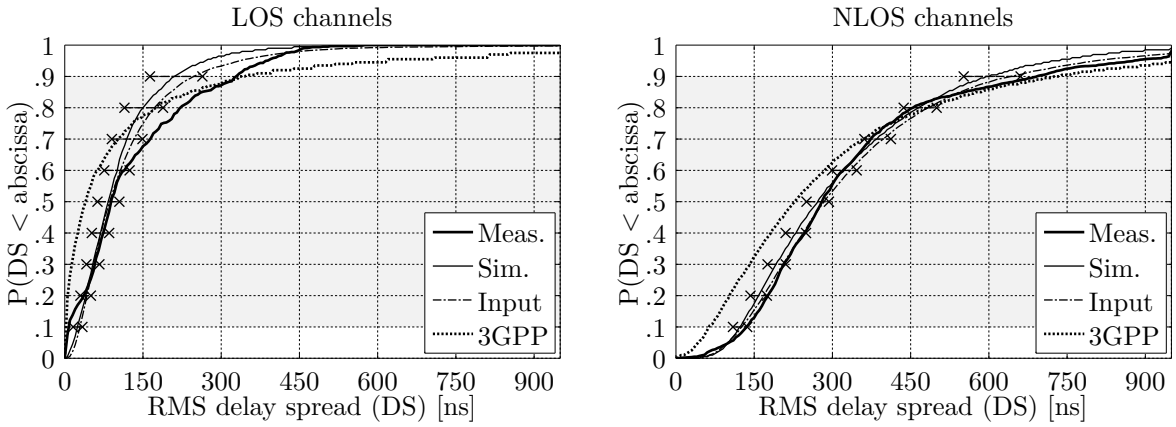

	LOS			10 - 90%	NLOS			10 - 90%
	μ	σ	μ [ns]	Range [ns]	μ	σ	μ [ns]	Range [ns]
Meas. Results	-7.04	0.53	91.6	8.4 - 331	-6.55	0.28	282.0	135 - 695
QuaDRiGa In	-7.05	0.35	89.1	34 - 246	-6.54	0.27	288.4	129 - 640
QuaDRiGa Out	-7.09	0.38	83.7	25 - 212	-6.57	0.27	272.1	123 - 605
3GPP-3D In	-7.03	0.66	93.3	0 - 694	-6.44	0.39	363.1	85 - 1104
3GPP-3D Out	-7.29	0.72	39.1	0.0 - 347	-6.64	0.43	228.1	66 - 736

Figure 4.11: RMS delay spread distributions in Dresden, Germany

4.3.4 Azimuth of Departure Angular Spread

The results for the ASD are shown in Figure 4.12. The measurements indicate relatively small values in both propagation conditions. The LOS channels have an average departure angular spread of 7.2°. Typical values are in between 2.4 and 16°. The NLOS channels have a larger average value of 12.7° with a typical range from 7.3 to 22°. These values do not get altered significantly by the antennas in the channel model. The values after the iterative fitting and the results of the channel model agree well with the measurements.

The results reported in [23] do not distinguish between LOS and NLOS propagation. An average ASD of 4.7° was reported. This is much smaller compared to the current results. As for the KF and the DS, there is also a difference in the values calculated from the 3GPP-3D simulations in case of LOS propagation. The average input value of 14.1° gets reduced to 9.6° due to the angular mapping which leads to a reduction of the NLOS path power. However, the effect is less strong compared to the DS results because the transmit antenna is de-embedded by the algorithm used for calculating the angles (see Section 3.1.3). For the NLOS channels, input and output values are almost the same.

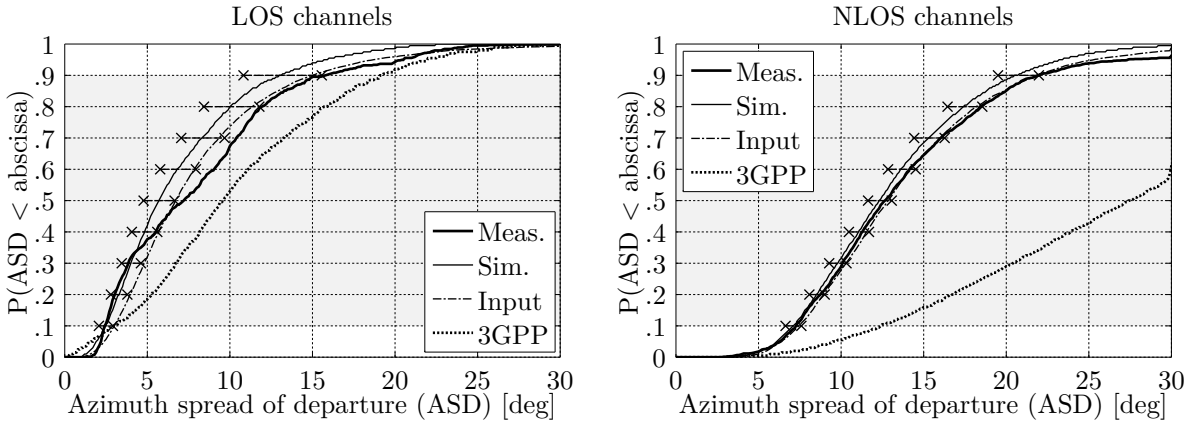

	LOS			10 - 90%	NLOS			10 - 90%
	μ	σ	μ [°]	Range [°]	μ	σ	μ [°]	Range [°]
Meas. Results	0.86	0.30	7.2	2.4 - 16	1.10	0.20	12.7	7.3 - 22
QuaDRiGa In	0.83	0.27	6.8	3.2 - 15	1.11	0.18	12.9	7.6 - 22
QuaDRiGa Out	0.75	0.28	5.7	2.5 - 13	1.09	0.18	12.4	7.1 - 21
3GPP-3D In	1.15	0.28	14.1	6.7 - 33	1.41	0.28	25.7	12 - 58
3GPP-3D Out	0.98	0.35	9.6	3.1 - 19	1.44	0.21	27.5	12 - 42

Figure 4.12: Azimuth spread of departure distributions in Dresden, Germany

4.3.5 Azimuth of Arrival Angular Spread

The results for the ASA are shown in Figure 4.13. The measurement results indicate relatively large values of up to 90° in both propagation conditions. Note here, that with an equal amount of power arriving from all directions, an RMS-ASA of 97.6° would be calculated. Values around 90° thus indicate that there is significant multipath scattering around the receiver and MPCs arrive from all directions.

In the LOS case, a significant portion of the multipath power must come from the opposite direction of the direct component in order to achieve such high angular spreads. Since the arrival angles are distributed on a sphere, arbitrary angular spreads are not possible, especially

if the KF is high and most of the power comes from one direction. Typical LOS-KF values range from 0 to 15 dB. Still, the measurements indicate a wide range for the ASA from 18° to 79°. This is only possible if there is a strong negative correlation between the KF and the ASA, *e.g.*, with a low KF, high ASDs are possible and vice versa. Indeed, results presented in Section 4.4 on Page 92 show a correlation coefficient $\rho_{\mathrm{KF,ASA}}$ of -0.85 for the measurements.

The iterative fitting of the channel model parameters further indicates that the true angular spread might even be 10° larger. This is an interesting observation since, in the model, there is a dependency of the maximal achievable angular spread on the KF (see Figure 2.4 on Page 25). For example, for a KF of 10 dB, it is only possible to obtain an ASA of 40°. The combined Rx-antenna patterns almost provide omni-directional coverage. Hence, it is unlikely that the antenna attenuates significant portions of the multipath power. Thus, the 10° offset after the fitting is most likely an effect caused by the maximal achievable angular spread in the model.

The measured NLOS channels have a slightly larger ASA ranging from 38° to 88°. The average ASA_{μ} is almost identical for the measurements, the model input (after iterative fitting), and the model output. However, the model output does not agree very well to the input for values above 70°. As for the LOS channels, this is due to the maximal achievable angular spread which is limited to roughly 100° for KF values below 0 dB. Since the correlation with the KF is almost zero for NLOS channels, only high ASA values are affected by the limit. Nevertheless, the distributions for the measured data and the model input agree almost perfectly. It might thus be better to use a different distribution function for the angular spreads that does not produce such high values that are subsequently truncated by the model.

As for the ASD, the results reported in [23] do not distinguish between LOS and NLOS propagation. An average ASD of 35.5° was reported. This seems reasonable for the LOS case, but the value is only half as big as the value obtained for the NLOS channels in the current evaluation. There is also a significant difference in the values calculated from the 3GPP-3D simulations in case of LOS propagation. The average input value of 64.6° gets reduced to 28.7° due to the angular mapping which leads to a reduction of the NLOS path power. This reduction does not happen for the NLOS channels.

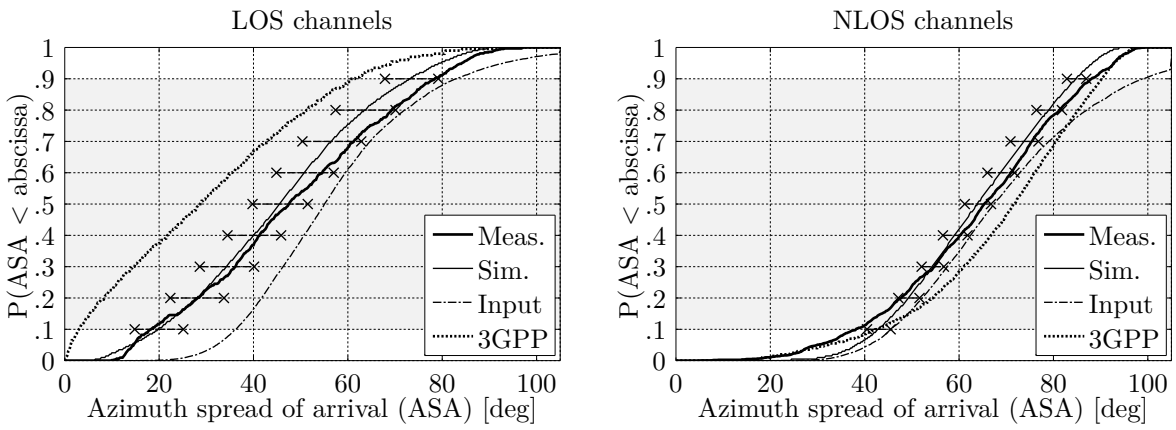

	LOS			10 - 90%	NLOS			10 - 90%
	μ	σ	μ [°]	Range [°]	μ	σ	μ [°]	Range [°]
Meas. Results	1.68	0.23	47.6	18 - 79	1.82	0.15	65.5	38 - 88
QuaDRiGa In	1.74	0.14	55.0	37 - 84	1.83	0.13	67.6	46 - 99
QuaDRiGa Out	1.66	0.24	45.7	20 - 73	1.81	0.11	64.0	43 - 85
3GPP-3D In	1.81	0.20	64.6	36 - 116	1.87	0.11	74.1	53 - 102
3GPP-3D Out	1.46	0.55	28.7	3.2 - 62	1.86	0.14	71.7	43 - 90

Figure 4.13: Azimuth spread of arrival distributions in Dresden, Germany

4.3.6 Elevation of Arrival Angular Spread

The results for the ESA are shown in figure 4.14. The measurements indicate relatively small values in both propagation conditions. The LOS channels have an average ESA of 7.7°. Typical values are in between 3.8 and 13°. The NLOS channels have a larger average value of 11° with a typical range from 6.8 to 17°. The values obtained by the iterative fitting of the model parameters are slightly larger. Results reported in [23] show a slightly larger ESA with average values around 15.5°. Those values were obtained from the same measurement data but with a different estimation method. The reason for this difference is unclear. Measurement results for the urban-macrocell scenario at 2.15 GHz and 24 m average BS height [131] show also a slightly larger elevation spreads around 15°.

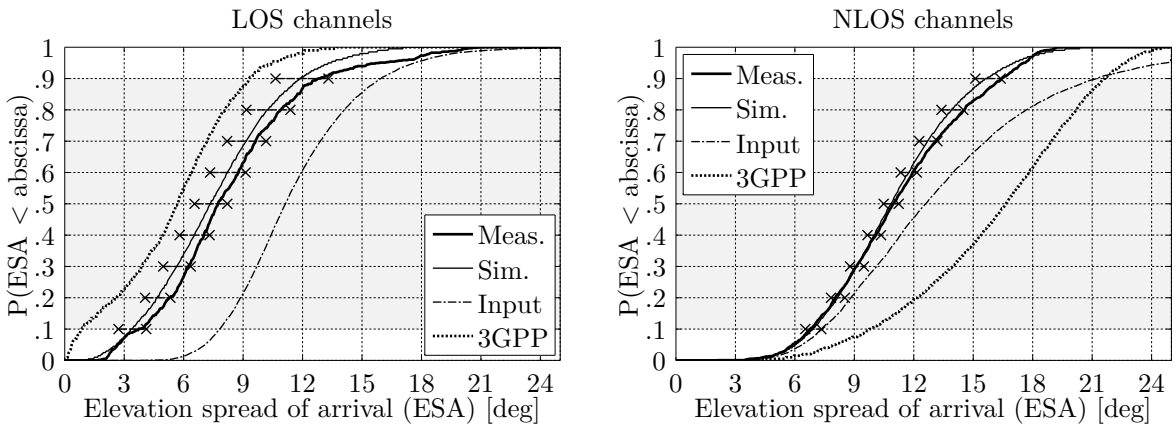

	LOS			10 - 90%	NLOS			10 - 90%
	μ	σ	μ [°]	Range [°]	μ	σ	μ [°]	Range [°]
Meas. Results	0.89	0.21	7.7	3.8 - 13	1.04	0.15	11.0	6.8 - 17
QuaDRiGa In	1.05	0.12	11.2	8.0 - 16	1.10	0.18	12.6	7.5 - 22
QuaDRiGa Out	0.86	0.22	7.4	3.4 - 12	1.04	0.14	10.9	6.9 - 16
3GPP-3D In	0.95	0.16	8.9	5.6 - 14	1.26	0.16	18.2	11 - 29
3GPP-3D Out	0.75	0.44	5.7	0.9 - 9.3	1.22	0.14	16.7	9.9 - 22

Figure 4.14: Elevation spread of arrival distributions in Dresden, Germany

4.3.7 Cross-Polarization Ratio

The results for the NLOS-XPR are shown in Figure 4.15. The presented results exclude the influence of the LOS component as discussed in Section 3.2.5 on Page 62. The results obtained from the LOS and NLOS channels show very similar results having values around 24 dB. This similarity makes sense since only NLOS paths were used for the evaluation. The high values indicate that multipath propagation does not alter the polarization of the scattered waves significantly. The new model uses a combination of linear transformations to obtain the polarization-coupling matrix (see Section 2.5.3, Page 36). This method seems to produce accurate results when measurements, model input and model output are compared. The input and output results for the 3GPP-3D model show some difference. The results are 4-5 dB larger compared to the model input. The reason might be the influence of the random components in the polarization coupling matrix (2.67).

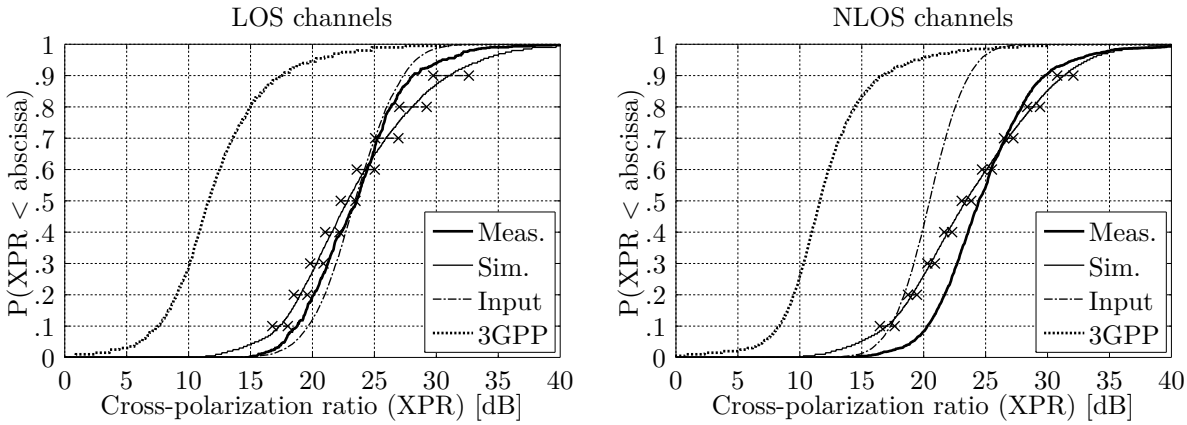

	LOS		NLOS	
	μ [dB]	σ [dB]	μ [dB]	σ [dB]
Meas. Results	23.6	3.9	24.5	4.2
QuaDRiGa In	23.5	3.0	20.5	2.5
QuaDRiGa Out	22.9	5.6	23.4	5.7
3GPP-3D In	8.0	4.0	7.0	3.0
3GPP-3D Out	11.8	5.5	11.8	5.1

Figure 4.15: Cross-Polarization Ratio in Dresden, Germany

4.4 Inter-Parameter Correlation Values

In this section, the inter-parameter correlations values for the LSPs are presented. There are six LSPs that could be extracted from the measurement data. Hence, there are in total 15 inter-parameter correlations values. This number gets doubled due to the separation into LOS and NLOS propagation. For each of the 30 parameters there is one value that is calculated from the measurements, one that serves as input to the model, and there are 16 values that are obtained at the model output when initializing the model several times. A compact presentation of the results for both the new model and the 3GPP-3D model is given in Figures 4.16 to 4.19.

The plots are structured as follows: The two LSPs and the propagation conditions for which the inter-parameter-correlation was evaluated is indicated on the left hand side of Figures 4.16 to 4.19. The gray bar, ranging from -1 to 1, presents the possible range of the parameter. A value below zeros indicates that the two LSPs are negatively correlated, *e.g.*, a low KF implies a high DS and vice-versa. A value above zero indicates that the LSPs are positively correlated, *e.g.*, a high ASA also leads to a high ESA. A downward pointing triangle in the top part of the bar indicates the value that was calculated from the measurements. An upward pointing triangle in the lower part of the bar indicates the value that was set at the input of the model. This value is the same as in Table 4.3 on Page 83. The dark shaded area then indicates the range of values that were calculated at the output of the model. The white dots in the bottom indicate the 16 individual values from each resimulation run. The vertical line shows the average of the 16 values. The width of the area, *i.e.*, the range from the beginning of the shaded area to the middle line and the range from the middle line to the end, is determined by the STD of the 16 values. Hence, the total width of the shaded area is twice the STD.

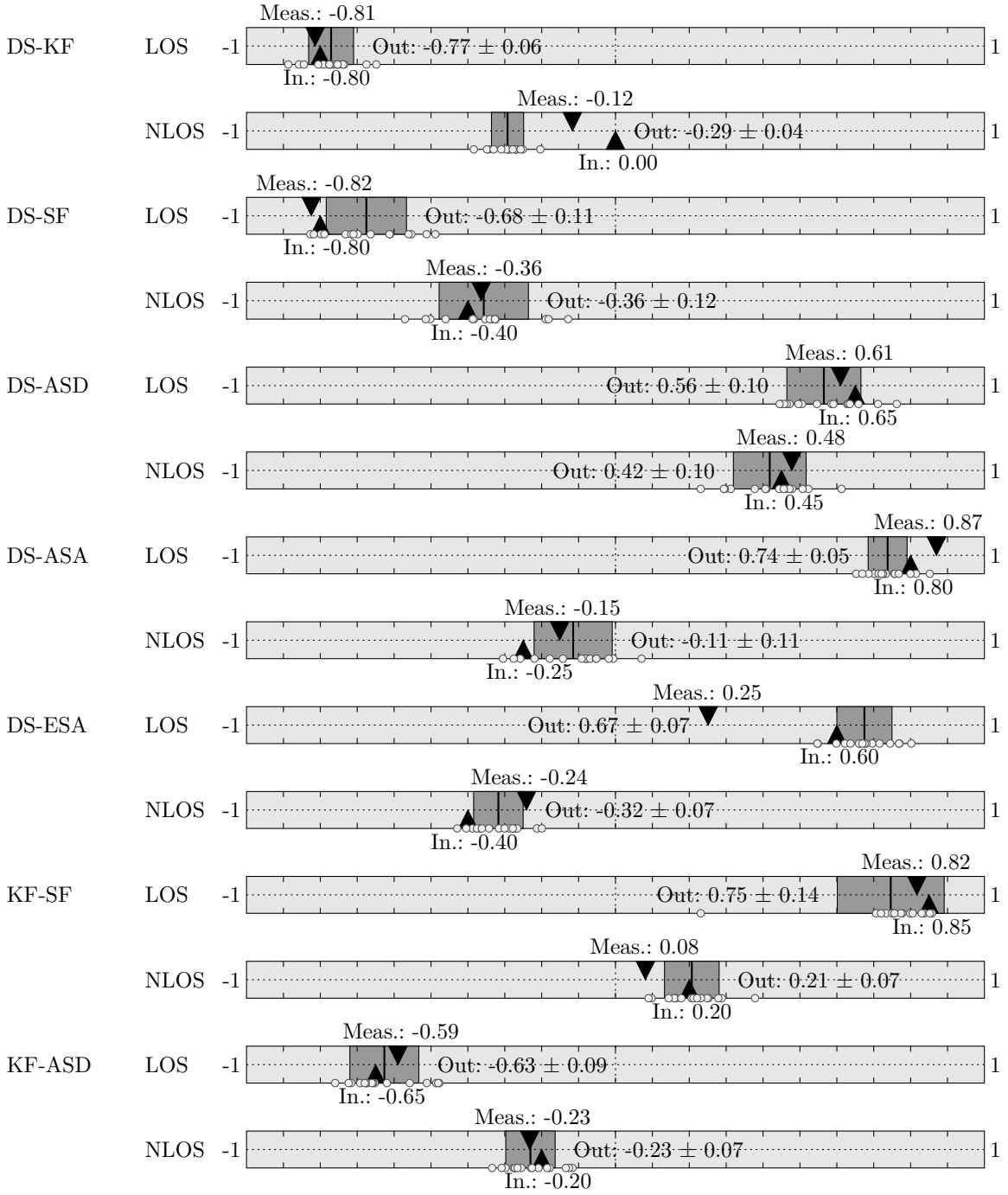

Figure 4.16: Inter-parameter correlation values in Dresden (part 1)

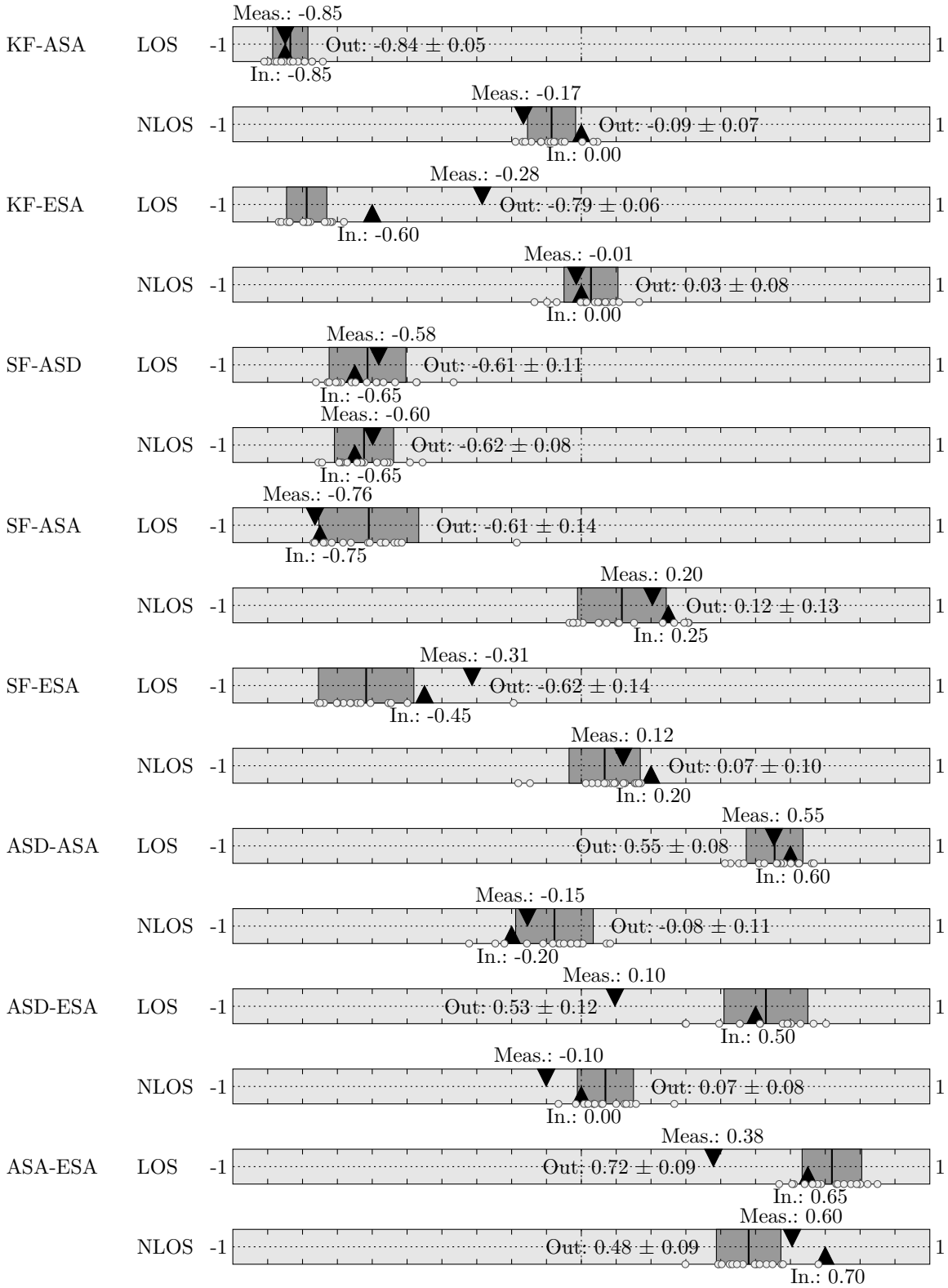

Figure 4.17: Inter-parameter correlation values in Dresden (part 2)

Discussion of the results The measurement results and the results obtained from the new model are shown on pages 93 and 94. In most of the cases, there is a good agreement between model and measurement. In case of LOS propagation, almost all parameters show high correlation values. The KF is highly correlated with the SF ($\rho_{\mathrm{KF,SF}} = 0.82$). This means that areas with an high overall power are dominated by the direct component. Subsequently, this leads to low values for the DS, the ASD, the ASA, and the ESA, all of which have a negative correlation coefficient with both the KF and the SF. At the same time, delay and angular spreads are positively correlated with each other.

In case of NLOS propagation, KF and SF are almost uncorrelated. The direct component has no significant effect on the channel statistics. Subsequently, the KF is not correlated with any other LSP ($|\rho| \leq 0.2$). The shadow fading shows negative correlation with the DS ($\rho_{\mathrm{DS,SF}} = -0.36$) and the ASD ($\rho_{\mathrm{SF,ASD}} = -0.6$) while DS and ASD are positively correlated ($\rho_{\mathrm{DS,ASD}} = 0.48$). This indicates that the scattering clusters are more spread out in areas with low received power which leads to longer propagation delays and a larger angular spread at the transmitter. Interestingly, the SF is positively correlated with the ASA ($\rho_{\mathrm{SF,ASA}} = 0.2$) and the ESA ($\rho_{\mathrm{SF,ESA}} = 0.12$). This indicates that, in NLOS areas with high power, the MPCs arrive at the receiver from all directions. However, the ASA and the ESA are slightly negatively correlated with the DS ($\rho \leq -0.15$). Hence, the paths must be clustered together in the delay domain since otherwise the DS would be increased as well. Thus, they are likely to be caused by local scattering close to the receiver. An implication of this is that there might be Keyhole effects in the channel, *e.g.*, when a single path is scattered multiple times within a street canyon.

The results can be summarized in the following way: *(1)* There are areas which are dominated by LOS propagation. They have the highest received power, a high KF, and short delay and angular spreads. *(2)* The NLOS areas have a negligible KF. They can be further classified in two ways: *(2a)* Areas which have increased values for the SF are often dominated by local scattering close to the receiver. In this case, values for the DS and the ASD are low while at the same time ASA and ESA are high. *(2b)* The areas with the lowest power are served by a few scattered MPCs. The values for the SF, the ASA and the ESA are low. However, the departure angular spread and the DS are increased.

Discussion of the 3GPP-3D results The results obtained from the 3GPP-3D model are shown on pages 96 and 97. The indicators for the measured values (downward facing triangle on the top) are identical to the ones in Figures 4.16 and 4.17, *i.e.*, they represent the results of the Dresden measurements. The input values of the model (upward facing triangle in the bottom) were taken from [49]. They are also listed in Table 4.3 on Page 83. A general observation is that the range of the output parameters after running the model 16 times is significantly smaller compared to the new model. This is due to the drop-based user placement (see Figure 4.5 for an illustration) and the simple time-evolution method used by the 3GPP-3D model. All LSPs stay constant within a drop, *i.e.*, they do not evolve over time. Subsequently, their correlation values also stay constant.

In case of LOS propagation, input and output values of the model do not agree in most of the cases. The values from [49] indicate that the KF shows no significant correlation with any other LSP. However, the measurements show the opposite. In addition, the angular mapping function together with a high-gain transmit antenna increases the KF values at the output of the model (see discussion on Page 87). Many MPCs are heavily attenuated by the antenna pattern at the transmitter. This leads to a very strong negative correlation of the KF with the DS, the ASD, the ASA, and the ESA (all $\rho \leq -0.8$). Those values do not relate in any way

to the input values of the model. For example, the ASD and the KF should be uncorrelated according to the model input. However, at the model output, a correlation coefficient of -0.75 is calculated. Subsequently, this also affects all the other correlation values, namely DS-ASD, DS-ASA, DS-ESA, ASD-ASA, ASD-ESA, and ASA-ESA, which show very high positive values ($\rho \geq 0.7$) independent of the model inputs.

In case of NLOS propagation, input and output values are in better agreement with some exceptions. Most of those exceptions occur for the ESA and the ASD. For example, ASD and the ESA should be uncorrelated but at the model output a coefficient of 0.72 is obtained. An explanation could be the very short decorrelation distance which is set to only 2-3 meters for both parameters. Hence, there is a very high fluctuation of the parameters even at short distances. This could alter the inter-parameter correlation properties at the output of the model when the maps are interpolated.

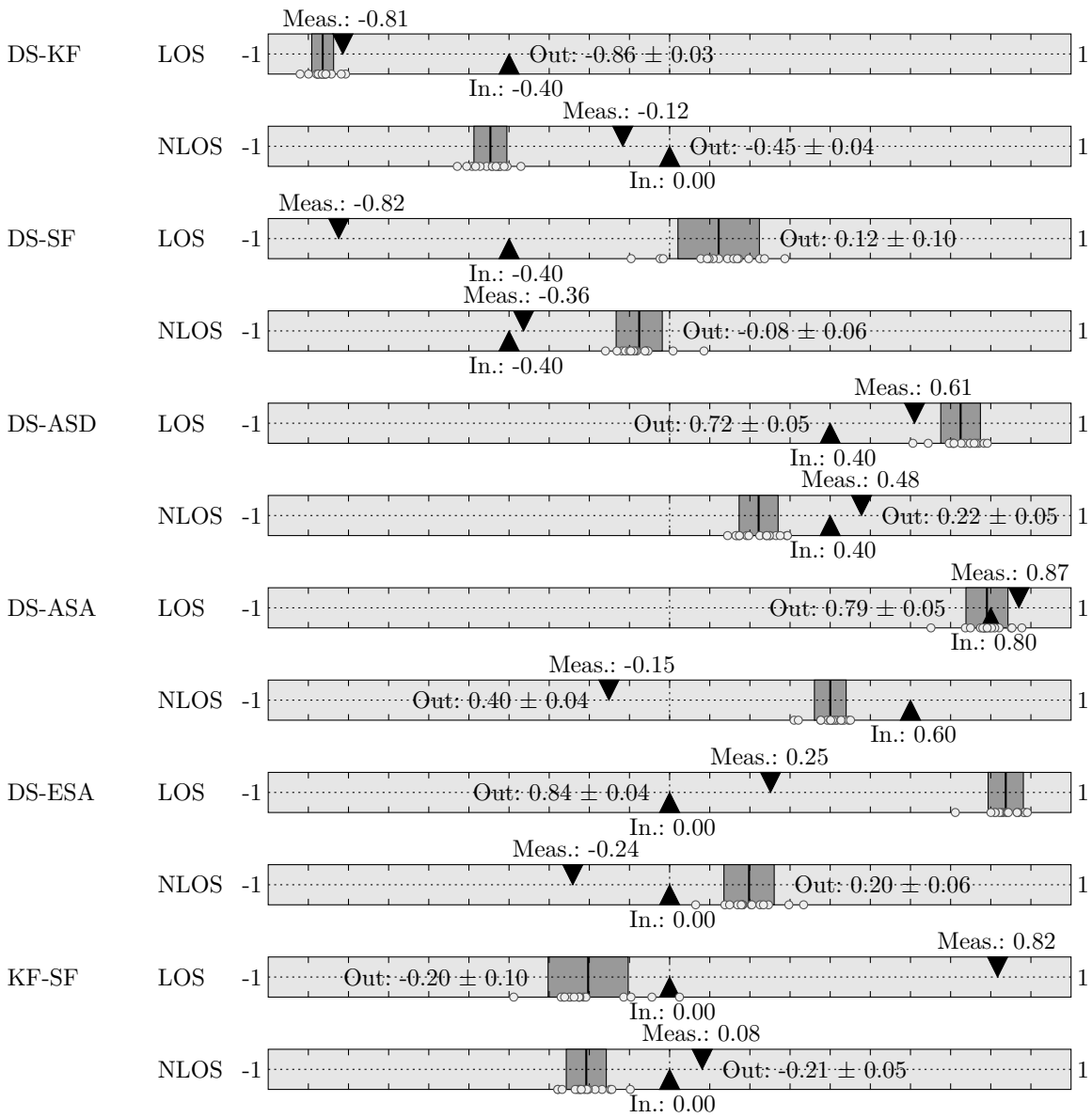

Figure 4.18: Inter-parameter correlation values extracted from the 3GPP-3D model (part 1)

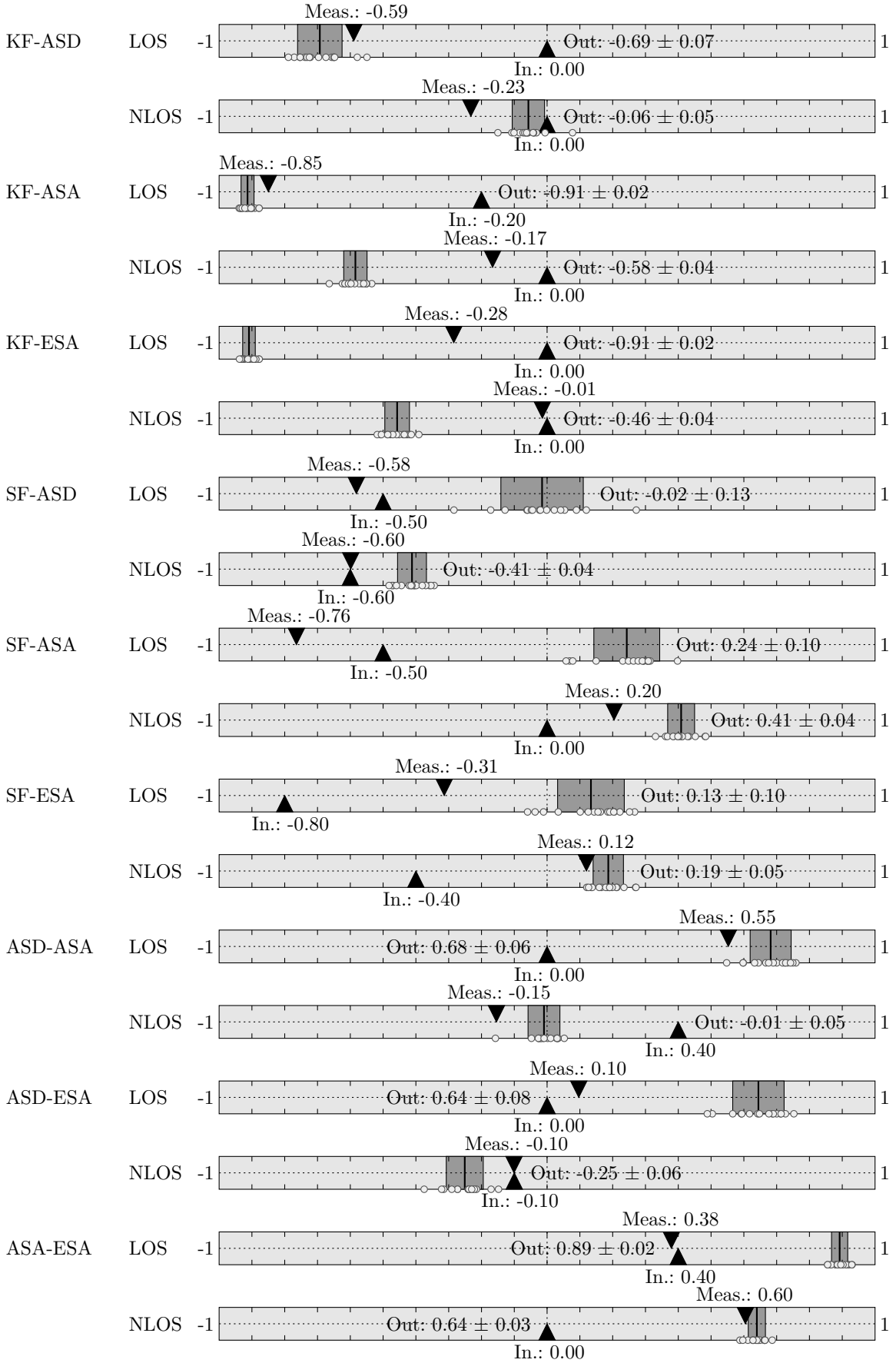

Figure 4.19: Inter-parameter correlation values extracted from the 3GPP-3D model (part 2)

4.5 Decorrelation Distances

The results for the decorrelation distances are presented in Figure 4.20. The analysis could only be done for the measurement data and the output of the new model. The 3GPP-3D model does not support time-evolution of the LSPs. Hence, it is not possible to obtain continuous samples of the parameters. However, this is required in order to estimate the decorrelation distances (see Section 3.2.6, Page 63). The results are presented in a similar way as the results for the inter-parameter correlation values. The gray bar depicts a range from 0 m to 400 m. A downward pointing triangle in the top part of the bar indicates the value that was calculated from the measurement data. An upward pointing triangle in the lower part of the bar indicates the value that was set at the input of the model (see Table 4.2 on Page 82). The dark shaded area indicates the range (twice the STD) of values at the output of the model. The vertical line shows the average of the 16 values that were obtained by running the model 16 times. The individual values are indicated by white dots in the bottom of the bar.

As described in Section 2.1 (Page 18), the channel model first generates the distance-dependent correlation by filtering and then applies the inter-parameter correlation by a multiplication with a matrix. However, if the inter-parameter correlation values are high, as it is the case for almost all LSPs in case of LOS propagation, the distance-dependent correlation will be distorted. For example, the KF is highly correlated with the SF ($\rho_{\mathrm{KF,SF}} \approx 0.85$). Thus, the autocorrelation maps for KF and SF will be very similar. As a consequence, the two decorrelation-distances are not independent of each other. For this reason, the model output values show a larger spread and are less accurate when comparing them with the input values. The same is true for ASA-LOS and ESA-LOS. The ASA has an input decorrelation-distance of 120 m while the ESA has only 80 m. Both parameters are correlated with $\rho_{\mathrm{ASA,ESA}} = 0.655$. As a result, the decorrelation-distance of the ASA at the model output gets reduced to 62 m.

In case of NLOS propagation, the output values agree better and have a smaller range. However, there are discrepancies for some values. The decorrelation distance for the DS was set to 70 m at the model input but an average value of 101 m was calculated at the output. A reason might be the correlation with the ASD ($\rho_{\mathrm{DS,ASD}} = 0.45$) which has a larger decorrelation distance of 150 m. This increases the decorrelation distance for the DS and, at the same time, the decorrelation distance of the ASD gets reduced to an average value of 122 m. The same effect is responsible for the increased SF values at the model output since the SF also has a high (negative) correlation with the ASD ($\rho_{\mathrm{SF,ASD}} = -0.75$). The KF, however, has no noteworthy correlation with any other LSP and thus it has the narrowest spread and agrees well with the model input.

Almost all results of the current evaluation show significantly larger decorrelation distances than those reported in [23] (see Table 4.2 for an overview). In case of LOS propagation, [23] also reported high values of 30 to 130 meters for the SF, the KF, and the DS. However, all decorrelation distances for the four angular spreads in both LOS and NLOS propagation are below 5 m and many of them are only 2 m. This would imply that in between two sampling points for the LSPs, which are at a distance of 3.3 m, the angular spreads are almost completely uncorrelated. The current analysis of the measurement data shows much higher values in between 35 m for ESA-LOS and 207 m for the ASD-LOS which implies a high consistency for the angular spreads, especially for the ASD. Larger values between 15 and 50 m are also common in the 3GPP-3D model [49], although they are not as large as in the current evaluation.

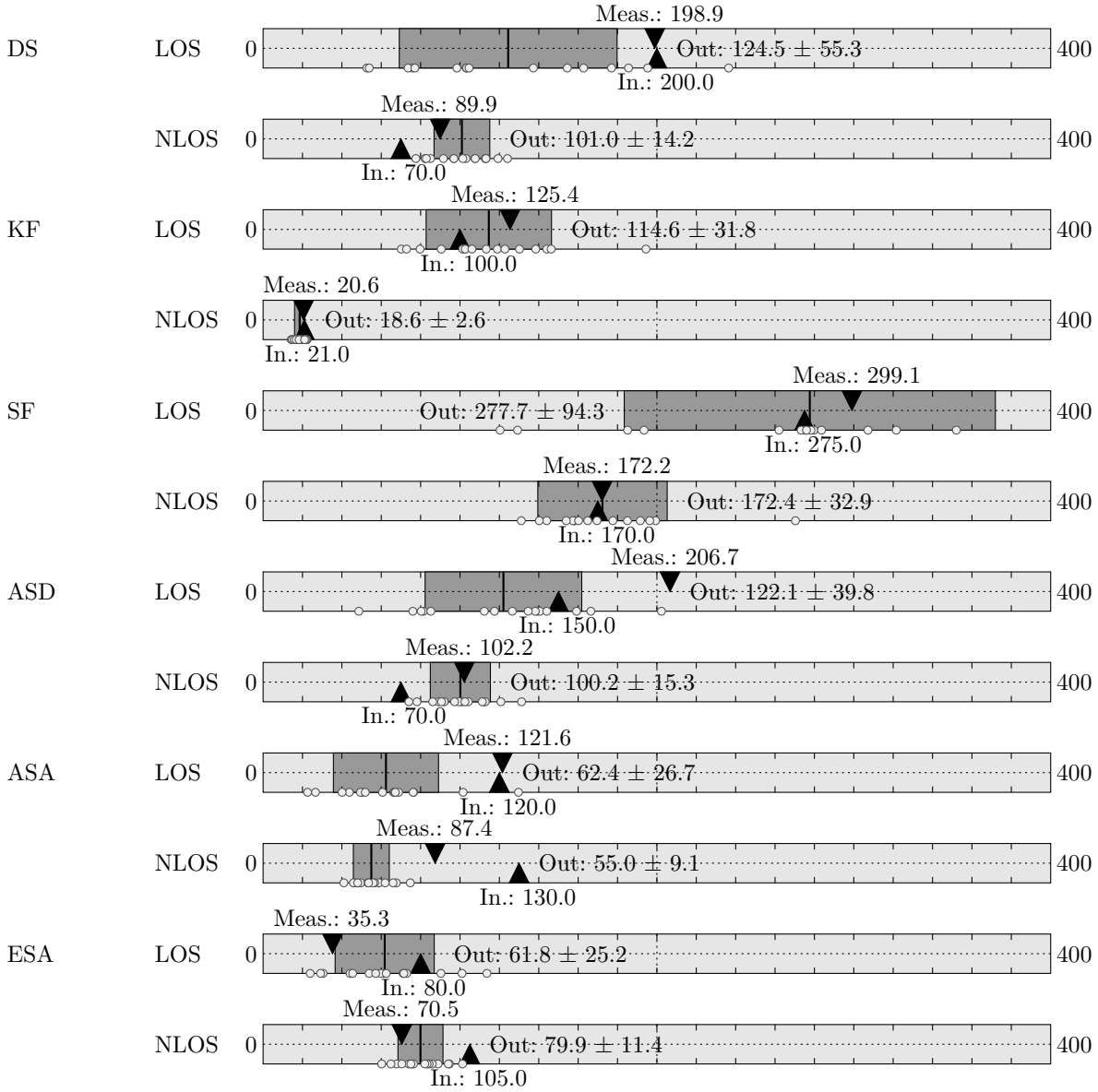

Figure 4.20: Decorrelation distances in Dresden, Germany in units of [m]

4.6 Performance Metrics

4.6.1 Signal to Noise Ratio

Figure 4.21 shows the results for the SNR in Dresden measurement campaign. In the data, the average thermal noise power was -90.2 dBm. With 36 dBm transmit power, the effective path gain must be at least -126.2 dB in order to achieve a SNR of more than 0 dB. The results (except for *Tap est.*) are therefore calculated using a link budget of 126.2 dB. Hence, the curves are equal to the ones for the effective path gain in Figure 4.6 but shifted by 126.2 dB. As for the LSPs, there is one empirical CDF that was calculated from the measurement data after preprocessing (thick solid line), *i.e.*, after extracting the MPCs from the raw data. A second CDF (thin solid line) was calculated from the output of the model. A third (dotted) line represents the results from the 3GPP-3D model.

The last (dashed) CDF was calculated directly after extracting the MPC from the raw measurement data. It represents the SNR that was obtained by dividing the sum power of the specular paths by the remaining power after subtracting the reconstructed CIR from the raw data (see Section 3.1.2 on Page 49 for details). Ideally, if there is only thermal noise, if the MPC extraction works perfectly, and if the assumptions on the link budget are correct, then this curve would match the predictions made by the model. However, this is only the case for NLOS. For SNR values above 10 dB the curves deviate.

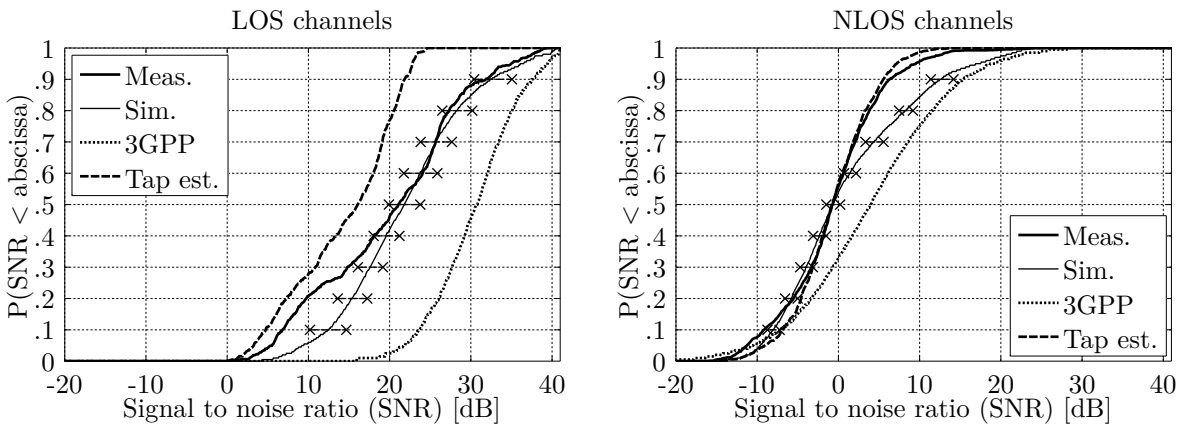

	LOS		NLOS	
	μ [dB]	σ [dB]	μ [dB]	σ [dB]
Meas. Results	21.1	9.1	-0.7	6.1
QuaDRiGa Out	21.8	7.9	-0.6	8.1
3GPP-3D Out	30.7	5.4	4.0	9.0
Tap Est.	16.1	6.4	-0.7	4.9

Figure 4.21: SNR distributions in Dresden, Germany

For the LOS channels, there is on average a 5 dB difference between the predicted SNR and the one estimated from the MPC extraction. Also, none of the of the estimates exceeds 23 dB SNR while in the prediction there are values up to 40 dB. This can have several reasons:

1. Some parts of the measured CIR cannot be identified as specular MPCs. Those are called *dense multipath components* [132]. They might contribute to the capacity of a MIMO link but they cannot be tracked by the preprocessing of the data, *i.e.*, they are too similar to noise to be identified as specular paths.

2. There can be calibration errors in the measurement system. Prior to the measurements, the frequency response (FR) of the measurement system at different adaptive gain control (AGC) levels was measured and calibrated out of the data. However, if there are calibration errors, the FR of a path is not flat. The MPC estimation then tries to approximate the FR of the system by additional *ghost* paths. However, it is not possible to approximate the system FR perfectly with a limited number of *ghost* paths. Hence, a part of the signal power will be identified as noise.

3. The dynamic range in the system is limited. In a pure LOS channel, the dynamic range in the CIR can exceed 60 dB, *i.e.*, the power of the direct component on a single MIMO sublink might be more than 60 dB higher compared to the thermal noise floor. In this case, the noise floor can increase due to limiting effects in the radio chain, *e.g.*, numeric noise in the analog to digital converters, nonlinearities in the amplifiers, clipping effects, *etc.*

4. Another effect might be caused by the antennas which do not have a linear FR at 100 MHz bandwidth. The antenna FR was not calibrated out of the data. Hence, this also causes *ghost* paths when the FR is approximated. In the resimulated channels, however, no frequency selectivity of the antenna response was assumed.

Mapping all the power in the raw CIR to specular components might result in a very high number of paths (several hundred), many of them being *ghosts* due to the nonlinear FR of the system and the antennas. However, this would cause exceptional long computing times for the MPC estimation and the data analysis. Therefore, the maximum number of paths was limited to 65. All the remaining power after detecting 65 paths is considered to be noise.

The relationship between the number of detected paths and the SNR is shown in Figure 4.22. The solid black curve shows the average number of paths that was detected at a given SNR. The gray shaded area represents the range in the results. The lower end of this area corresponds to the 10-percentile and the higher end to the 90-percentile of the CDF. As can be seen, the number of paths increases with increasing SNR and gets close to the limit above 10 dB SNR. This confirms the assumption that 65 specular paths cannot capture all the received power above the thermal noise floor - especially in the LOS channels. Between 1% and 10% of the signal power is treated as noise. The estimated SNR is therefore limited to values around 20 dB. However, since more than 90% of the power is included in the detected paths, no significant impact on the other results is expected.

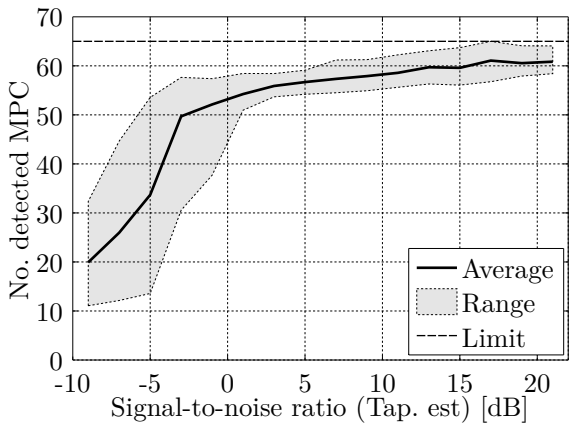

Figure 4.22: Number of detected paths vs. SNR in the Dresden measurement data

4.6.2 Single-User Capacity at a Fixed SNR

The results for the single-user capacity (see Section 3.3.1 on Page 65) are shown in Figure 4.23. In this evaluation, the capacity of the entire 16×58 MIMO channel matrix was evaluated at a fixed SNR of $\sigma = 10$ dB. Thus, the received power has been removed from the evaluation and only spatial propagation effects can have an influence on the capacity. The lower bound of the capacity in this case is the Keyhole capacity $C^{[\mathrm{KH}]}$, *i.e.*, the capacity with only one spatial degree of freedom. The upper bound $C^{[\mathrm{parallel}]}$ is reached when there are 16 parallel spatial data streams. Their values can be computed as

$$C^{[\mathrm{KH}]} = \log_2(1 + 10 \cdot 58) \approx 9.18 \text{ bps/Hz}, \tag{4.3}$$

$$C^{[\mathrm{parallel}]} = 16 \cdot \log_2(1 + 10/16 \cdot 58) \approx 83.51 \text{ bps/Hz}. \tag{4.4}$$

The LOS channels have an average capacity of 31.7 bps/Hz. 15% of those channels have a capacity below 20 bps/Hz which is roughly twice the Keyhole capacity, indicating that there are only two spatial degrees of freedom due to the two polarizations. Multipath scattering provides no additional capacity in this case, independent of the number of antennas. The LOS capacity is predicted well by the new channel model - having only a 1.1 bps/Hz higher value compared to the measurements. The 3GPP-3D model also predicts the capacity well for LOS propagation.

In case of NLOS propagation, the measured channels have an average capacity of 46.3 bps/Hz. The new channels model predicts a capacity of 48.5 bps/Hz. As for the LOS channels, this value is roughly 5% larger compared to the measurements. The common Rayleigh i.i.d. model, which uses random coefficients in the MIMO matrix, predicts a capacity of 80.2 bps/Hz. This value does not agree with the measurement results. Hence, this model might not be suitable for the current setup. The 3GPP-3D model predicts 56.6 bps/Hz for NLOS channels. This larger value can be explained by the larger ASD and ESA which leads to less correlation in the MIMO matrix compared to the new model.

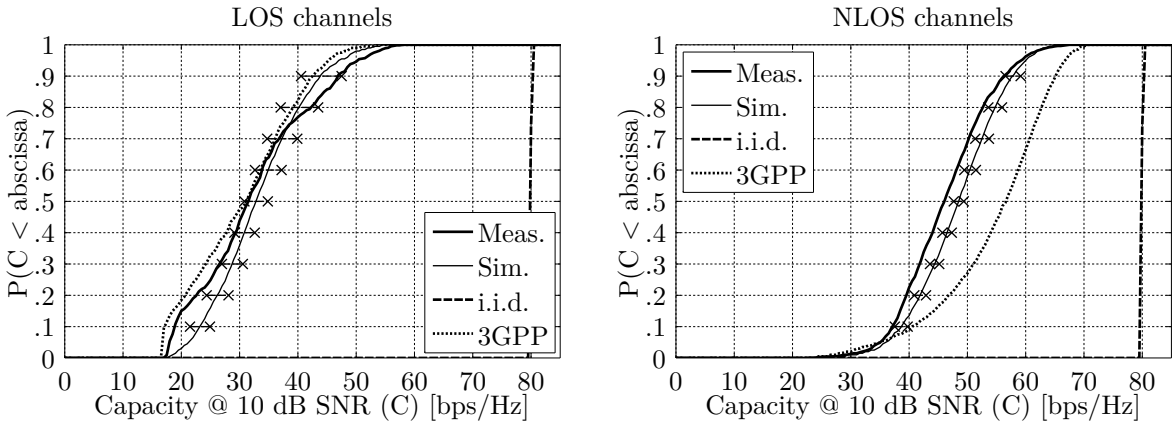

	LOS		NLOS	
	μ [dB]	σ [dB]	μ [dB]	σ [dB]
Meas. Results	31.7	10.0	46.3	7.5
QuaDRiGa Out	32.8	7.9	48.5	7.3
3GPP-3D Out	31.1	9.3	56.6	9.6
Rayleigh i.i.d.	80.2	0.1	80.2	0.1

Figure 4.23: Capacity distributions in Dresden, Germany

The results indicate that the capacity improvement by using single-link MIMO in an outdoor setup is limited. The highest gain can be achieved by using two polarizations which guarantees at least two spatial degrees of freedom. The strong fluctuations also emphasize the importance of adjusting the transmission mode to the channel rank [133] and applying multiuser MIMO techniques [56].

4.6.3 Multi-User Singular Value Spread

Results for the multi-user SV spread are presented in Figure 4.24. The SV spread is a measure of the orthogonality of user signals. The lower the values of this metric is the less correlation there is in the user channel vectors. A detailed introduction and discussion of this metric can be found in Section 3.3.3 on Page 66. Here, the results from the measurements in Dresden, Germany are presented and discussed.

One important aspect is the selection of the antennas that are used to calculate this metric. The array antennas that were used during the measurements have many more elements then in realistic deployments. However, in a multiuser MIMO setup, the combined number of receive antennas of all MTs is usually smaller or equal to the number of transmit antennas at the BS. The transmit array antenna has only 16 elements and, therefore, at most 16 spatial data streams can be supported. To obtain more realistic results, a subset of the receive antenna elements at the MTs has to be used. The evaluations are done for two different configurations.

1. ***Multi-antenna receivers***: Each user is equipped with four receive antennas. The chosen elements are the ones with the numbers 1 and 3 for vertical polarization, and 6 and 8 for horizontal polarization (see Figure 4.3 on page 77 for details). Then, four terminals are selected as described in Section 3.3.3. The compound channel matrix has a total of 16 transmit antennas and 16 receive antennas. This configuration can serve four spatial streams to each user if there is sufficient multipath propagation.

2. ***Single-antenna receivers***: Each user is equipped with a single receive antenna, as suggested by [122]. At the BS, only the eight vertically polarized antenna elements are used. At the terminal, the vertically polarized element with the highest received power is chosen from the sides of the cube (*i.e.*, from elements 1, 2, 3 or 4 in Figure 4.24). Then, eight terminals are selected. The compound channel matrix has a total of 8 transmit antennas and 8 receive antennas. This configuration attempts to serve one spatial data stream per user, provided that they are separated well in the spatial domain.

In the ***multi-antenna configuration*** each terminal can receive up to four data streams. However, in many cases, especially for LOS propagation, the compound 16×16 channel matrix becomes near-singular when there is too little multipath scattering to support four data streams per user. If all 16 channel vectors are orthogonal to each other, the channel matrix would have 16 identical singular values and the SV spread would be 0 dB. The median SV spread in the measured channels 22.9 dB which indicates that there is significant correlation between the user signals.

The Rayleigh i.i.d. model (see Section 1.2.2) uses random complex-valued entries in the MIMO channel matrix. The same path gain model as in the new channel model is assumed. However, this has little relevance for the SV spread since it affects all singular values in the same way. The predicted SV spread is 15.9 dB, 7 dB less than in the measurements. Clearly, this simple model is not adequate the correctly model the interdependence of the user signals in a multi-user channel. The 3GPP-3D model predicts a SV spread of 19.2 dB, 3.7 dB less than in the measurements.

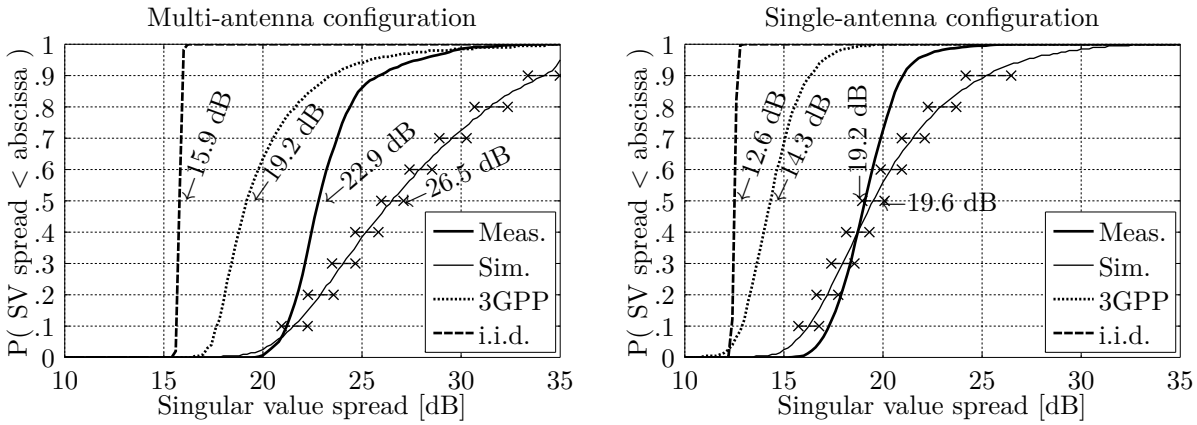

Figure 4.24: Multi-user singular value spread in Dresden, Germany

There might be two reasons for this difference. First, the larger angular spread compared to the measurements increase the capacity in the single-link MIMO channels. Hence, there is less correlation in the channel vectors and the SV spread gets lowered. Second, the channel vectors of different users are uncorrelated in the model while in the measurements and in the new model spatial correlation is included. The new channel model predicts a median SV spread of 26.5 dB, 3.6 dB more compared to the measurements. It seems that in the new model, there is more correlation between coefficients of the 4×16 the MIMO matrices of the individual links between the BS and the four MTs. This could be caused by the compact antenna configuration used at the MTs. The cube antenna, which was used for the capacity evaluation, has a diameter of only 5 cm (0.42 λ). The two polarizations can always support two data streams. However, a third and a fourth stream cannot be supported well and the SV spread increases.

In the ***single-antenna configuration*** each terminal has only one receive antenna and can receive only one spatial data stream. Unlike in the multi-antenna case, the antenna spacing at the MT has no influence on the results. However, if the terminals are not well separated, *i.e.*, if their mutual channel vectors (which contain the coefficients of the eight transmit antennas) are not orthogonal, the SV spread will increase. The results for the measured data show an average SV spread of 19.2 dB. The Rayleigh i.i.d. model predicts 12.6 dB in this case. These generally lower values compared to the multi-antenna case are caused by the smaller matrix size (8×8 instead 16×16). Nevertheless, the SV spread obtained from the measured channels is 6.6 dB larger compared to the i.i.d. channels. This indicates that the measured channel vectors are not orthogonal between the users, especially if the users are chosen randomly as it was done for the current evaluation. The predictions made by the 3GPP-3D model (14.3 dB) are closer to the results obtained from the i.i.d. model. If the users are close together, their small-scale fading channels are uncorrelated in the model. However, this is not the case in the measurements. The new model places the MTs on the same tracks as in the measurements. Hence, spatial correlation is included. The predictions made by this approach are only 0.4 dB larger than in the measured data, indicating a good match between model and reality.

4.6.4 Dirty-Paper Coding Capacity

While the SV spread gives an indication on how well users can be separated in the spatial domain, it does not provide a measure of the overall performance, *i.e.*, the achievable data-rate in a multiuser channel. For this, a different metric, the DPC capacity, is used. An introduction to this metric is given in Section 3.3.4. Here, the results obtained from the Dresden measurements are presented. The same antenna configuration and user selection methods as for the SV spread are used. The results are presented for two normalizations of the compound channel matrix. First, the matrix is normalized according to (3.62) where a fixed SNR of $\sigma = 10$ dB gets divided by the number of BS antennas. This has the advantage that the influence of the PG is removed from the results and only spatial propagation characteristics, *i.e.*, multipath and polarization effects, are considered. Second, the power is not removed and the capacities are calculated at their actual SNR.

In the ***Dresden multi-antenna configuration***, one BS with 16 transmit antennas serves four terminals, each having four receive antennas. The results are shown in Figure 4.25. The top part of the Figure shows the evaluation results for a fixed SNR of $\sigma = 10$ dB. The bottom part shows the same evaluation using the actual SNR of the channel. The SNR is defined as the average channel power divided by the average noise power per MIMO sublink. The capacity formulas, however, assume that the SNR is divided by the number of transmit antennas. Therefore, with 16 transmit antennas, $\sigma = 10$ dB corresponds to an SNR of -2 dB. The left part of the Figure shows the empirical cumulative distribution functions of the results while the right part shows the dependency of the capacity on the SNR.

For the fixed σ, it is possible to define some bounds of the capacity that help discussing the performance of the model. The lower bound is reached when the compound channel matrix has only one spatial degree of freedom, *e.g.*, all users are at the same position which can only be served by a keyhole channel. The BS can send a narrow beam towards this position. The users then have to share the radio resources either in the time or frequency domain. The resulting capacity in this case (3.71) is 9.3 bps/Hz. Such low values cannot be found in the evaluation results. In a second scenario, the users can be separated in the spatial domain, but each user can only receive one data stream. The compound channel matrix is composed of four keyhole matrices, one for each user. The BS can form narrow beams towards the users to maximize the received power. The resulting capacity (3.73) is 29.3 bps/Hz. This limit is shown in Figure 4.24 as "4 single-stream users". The upper bound is reached when each user can receive four orthogonal data streams and all channel vectors are orthogonal to each other. The resulting capacity (3.73) is 55.4 bps/Hz.

The median DPC capacity in the measured channels is 33.9 bps/Hz. It seems that the users can be relatively well separated but cannot be served with four data streams. However, at least two data streams can be supported due to the two polarizations which lead to higher capacity values compared to the single-stream users. When i.i.d. channels are used, the predicted capacity is 44.1 bps/Hz. This is in line with the low values for the SV spread. The uncorrelated channel vectors in this model indicate a much higher capacity compared to the real world scenarios. The predictions from the 3GPP-3D model (41.2 bps/Hz) are 21% lager compared to the measurements. This is probably caused by the larger angular spreads and the missing spatial consistency. The predictions from the new channel model are roughly 11% larger than in the measurements (37.5 bps/Hz).

The top, right part of Figure 4.25 shows the DPC capacity as a function of the SNR. The thick black curve shows the average value for the measurement data. The surrounding gray area shows the range where the lower end corresponds to the 10-percentile and the higher end to

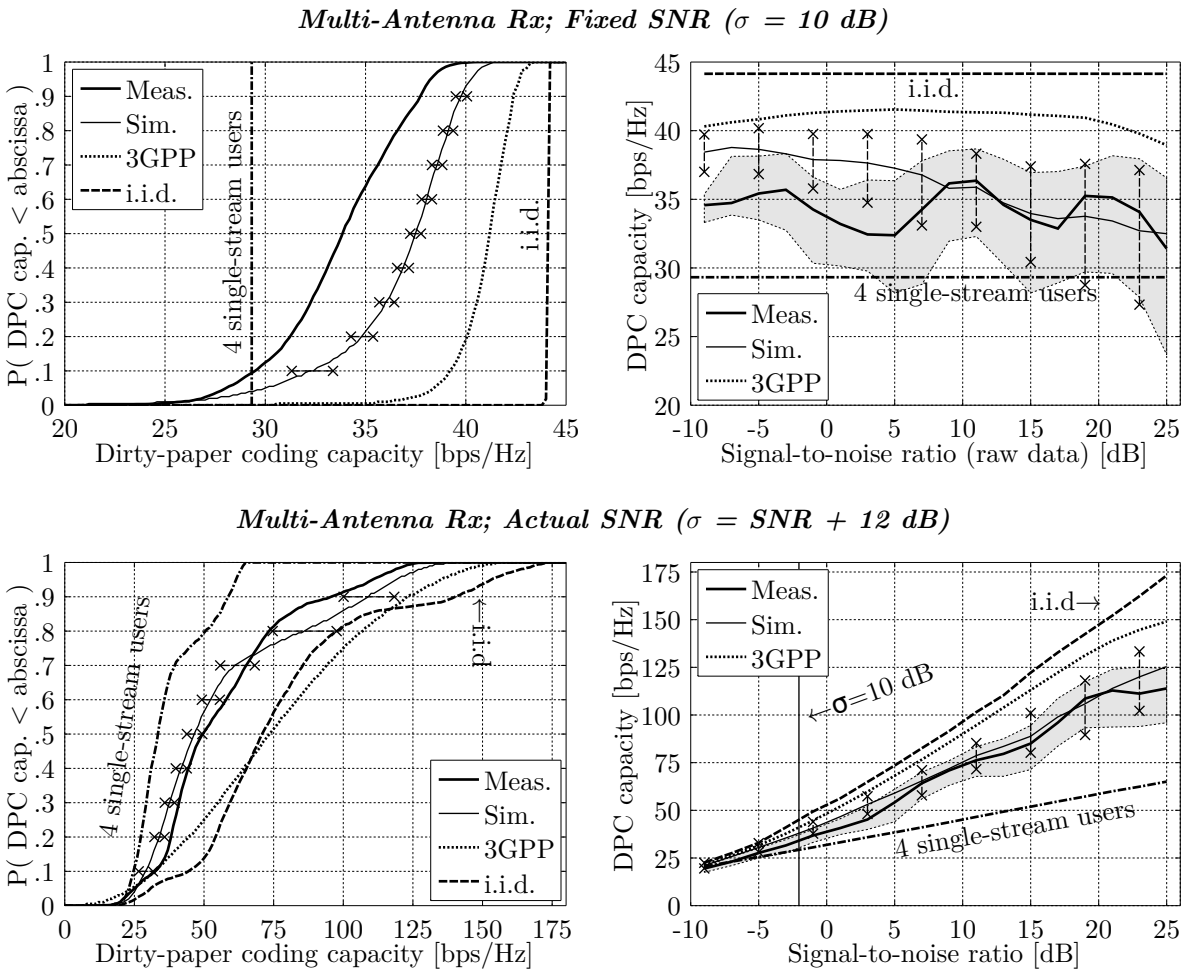

Figure 4.25: DPC capacity for the multi-antenna configuration in Dresden, Germany. The BS has 16 antennas that serve four 4-antenna users in parallel. Top left: The capacity distribution at a fixed SNR. Top right: The dependency of the capacity (calculated at a fixed SNR) on the real SNR in the channel. Bottom left: The capacity distribution at the real SNR in the channel. Bottom right: The dependency of the capacity (calculated at the real SNR) on the real SNR in the channel.

the 90-percentile. The thin line shows the average obtained by the model. Here, the errorbars indicate the range. The evaluation SNR in (3.62) was always set to $\sigma = 10$ dB, independent from the SNR in the data. The higher capacity values that are predicted by the channel model happen mostly at low SNR (SNR < 10 dB). This might be due to the NLOS propagation where there are more MPCs observable in the model. There is a trend towards a lower DPC capacity at higher SNR in the channel model. This is not visible in the measurement results.

The two lower sub-figures show the results at the real SNR, *i.e.*, the received power was not normalized out of the data before calculating the capacity[1]. The figure on the left shows the CDFs of the capacities of the measured channels (thick line), the results from the new model (thin line), the i.i.d. channels (thick, dashed line), the 3GPP-3D model (dotted line) and the capacity that could be achieved with four users that can only receive a single spatial data stream.

There are significant gains due to spatial multiplexing and multiuser MIMO. The median ca-

[1]The results depend on the received power and the spatial propagation characteristics. Since there is a power difference between measurements and simulation for the BS2-NLOS channels due to two high buildings blocking the LOS very close to the transmitter, BS2 was excluded from this evaluation. See discussion on page 84 for more details.

pacity in the measured data is 50.2 bps/Hz. The Rayleigh i.i.d. model and the 3GPP-3D model overestimate the gains by predicting 72 bps/Hz, an increase of more than 40% compared to the measurement results. In the i.i.d. model this is caused by the well-conditioned channel matrix due to the random channel coefficients. In the 3GPP-3D model there is an additional increase caused by the higher PG values. There are at least 3 dB more power in the (NLOS) channel coefficients generated by this model (see Section 4.3.1). This leads to an additional increase of the capacity results. In order to obtain correct performance estimates, it is essential to correctly model the PG in the propagation scenario. The new channel model provides more accurate results by predicting 46.5 bps/Hz, 7% less compared to the measured channels. However, the PG coefficients were adjusted to match the measurements. Hence, a better capacity prediction can be expected.

The same evaluation was done for the ***single-antenna configuration***. The results are depicted in Figure 4.26. At a fixed SNR $\sigma = 10$ dB, the lower bound (3.71) of the capacity is 6.3 bps/Hz. As for the multi-antenna case, such values could not be observed in the measurements. The upper bound (3.73) is 27.7 bps/Hz. This value can be reached when the users have orthogonal

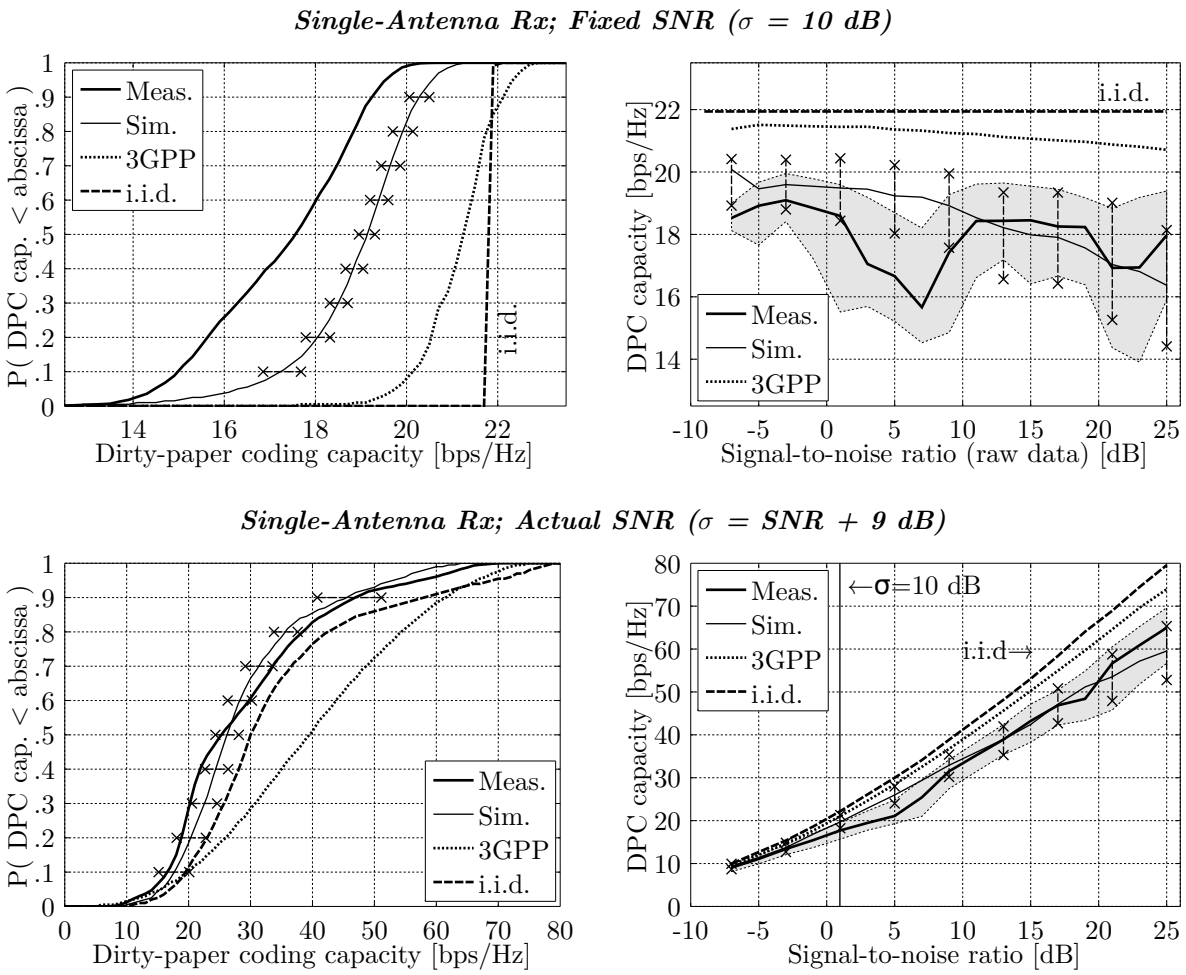

Figure 4.26: DPC capacity for the single-antenna configuration in Dresden, Germany. The BS has eight antennas that serve eight users in parallel. Top left: The capacity distribution at a fixed SNR. Top right: The dependency of the capacity (calculated at a fixed SNR) on the real SNR in the channel. Bottom left: The capacity distribution at the real SNR in the channel. Bottom right: The dependency of the capacity (calculated at the real SNR) on the real SNR in the channel.

channel vectors. The median (measured) DPC capacity at $\sigma = 10$ dB is 17.7 bps/Hz. The new channel model predicts 19.1 bps/Hz in this case, 8% more than in the measurements. The 3GPP-3D model predicts 21.2 bps/Hz and the i.i.d. capacity is 21.9 bps/Hz which corresponds to an error of 20% and 24%, respectively. Hence, the new model is able to significantly improve the performance predictions.

When the real SNR is included, a capacity of 25.8 bps/Hz is calculated from the measured channels. The new model predicts 26.2 bps/Hz in this case (2% error). This prediction is better than for the fixed-SNR evaluation. This is probably caused by a lower average PG in the model that leads to a slightly lower SNR and, thus, to lower capacities. The predicted capacity with i.i.d. channels, using the same path-gain model as for the new channel model, is 30.5 bps/Hz which is 18% more compared to the measured data. Again, the 6% improvement compared to the fixed-SNR evaluation might be caused by the PG model which is identical to the one from the new channel model and thus also matches the measurements. The largest prediction error can be seen in the results obtained from the 3GPP-3D model. Here, the effects from the missing spatial correlation and the increased receive power due to the increased PG compared to the measurements add up which leads to a 53% higher capacity prediction compared to the measurements.

One of the main advantages of geometry-based stochastic channel models is their scalability. The antenna configuration can be changed while the propagation characteristics of the environment are kept fixed. This can be used to find the ideal configuration of a communication system without the need for expensive prototypes and measurements. However, the scalability has not been confirmed yet. Therefore, two additional evaluation results are presented. First, the same single-antenna configuration as above is studied but with a varying number of users. Second, the number of users is kept fixed and the number of antenna elements at the BS is increased. Both cases are important to evaluate so-called massive MIMO systems that use a large number of antennas at the BS to serve a relatively small number of terminals.

The results for the ***varying number of users*** are presented in Tables 4.4 (fixed SNR) and 4.5 (real SNR). The tables compare five cases: the results from the measurements, the results from the new channel model (QuaDRiGa), the 3GPP-3D model, the Rayleigh i.i.d. model, and the capacity for orthogonal user channels. The latter values describe the upper bound of the capacity at a fixed SNR. They were calculated using (3.73). The relative error compared to the measurement results is shown in the row marked as "err. (%)". The PG model used for the new model (QuaDRiGa), the Rayleigh i.i.d., and orthogonal channels was matched to the measurements. The 3GPP-3D model uses the default UMa PG model from [49] which explains why the 3GPP-3D capacity exceeds the capacity of orthogonal channels. However, only the results in Table 4.5 are affected by this.

Table 4.4: DPC capacity in units of [bps/Hz] in Dresden for a varying number of users at $\sigma = 10$ dB

No. users		1	2	3	4	5	6	7	8
Meas. Results	median	6.1	9.8	12.0	13.7	15.0	16.0	16.9	17.7
QuaDRiGa	median	6.2	10.1	12.9	14.9	16.4	17.5	18.4	19.1
	err. (%)	*2.5*	*3.5*	*7.2*	*8.8*	*9.9*	*9.5*	*9.2*	*8.4*
3GPP-3D	median	6.3	10.4	13.5	15.9	17.7	19.1	20.3	21.2
	err. (%)	*4.0*	*6.1*	*11.9*	*15.5*	*18.5*	*19.6*	*20.3*	*20.0*
Rayleigh i.i.d.	median	6.3	10.4	13.5	16.1	18.1	19.7	20.9	21.9
	err. (%)	*3.1*	*5.8*	*12.4*	*17.0*	*20.9*	*22.9*	*24.2*	*24.3*
Orthogonal	median	6.3	10.7	14.4	17.6	20.4	23.0	25.4	27.7
	err. (%)	*4.6*	*9.5*	*19.3*	*27.9*	*36.7*	*44.0*	*50.9*	*56.8*

Table 4.5: DPC capacity in units of [bps/Hz] in Dresden for a varying number of users at the actual SNR

No. users		1	2	3	4	5	6	7	8
Meas. Results	median	7.9	13.1	16.8	19.4	21.1	23.7	24.0	25.8
QuaDRiGa	median	7.5	12.7	16.6	19.6	22.0	23.7	25.1	26.2
	err. (%)	*-4.6*	*-3.7*	*-1.4*	*1.3*	*4.1*	*0.3*	*4.3*	*1.7*
3GPP-3D	median	9.1	16.0	21.9	26.8	31.1	34.4	37.4	39.5
	err. (%)	*15.7*	*21.6*	*30.1*	*38.3*	*47.4*	*45.4*	*55.7*	*53.4*
Rayleigh i.i.d.	median	7.7	13.0	17.5	21.2	24.3	26.9	29.0	30.5
	err. (%)	*-3.0*	*-0.9*	*4.1*	*9.5*	*15.2*	*13.7*	*20.6*	*18.4*
Orthogonal	median	7.8	13.5	18.4	22.9	27.2	30.9	34.6	38.0
	err. (%)	*-1.9*	*2.6*	*9.5*	*18.4*	*28.7*	*30.8*	*43.8*	*47.5*

For a single user, all values are in good agreement. When the number of users increases, multiplexing gains from adding new users decrease. The capacity gains for more than four users are below 1 bps/Hz per user. The predictions from the new model agree well with the measurements, having errors below 10%. However, the other channel models tend to overestimate the capacity.

In the next step, the ***number of antennas is increased*** while the number users is kept fixed at $n_u = 4$. This evaluation can only be done in the channel model by replacing the transmit antenna with a synthetic array antenna. This was done by modeling a single patch element by

$$F^{[\theta]}(\theta, \phi) = 1.54 \cdot \sqrt{0.0015 + 0.9985 \cdot (\cos\theta)^{2.6} \cdot \exp\left(-1.23 \cdot \phi^2\right)} \tag{4.5}$$

The parameters (1.54, 0.0015, -1.23 and 2.6) were found by fitting the synthetic pattern to the ones from the anechoic chamber measurements. The synthetic pattern has an azimuth FWHM beam width of 87° and an elevation beam width of 81°. The front-to-back ratio is 28.2 dB. The gain of the single element is 3.75 dBi. This value already includes the attenuation caused by the switch, the power divider and the cables. Then, three array antenna configurations are considered for the evaluation of the DPC capacity:

1. The 32 patch elements are arranged in the same way as for the measurements, *i.e.*, they are arranged in a 2-D planar ULA with 62.5 mm element spacing. The elements in elevation direction are coupled by power dividers to reduce the elevation FWHM to 23° (see Section 4.1). Thus, there are only 8 effective antenna elements with a gain of 9.75 dBi. The transmit power per element is set to 36 dBm, the noise floor is -90.2 dBm.

2. The same configuration as in case (1.) is used. However, the elements are not coupled by power dividers. Thus, the array has 32 elements with 3.75 dBi gain per element. The transmit power per element is set to 30 dBm to keep the sum-power constant.

3. The number of rows and columns in the planar array is doubled. Thus, there are now 16 columns and 8 rows. The total number of elements is 128, and the transmit power per element is reduced to 24 dBm.

Figure 4.27 and Table 4.6 present the results for the DPC capacity. The error percentages refer to the results from the new channel model. After replacing the measured antenna patterns with the synthetic ones, only minimal differences can be found when comparing the results for the capacity at $\sigma = 10$ dB (four users). The small-scale-fading (SSF) part of the model is not affected by the antenna. When the actual SNR of the channel is used, the predicted capacities from the models are roughly 0.7 bps/Hz smaller compared to the results from Table 4.5. The synthetic antenna patterns seem to lower the radiated power which might explain this observation.

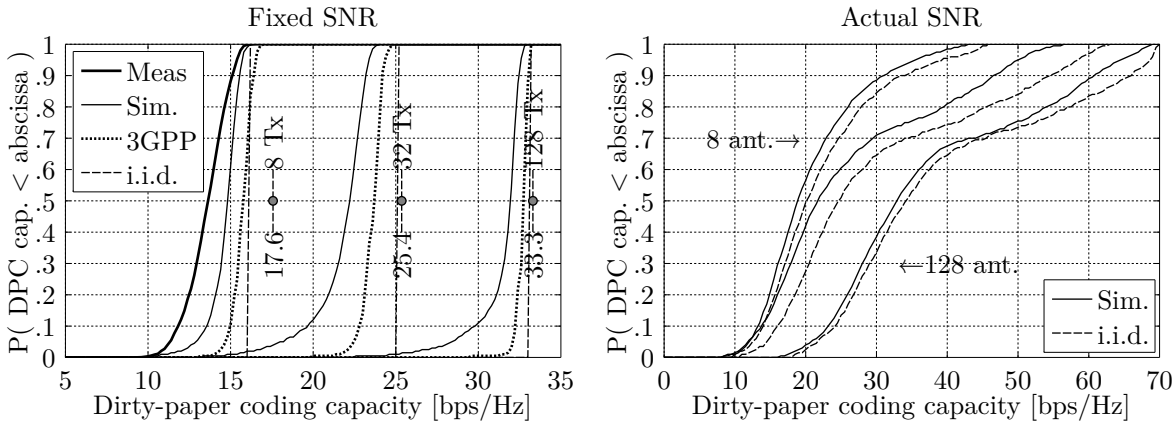

Figure 4.27: DPC capacity for different numbers of transmit antennas in Dresden, Germany. Left: The capacity distribution at a fixed SNR. The gray dots indicate the capacity for four users with orthogonal channel vectors. Right: The capacity distribution at the real SNR in the channel.

Table 4.6: DPC capacity prediction for different numbers of Tx-Antennas in units of [bps/Hz]

		Fixed SNR			Actual SNR		
No. Tx Antennas		8	32	128	8	32	128
Meas. Results	median	13.7	*N/A*	*N/A*	19.4	*N/A*	*N/A*
QuaDRiGa	median	14.8	22.2	31.9	18.9	21.7	33.0
3GPP-3D	median	15.8	23.6	32.7	26.2	29.1	40.6
	err. (%)	*6.3*	*6.5*	*2.3*	*39.0*	*33.8*	*23.1*
Rayleigh i.i.d.	median	16.1	25.0	33.2	20.2	24.7	34.2
	err. (%)	*8.3*	*12.6*	*4.0*	*7.0*	*13.8*	*3.7*
Orthogonal	median	17.6	25.4	33.3	22.2	25.1	34.7
	err. (%)	*18.4*	*14.2*	*4.3*	*17.7*	*15.5*	*5.2*

When increasing the number of transmit antennas while keeping the sum-power and the number of MTs constant, there are significant capacity gains, both with fixed SNR and at the actual SNR in the channel. The average capacity at $\sigma = 10$ dB increases from 14.8 bps/Hz (8 transmit elements with 9.75 dBi gain) to 22.2 bps/Hz (32 transmit elements with 3.75 dBi gain). When using the real SNR of the channel, the capacity increases from 18.9 to 21.7 bps/Hz. In both cases the size of the transmit array is the same (roughly 0.5 m wide and 0.25 m high). When the number of elements is further increased (128 transmit elements, 1 m width, 0.5 m height), an additional capacity gain of roughly 10 bps/Hz is estimated for both fixed and actual SNR.

Another observation is that, with a large number of transmit antennas, the variance of the capacity decreases and the DPC capacity is close to the capacity of orthogonal channel vectors. With 128 transmit antenna elements, the differences between the predicted capacities of the four approaches (QuaDRiGa, 3GPP-3D, Rayleigh i.i.d. and orthogonal channels) is less than 5%. Only the capacity prediction of the 3GPP-3D model using the actual channel SNR is 23% larger compared to the new channel model. This is due to the different PG model. The Rayleigh i.i.d. and orthogonal channels use the same PG model as the new channel model. Hence, it might be sufficient to use simplified SSF models such as the Rayleigh i.i.d. model to predict the achievable rates for massive MIMO channels that have many more transmit antenna elements than users. However, is not possible to correctly evaluate beamforming strategies such as maximum ratio transmission or zero-forcing in this case because the geometric properties (*e.g.*, the departure and arrival directions) are not modeled. This will also lead to erroneous results in multi-cell scenarios where the interference caused by different BSs depends on the beamforming strategy.

4.7 Summary

A measurement campaign from downtown Dresden, Germany, has been evaluated in order to derive the model parameters and validate the channel model from Chapter 2. The measurements were done in an urban-macrocell scenario at a carrier frequency of 2.53 GHz. The measurement data was processed as described in Chapter 3 and the large-scale parameters (LSPs) and performance metrics were calculated. Then, the channel measurements were resimulated with the new model in order to confirm that the same LSPs and performance metrics can be extracted from the model output. A reference simulation using the 3GPP-3D model [49] was done to show how the changes in the new modes affect the results. For this, the parameters from [49] for the UMa scenario were used. The key findings are:

- The resimulated channels using the new channel model produce almost identical results as the measured channels for all evaluated LSPs. The performance predictions for the single-link MIMO channels agree well. In the evaluated multi-user MIMO configurations, up to 10% higher dirty-paper coding capacities are predicted by the new model when the SNR is kept fixed in the capacity formula (*i.e.*, the influence of the PG is removed). However, this is still a significant improvement compared to the 3GPP-3D and the Rayleigh i.i.d. model which predict up to 24% higher capacities.

- The 3GPP-3D model predicts roughly 10 dB more power in the line of sight (LOS) and 4 dB in the non-line of sight (NLOS) scenario compared to the measurements. This is caused by a mismatch in the path gain (PG) model. As a result, up to 50% larger capacities are predicted by the 3GPP-3D model when the actual SNR of the channel is included in the capacity formula. When the PG values are fitted to the measurements, correct results can be obtained from the new channel model.

- When generating the departure and arrival angles in the 3GPP-3D model (see [49], page 26), a high Ricean K-factor leads to clustering of the angles of the NLOS paths (see Fig. 4.9 for an illustration). When high-gain antennas (such as in the measurements) are used at the BS, the NLOS path clusters are attenuated since they fall outside of the main beam of the antenna. This has severe effects on the generated channel coefficients in LOS propagation conditions, where the KF is high. When comparing the input parameters of the 3GPP-3D model with the results obtained from the generated channels, the KF is increased by 3.5 dB, the angular spreads and the delay spread are decreased by up to 50%, and all inter-parameter correlation values at the output of the model do not agree with the model input. This mismatch will increase further when the antenna gain increases, such as when using commercial BS antennas. The new model uses a different method to generate the angles where this mismatch cannot be observed.

- In the new measured and resimulated channels, different users are placed on the same track. If they are close together, their fast-fading channel coefficients are correlated since they are served by the same scattering clusters. The 3GPP-3D model does not support extended terminal trajectories and, therefore, no fast-fading correlation can be included. Each user gets initialized with a different set of scattering clusters. As a consequence, lower values for the singular value spread and higher values for the DPC capacity are predicted for the multi-user MIMO evaluation. With single-antenna users, the 3GPP-3D predicts 20% and the Rayleigh i.i.d. model predicts 24% higher DPC capacities than in the measurements. The predictions made by the new model are only 10% higher which indicates that there is still less correlation than in the measurements. However, a significant improvement can be seen.

The results indicate that the new model is significantly better to evaluate multi-user MIMO channels. In these evaluations, the inter-cell interference caused by different BSs has not been considered. However, this is an important aspect since interference is the major limiting factor in todays mobile broadband networks. Spatial channel models, such as the 3GPP-3D model, are therefore almost always used to study wireless communication systems in interference-limited conditions. The interdependence of the channels of several BSs is studied in the next chapter where measurement data from downtown Berlin, Germany, could be used for this case.

5 Validation of the Model for Multi-Cell Transmission

The substantial effort that is needed to perform channel measurements makes it difficult to simultaneously measure the channel coefficients from multiple BSs. Hence, the compound multi-cell multi-user MIMO channel can usually not be coherently recorded. One way to obtain early multi-cell results from single-link measurements is to combine the channels from individual measurements in a post processing step [19]. However, the number of links that can be characterized is still very limited and it is difficult to generalize the findings and draw conclusions for realistic network deployments with hundreds of BSs and MTs. More realistic performance evaluations are therefore done using channel models. The model parameters are extracted from single-link measurement data with a high spatial and temporal resolution. Such measurements require sophisticated array antennas and channel sounders in order to resolve the departure and arrival directions of the multipath components. However, it is an open issue how well the performance predictions from such simulations match the performance of real network deployments. Therefore, a second measurement campaign was done in Berlin, Germany, using a different measurement setup. This setup consisted of three BS sites, having six sectors in total. All sectors were equipped with commercial panel antennas and GPS-disciplined Rubidium clocks that allowed phase-coherent operation in the same frequency band. As a result, the multi-cell channel could be coherently recorded at the MT position and it was possible to validate the channel model from Chapter 2 in a multi-cellular environment. With this setup, the direct comparison of metrics such as the geometry factor (GF), the multi-cell delay spread, and the interference-limited capacity could be done. Such metrics are important to determine the performance of transmission schemes in a system-level environment with dozens of BSs and MTs. However, due to the small number of antennas that was supported by each BS and the MT in the measurements, the departure and arrival directions of MPCs could not be resolved. The parameter tables were completed using results from the literature.

An earlier evaluation of the data was presented in [12]. However, after the publication of the paper, new functionality was added to the model, *e.g.*, the multi-bounce scattering model from Section 2.4. The extraction of the multipath components (see Section 3.1.2) did not process entire MIMO links but was limited to SISO. Hence, for the results reported here, the raw measurement data was processed again and the channel model was used with all new features enabled. Only minor deviations from the results in [12] were found. Additional evaluations were done for the multi-user MIMO case where the influence of inter-cell interference on the achievable performance was studied. Generally, the results from the measurements and the model are in good agreement and it can thus be concluded that the generalization from single-link measurements to multi-cell channel models is valid.

This Chapter is organized as follows: In Section 5.1, the measurements are described. Then, in Section 5.2, the measurement results, the BS and MT positions, and the antenna characteristics are used to parameterize the channel model from Chapter 2. The model is used to *resimulate* the measurement campaign. The *resimulated* channel coefficients are processed in the same way as the raw measurement data and a subset of the large-scale parameters is calculated from

the two data sets as described in Chapter 3. The results in Section 5.3 show that, for almost all parameters, there is a good agreement between the predictions made by the model and the results from the measurements. The performance metrics, which provide a measure of the achievable data rate of a communication system, are discussed in Section 5.5. In addition to the evaluations in Chapter 4, it is also possible to study the influence of the inter-cell interference on the results, which is done for the dirty-paper coding capacity in Section 5.5.5.

5.1 Multi-cell Measurements in Berlin, Germany

The measurement setup replicated a small pre-commercial LTE-advanced system consisting of six sectors. All sectors were equipped with commercial Kathrein XPol panel antennas[1] with a half-power beam width of 60° in azimuth and 6° in elevation direction (polarization ±45°, 18 dBi gain). The commercial hardware used in the Berlin testbed was limited to a maximal SNR of 30 dB which is sufficient to transmit 64 quadrature amplitude modulation (QAM) symbols. Even if there is more power in the link budget, the maximum SNR is capped to this value. All BS sites were synchronized using GPS-disciplined Rubidium clocks that allowed phase-coherent operation in the same frequency band. Reference signals [134] consisting of 144 pilot tones for each BS served for coherently identifying up to six cells. Additional orthogonal sequences over four consecutive symbols allowed the identification of multiple antennas per cell. Detailed information on the testbed is available in [18, 20, 135, 136].

At the Rx side, a customized terminal equipped with a pair of dipole-like antennas[2] (4 dBi gain) was used. These antennas were mounted on the roof of a car and slanted by ±45°. The terminal was synchronized over the air to simplify the measurement procedure and to eliminate additional calibration steps. The system automatically adjusted the multi-cell CIR within the 4.7 μs guard interval of the underlying OFDM system which removed the mean multi-cell delay from the data. The MT detected the reference signals and converted them into an Ethernet packet stream as described in [20]. This data stream was tapped at the terminal and recorded to a notebook computer.

Custom import filters provide access to the stored CIRs. The import filters extract a $2 \times 12 \times 144$ channel tensor every 10 ms. The dimensions correspond to the number of Rx antennas, the total number of Tx antennas, and the number of samples in the frequency domain, respectively. The preprocessing of the data was then done in a similar fashion as for the Dresden data. First, the MPCs were extracted using the algorithm from Section 3.1.2. Then, the LSP were computed and the measurement setup was replicated in the channel model. Both the preprocessed data and the output of the channel model have the same format. Thus, identical routines can be used to obtain the LSPs.

[1] Type No. 800 10541
[2] HUBER+SUHNER SWA 2459/360/4/45/V; Type: 1399.17.0040

Table 5.1: Parameters for the multi-cell measurements in Berlin

Parameter	Value
Frequency Range	2.68 GHz (center freq.) ; 18.36 MHz (bandwidth) ; 144 carriers
CIR length	4.7 μs ; update every 10 ms
Link Budget	36.5 dBm Tx power per antenna ; -96 dBm noise floor
Max. MT speed	10 km/h
Measurement Track	$2 \cdot 3.1$ km (two downtilt settings)
Tx antenna configuration	2 elements, XPOL ±45°, 18 dBi gain, 60° azimuth, 6° elevation
Rx antenna configuration	2 Dipole antennas, XPOL ±45°, 4 dBi gain, 360° azimuth, 80° elevation

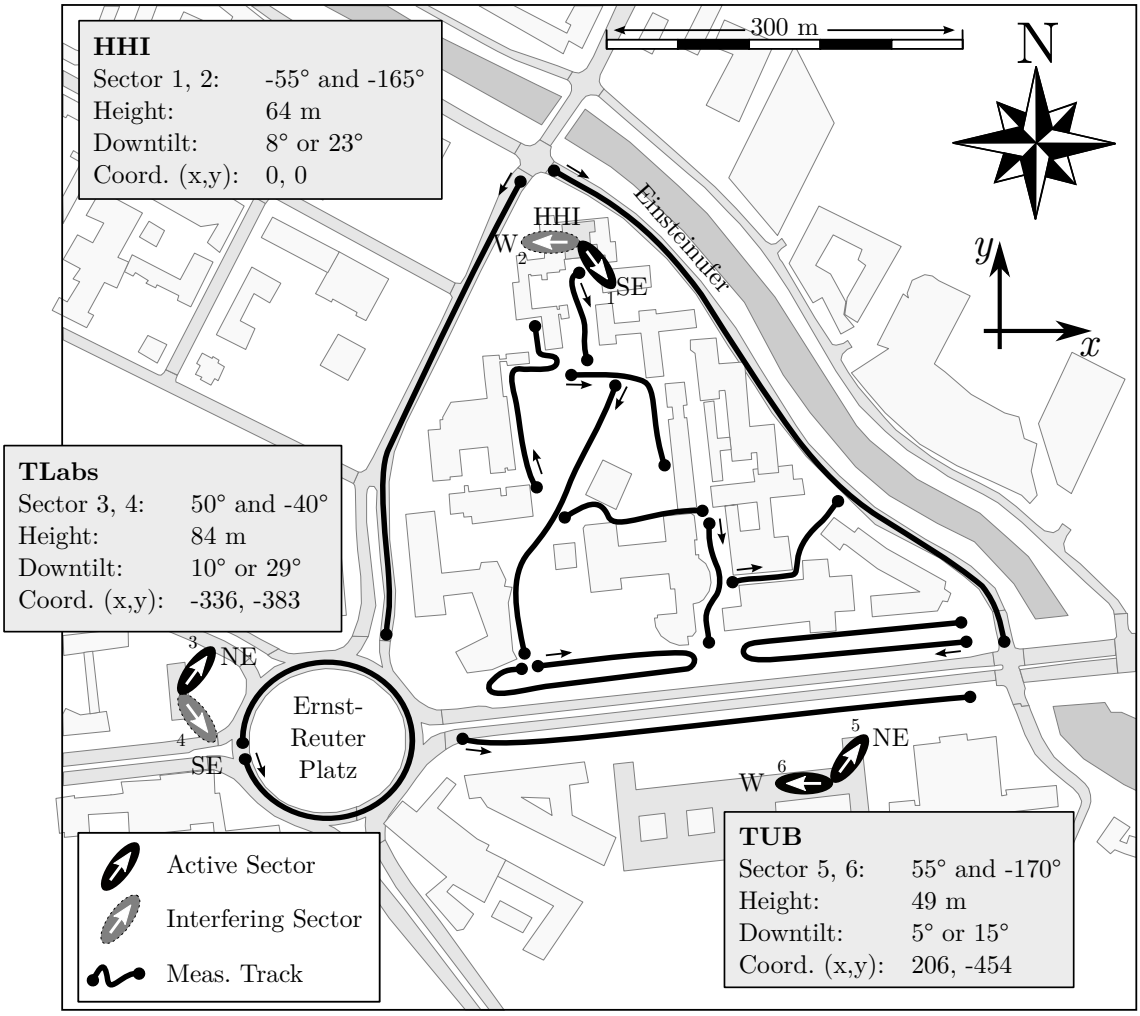

Figure 5.1: Map of the measurement area in Berlin, Germany, showing the transmitter and receiver positions and the orientations of the antennas.

Figure 5.1 shows an overview of the measurement setup, providing the coordinates and heights (in units of meters), the antenna orientations, and the downtilt settings for each BS site. Three BSs are located around the Ernst-Reuter-Platz in downtown Berlin, Germany. They are at the rooftop of the Heinrich Hertz Institute (HHI), the Deutsche Telekom Laboratories (TLabs) and the main building of the Technische Universität Berlin (TUB). Each BS serves two sectors which are indicated by ellipses with an white arrow on top. The four innermost sectors, indicated by black ellipses, form a so-called *cooperation cluster*, *i.e.*, they jointly serve the users within those sectors on the same time and frequency resources. In this joint transmission mode, the eight transmit antennas of the *active sectors* form a distributed array antenna. The outer sectors cause out-of-cluster interference. The 12 measurement tracks with a total length of 3.1 km are plotted as thick black lines. The measurements were repeated twice with different downtilt settings. In the first setting, the main beam of the high-gain antenna reached the ground at 90% of the inter site distance (ISD) (450 m). In the second setting, the downtilt was increased such that this distance was reduced to 33% of the ISD (170 m). In this way, different interference levels can be investigated and it is possible to evaluate how well the channel model can predict the performance for different downtilt settings.

5.2 Resimulation of the Measurement Campaign

As for the evaluations in Dresden, a replication of the Berlin testbed was created in the channel model. The parameter tables from [12] are included on Pages 82 and 83, respectively. Since the Berlin measurements utilized less antennas than in Dresden, only a subset of the LSPs could be extracted. The missing parameters were taken from the literature. The BS positions and MT tracks are depicted in Figure 5.1 on Page 115.

Channel Model Setup The Tx-positions, sector orientations and Rx-tracks were imported into the channel model. The measurement tracks were then split into 190 segments. Each segment had an average length (including the overlapping part) of 24 m with a standard deviation of 6 m. A separation into LOS and NLOS parts was done based on the overall received power and a 3-D model of downtown Berlin, Germany. It is assumed that there is no inter-site correlation of the LSPs due to the large ISD (500 m) and the high angular separation of the three BS sites at the MT [116]. However, inter-sector correlations at the same BS are included implicitly since the antennas of different sectors are combined into one array antenna.

Parameterization of the Model In a first attempt, the parameters from the WINNER UMa [47, 48] scenario were used to resimulate the measurement campaign. However, some differences between the measurement results and the WINNER parameters were found. For example, many WINNER results (*e.g.*, [23, 47, 96]) show median DS values of around 40 ns for LOS and 70-230 ns for NLOS. Results from the measurements with low downtilts (0.9 ISD), however, show larger DS values of 200 and 300 ns, respectively. This was also reported by other authors (*e.g.*, [89, 95, 130]). The measurement results also indicated lower KF values, *i.e.*, strong echoes were found even if the direct component was present. In some cases, the power of those echoes could even exceed the LOS power. Therefore, it was necessary to adjust some parameters in order to increase the match with the testbed. After all, the intention is to show that the model creates channels with similar properties as real data.

It is not possible to de-embed the antenna patterns because the spatial resolution of the antennas is not sufficient to calculate the departure and arrival angles of the MPCs. Therefore, the antenna-influence was removed by an iterative data-fitting method. First, a parameter (*e.g.*, the DS) was calculated from the measured data[3] Then, the log-normal distribution of the parameter was calculated. The median value (*e.g.*, DS_μ) and the STD (DS_σ) were obtained. Then, the model was used to resimulate the channel coefficients and calculate $\mathrm{DS}_\mu^{[\mathrm{model}]}$ and $\mathrm{DS}_\sigma^{[\mathrm{model}]}$ from the output. However, due to the weighting by the antenna pattern, some propagation paths are amplified and others are attenuated. This increases the width of the distribution of the DS. In the next step, the values at the input of the channel model were adjusted in order to account for this difference. The procedure was repeated until the values $\mathrm{DS}_\mu^{[\mathrm{model}]}$, $\mathrm{DS}_\sigma^{[\mathrm{model}]}$ converged to DS_μ, DS_σ from the measurements. The same was done for the other LSPs as well. The model parameters for the Berlin UMa scenario are listed in Table 4.2 on Page 82. Table 4.3 on Page 83 provides the cross-correlation values between the LSPs.

To calculate the angular spreads, array antennas with a high spatial resolution, such as those used by [22, 23] and [8], are needed. However, those antennas are not compatible with the Berlin testbed. It was only possible to directly validate the values for DS, PG, SF, and KF. To

[3] The measurement data where the downtilt was set to maximize the gain at 90% of the ISD was used for this evaluation.

fill the gaps, results from other measurement campaigns were used. Hence, Table 4.2 includes the averages of the results from measurement campaigns in Dresden, Germany [23], Ilmenau, Germany, [96] and the WINNER parameters [47, 48].

Antennas It was made sure by extensive testing and debugging that for each parameter in the tables, the implementation of the model from Chapter 2 produces exactly the same value in the output channel coefficients. However, the table is only valid for omnidirectional radiation patterns. High-gain BS-antennas were included by a measured 3-D pattern provided by Kathrein. It contains the radiated power vs. azimuth and elevation angle for one polarization at a fixed electrical downtilt of 10°. Mechanical tilts were added by rotating the antennas as described in Section 2.5.2 to obtain the same downtilts as for the measurements. The polarization for the second port and the cross-polarization isolation between the ports had to be approximated as well. Since there was no measured 3-D pattern of the receive antenna, it was approximated it by a dipole. However, with those antennas, the LSPs extracted from the channel coefficients differ from the values in the table. This needs to be taken into account when discussing then LSPs in the next section.

5.3 Large-Scale Parameters

The results for the LSPs are presented and discussed in a similar way as in [12]. The figures in the following sections (see for example Figure 5.2) contain five curves. The solid lines show the results for the low downtilt, *i.e.*, the main beam reaches the ground at 0.9 ISD or 450 m. The dashed lines show the results for the high downtilt (0.3 ISD, 170 m). The thick lines are for the measurements, the thin lines for the model results. An additional dotted line shows the input parameters of the channel model. Those are obtained by reading the values from the parameter maps and may help to discuss the influence of the transmit antennas and the downtilt.

The results can be grouped into two categories: single-link parameters (PG, DS, KF, single-link capacity) and multi-link parameters (GF, multi-cell DS, and interference limited capacities). Small-scale fading, *i.e.*, fast fluctuations of the received power of a MPC, can lead to strong fluctuations of the parameters even in subsequent snapshots. Therefore, the LSP values obtained from snapshots with a range of 3.3 m were averaged in order to reduce this effect (a more detailed discussion can be found in Section 3.2). Along the 3.1 km measurement track there are 928 such *averaging intervals*. Hence, there are 928 values for each multi-link parameter and 5,568 values ($928 \cdot 6$ sectors) for each single-link parameter. The simulation was repeated 16 times. Hence, there are 16 CDFs and 16 median values (2-quantile) for each parameter. The average of those 16 values is plotted in the point where the ordinate shows a value of 0.5. The STD above and below the mean of those 16 samples determines the width of the errorbar. Squared endings are for the low tilt (0.9 ISD) and round endings for the high downtilt (0.3 ISD). Generally, the results for the low downtilt agree better than for the high downtilt since the model parameters were adjusted in Table 4.2 for the low downtilt data.

5.3.1 Effective Path Gain

The effective PG combines the directional antenna gain, the SF, and the distance-dependent PG. The results are shown in Figure 5.2. The measured power levels of the LOS and NLOS areas were fitted to the Hatha model [64] as

$$\mathrm{PG}^{[\mathrm{LOS}]} = -21.0 \cdot \log_{10} d_{[\mathrm{km}]} - 110.5, \tag{5.1}$$

$$\mathrm{PG}^{[\mathrm{NLOS}]} = -28.5 \cdot \log_{10} d_{[\mathrm{km}]} - 123.5. \tag{5.2}$$

The LOS results agree very well with the results from the Dresden measurements (see Section 4.3.1). However, the NLOS PG coefficient is much lower than in Dresden (28.5 instead of 46). Thus, the received power is more homogenously distributed in Berlin. A reason might be the smaller coverage area (only 500 m ISD), and the elevated BS positions (49 to 84 m compared to 27 to 55 m in Dresden).

At low downtilts (0.9 ISD), the average effective PG is increased due to the antenna gain. Without antennas, the channel model would predict a median value of -104.6 dB. The antenna increases this value by 2.2 dB to -102.4 dB. The opposite happens at high downtilts (0.3 ISD) where the effective PG is decreased by 1.5 dB to -106.1 dB. The same effect can be seen in the measured data. However, the difference between high and low downtilts is much larger (10.7 dB in the measured data instead of 3.7 dB in the resimulated data). A possible explanation can be found in the antenna patterns. At high downtilts, the main beam focusses the power at a small area close to the BS. The rest of the trajectory is covered by the remainder of the pattern, *e.g.*, the sidelobes. The measured pattern was only available for 10° electric downtilt. Importing this pattern in the channel model and adding mechanical tilts leads to a different *footprint* of the antenna pattern on the ground which also changes the effective PG. In addition to that, if the radiated power is localized in a small area, and if the MT is close to one of those areas,

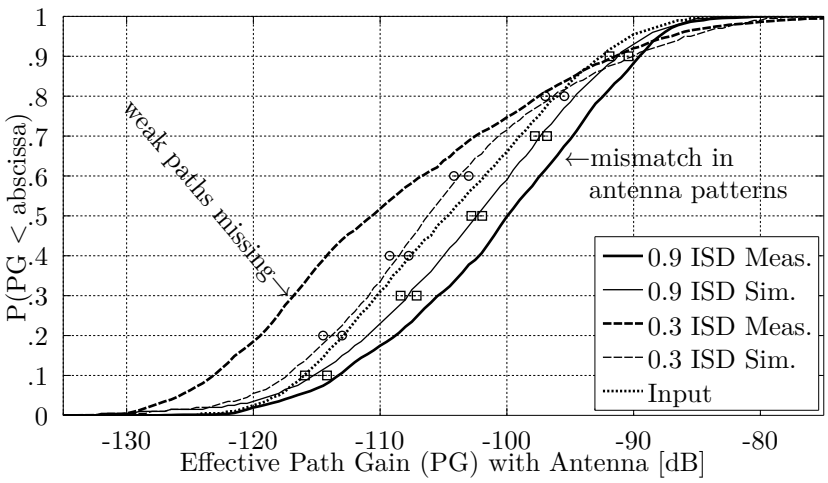

	Combined		LOS		NLOS	
	μ [dB]	σ [dB]	μ [dB]	σ [dB]	μ [dB]	σ [dB]
Model Input	-104.6	8.8	-98.4	5.9	-111.5	6.7
0.9 ISD Meas.	-99.7	8.9	-95.8	8.7	-102.9	8.2
0.9 ISD Sim.	-102.4	9.2	-97.8	8.1	-106.9	8.1
0.3 ISD Meas.	-110.4	12.1	-103.6	11.5	-116.2	10.5
0.3 ISD Sim.	-106.1	10.4	-101.1	9.5	-111.4	7.7

Figure 5.2: Effective path gain distributions in Berlin, Germany

the received power is dominated by the BS serving this area. In the measurement system, the achievable SNR is limited. Thus, weak paths from links to other BSs often fall below the noise floor and cannot be resolved. This reduces the effective PG calculated from the measured data. The model, on the other hand, does not have this limitation.

5.3.2 Ricean K-Factor

The KF (Figure 5.3) is influenced by the LOS probability and the antenna gain. For the estimation of the KF, a certain number of paths has to be detected. When the SNR is too low, many paths fall below the noise floor. Thus, the KF was only evaluated for parts of the measurement track where the raw SNR in the measurement data was at least 5 dB. This includes 95% of the low downtilt data and 80% of the high downtilt data.

In the resimulated channels, lower downtilts (0.9 ISD) result in a 1.2 dB higher KF compared with the data set with high downtilts. This is reasonable, because at high downtilts the beam of the high-gain antenna illuminates only a small area close to the BS. The KF is reduced in all other areas because the direct component is attenuated. In the measured data, on the other hand, high downtilts result in a better KF. However, this can also be explained by the missing MPCs due to the reduced resolution of the measurement system.

K-Factor (LOS only) If the KF is small, the detection of the LOS path might fail because a later, stronger path may be taken as the first one by accident. For this reason, in Figure 5.3 (right), the evaluation was limited to areas where there is a LOS connection between Tx and Rx. Here, the match between the four curves is better. The effect of the high-gain antennas on the KF can be seen when comparing the parameters in Table 4.2 (model input) with the results in Figure 5.3 (model output). The LOS-KF in Table 4.2 follows a normal distribution

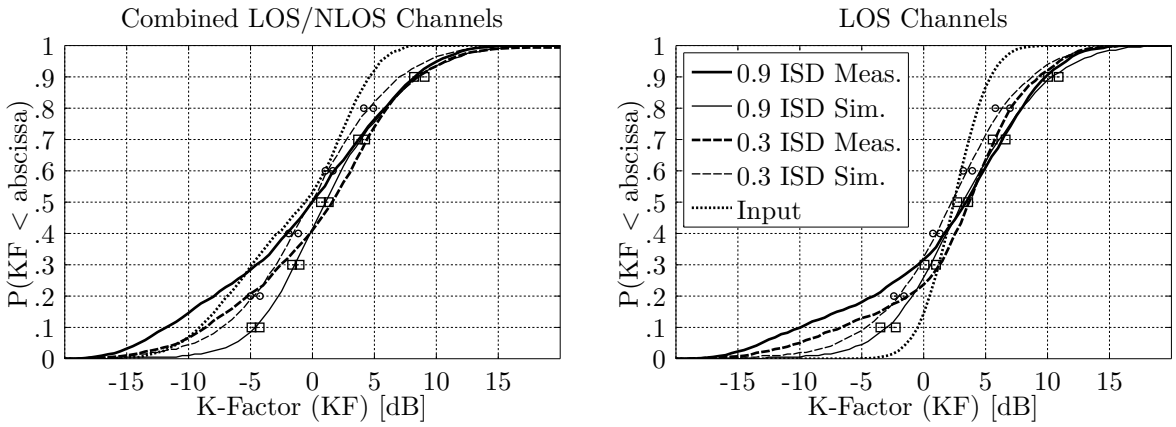

	Combined			LOS			NLOS		
	%	μ [dB]	σ [dB]	%	μ [dB]	σ [dB]	%	μ [dB]	σ [dB]
Model Input	*100*	-0.6	5.3	*51*	2.6	2.3	*49*	-6.0	3.6
0.9 ISD Meas.	*96*	0.2	7.4	*95*	3.7	7.3	*97*	-2.8	6.2
0.9 ISD Sim.	*93*	1.1	5.2	*95*	3.2	5.3	*89*	-1.0	4.0
0.3 ISD Meas.	*79*	1.8	6.5	*83*	3.9	6.0	*76*	-1.7	6.1
0.3 ISD Sim.	*81*	-0.1	5.7	*90*	2.2	5.3	*71*	-3.0	4.5

Figure 5.3: Ricean K-factor distributions in Berlin, Germany

with $\mathcal{N}(2.7, 2.3^2)$. In some areas the weighting by the antenna pattern amplifies the direct component, and the KF increases. In other areas, outside the cell, the direct component is attenuated and the KF decreases. This explains the larger spread in the empirical distributions.

5.3.3 RMS Delay Spread

The DS in Figure 5.4 depends on the KF and the LOS probability which was 51% in the Berlin testbed. At low SNR, the calculation of the DS becomes erroneous since many MPCs fall below the noise floor. Thus, the evaluation was limited to areas where the SNR was at least 5 dB.

An interesting observation is that the antennas have little influence on the DS. This becomes clear when comparing the DS from Table 4.2 (model input) with the DS in Figure 5.4. The median LOS value from Table 4.2 (excluding antennas) is 204 ns. The corresponding values that were calculated from the model output are 191 ns for low and 202 ns for high downtilts. For NLOS channels, Table 4.2 uses 339 ns as input and the model outputs are 285 ns and 299 ns, respectively.

The measurement results at higher downtilts (0.3 ISD), however, are significantly shorter compared to the model input (80 ns difference for LOS and 105 ns difference for NLOS). This known effect comes from the thresholding used to remove the noise from the data [118]. In the measurement system the noise floor is 30 dB below the peak power in the multi-cell CIR. At high

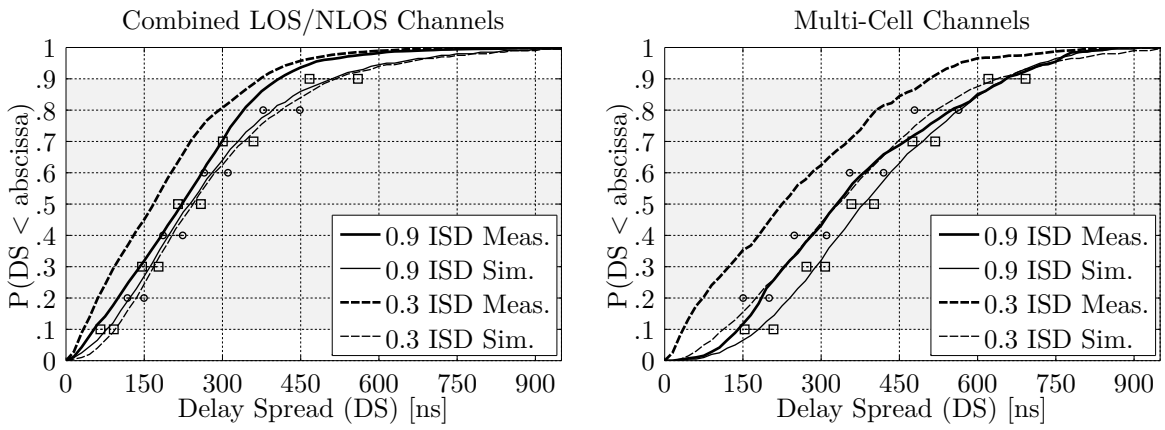

	Combined LOS/NLOS			10 - 90%	Multi-Cell Channels			10 - 90%
	μ	σ	μ [ns]	Range [ns]	μ	σ	μ [ns]	Range [ns]
0.9 ISD Meas.	-6.64	0.33	230	64 - 417	-6.47	0.25	338	149 - 667
0.9 ISD Sim.	-6.63	0.34	236	78 - 509	-6.42	0.23	380	180 - 655
0.3 ISD Meas.	-6.76	0.37	176	40 - 380	-6.63	0.41	233	41 - 516
0.3 ISD Sim.	-6.61	0.30	244	92 - 525	-6.48	0.30	332	115 - 644

	LOS			10 - 90%	NLOS			10 - 90%
	μ	σ	μ [ns]	Range [ns]	μ	σ	μ [ns]	Range [ns]
Model Input	-6.69	0.30	204	81 - 497	-6.47	0.20	339	189 - 606
0.9 ISD Meas.	-6.71	0.38	195	40 - 423	-6.60	0.23	252	115 - 405
0.9 ISD Sim.	-6.72	0.38	191	55 - 479	-6.55	0.23	285	140 - 544
0.3 ISD Meas.	-6.91	0.37	124	30 - 335	-6.63	0.31	233	75 - 407
0.3 ISD Sim.	-6.70	0.33	202	73 - 496	-6.53	0.22	299	152 - 558

Figure 5.4: RMS delay spread distributions in Berlin, Germany

downtilts the power difference between the serving cell and interfering cells can easily exceed 20 dB due to the antenna gain. This leaves a dynamic range of only 10 dB for the detection of MPCs in the interfering links. Hence, the channels seem to have a shorter DS because weak MPCs cannot be resolved. The resimulated channels do not have this limitation and thus show a larger DS.

Multi-Cell Delay Spread The multi-cell DS (Figure 5.4, right) is calculated from the combined CIR of all BSs. Hence, it includes the different mean-delays. This is important if a MT is connected to several BSs at the same time, *e.g.*, when using soft handover or joint transmission. For the low downtilts, the measurement results show an increase of the median DS from 230 ns to 338 ns. The model predicts a slightly larger value of 380 ns. However, the maximum delay spread does not increase. All channels, single-cell and multi-cell, have a delay spread of less than 900 ns.

The results for the high downtilts, however, show some differences. Both the measured results for single-cell and multi-cell are shorter than the predictions from the model. The reason is likely to be the same as discussed above: The measurement setup cannot resolve sufficient MPCs if the power difference between serving and interfering links is high.

5.4 Inter-Parameter Correlation Values and Decorrelation Distances

Figure 5.5 summarizes the results for the inter-parameter correlation values and Figure 5.6 for the decorrelation distances. For each of the parameters, there is one value that is calculated from the measurements, one that serves as input to the model and 16 values that are obtained at the model output when initializing the model several times. The results are obtained from the dataset with low downtilts (0.9 ISD).

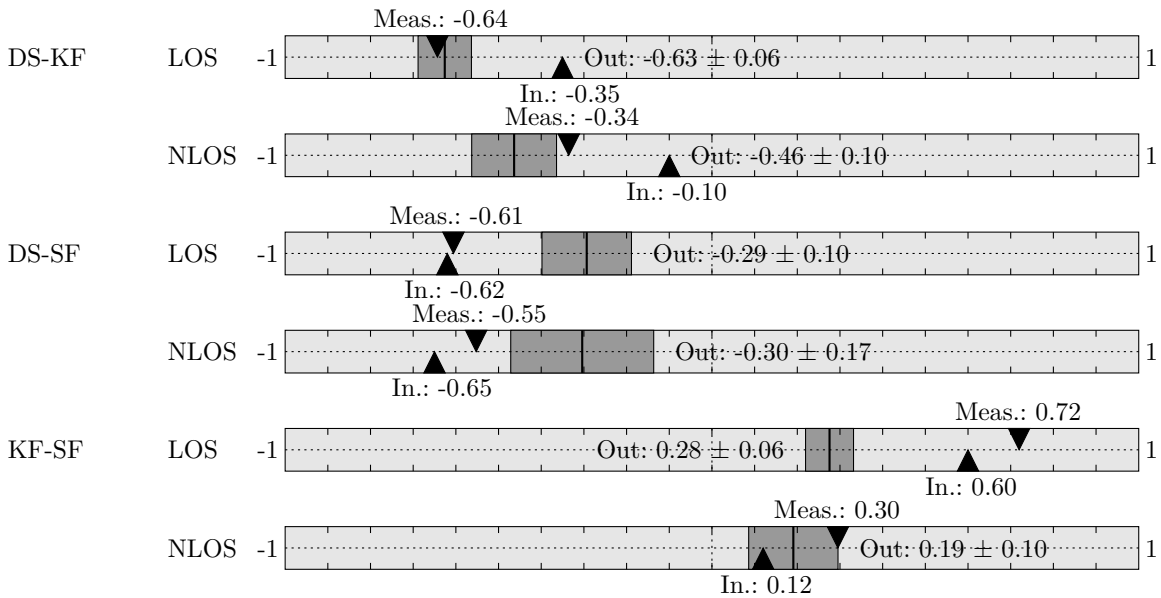

Figure 5.5: Inter-parameter correlation values in Berlin, Germany

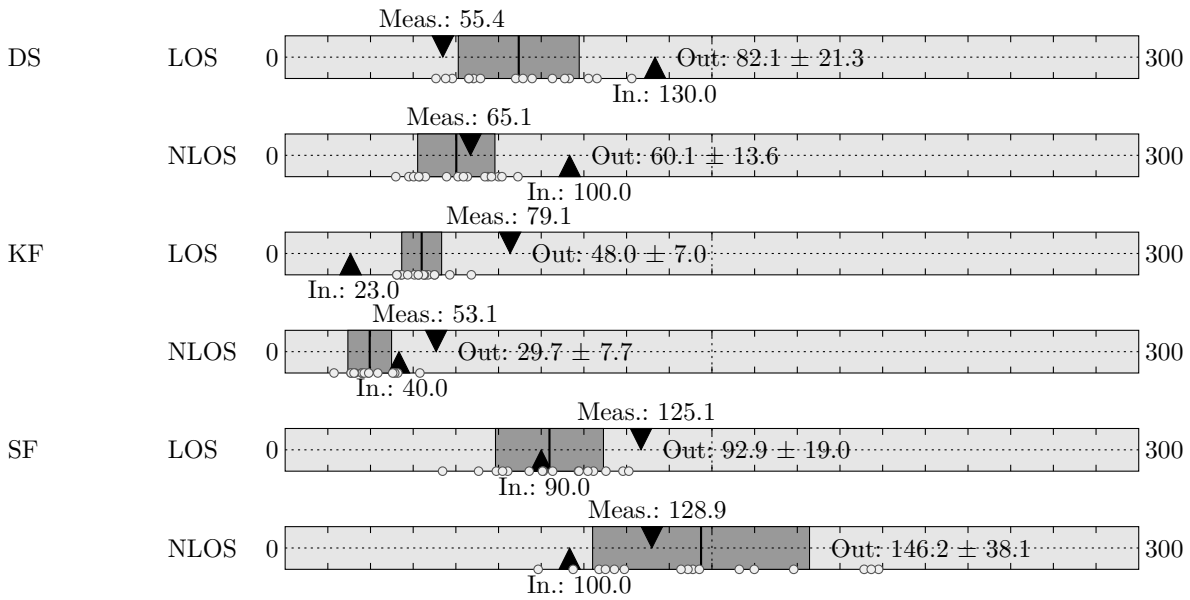

Figure 5.6: Decorrelation distances in Berlin, Germany in units of [m]

The plots are structured as follows: The LSPs and the propagation conditions are indicated on the left hand side of the Figures. The gray bar presents the range of the parameter. A downward pointing triangle in the top part of the bar indicates the value that was calculated from the measurements. An upward pointing triangle in the lower part of the bar indicates the value that was set at the input of the model. The dark shaded area indicates the range of values that were calculated at the output of the model. The vertical line shows the average of the 16 values. The width of the area, *i.e.*, the range from the beginning of the shaded area to the middle line, and from the middle line to the end, is determined by the STD of the 16 values. Hence, the total width of the shaded area is twice the STD.

In case of LOS propagation, the parameters show high correlation values. The KF is correlated with the SF ($\rho_{\mathrm{KF,SF}} = 0.72$). This means that areas with a high overall power are dominated by the direct component. Subsequently, this leads to low values for the DS which has a negative correlation coefficient with both the KF and the SF ($\rho <$ -0.6). However, it seems that those values cannot be predicted well by the model where the average value $\rho_{\mathrm{KF,SF}}$ is only 0.28 despite the input value of 0.6 and $\rho_{\mathrm{DS,SF}} =$ -0.29 with an input setting of -0.62. This indicates that the true cross-correlation between DS and SF might even be smaller than -0.6. However, that would destroy the positive definiteness of the cross-correlation matrix.

In both scenarios (LOS and NLOS), the decorrelation distances agree well in most of the cases. The results are better than for the Dresden measurements (Section 4.5) where larger deviation were found. This can be attributed to the smaller values for the inter-parameter correlations (see Table 4.3). The decorrelation distances from the 3GPP-3D model (see Table 4.2) are only half as big as in the measurements. However, the current results agree very well with [137].

5.5 Performance Metrics

5.5.1 Geometry Factor

The GF is a lower bound for the SINR, *i.e.*, the power of the serving sector divided by the interference power and noise. Thus, the GF is mainly influenced by the PG and the antenna directivity. The results are shown in Figure 5.7.

At higher downtilts (0.3 ISD), the coverage area of a sector is small and little power is radiated into the neighboring cells. Hence, the interference situation can be improved by increasing the downtilt. This is predicted well by the channel model. In case of low downtilts (0.9 ISD), the model predicts a GF that is roughly 1.4 dB better compared with the measurements. Two reasons could be behind this: First, the exact positions of the buildings on the campus are not included in the model. Thus, the effective path gain at the MT positions is different for each initialization of the model. Second, the antenna patterns in the model do not perfectly match the real ones in the measurement. This changes the GF since the power distribution on the ground differs from the measurements.

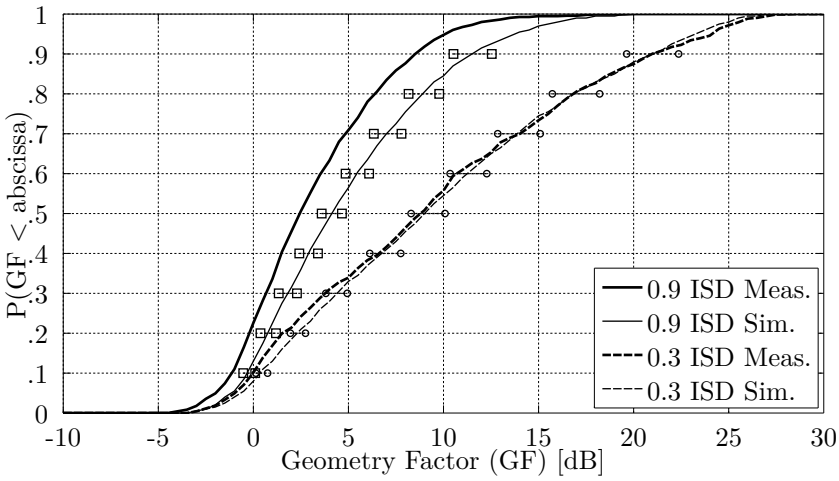

	Combined	
	μ [dB]	σ [dB]
0.9 ISD Meas.	2.7	3.8
0.9 ISD Sim.	4.2	4.7
0.3 ISD Meas.	9.0	7.8
0.3 ISD Sim.	9.1	7.5

Figure 5.7: Geometry factor distributions in Berlin, Germany

5.5.2 Single-User Capacity at a Fixed SNR

The results for the single-user capacity (see Section 3.3.1 for an introduction) are shown in Figure 5.8. In this evaluation, the capacity of the 2×2 MIMO channel matrix of each BS-MT link was evaluated at a fixed SNR of $\sigma = 10$ dB. Thus, the received power was removed from the evaluation and only spatial propagation effects could have an influence on the capacity. The evaluation was limited to areas where the SNR in the data was at least 5 dB. This covered 96% of the measurement locations for the low downtilts (0.9 ISD) and 79% for the high downtilts

(0.33 ISD). The lower bound of the capacity is the Keyhole capacity $C^{[\mathrm{KH}]}$, *i.e.*, the capacity with only one spatial degree of freedom. The upper bound $C^{[\mathrm{parallel}]}$ is reached when there are two parallel spatial data streams. Their values can be computed as

$$C^{[\mathrm{KH}]} = \log_2(1 + 10 \cdot 2) \approx 4.39 \text{ bps/Hz}, \tag{5.3}$$

$$C^{[\mathrm{parallel}]} = 2 \cdot \log_2(1 + 10/2 \cdot 2) \approx 6.91 \text{ bps/Hz}. \tag{5.4}$$

At low downtilts, the median measured capacity of 5.44 bps/Hz is predicted well by the channel model (5.37 bps/Hz). However, at high downtilts, the measured capacity is only 5.21 bps/Hz while the predictions from the channel model remain unchanged (5.37 bps/Hz). Intuitively, the predictions from the model make sense because the only difference between the two resimulated data sets is the downtilt. However, the influence of the received power, which is mainly affected by the downtilt, is removed from the capacity evaluation by fixing the SNR to $\sigma = 10$ dB.

Another observation is the difference in the width of the distributions. The resimulated channels show a wider spread in the capacity results compared to the measurements. A reason for this could be discrepancies in the values for the angular spreads. However, it is difficult to quantify this influence without access to accurate angular spread measures. It is also possible that the measurement system causes some random phase fluctuations within different MIMO sublinks due to the over-the-air synchronization. Such a random component would explain the steeper distribution of the measurement results. Nevertheless, compared with the distribution of an i.i.d. channel, there are significant fluctuations in all the results. Clearly, it is important to adjust the transmission mode to the channel rank as suggested by [133].

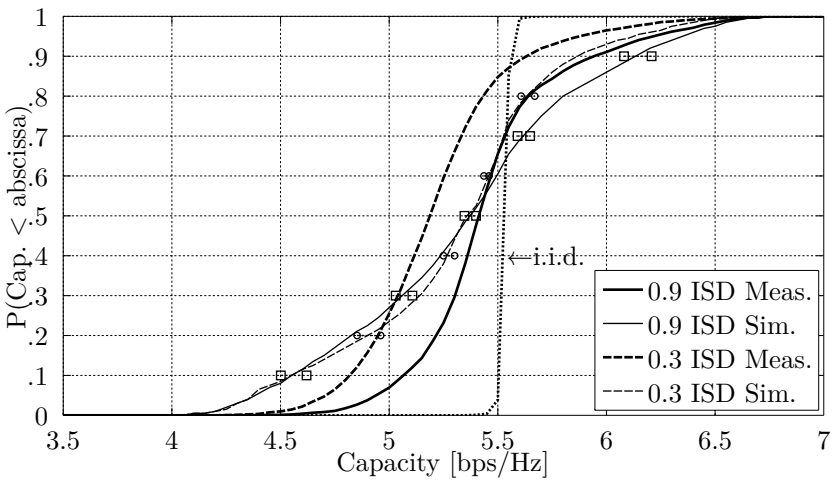

	Combined		LOS		NLOS	
	μ [dB]	σ [dB]	μ [dB]	σ [dB]	μ [dB]	σ [dB]
0.9 ISD Meas.	5.44	0.36	5.50	0.42	5.39	0.22
0.9 ISD Sim.	5.37	0.57	5.51	0.63	5.26	0.44
0.3 ISD Meas.	5.21	0.35	5.29	0.39	5.15	0.25
0.3 ISD Sim.	5.37	0.49	5.44	0.56	5.30	0.34
Rayleigh i.i.d.	5.56	5.56	5.56	5.56	5.56	5.56

Figure 5.8: Capacity at a fixed SNR in Berlin, Germany

5.5.3 Multi-User Singular Value Spread

Results for the multi-user SV spread are presented in Figure 5.9. The SV spread is a measure of the orthogonality of users signals. A detailed introduction and discussion of this metric can be found in Section 3.3.3.

In Berlin, the BSs had two cross-polarized transmit antennas and the MTs had two receive antennas. The SV spread is evaluated for the four *active sectors* shown in Figure 5.1. These BSs form a so-called cooperation cluster, *i.e.*, they coherently process the signals for the served MTs. The compound channel has eight distributed transmit antennas. To evaluate the correlation properties in the channel, two configurations are considered:

1. ***Dual-antenna receivers***: Each BS serves one dual-antenna MT with two spatial data streams (single-user MIMO). The terminals perform a handover to the BS with the highest receive power. Hence, in addition to the path-gain window, users are chosen such that each of the four active BSs serves one user. Therefore, the compound 8×8 channel matrix has a block-diagonal structure and becomes near-orthogonal due to the two polarizations.

2. ***Single-antenna receivers***: As in Dresden, the terminals select their best receive antenna. Each BS then serves two MTs with a different data stream. Terminals are picked randomly. As for the dual-antenna MTs, they are required to perform a handover and are always served by their best BS. However, if the terminals are not well separated, *i.e.*, if their channel vectors are not orthogonal, the SV spread might increase.

The median SV spread for the dual-antenna receivers calculated from the measured channel data for the low downtilt (0.9 ISD) is 13.5 dB which is only 0.8 dB more compared to the Rayleigh i.i.d. channels. The values for the high downtilt (0.33 ISD) are very similar. Those values are predicted well by the channel model (there is only 1 dB difference). When using single-antenna receivers and serving eight instead of four terminal simultaneously, almost identical values can

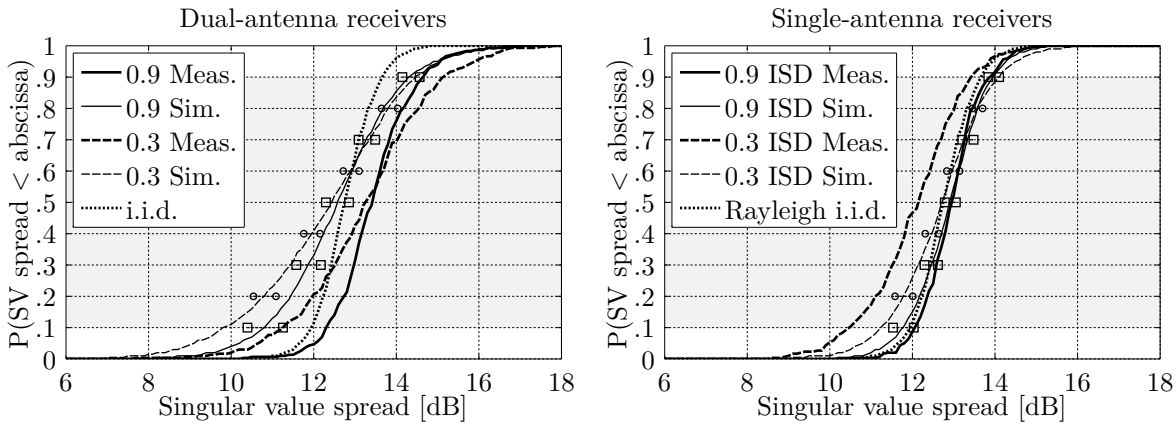

	Dual-antenna Rx			Single-antenna Rx		
	med.	cdf.1	cdf.9	med.	cdf.1	cdf.9
0.9 ISD Meas.	13.5	12.3	14.7	13.0	12.1	13.9
0.9 ISD Sim.	12.6	10.8	14.3	12.9	11.8	14.0
0.3 ISD Meas.	13.3	11.3	15.2	12.1	10.5	13.5
0.3 ISD Sim.	12.3	9.8	14.5	12.7	11.2	14.1
Rayleigh i.i.d.	12.7	12.2	13.3	12.7	12.2	13.3

Figure 5.9: Singular value spread in Berlin, Germany

be obtained. The results from the measurements as well as the resimulated channels are very close to the ones for the dual-antenna configuration. Hence, one can conclude that using a distributed antenna system with cross-polarized antennas and assigning the users to their best serving BS is a good strategy. The resulting compound channel matrix is well-conditioned. For comparison, in the Dresden measurement campaign, the eight transmit antennas were installed at a single BS. The median SV spread was 19.2 dB in this case.

5.5.4 Dirty-Paper Coding Capacity

The DPC capacity is the upper bound of the achievable rates in a multi-user system. The results are depicted in Figure 5.10. The results are presented for two normalizations of the compound channel matrix (see Section 3.3.4 for an introduction). First, the matrix is normalized to a fixed SNR of $\sigma = 10$ dB. This has the advantage that the influence of the power is removed from the results and only spatial propagation characteristics, *i.e.*, multipath and polarization effects, are considered. Second, the power is not removed and the capacities are calculated at their actual SNR.

When the SNR is fixed it is possible to define some bounds of the capacity that help discussing the results. The lower bound is reached when the compound channel matrix has only one spatial degree of freedom, *e.g.*, all users are at the same position which can only be served by a (compound) keyhole channel. If the (distributed) BS has no channel knowledge, it cannot perform any spatial processing, *e.g.*, beamforming ore precoding. The users have to share the radio resources either in the time or frequency domain. In this case, the ergodic keyhole capacity at $\sigma = 10$ dB with equal power allocation is (3.70) 6.3 bps/Hz. If the BS has perfect channel knowledge, it can precode the users' signals such that the waveforms that are transmitted by the eight distributed antennas add up constructively at the MT position. The DPC capacity is (3.71) is 9.3 bps/Hz in this case. This increase of the capacity comes from the 9 dB increase of the effective received power due to the constructive interference. However, low capacity values could not be observed in the measured channels. A special case arises when the four dual-antenna users can be separated in the spatial domain but each user can only receive one data stream. The compound channel matrix is composed of four keyhole matrices. Without channel knowledge at the BS, a capacity of (3.72) 17.6 bps/Hz could be achieved in this case. Optimum power allocation would disable one data stream per user and shift the power to the remaining stream. The capacity (3.73) in this case is 21.4 bps/Hz. When there are eight orthogonal channel vectors, a capacity of 27.7 bps/Hz can be achieved. In this case, it is irrelevant if there is channel knowledge at the BS.

The median measurement results are very close to the upper bound of the capacity. At the low downtilts (0.9 ISD), the median capacity is 26.0 bps/Hz for the four dual-antenna users and 26.3 bps/Hz for the eight single-antenna users. The distributions range from 23.2 to 27.5 bps/Hz. The values are roughly 1 bps/Hz lower for the high downtilts (0.9 ISD). This difference is predicted also by the channel model. However, for the single-antenna users the model predicts 1 bps/Hz lower values for both the low and high downtilts. There seems to be slightly more SSF correlation between the users in the model than in the measurements. For comparison, when the eight antennas are co-located at the same BS as it was the case in the Dresden measurements, a median capacity of 17.7 bps/Hz could be achieved with eight single-antenna users (see Table 4.4 on Page 108). The distributed antenna configuration in Berlin and the handover of users to their best cells leads to significant capacity gains.

Fixed SNR (σ = 10 dB)

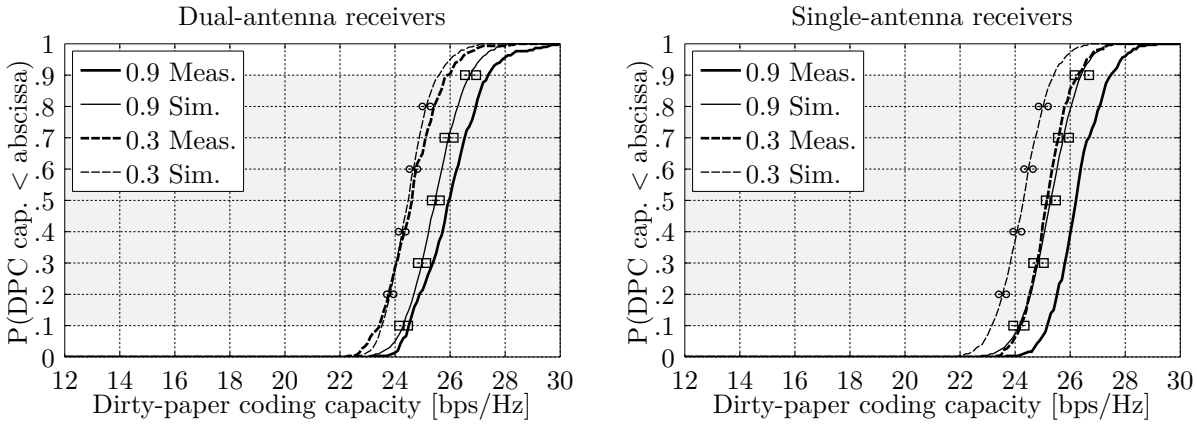

	Dual-antenna Rx			Single-antenna Rx		
	med.	cdf.1	cdf.9	med.	cdf.1	cdf.9
0.9 ISD Meas.	26.0	24.6	27.4	26.3	25.2	27.5
0.9 ISD Sim.	25.5	24.3	26.7	25.3	24.1	26.4
0.3 ISD Meas.	24.7	23.5	25.9	25.3	24.3	26.3
0.3 ISD Sim.	24.5	23.5	25.6	24.3	23.2	25.4

Actual SNR (σ = SNR + 9 dB)

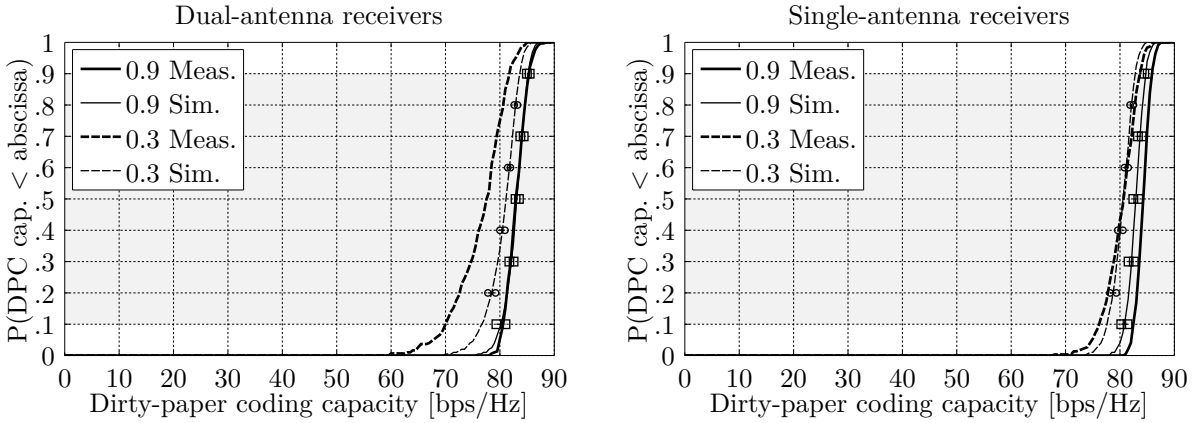

	Dual-antenna Rx			Single-antenna Rx		
	med.	cdf.1	cdf.9	med.	cdf.1	cdf.9
0.9 ISD Meas.	83.2	80.9	85.5	84.5	82.7	86.1
0.9 ISD Sim.	82.9	80.2	85.2	82.8	80.8	84.7
0.3 ISD Meas.	76.8	70.0	82.2	80.4	76.4	83.9
0.3 ISD Sim.	80.6	76.7	83.6	80.4	77.6	82.8

Figure 5.10: DPC capacity in Berlin, Germany. Top: The capacity distribution at a fixed SNR. Bottom: The capacity distribution at the actual SNR in the channel.

When the actual SNR from the channel is used, the capacity in the Berlin testbed triples. This is shown in the bottom part of Figure 5.10. Due to the handover to their best cell, users always experience good reception condition. The SNR limit of the prototype measurement system, which was 30.8 dB, is included in the curves. In most cases, the capacity was noise-limited, *i.e.*, users could almost always achieve the 30.8 dB SNR. Only with the high downtilts (0.3 ISD) there were some users that were power-limited, *i.e.*, they were outside the main beam and thus had a lower SNR. Due to joust transmission, interference was eliminated and external interference was not present in this evaluation (this case is discussed in the next section). In the single-antenna configuration, an average sum-capacity of 84.5 bps Hz was achieved for the four cooperating sectors at the low downtilts (0.9 ISD). This value was reduced to 80.4 bps Hz at high downtilts (0.3 ISD).

5.5.5 Dirty-Paper Coding Capacity with Inter-Cell Interference

The results from the previous section show significant gains for joint transmission. However, those results did not include external interference. Hence, in reality, the gains will be lower. In this section, interference is included in the evaluation for the DPC capacity as described in Section 3.3.5 on Page 71. The previously disabled *interfering sectors* in Figure 5.1 (Page 115) are used for this purpose. In addition, several techniques to mitigate the interference are compared. Those are frequency reuse, massive MIMO and joint transmission. The results are presented in Table 5.3 and Figure 5.12.

Transmission schemes It is assumed that each *active sector* always serves two single-antenna MTs. The users select the best of their two receive antennas based on the power. The MTs are placed randomly on the measurement track. No further constraints are applied. Hence, there might be power differences between the users. However, if the users get assigned to their best serving sector (as it is done for most of the schemes), they will often have similar received powers. The sum-transmit power per sector is fixed to 39.5 dBm (8.93 W), independent of the number of transmit antennas. The following transmission schemes are compared:

- *Isolated cell*
  Each of the four *active sectors* is treated independently as if there were no interfering sectors. The full spectrum is available for each sector. This scheme is unrealistic in practice but helps to discuss differences between measured and resimulated channels at low SNR and longer distances.

- *Frequency reuse 4 (FR4)*
  Each sector gets a different frequency band. Users perform a handover to their best serving sector based on the average received power. Channels are assumed to be interference-free. However, only 25% of the spectrum is available in each sector. Thus, the capacity results are divided by a factor of four to incorporate the reuse factor.

- *Frequency reuse 4 (FR4) with massive MIMO*
  This scheme can only be evaluated using the channel model. The active sectors are equipped with a massive MIMO array antenna with up to 144 antennas. The sum-power remains the same. However, the excess amount of transmit antennas enables beamforming gains that can increase the spectral efficiency. As above, users perform a handover to their best sector, and each sector utilizes 25% of the total spectrum.

- *Frequency reuse 1 (FR1)*
  Each sector is treated independently. Users are assigned to the four *active sectors*. Within those, they are assigned to their best serving sector. However, the interference from the outer *interfering sectors* is included as well. Thus, each user sees the channel of its serving BS and five interfering channels. It is assumed that the BSs have no knowledge of the interfering channels but know the channels of their own users.

- *Frequency reuse 1 (FR1) with massive MIMO*
  This scheme can only be evaluated using the channel model. The active sectors are equipped with a massive MIMO array antenna. It is assumed that the BSs know the channels of their own users but not the interfering channels. Thus, each active sector optimizes the transmit strategy, *i.e.*, the beamforming weights, as if there was no interference. The two outer *interfering sectors* do not use massive MIMO but keep their conventional antennas.

- *Joint transmission, no external interference*
  The four active sectors form a cooperation cluster and jointly serve eight users. Thus, the antennas of the cooperating BSs resemble a distributed array antenna with eight elements. The transmit power per sector remains constant. Thus, the distributed array has a sum-power of 45.5 dBm. Users are assigned to their best serving sector. To make the schemes comparable, the capacity is measured in bps/Hz per sector. Hence, the values from the previous Section have to be divided by a factor of four, *i.e.*, if the distributed eight-element array antenna has a sum-capacity of 80 bps/Hz, each of the four sectors sector achieves on average 20 bps/Hz.

- *Joint transmission, with external interference*
  The previous scheme is unrealistic because out-of-cluster interference is ignored. Therefore, the two *interfering sectors* are used to cause uncoordinated interference which is included in the capacity calculation. The BS optimizes the transmit strategy as if there was no interference.

Massive MIMO antennas In order to study the effect of massive MIMO in the interference limited setup, a model for the transmit antenna had to be created. This model consists of 16 individual elements, eight for +45° polarization and eight for -45°. The eight elements for one polarization are coupled with a power-divider. Additional phase-shifts enable electrically adjustable downtilts. A reference antenna pattern was provided by Kathrein. For the massive MIMO antenna, a simplified model of a single antenna element was created. This is described in detail in Appendix A.2. The element has a FWHM beam width of 68°, both in elevation and azimuth direction, and a gain of 9.6 dBi. Then, four different array antenna configurations are considered. The parameters are summarized in Table 5.2 and the array configuration is sketched in Figure 5.11.

For the first "massive MIMO antenna", a model of the 2-port Kathrein antenna was created by using a fixed phase offset between the single elements to achieve the same 10° electric downtilt as for the reference antenna pattern. Thus, this antenna is used to test how much the results differ when replacing the measured antennas with the modeled ones. Mutual coupling between the elements was ignored. Hence, there are differences in the sidelobes of the antennas (see Figure A.2 on Page 140). This will also have an effect on the interference experienced by the users in other sectors. The transmit power per antenna is set to 36.5 dBm. The gain of the antenna is 18.5 dBi.

Table 5.2: Overview of the massive MIMO antenna configurations in Berlin, Germany

No elements		2	16	64	144
Electric downtilt	deg	10	0	0	0
Mechanic Downtilt[a]	deg	13/19/5	23/29/15	23/29/15	23/29/15
Tx. power per element	dBm	36.5	27.5	21.5	18.0
	mW	4,470	560	140	60
Max. beamforming gain	dB	18.5[b]	19.0[c]	28.2[c]	30.0[c]
Az. beam width	deg	67.1	67.1	6.1	5.7
El. beam width	deg	6.5	6.1	6.1	5.7
Element spacing	λ	1.0	1.0	1.0	0.71
Array height	m	1.1	1.1	1.1	1.1
Array width	m	0.2	0.2	1.1	1.1

[a]The first value is for the HHI BS, the second for the TLabs BS and the third for the TUB BS. See also Section 5.1 on Page 114 for details.
[b]This value is fixed due to the fixed precoding weights (see Appendix A.2, Page 140).
[c]This value is variable, depending on the transmit strategy.

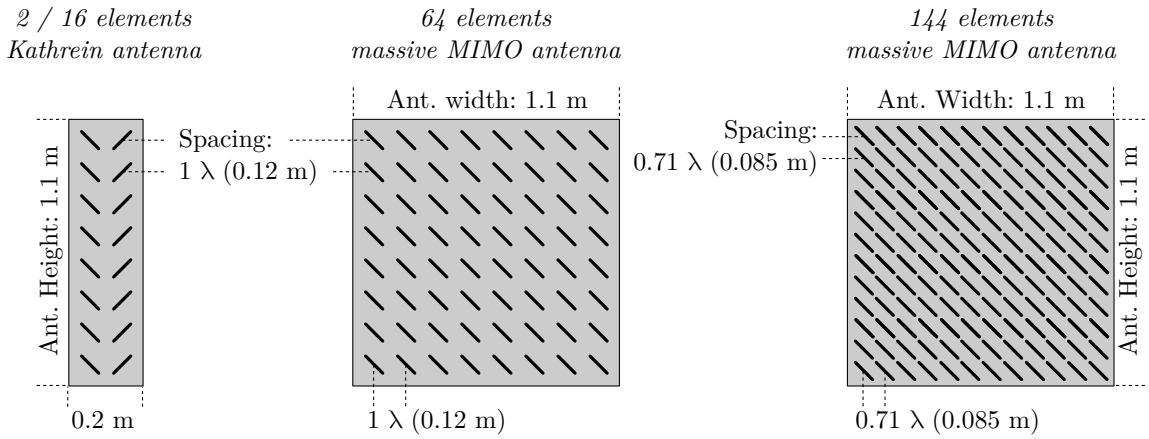

Figure 5.11: Massive MIMO antennas for interference mitigation in Berlin, Germany

For the second antenna, the fixed coupling between the antenna elements is removed and each element can be used directly for the MIMO processing. The effective transmit power per element is reduced to 27.5 dBm to maintain the sum-power per sector. The antenna layout is depicted in Figure 5.11 on the left. The mechanical downtilt was increased to match the values for the high-downtilt scenario, *i.e.*, the maximum antenna gain is achieved at 170 m distance from the BS (0.3 ISD). The minimum FWHM is 6.1° in elevation direction and 67.1° in azimuth direction. The MIMO processing, however, can now adjust the beam direction in elevation direction to improve the performance for the served user and to reduce interference.

For the third antenna, the -45° polarization is discarded and the +45° column is replicated eight times (see Figure 5.11, middle). The element spacing of 1 λ is maintained. Thus, this 64-element planar antenna has a size of roughly 1 m × 1 m. The minimum azimuth FWHM is reduced to 6.1° while the transmit power is reduced to 21.5 dBm. The maximum beamforming gain of the antenna is 28.2 dBi if all the power is directed towards a single user.

A fourth antenna was created by packing the elements closer together (see Figure 5.11, right). With +45° polarization, an element spacing of $\lambda/\sqrt{2}$ is feasible, and 144 elements can be stacked in an 12 × 12 planar array. The array antenna size is not increased in this case. However, the beam with also does not change much compared to the 64 element array. The minimum azimuth

FWHM is now 5.7°, both in azimuth and elevation direction. The antenna gain is increased to 30 dBi while the transmit power per element is reduced to 18 dBm. The main difference is that this antenna has a stronger sidelobe suppression which reduces the interference experienced by other terminals.

Results Table 5.3 provides an overview of the results. The table is structured as follows: the transmission scheme is listed on the left, followed by the number of transmit antennas in the cooperation cluster, and the size of the coverage area. A value of 0.9 ISD means that the low downtilts were used where the main beam hits the ground at 90% of the inter site distance (ISD). Likewise, a value of 0.3 ISD means that the high downtilt settings were used. Then, the results are presented for the measured data, the new (QuaDRiGa) channel model, and the Rayleigh i.i.d. channel model. The latter includes the PG, SF and the average antenna gain at the MT positions. Hence, power differences between the users are included (also the differences between LOS and NLOS propagation), but the MIMO channel coefficients are modeled by an i.i.d. matrix. For each transmission scheme and data set, the average value (*avg.*), the low value for the CDF that could be achieved in more than 90% of the cases (*cdf.1*), and the high value for the CDF that could be achieved in more than 10% of the cases (*cdf.9*). The column denoted as *err.* shows the relative error compared to the measured data, if not stated otherwise in the footnotes of the table. All results include the actual receive power, *i.e.*, they use the normalization where the channel matrices are normalized to the actual SNR in the channel.

Table 5.3: DPC capacity prediction for different transmission schemes and numbers of Tx-Antennas in units of [bps/Hz per sector]

				Measured			QuaDRiGa				Rayleigh i.i.d.			
Row	Scheme	n_t	ISD	avg.	cdf.1	cdf.9	avg.	cdf.1	cdf.9	err.	avg.	cdf.1	cdf.9	err.
1	Isolated cell	2	0.9	18.7	16.4	20.3	17.1	12.4	20.5	*-8.8*	17.4	13.5	20.3	*-6.6*
2		2	0.3	13.8	9.6	17.9	15.9	11.6	19.9	*16.7*	16.2	12.2	20.1	*19.8*
3	Freq. reuse 4	2	0.9	5.1	4.9	5.3	5.0	4.7	5.3	*-1.0*	5.0	5.0	5.1	*-0.9*
4		2	0.3	4.9	4.4	5.4	**4.9**[a]	**4.5**	**5.3**	*0.1*	5.0	4.7	5.1	*0.9*
5	Freq. reuse 4	2	0.3	*N/A*	*N/A*	*N/A*	4.9	4.4	5.3	*-0.0*[b]	4.9	4.4	5.1	*-0.4*[c]
6	massive MIMO	16	0.3	*N/A*	*N/A*	*N/A*	8.1	7.3	8.6		8.1	7.3	8.6	*0.5*[c]
7		64	0.3	*N/A*	*N/A*	*N/A*	9.2	8.2	10.2		9.3	8.2	10.2	*0.3*[c]
8		144	0.3	*N/A*	*N/A*	*N/A*	**9.8**[a]	**8.7**	**10.9**		9.9	8.7	10.9	*0.4*[c]
9	Freq. reuse 1	2	0.9	2.2	0.8	3.9	**2.6**[a]	**1.1**	**4.5**	*23.8*	2.7	1.3	4.5	*29.8*
10		2	0.3	3.2	0.6	6.9	**4.0**[a]	**0.8**	**8.2**	*31.0*	4.1	1.0	8.2	*36.1*
11	Freq. reuse 1	2	0.3	*N/A*	*N/A*	*N/A*	4.8	1.0	10.0	*19.2*[b]	4.8	1.1	9.7	*0.5*[c]
12	massive MIMO	16	0.3	*N/A*	*N/A*	*N/A*	9.9	4.3	15.8		10.2	4.8	15.8	*4.0*[c]
13		64	0.3	*N/A*	*N/A*	*N/A*	13.4	7.1	19.8		13.4	7.7	19.2	*1.2*[c]
14		144	0.3	*N/A*	*N/A*	*N/A*	**15.6**[a]	**7.9**	**22.9**		15.6	9.1	21.6	*2.6*[c]
15	Joint trans.	8[d]	0.9	21.1	20.7	21.5	20.7	20.2	21.2	*-1.9*	20.8	20.4	21.1	*-1.7*
16	interference free	8[d]	0.3	20.1	19.1	21.0	**20.1**[a]	**19.4**	**20.7**	*-0.1*	20.2	19.6	20.6	*0.5*
17	Joint trans.	8[d]	0.9	5.3	4.0	6.6	6.0	4.6	7.5	*15.1*	6.2	4.9	7.6	*19.4*
18	with ext. int.	8[d]	0.3	5.0	3.0	7.0	**6.4**[a]	**4.8**	**8.1**	*33.6*	6.5	4.9	8.2	*36.8*

[a] This curve is included in Figure 5.12.

[b] This value shows the difference of the results with synthetic antennas compared to the measured pattern, i.e. the values in the row above.

[c] This value shows the difference to the QuaDRiGa resultsu sing the same PG model.

[d] 4 active sectors with 2 transmit antennas, each. The capacity is normalized to [bps/Hz per sector].

Additional illustrations of the results are provided in Figures 5.12 and 5.13. Figure 5.12 shows the CDFs for several transmission schemes. Those are highlighted in bold text in Table 5.3. All of them were obtained from the channel model. Figure 5.13 on page 134 shows the *interference footprint* for different transmission schemes and exemplary user positions. The term *interference footprint* refers to the geometry factor (see Section 3.3.2, Page 66) that would be achieved when taking only the antenna patterns, precoding strategy, and path gain into account. The precoders were calculated for the given user positions using maximum ratio transmission [57]. The *interfering sectors* did not apply any precoding strategy.

Discussion of the Results

Isolated cell
Measurement results for the isolated cells without interference and handover show an average DPC capacity of 18.7 bps/Hz for the low downtilt (0.9 ISD) and 13.8 bps/Hz for the high downtilt (0.3 ISD). For the low downtilt, the model predicts a 8.8% smaller capacity with a higher spread while at the high downtilt the predicted capacities are 16.7% higher than in the measurements. This can be explained by the results for the effective PG which show a similar difference (see Section 5.3.1, Page 118).

In Dresden, the average capacity for two users was 13.1 bps/Hz (see Table 4.5, Page 109). There were eight transmit antennas per BS in Dresden. However, there was also a the lower LOS probability (20% compared to 50% in Berlin) and a lower path gain. The capacity could be predicted with high accuracy (2.9% error). A major difference was that calibrated antenna patterns were available in Dresden, both for the transmitter and the receiver, while many approximations had to be made in Berlin. It seems that the accuracy of the antenna model has a significant impact on the accuracy of the performance predictions. The Rayleigh i.i.d. model predicts a slightly higher capacity which is in line with the observations from the Dresden data.

Frequency reuse 4 (FR4)
The model predictions for FR4 with handover between cells are almost identical to the measurement results. On average, a capacity of 5 bps/Hz per sector could be achieved for both downtilt settings (including the reuse factor). It seems that all antenna models show a high accuracy within the coverage area of a cell. This is also visible when comparing row 4 and row 5 in Table 5.3. Predictions with the massive MIMO antenna model are almost identical to the measured results.

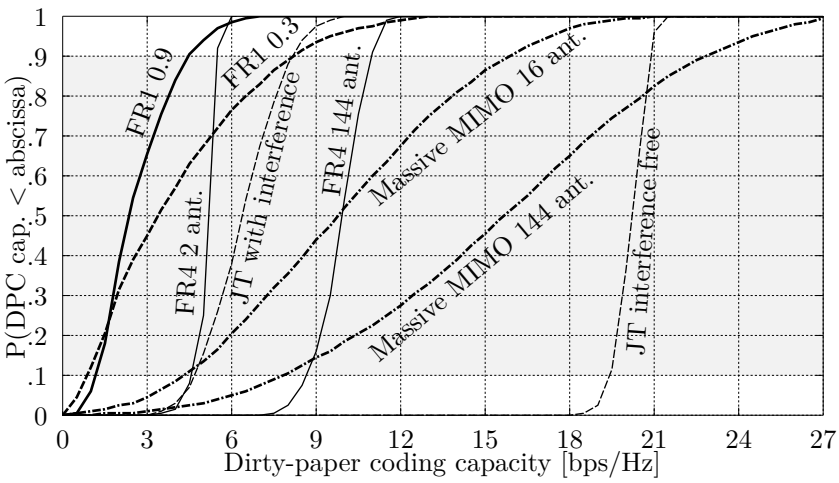

Figure 5.12: Empirical CDFs of the DPC capacity with different interference mitigation strategies in Berlin, Germany

When the number of transmit elements is increased while the sum-power is kept constant, significant beamforming gains are possible. Elevation beamforming (row 6) increases the capacity by 65% without changing the antenna dimensions. With full massive MIMO (row 8), the capacity is doubled. Due to frequency reuse and handover, fairness among the users is maintained, *i.e.*, 90% of the users can achieve at least 90% of the average capacity, independent of the number of transmit antenna elements.

Frequency reuse 1 (FR1)
FR1 with low downtilts has the worst performance (see row 9 in Table 5.3). The average capacity results from the measures channels show 2.2 bps/Hz per sector. In 10% of the cases, the capacity was below 0.8 bps/Hz. Increasing the downtilt, and thus reducing the coverage area per sector, increases the average capacity to 3.2 bps/Hz. However, for roughly 30% of the users, increasing the downtilt does not show any performance gain. This can be seen in the empirical CDFs in Figure 5.12.

The values predicted by the channel model are up to 31% higher compared to the measurements. A possible explanation is that antenna model, especially the accuracy for the sidelobes, does not match well with the measurements. It seems that in the measurements, there was more interference than in the resimulated channels. An indication for this sensitivity is the prediction with the artificial antenna model in row 11. The artificial antenna (see Appendix A.2, Page 140) ignores mutual coupling and thus shows some significant differences in the radiated power outside the main lobe. This increases the predictions from the model by another 20% compared to the results obtained with the adopted reference pattern from Kathrein.

FR1 and massive MIMO
If the conventional antenna is replaced by a massive MIMO array antenna, significant gains are possible with full frequency reuse. Elevation beamforming with 16 antenna elements doubles the average capacity from 4.8 bps/Hz (fixed elevation beam width) to 9.9 bps/Hz (variable elevation beam width). The effect is illustrated in Figure 5.13 on the left hand side. The three BS positions are marked with a square. Eight user positions are shown as black dots. The users are positioned in a way that each *active sector* serves two users. The two *interfering sectors* don't have any users but cause interference to the existing users. The top-left figure shows the GF for the fixed elevation beams (corresponding to row 11 in Table 5.3). Some users are well within the coverage area of the sectors and have a high GF (white areas). However, some of the users are at the cell edge have a very poor performance (gray areas). When the BSs are allows to adjust the precoding weights to alter the beam width and tilt in elevation direction (bottom left figure, corresponding to row 12 in Table 5.3), all of the users achieve a good performance.

If, in addition, azimuth beamforming is possible, the average capacity reaches 15.6 bps/Hz with 144 transmit antenna elements. However, there is also a large spread as can be seen in the CDF in Figure 5.12. The effect of massive MIMO is illustrated in Figure 5.13 in the bottom right. Here, each user gets illuminated by a narrow beam. The downside of this approach is that the interference caused in the neighboring sectors is unpredictable. This is visible for the *interfering sectors* which are deformed and have a lower GF compared to the conventional approach in the top left. This also explains the large spread in the results. Deploying massive MIMO in a conventional macro-cell setup requires some coordination between the neighboring sectors in order to mitigate the interference.

Joint transmission
Rows 15 and 16 of Table 5.3 show the DPC capacity for joint transmission without external interference, *i.e.*, only the *active sectors* are considered. The results are identical to the ones from Section 5.5.4 except for an additional factor of 0.25 to obtain the average capacity per sector. The joint transmission capacity is roughly four times the FR4 capacity from rows 3 and 4. Thus, it is possible to remove all the interference within the cooperation cluster.

If the *interfering sectors* are included in the analysis (rows 17 and 18), the achievable rate drops significantly. The average capacity is now only 6.0 bps/Hz. The effect of joint transmission is illustrated in Figure 5.13 on the top right. The *active sectors* cooperate and their mutual interference is removed. However, large areas still have a low GF due to the influence of the two *interfering sectors*. In many cases, especially for the TLabs BS, no improvements can be seen. It is important to carefully select the users that are served by joint transmission and assign them to suitable cooperation clusters. This requires efficient scheduling algorithms to address the interference-management problem. Also, backhaul requirements for the data exchange can be significant [31].

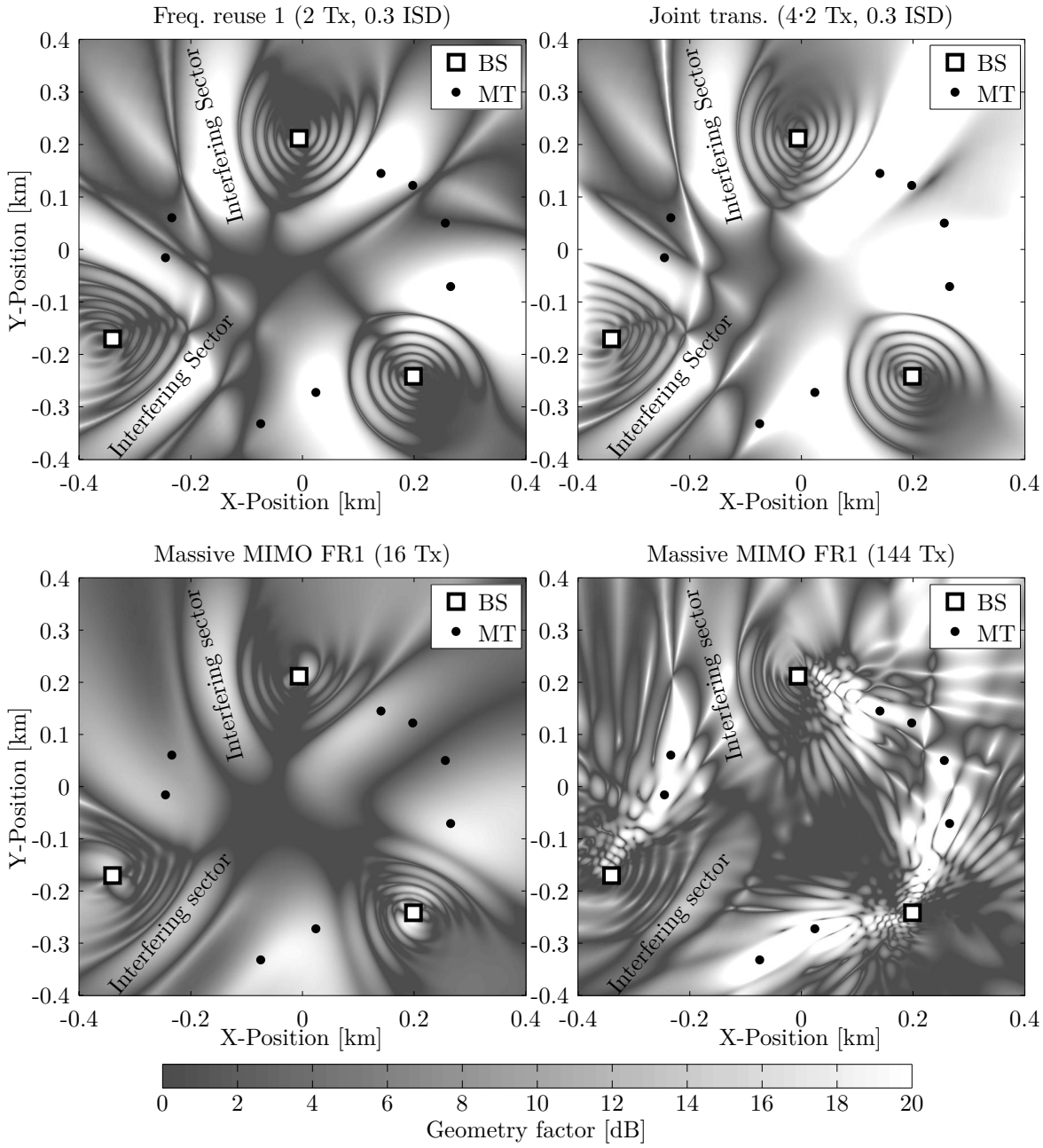

Figure 5.13: Interference footprint for different transmission schemes in Berlin, Germany

6 Conclusions

GSCMs such as the 3GPP SCM and the WINNER model allow the separation of antenna and propagation effects. They are thus ideal candidates to evaluate the performance of massive MIMO systems and joint transmission (JT) coordinated multi-point (CoMP) with realistic radio channels. In this thesis, several extensions of the WINNER channel model [47, 48] and the 3GPP-3D model [49] were proposed that enable a more accurate description of the physical propagation environment. In order to confirm the correctness of the model, measurements in downtown Dresden, Germany, and downtown Berlin, Germany, were evaluated and the results were compared with the model. For this, an extensive parameterization of the model was done in order to separate the influence of large-scale and small-scale propagation effects.

The new model was able to predict the single and multi-user performance of a (near) massive MIMO system with high accuracy. The dirty-paper coding (DPC) capacity of two multi-user setups was evaluated. Independent of the number of antennas at the user terminal, the model correctly predicted the channel rank and the capacity within 15% error. It was also shown that i.i.d. Rayleigh fading models tend to overestimate the achievable rate in this case. The new model can thus be used to test and evaluate different antenna and user constellations in order to find the best massive MIMO system configurations.

It was shown that it is possible to generate channel traces with similar characteristics as measured data. This will speed up the evaluation of new algorithms, since it is now possible to obtain realistic performance results in an early stage of development. Existing parameter tables from previous geometry-based stochastic channel models can be used. Hence, the new model enables virtual field trials in many scenarios. Simulations were done with the 3GPP-3D parameters and results were compared with the new model and the measurements. There were some differences. Due to this, it is important to carefully check the existing parameter tables against real-world scenarios. However, this would have exceeded the scope of this work.

Besides the new features that were introduced to enable accurate performance predictions for massive MIMO and JT CoMP in cellular environments, many future technologies for 5G wireless communications pose open questions regarding additional extensions of the channel model. Some of them are:

- *2-D correlated small-scale fading*
  Correlated small-scale fading is currently only implemented along the user trajectory. Therefore, if user positions are assigned randomly and each user has its own trajectory, all users in the model will experience uncorrelated fading since each user gets initialized with a new set of scatting clusters. This becomes an issue if the users are close together because correlation will decrease the capacity in this case. A solution was proposed in the COST channel model [51] where scattering clusters are generated globally and visibility regions are assigned to them. However, mapping the angular spreads at the user positions to globally defined scattering clusters is problematic and often requires several new parameters. Another solution could be an extension of the *segment* concept towards two dimensions or by using a distance-dependent correlation function similar to the parameter maps for all random variables in the model.

- *Birth and death of scattering clusters*
  It is an open issue how the published findings on the birth/death probability of individual scattering clusters [91, 92] can be mapped to the temporal evolution of the LSPs. For example, randomly creating and removing paths as suggested by [90] would significantly alter the delay and angular spread.

- *Inter-site correlations of the LSPs*
  Inter-site correlations of the LSPs can be included by incorporating more advanced algorithms [138–140] for generating the parameter maps for the initial parameters. Also, incorporating real topology maps and city layout plans into the map generation process could greatly enhance the level of detail for the performance predictions and allow accurate network planning.

- *Mutual coupling of the antenna elements*
  It has been shown in [141] that mutual coupling alters the radiation patterns for closely spaced antennas. Evaluations of the Berlin measurement data and comparison of the capacity results for different antenna models in Section 5.5.4 also indicate that this seems to have a significant impact on the interference caused by such antennas. Thus, it is important to incorporate mutual coupling into the antenna models in order to get realistic performance predictions.

- *mmWave communications*
  There is an enormous amount of spectrum at mmWave frequencies ranging from 6 to 300 GHz that could be used for mobile communications [43]. Array antennas are a key feature in mmWave systems in order to compensate for the high path loss. However, for most of the mmWave spectrum, propagation conditions are not fully understood, *i.e.*, there are only few parameter tables available to be used in GSCMs and additional features such as moving scatterers might be needed. Hence, at the moment, performance predictions for such systems based on simulation studies are rather unreliable.

- *Moving transmitters*
  In many use cases such as device-to-device (D2D), machine-to-machine (M2M), or car-to-car wireless communications, both transmitter and receiver might be mobile. However, the current concept of using *parameter maps* for obtaining correlated LSPs will no longer work in this case since it requires that one of the devices is stationary. If both ends are mobile, a new approach for modeling the spatio-temporal correlation properties of the channel coefficients is needed.

The results presented in this thesis show that the extensions introduced in the new model enable accurate performance predictions for massive MIMO and JT CoMP in infrastructure-based deployment scenarios. When compared with measurements, the predictions made by the model for the distributions of many channel parameters are accurate. Also, the current framework of the model allows the implementation of many additional features to face future requirements.

A Appendix

A.1 Departure and Arrival Angles (Adopted WINNER Method)

In the WINNER model, the azimuth arrival and departure angels are modeled using a wrapped Gaussian distribution (see [47], page 39).

$$P(\phi) = \frac{1}{\sigma_\phi \sqrt{2\pi}} \cdot \exp\left(\frac{-\phi^2}{2{\sigma_\phi}^2}\right) \tag{A.1}$$

The wrapping is applied later by (A.4) when the discrete cluster angles are drawn from the statistics. Since the above formula assumes a continuous spectrum, whereas the channel model uses discrete paths, the variance must be corrected by a function $C_\phi(L, K)$. This function ensures that the input variance σ_ϕ is correctly reflected in the generated angles. The same approach was taken by the WINNER model. However, [47] does not explain how the correction values were obtained.

Generation of azimuth and elevation angles The individual angles ϕ_l are obtained by first normalizing the power angular spectrum so that its maximum has unit power. The scaling factor $1/(\sigma_\phi\sqrt{2\pi})$ can thus be omitted. The path powers P_l (2.19) are also normalized such that the strongest peak with unit power corresponds to an angle $\phi = 0$. All other paths get relative departure or arrival angles depending on their power,

$$\phi_l^{[1]} = \frac{\sigma_\phi}{C_\phi(L, K)} \cdot \sqrt{-2 \cdot \ln\left(\frac{P_l}{\max(P_l)}\right)}. \tag{A.2}$$

Next, two random variables, X_l and Y_l are drawn, where $X_l \sim \{-1, 1\}$ is the positive or negative sign and $Y_l \sim \mathcal{N}(0, \left(\frac{\sigma_\phi}{7}\right)^2)$ introduces a random variation on the angle. The angles $\phi_l^{[1]}$ are then updated to

$$\phi_l^{[2]} = X_l \cdot \phi_l^{[1]} + Y_l. \tag{A.3}$$

If the power P_l of a path is small compared with the strongest peak, its angle $\phi_l^{[2]}$ might exceed $\pm\pi$. In this case, it is wrapped around the unit circle by a modulo operation

$$\phi_l^{[3]} = \left(\phi_l^{[2]} + \pi \mod 2\pi\right) - \pi. \tag{A.4}$$

In case of elevation spreads, the possible range of elevation angles goes from $-\pi/2$ to $\pi/2$. In this case, the values $\phi_l^{[3]}$ need an additional correction. This is done using (2.34). The positions of the Tx and Rx are deterministic, and so are the angles of the LOS component. This is taken into account by updating the values of the angles in order to incorporate the LOS angle

$$\phi_1^{[4]} = 0 \tag{A.5}$$

$$\phi_l^{[5]} = \phi_l^{[4]} + \phi^{LOS}. \tag{A.6}$$

Finally, the NLOS cluster-paths are split into 20 sub-paths to emulate intra cluster angular spreads.

Calculation of $C_\phi(L,K)$ The correction function $C_\phi(L,K)$ takes the influence of the KF and the varying number of clusters on the angular spread into account. To approximate the function, random powers P_l and angles ϕ_l are generated with the correction function set to $C_\phi = 1$. The powers are calculated as described in Section 2.2 with different values of K included. Based on those values, the actual RMS angular spread $\sigma_\phi^{[\text{actual}]}$ is calculated using equations (2.24), (2.25), and (2.26). The correction function follows from comparing $\sigma_\phi^{[\text{actual}]}$ with σ_ϕ. However, two aspects need to be considered:

1. Due to the randomization of the angles in (A.3), the average angle over a sufficiently large quantity ($\approx$ 1000 realizations) of $\sigma_\phi^{[\text{actual}]}$ has to be used. This value is denoted as $\sigma_\phi^{[\text{avg.}]}$.
2. There is a nonlinear relationship between the angular spread $\sigma_\phi^{[\text{avg.}]}$ of the simulated data and the initial value σ_ϕ. This comes from the logarithm in (A.2) and the modulo in (A.4). However, for small values, the relationship can be approximated by a linear function. The maximum angular spread $\sigma_\phi^{\max}$ is defined as the point where the error between the corrected value $\frac{\sigma_\phi}{C_\phi(L,K)}$ and $\sigma_\phi^{[\text{avg.}]}$ is 10°.

For a range of typical values $L \in [2, 42]$ and $K^{[\text{dB}]} \in [-20, 20]$, $C_\phi(L,K)$ can be numerically calculates as

$$C_\phi(L,K) = \frac{1}{\sigma_\phi^{\max}} \cdot \int_0^{\sigma_\phi^{\max}} \frac{\sigma_\phi^{[\text{avg.}]}(\sigma_\phi)}{\sigma_\phi} d\sigma_\phi \ , \tag{A.7}$$

where the σ_ϕ-dependency of $\sigma_\phi^{[\text{avg.}]}(\sigma_\phi)$ comes from the individual angles ϕ_l.

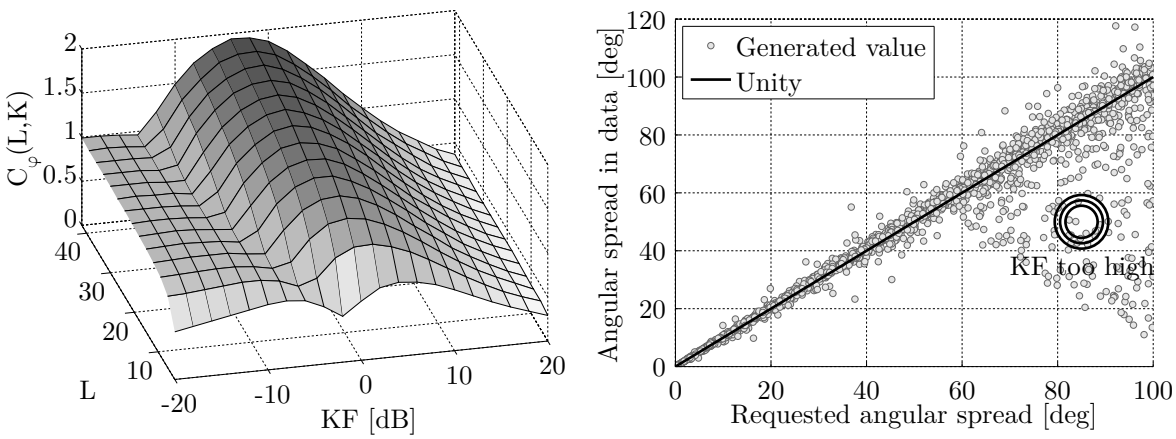

Figure A.1: Visualization of the angular spread correction function $C_\phi(L,K)$. Left: Surface plot of $C_\phi(L,K)$ for different values of L and K. Right: Scatter-plot of the initial angular spread σ_ϕ vs. the output of the model (with correction).

Correction of the angular spread in the WINNER model The proposed correction function for the WINNER model (see [47], pp. 39) works as follows: The individual angles (A.2) are calculated by

$$\phi_l^{[1]} = \frac{2 \cdot \frac{\sigma_\phi}{1.4}}{C} \cdot \sqrt{-\ln\left(\frac{P_l}{\max(P_l)}\right)}, \tag{A.8}$$

where C depends on the numbers of paths (see Table A.1). The KF is corrected by a polynomial of third grade. With the constant coefficients in (A.8) and the factor of 2 in the square root of

(A.2), the correction function $C_\phi(L, K)$ of the WINNER model is

$$C_\phi^{\text{WINNER}}(L, K) = C \cdot \left(1.1035 - 0.028 \cdot K - 0.002 \cdot K^2 + 0.0001 \cdot K^3\right). \tag{A.9}$$

A comparison the both functions for different values of L and K is given in Table A.2. In the second column, the letter W indicates the value for the WINNER model and the letter Q indicates the value of the adopted function. The polynomial has a value of 1 at KF values -11.65, 3.11, and 28.54. At those points, the WINNER correction function is independent of the KF. The corresponding rows are highlighted in the table. Generally, both functions are similar. They agree best as KF values around -14, -3, and 12 but show differences at other values.

Table A.1: Correction values from [47] for different numbers of paths

L	4	5	8	10	11	12	14	15	16	20
C	0.779	0.860	1.018	1.090	1.123	1.146	1.190	1.211	1.226	1.289

Table A.2: Comparison of the correction functions

KF		Number of paths (L)									
[dB]	W/Q	4	5	8	10	11	12	14	15	16	20
-11.7	W	0.779	0.860	1.018	1.090	1.123	1.146	1.190	1.211	1.226	1.289
	Q	0.765	0.822	0.904	0.923	0.929	0.935	0.935	0.935	0.935	0.943
-8.0	W	0.895	0.988	1.169	1.252	1.290	1.316	1.366	1.391	1.408	1.480
	Q	0.790	0.820	0.857	0.870	0.880	0.890	0.977	1.020	1.070	1.250
-4.0	W	0.917	1.012	1.198	1.283	1.322	1.349	1.401	1.425	1.443	1.517
	Q	0.713	0.777	1.047	1.213	1.277	1.340	1.427	1.470	1.500	1.613
0.0	W	0.860	0.949	1.123	1.203	1.239	1.265	1.313	1.336	1.353	1.422
	Q	0.830	0.990	1.277	1.380	1.420	1.460	1.520	1.550	1.570	1.637
3.1	W	0.779	0.860	1.018	1.090	1.123	1.146	1.190	1.211	1.226	1.289
	Q	0.926	1.029	1.221	1.295	1.325	1.354	1.391	1.409	1.425	1.481
4.0	W	0.752	0.831	0.983	1.053	1.085	1.107	1.149	1.170	1.184	1.245
	Q	0.930	1.020	1.190	1.257	1.283	1.310	1.343	1.360	1.373	1.420
8.0	W	0.625	0.690	0.817	0.875	0.901	0.920	0.955	0.972	0.984	1.035
	Q	0.820	0.870	0.967	1.003	1.017	1.030	1.057	1.070	1.077	1.103
12.0	W	0.508	0.561	0.664	0.711	0.733	0.748	0.776	0.790	0.800	0.841
	Q	0.627	0.653	0.707	0.727	0.733	0.740	0.760	0.770	0.773	0.793
16.0	W	0.431	0.476	0.563	0.603	0.621	0.634	0.658	0.670	0.678	0.713
	Q	0.443	0.457	0.490	0.503	0.507	0.510	0.517	0.520	0.523	0.537
20.0	W	0.423	0.467	0.553	0.592	0.610	0.623	0.647	0.658	0.666	0.701
	Q	0.300	0.310	0.320	0.323	0.327	0.330	0.337	0.340	0.343	0.350

A.2 Model of the Transmit Antenna in Berlin

The evaluation of massive MIMO in Section 5.5.5 requires a flexible model of the transmit antenna where the number of elements can be changed. This model is derived from the high-gain BS-antennas. In the model, eight single antenna elements are stacked on top of each other with 1 λ spacing at a center frequency of 2.495 GHz. Thus, the antenna has a height of approximately 1 m. The field pattern of a single antenna element is approximated by

$$F^{[\theta]}(\theta,\phi) = 3 \cdot \sqrt{0.0005 + 0.9995 \cdot (\cos\theta)^{3.7} \cdot \exp\left(-2 \cdot \phi^2\right)}, \tag{A.10}$$

$$F^{[\phi]}(\theta,\phi) = 0. \tag{A.11}$$

The parameters (3, 0.0005, 3.7 and -2) were found by fitting the synthetic pattern to the ones provided by Kathrein. A single antenna element has a FWHM beam width of 68°, both in elevation and azimuth direction. The front-to-back ratio is 33 dB. The gain of the element is 9.6 dBi. The Kathrein antenna has two feed ports, one for +45° and one for -45° polarization. Thus, the antenna array is constructed from 16 individual elements, eight for each polarization.

The element orientation is matched to the polarization by rotating the eight elements in the first column by -45° and the elements in the second column by +45° around the x-axis in GCS as described in Section 2.5.2. The electric downtilt is included by a coupling matrix $\mathbf{C}$ which maps the signal from antenna port p to transmit element t

$$c_{t,p} = \sqrt{\frac{1}{n_t}} \cdot \exp\left(-2\pi \cdot j \cdot \frac{e_{t,p,z} \cdot \sin(\beta)}{\lambda}\right), \tag{A.12}$$

where $e_{t,p,z}$ is the relative position of transmit element t to the array center in z direction, β is the tilt angle in radians, and λ is the wavelength. The receive signal then follows from

$$\mathbf{y} = \mathbf{H} \cdot \mathbf{C} \cdot \mathbf{x} + \mathbf{v}. \tag{A.13}$$

The effective antenna pattern is shown in Figure A.2 where it is compared with the measured pattern of the Kathrein antenna. The resulting antenna pattern has a gain of 18.3 dBi which is very close to the measured pattern (18.5 dBi). The beamwidth of the main beam is almost identical. However, the position and magnitude of the sidelobes is different. This can be explained by the missing mutual coupling in the antenna model and a mismatch in the approximation of the single elements.

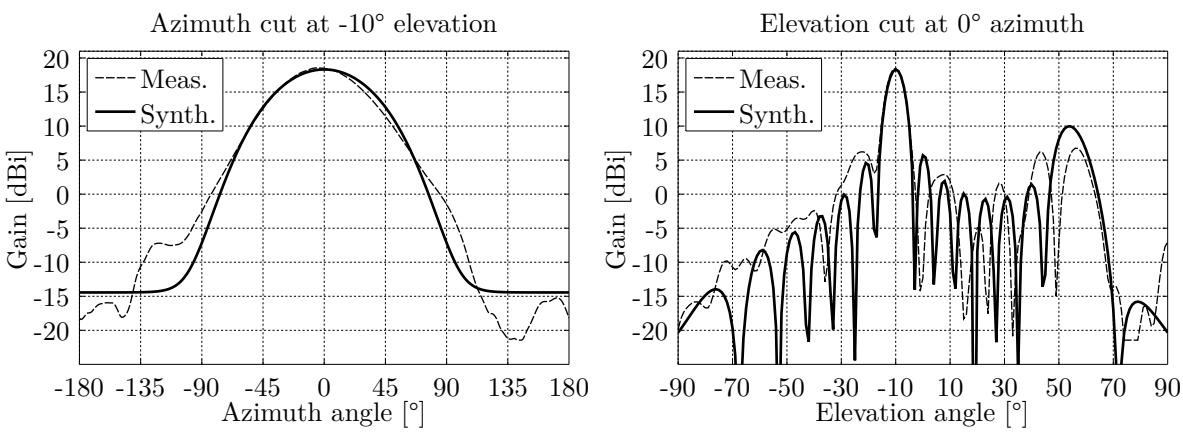

Figure A.2: Comparison of the synthetic and the measured antenna patterns in Berlin, Germany

Bibliography

Own Publications

[1] S. Jaeckel, "Mit Space-Time-Processing zu hochbitratigen mobilen Anwendungen," *Wissen Heute*, vol. 10, 2005.

[2] ——, "Konzeption, Durchführung und Auswertung breitbandiger zellularer MIMO Kanalmessungen im 5 GHz Bereich," Bachelorthesis, Deutsche Telekom AG Fachhochschule Leipzig, 2005.

[3] S. Jaeckel and V. Jungnickel, "Multi-cell outdoor MIMO-measurements," *VDE Kongress '06*, vol. 1, pp. 101–106, 2006.

[4] S. Jaeckel, "Concepts and implementation of multiantenna multicast services for future mobile networks," Masterthesis, Deutsche Telekom, Hochschule für Telekommunikation, Leipzig (HfTL), 2007.

[5] S. Jaeckel and V. Jungnickel, "Scalable video transmission in multiantenna broadcast systems," *Proc. Europ. Wrieless Conf. '08*, 2008.

[6] ——, "On the optimality of frequency-domain equalization in DFT-spread MIMO-OFDM systems," *Proc. IEEE WCNC '08*, pp. 1172–1177, 2008.

[7] S. Jaeckel, L. Jiang, V. Jungnickel, L. Thiele, C. Jandura, G. Sommerkorn, and C. Schneider, "Correlation properties of large and small-scale parameters from multicell channel measurements," *Proc. EUCAP '09*, pp. 3406–3410, 2009.

[8] S. Jaeckel, L. Thiele, A. Brylka, L. Jiang, and V. Jungnickel, "Intercell interference measured in urban areas," *Proc. IEEE ICC '09*, 2009.

[9] S. Jaeckel and V. Jungnickel, "Estimating MIMO capacities from broadband measurements in a cellular network," *Proc. EUCAP '10*, 2010.

[10] S. Jaeckel, L. Thiele, and V. Jungnickel, "Interference limited MIMO measurements," *Proc. IEEE VTC '10 Spring*, 2010.

[11] S. Jaeckel, K. Börner, L. Thiele, and V. Jungnickel, "A geometric polarization rotation model for the 3-D spatial channel model," *IEEE Trans. Antennas Propag.*, vol. 60, no. 12, pp. 5966–5977, 2012.

[12] S. Jaeckel, L. Raschkowski, K. Börner, and L. Thiele, "QuaDRiGa: A 3-D multi-cell channel model with time evolution for enabling virtual field trials," *IEEE Trans. Antennas Propag.*, vol. 62, pp. 3242–3256, 2014.

[13] S. Jaeckel, M. Peter, K. Sakaguchi, W. Keusgen, and J. Medbo, "5G channel models in mm-wave frequency bands," *European Wireless*, pp. 25–30, 2016.

[14] S. Jaeckel, L. Raschkowski, K. Börner, L. Thiele, F. Burkhardt, and E. Eberlein, "QuaDRiGa - Quasi Deterministic Radio Channel Generator, User Manual and Documentation," Fraunhofer Heinrich Hertz Institute, Tech. Rep. v1.4.1-551, 2016.

Co-Authored Publications

[15] V. Jungnickel, S. Jaeckel, L. Thiele, U. Krueger, A. Brylka, and C. Helmolt, "Capacity measurements in a multicell MIMO system," *Proc. IEEE Globecom '06*, 2006.

[16] L. Jiang, V. Jungnickel, S. Jaeckel, L. Thiele, and A. Brylka, "Correlation analysis of multiple-input multiple-output channels with cross-polarized antennas," *Proc. IEICE APCC'08*, 2008.

[17] L. Jiang, L. Thiele, A. Brylka, S. Jaeckel, and V. Jungnickel, "Polarization characteristics of multiple-input multiple-output channels," *Proc. IEEE PIMRC '08*, 2008.

[18] V. Jungnickel, L. Thiele, T. Wirth *et al.*, "Coordinated multipoint trials in the downlink," *Proc. IEEE Globecom Workshops '09*, 2009.

[19] V. Jungnickel, S. Jaeckel, L. Thiele, L. Jiang, U. Krüger, A. Brylka, and C. Helmolt, "Capacity measurements in a cooperative multicell MIMO network," *IEEE Trans. Veh. Technol.*, vol. 58, pp. 2392–2405, June 2009.

[20] V. Jungnickel, A. Forck, S. Jaeckel *et al.*, "Field trials using coordinated multi-point transmission in the downlink," *Proc. IEEE PIMRC '10 WDN-Workshop*, 2010.

[21] K. Manolakis, S. Jaeckel, E. Marquez, and V. Jungnickel, "Impact of path loss and delay spread on base station cooperation," *Proc. EUCAP '11*, 2011.

[22] M. Narandzic, M. Käske, S. Jäckel, G. Sommerkorn, C. Schneider, and R. S. Thomä, "Variation of estimated large-scale MIMO channel properties between repeated measurements," *Proc. IEEE VTC '11 Spring*, 2011.

[23] M. Narandzic, C. Schneider, M. Käske, S. Jaeckel, G. Sommerkorn, and R. Thomä, "Large-scale parameters of wideband MIMO channel in urban multi-cell scenario," *Proc. EUCAP '11*, 2011.

[24] R. Fritzsche, J. Voigt, C. Schneider, S. Jaeckel, and C. Jandura, *Obtaining Channel Model Parameters through Channel Sounding or Ray-Tracing*, ser. Coordinated Multi-Point in Mobile Communications. Cambridge University Press, 2011, ch. 14.2.

[25] V. Jungnickel, A. Forck, S. Jaeckel, S. Wahls, L. Thiele, T. Haustein, W. Zirwas, H. Droste, and G. Kadel, *Realtime Implementation and Field Trials for Downlink CoMP*, ser. Coordinated Multi-Point in Mobile Communications. Cambridge University Press, 2011, ch. 13.3.

[26] K. Börner, J. Dommel, S. Jaeckel, and L. Thiele, "On the requirements for quasi-deterministic radio channel models for heterogeneous networks," *2012 International Symposium on Signals, Systems, and Electronics (ISSSE)*, 2012.

[27] V. Jungnickel, S. Jaeckel, K. Borner, M. Schlosser, and L. Thiele, "Estimating the mobile backhaul traffic in distributed coordinated multi-point systems," *Proc. IEEE WCNC '12*, pp. 3763–3768, April 2012.

[28] V. Jungnickel, A. Brylka, U. Krueger, S. Jaeckel, M. Narandzic, M. Kaeske, M. Landmann, and R. Thomae, "Spatial degrees of freedom in small cells: Measurements with large antenna arrays," *Proc. IEEE VTC '13 Spring*, 2013.

[29] M. Lossow, S. Jaeckel, V. Jungnickel, and V. Braun, "Efficient MAC protocol for JT CoMP in small cells," *Proc. IEEE ICC '13 Workshops*, pp. 1166–1171, 2013.

[30] K. Manolakis, S. Jaeckel, V. Jungnickel, and V. Braun, "Channel prediction by doppler-delay analysis and benefits for base station cooperation," *Proc. IEEE VTC '13 Spring*, 2013.

[31] V. Jungnickel, K. Manolakis, S. Jaeckel, M. Lossow, P. Farkas, M. Schlosser, and V. Braun, "Back-

haul requirements for inter-site cooperation in heterogeneous lte-advanced networks," *Proc. IEEE ICC'13 OWITSN Workshop*, 2013.

[32] E. Eberlein, F. Burkhardt, G. Sommerkorn, S. Jaeckel, and R. Prieto-Cerdeira, "MIMOSA - analysis of the MIMO channel for LMS systems," *Space Communications*, vol. 22, no. 2-4, pp. 145–158, 2013.

[33] F. Burkhardt, E. Eberlein, S. Jaeckel, G. Sommerkorn, and R. Prieto-Cerdeira, "MIMOSA–a dual approach to detailed land mobile satellite channel modeling," *International Journal of Satellite Communications and Networking*, 2014.

[34] F. Burkhardt, S. Jaeckel, E. Eberlein, and R. Prieto-Cerdeira, "QuaDRiGa: a MIMO channel model for land mobile satellite," *8th European Conference on Antennas and Propagation (EuCAP)*, 2014.

[35] J. Dommel, G. Boccolini, L. Raschkowski, S. Jaeckel, L. Thiele, T. Haustein, and N. Gonzalez Prelcic, "5G in space: PHY-layer design for satellite communications using non-orthogonal multi-carrier transmission," *7th Advanced Satellite Multimedia Systems Conference and the 13th Signal Processing for Space Communications Workshop (ASMS/SPSC)*, pp. 190–196, 2014.

[36] B. Holfeld, S. Jaeckel, L. Thiele, T. Wirth, and K. Scheppelmann, "Smart grid communications: LTE outdoor field trials at 450 MHz," *Proc. IEEE VTC '15 Spring*, 2015.

[37] S. Dimitrov, S. Erl, B. Barth, R. Suffritti, N. Privitera, G. Boccolini, A. B. Awoseyila, A. Kyrgiazos, B. G. Evans, S. Jaeckel, B. Sánchez, A. Y. Garcia, and O. Vidal, "Capacity enhancing techniques for high throughput satellite communications," *7th International Conference on Wireless and Satellite Systems*, 2015.

[38] S. Dimitrov, S. Erl, B. Barth, S. Jaeckel, A. Kyrgiazos, and B. Evans, "Radio resource management techniques for high throughput satellite communication systems," *European Conference on Networks and Communications (EuCNC) (accepted contribution)*, 2015.

[39] L. Thiele, M. Kurras, S. Jaeckel, S. Fähse, and W. Zirwas, "Interference-floor shaping for liquid coverage zones in coordinated 5G networks," *Proc. ACSSC '15*, 2015.

[40] M. Peter, K. Sakaguchi *et al.*, "H2020-ICT-671650-mmMAGIC/D2.1: Measurement campaigns and initial channel models for preferred suitable frequency ranges," Tech. Rep., 2016.

[41] B. Pitakdumrongkija, M. Ariyoshi, L. Raschkowski, S. Jaeckel, and L. Thiele, "Performance evaluation of massive MIMO with low-height small-cell using realistic channel models," *Proc. IEEE VTC '16 Fall*, 2016.

Other Cited Publications

[42] Cisco, "Cisco visual networking index: Forecast and methodology, 2014–2019," White Paper, 2015.

[43] F. Boccardi, R. Heath, A. Lozano, T. Marzetta, and P. Popovski, "Five disruptive technology directions for 5G," *IEEE Commun. Mag.*, vol. 52, no. 2, pp. 74–80, February 2014.

[44] F. Rusek, D. Persson, B. K. Lau, E. Larsson, T. Marzetta, O. Edfors, and F. Tufvesson, "Scaling up MIMO: Opportunities and challenges with very large arrays," *IEEE Signal Process. Mag.*, vol. 30, pp. 40–60, 2013.

[45] E. Larsson, O. Edfors, F. Tufvesson, and T. Marzetta, "Massive MIMO for next generation wireless systems," *IEEE Commun. Mag.*, vol. 52, no. 2, pp. 186–195, February 2014.

[46] 3GPP TR 25.996 v6.1.0, "Spatial channel model for multiple input multiple output (MIMO) simulations," Tech. Rep., 2003.

[47] P. Kyösti, J. Meinilä, L. Hentilä *et al.*, "IST-4-027756 WINNER II D1.1.2 v.1.1: WINNER II channel models," Tech. Rep., 2007. [Online]. Available: http://www.ist-winner.org

[48] P. Heino, J. Meinilä, P. Kyösti *et al.*, "CELTIC / CP5-026 D5.3: WINNER+ final channel models," Tech. Rep., 2010. [Online]. Available: http://projects.celtic-initiative.org/winner+

[49] 3GPP TR 36.873 v12.2.0, "Study on 3D channel model for LTE," Tech. Rep., 2015.

[50] L. Correia, Ed., *Mobile Broadband Multimedia Networks.* Elsevier, 2006, ch. 6.8: The COST 273 MIMO channel model, pp. 364–383.

[51] C. Oestges, N. Czink, P. D. Doncker *et al.*, *Pervasive Mobile and Ambient Wireless Communications (COST Action 2100).* Springer, 2012, ch. 3: Radio Channel Modeling for 4G Networks, pp. 67–147.

[52] J. Winters, "Optimum combining in digital mobile radio with cochannel interference," *IEEE Trans. Veh. Technol.*, vol. 33, no. 3, pp. 144–155, 1984.

[53] J. H. Winters, "On the capacity of radio communication systems with diversity in a rayleigh fading environment," *IEEE J. Sel. Areas Commun.*, vol. 5, no. 5, pp. 871–878, June 1987.

[54] I. E. Telatar, "Capacity of multi-antenna gaussian channels," *Europ. Trans. Telecommun.*, vol. 10, no. 6, pp. 585–596, 1999.

[55] G. Foschini, "Layered space-time-architecture for wireless communication in a fading environement when using multi-element antennas," *Bell Labs Technical Journal*, pp. 41–59, 1996.

[56] D. Gesbert, M. Kountouris, R. Heath, C.-B. Chae, and T. Salzer, "Shifting the MIMO paradigm," *IEEE Signal Process. Mag.*, vol. 24, no. 5, pp. 36–46, 2007.

[57] G. Caire and S. Shamai, "On the achievable throughput of a multiantenna gaussian broadcast channel," *IEEE Trans. Inf. Theory*, vol. 49, no. 7, pp. 1691–1706, 2003.

[58] S. Vishwanath, N. Jindal, and A. Goldsmith, "Duality, achievable rates, and sum-rate capacity of gaussian MIMO broadcast channels," *IEEE Trans. Inf. Theory*, vol. 49, no. 10, pp. 2658– 2668, 2003.

[59] D. Gesbert, S. Hanly, H. Huang, S. Shamai Shitz, O. Simeone, and W. Yu, "Multi-cell mimo cooperative networks: A new look at interference," *Selected Areas in Communications, IEEE Journal on*, vol. 28, no. 9, pp. 1380–1408, December 2010.

[60] R. Irmer, H. Droste, P. Marsch, M. Grieger, G. Fettweis, S. Brueck, H.-P. Mayer, L. Thiele, and V. Jungnickel, "Coordinated multipoint: Concepts, performance, and field trial results," *IEEE Communications Magazine*, vol. 49, no. 2, pp. 102–111, February 2011.

[61] H. Hu, Y. Zhang, and J. Luo, Eds., *Distributed Antenna Systems.* Auerbach, 2007.

[62] A. Richter, M. Landmann, and R. S. Thomä, "RIMAX - a flexible algorithm for channel parameter estimation from channel sounding measurements," *COST 273 TD(04) 045*, 2004.

[63] M. Landmann, "Limitations of experimental channel characterisation," Ph.D. dissertation, Teschniche Universität Ilmenau, 2008.

[64] M. Hata, "Empirical formula for propagation loss in land mobile radio services," *IEEE Trans. Veh. Technol.*, vol. 29, no. 3, pp. 317–325, 1980.

[65] S. Loyka and A. Kouki, "On MIMO channel capacity, correlations, and keyholes: Analysis of degenerate channels," *IEEE Trans. Commun.*, vol. 50, pp. 1886–1888, Dec. 2002.

[66] D. Chizhik, G. Foschini, and M. Gans, "Keyholes, correlations and capacities of multielement transmit and receive antennas," *IEEE Trans. Wireless Commun.*, vol. 1, pp. 361–368, Apr. 2002.

[67] D. Chizhik, J. Ling, P. Wolniansky, R. Valenzuela, N. Costa, and K. Huber, "Multiple-input-multiple-output measurements and modeling in Manhattan," *IEEE J. Sel. Areas Commun.*, vol. 21, pp. 321–331, 2003.

[68] M. Zhu, "Geometry-based radio channel characterization and modeling: Parameterization, implementation and validation," Ph.D. dissertation, Department of Electrical and Information Technology, Faculty of Engineering, LTH, Lund University, 2014.

[69] L. Materum, J. Takada, I. Ida, and Y. Oishi, "Mobile station spatio-temporal multipath clustering of an estimated wideband MIMO double-directional channel of a small urban 4.5 GHz macrocell," *EURASIP J. Wireless Commun. Netw.*, no. 2009:804021, 2009.

[70] A. Saleh and R. Valenzuela, "A statistical model for indoor multipath propagation," *IEEE J. Sel. Areas Commun.*, vol. 5, no. 2, pp. 128–137, 1987.

[71] D. Baum, J. Hansen, and J. Salo, "An interim channel model for beyond-3G systems," *Proc. IEEE VCT '05 Spring*, vol. 5, pp. 3132–3136, 2005.

[72] D. Baum, H. El-Sallabi, and T. J. et. al., "Final report on link level and system level channel models," Winner, Tech. Rep. IST-2003-507581 WINNER D5.4 v. 1.4, 2005.

[73] [Online]. Available: http://www.ist-winner.org

[74] ITU-R M.2135, "Guidelines for evaluation of radio interface technologies for IMT-Advanced," Tech. Rep. ITU-R M.2135-1, 2009.

[75] L. Raschkowski, P. Kyösti, and K. K. T. Jämsä, "ICT-317669-METIS/D1.4 METIS channel models," Tech. Rep., 2015.

[76] L. Liu, C. Oestges, J. Poutanen, K. Haneda, P. Vainikainen, F. Quitin, F. Tufvesson, and P. D. Doncker, "The COST 2100 MIMO channel model," *IEEE Wireless Communications*, vol. 19, no. 6, pp. 92–99, December 2012.

[77] [Online]. Available: http://www.easy-c.de

[78] 3GPP TR 25.996 v14.0.0, "Spatial channel model for multiple input multiple output (MIMO) simulations," Tech. Rep., 2017.

[79] H. Xiao, A. Burr, and L. Song, "A time-variant wideband spatial channel model based on the 3gpp model," *Proc. IEEE VCT '06 Fall*, 2006.

[80] M. Shafi, M. Zhang, A. Moustakas, P. Smith, A. Molisch, F. Tufvesson, and S. Simon, "Polarized MIMO channels in 3-D: models, measurements and mutual information," *IEEE J. Sel. Areas Commun.*, vol. 24, pp. 514–527, Mar. 2006.

[81] A. Zajic, G. Stuber, T. Pratt, and S. Nguyen, "Wideband MIMO mobile-to-mobile channels: Geometry-based statistical modeling with experimental verification," *IEEE Trans. Veh. Technol.*, vol. 58, no. 2, pp. 517–534, 2009.

[82] M. R. Andrews, P. P. Mitra, and R. de Carvalho, "Tripling the capacity of wireless communications using electromagnetic polarization," *Nature*, vol. 409, pp. 316–318, Jan 2001.

[83] M. Narandzic, M. Käske, C. Schneider, M. Milojevic, M. Landmann, G. Sommerkorn, and R. Thomä, "3D-antenna array model for IST-WINNER channel simulations," *Proc. IEEE VTC '07 Spring*, pp. 319–323, 2007.

[84] C. Oestges, B. Clerckx, M. Guillaud, and M. Debbah, "Dual-polarized wireless communications: From propagation models to system performance evaluation," *IEEE Trans. Wireless Commun.*, vol. 7, no. 10, pp. 4019–4031, 2008.

[85] Y. Zhou, S. Rondineau, D. Popovic, A. Sayeed, and Z. Popovic, "Virtual channel space-time processing with dual-polarization discrete lens antenna arrays," *IEEE Trans. Antennas Propag.*, vol. 53, pp. 2444–2455, Aug. 2005.

[86] F. Quitin, C. Oestges, F. Horlin, and P. De Doncker, "Multipolarized MIMO channel characteristics: Analytical study and experimental results," *IEEE Trans. Antennas Propag.*, vol. 57, pp. 2739–2745, 2009.

[87] R. C. Jones, "A new calculus for the treatment of optical systems, i. description and discussion of the calculus," *Journal of the Optical Society of America*, vol. 31, pp. 488–493, July 1941.

[88] J. Poutanen, K. Haneda, L. Liu, C. Oestges, F. Tufvesson, and P. Vainikainen, "Parameterization of the COST 2100 MIMO channel model in indoor scenarios," *Proc. EUCAP '11*, pp. 3606–3610, 2011.

[89] M. Zhu, F. Tufvesson, and G. Eriksson, "The COST 2100 channel model: Parameterization and validation based on outdoor MIMO measurements at 300 MHz," Lund University, Sweden, Tech. Rep., 2012.

[90] N. Czink, T. Zemen, J.-P. Nuutinen, J. Ylitalo, and E. Bonek, "A time-variant MIMO channel model directly parametrised from measurements," *EURASIP J. Wireless Commun. Netw.*, no. 2009:687238, 2009.

[91] K. Saito, K. Kitao, T. Imai, Y. Okano, and S. Miura, "The modeling method of time-correlated mimo channels using the particle filter," *Proc. IEEE VCT '11 Spring*, 2011.

[92] W. Wang, T. Jost, U. Fiebig, and W. Koch, "Time-variant channel modeling with application to mobile radio based positioning," *Proc. IEEE GLOBECOM '12*, pp. 5038–5043, 2012.

[93] [Online]. Available: http://www.quadriga-channel-model.de

[94] S. Gregson, J. McCormick, and C. Parini, *Principles of Planar Near-Field Antenna Measurements*. IET, 2007.

[95] A. Algans, K. Pedersen, and P. Mogensen, "Experimental analysis of the joint statistical properties of azimuth spread, delay spread, and shadow fading," *IEEE J. Sel. Areas Commun.*, vol. 20, no. 3, pp. 523–531, 2002.

[96] C. Schneider, M. Narandzic, M. Käske, G. Sommerkorn, and R. Thomä, "Large scale parameter for the WINNER II channel model at 2.53 GHz in urban macro cell," *Proc. IEEE VTC '10 Spring*, 2010.

[97] K. Bakowski and K. Wesolowski, "Change the channel," *IEEE Veh. Technol. Mag.*, vol. 6, pp. 82–91, 2011.

[98] L. Greenstein, V. Erceg, Y. Yeh, and M. Clark, "A new path-gain/delay-spread propagation model for digital cellular channels," *IEEE Trans. Veh. Technol.*, vol. 46, no. 2, pp. 477–485, 1997.

[99] M. Gudmundson, "Correlation model for shadow fading in mobile radio systems," *IET Electron Lett.*, vol. 27, no. 23, pp. 2145–2146, November 1991.

[100] N. J. Higham, "Newton's method for the matrix square root," *Mathematics of Computation*, vol. 46, no. 174, pp. 537–549, 1986. [Online]. Available: http://www.jstor.org/stable/2007992

[101] K. Pedersen, P. Mogensen, and B. Fleury, "Power azimuth spectrum in outdoor environments," *Electronics Letters*, vol. 33, no. 18, pp. 1583–1584, 1997.

[102] A. Ludwig, "The definition of cross-polarization," *IEEE Trans. Antennas Propagation*, vol. AP-21, pp. 116–119, 1973.

[103] C. Oestges, V. Erceg, and A. Paulraj, "Propagation modeling of MIMO multipolarized fixed wireless channels," *IEEE Trans. Veh. Technol.*, vol. 53, pp. 644–654, May 2004.

[104] V. Erceg, H. Sampath, and S. Catreux-Erceg, "Dual-polarization versus single-polarization MIMO

channel measurement results and modeling," *IEEE Trans. Wireless Commun.*, vol. 5, pp. 28–33, Jan. 2006.

[105] M. Landmann, K. Sivasondhivat, J. Takada, and R. Thomä, "Polarisation behaviour of discrete multipath and diffuse scattering in urban environments at 4.5 GHz," *EURASIP J. Wireless Commun. Netw.*, vol. 2007, no. 1, pp. 60–71, 2007.

[106] T. Svantesson, "A physical MIMO radio channel model for multi-element multi-polarized antenna systems," *Proc. IEEE VTC' 01 Fall*, vol. 2, pp. 1083–1087, 2001.

[107] F. Quitin, C. Oestges, F. Horlin, and P. De Doncker, "A polarized clustered channel model for indoor multiantenna systems at 3.6 GHz," *IEEE Trans. Veh. Technol.*, vol. 59, no. 8, pp. 3685–3693, 2010.

[108] R. Schmidt, "Multiple emitter location and signal parameter estimation," *IEEE Transactions on Antennas and Propagation*, vol. 34, no. 3, pp. 276–280, Mar 1986.

[109] M. Haardt and J. A. Nossek, "Unitary esprit: how to obtain increased estimation accuracy with a reduced computational burden," *IEEE Transactions on Signal Processing*, vol. 43, no. 5, pp. 1232–1242, May 1995.

[110] A. Richter, D. Hampicke, G. Sommerkorn, and R. S. Thoma, "Joint estimation of DoD, time-delay, and DoA for high-resolution channel sounding," *Proc. IEEE VTC '00 Spring*, vol. 2, pp. 1045–1049 vol.2, 2000.

[111] J. A. Fessler and A. O. Hero, "Space-alternating generalized expectation-maximization algorithm," *IEEE Transactions on Signal Processing*, vol. 42, no. 10, pp. 2664–2677, Oct 1994.

[112] B. Fleury, M. Tschudin, R. Heddergott, D. Dahlhaus, and K. Ingeman Pedersen, "Channel parameter estimation in mobile radio environments using the sage algorithm," *IEEE J. Sel. Areas Commun.*, vol. 17, no. 3, pp. 434–450, 1999.

[113] A. Richter, "Estimation of radio channel parameters: Models and algorithms," Ph.D. dissertation, Teschniche Universität Ilmenau, 2005.

[114] E. J. Candes, J. K. Romberg, and T. Tao, "Stable signal recovery from incomplete and inaccurate measurements," *Communications on Pure and Applied Mathematics*, vol. 59, no. 8, pp. 1207 – 1223, 2006.

[115] D. L. Donoho and I. M. Johnstone, "Ideal denoising in an orthonormal basis chosen from a library of bases," *Comptes Rendus Acad. Sci., Ser. I*, vol. 319, pp. 1317–1322, 1994.

[116] N. Jaldén, P. Zetterberg, B. Ottersten, and L. Garcia, "Inter-and intrasite correlations of large-scale parameters from macrocellular measurements at 1800 MHz," *EURASIP J. Wireless Commun. Netw.*, no. 2007:025757, 2007.

[117] L. Greenstein, D. Michelson, and V. Erceg, "Moment-method estimation of the ricean k-factor," *IEEE Communications Letters*, vol. 3, no. 6, pp. 175–176, 1999.

[118] T. Rappaport, *Wireless Communications. Principles and Practice*, 2nd ed. Prentice Hall, 2002.

[119] G. Durgin and T. Rappaport, "Basic relationship between multipath angular spread and narrow-band fading in wireless channels," *Electronics Letters*, vol. 34, no. 25, pp. 2431–2432, 1998.

[120] K. Yu, Q. Li, and M. Ho, "Measurement investigation of tap and cluster angular spreads at 5.2 GHz," *IEEE Transactions on Antennas and Propagation*, vol. 53, no. 7, pp. 2156–2160, July 2005.

[121] J. L. Rodgers and W. A. Nicewander, "Thirteen ways to look at the correlation coefficient," *The American Statistician*, vol. 42, p. 59–66, 1988.

[122] X. Gao, O. Edfors, F. Rusek, and F. Tufvesson, "Massive MIMO in real propagation environments," 2014. [Online]. Available: http://arxiv.org/abs/1403.3376

[123] Q. Spencer, C. Peel, A. Swindlehurst, and M. Haardt, "An introduction to the multi-user MIMO downlink," *IEEE Commun. Mag.*, vol. 42, no. 10, pp. 60–67, 2004.

[124] M. Costa, "Writing on dirty paper," *IEEE Trans. Inf. Theory*, vol. 29, no. 3, pp. 439 – 441, 1983.

[125] N. Jindal, W. Rhee, S. Vishwanath, S. Jafar, and A. Goldsmith, "Sum power iterative water-filling for multi-antenna gaussian broadcast channels," *IEEE Trans. Inf. Theory*, vol. 51, no. 4, pp. 1570–1580, 2005.

[126] E. A. Jorswieck and H. Boche, "Performance analysis of capacity of MIMO systems under multiuser interference based on worst-case noise behavior," *EURASIP J. Wireless Commun. Netw.*, vol. 2, pp. 273–285, 2004.

[127] W. Utschick and J. Brehmer, "Monotonic optimization framework for coordinated beamforming in multicell networks," *Signal Processing, IEEE Transactions on*, vol. 60, no. 4, pp. 1899–1909, April 2012.

[128] Z.-Q. Luo and S. Zhang, "Dynamic spectrum management: Complexity and duality," *Selected Topics in Signal Processing, IEEE Journal of*, vol. 2, no. 1, pp. 57–73, Feb 2008.

[129] R. Thomä, D. Hampicke, A. Richter, G. Sommerkorn, and U. Trautwein, "MIMO vector channel sounder measurement for smart antenna system evaluation," *Europ. Trans. Telecommun.*, vol. 12, pp. 427–438, 2001.

[130] 3GPP TR 25.996 v10.0.0, "Spatial channel model for multiple input multiple output (MIMO) simulations," Tech. Rep., 3 2011.

[131] K. Kalliola, K. Sulonen, H. Laitinen, O. Kivekas, J. Krogerus, and P. Vainikainen, "Angular power distribution and mean effective gain of mobile antenna in different propagation environments," *Vehicular Technology, IEEE Transactions on*, vol. 51, no. 5, pp. 823–838, Sep 2002.

[132] M. Käske, M. Landmann, and R. Thomä, "Modelling and synthesis of dense multipath propagation," *Proc. EUCAP '09*, pp. 264–2645, 2009.

[133] M. Schellmann, L. Thiele, T. Haustein, and V. Jungnickel, "Spatial transmission mode switching in multi-user MIMO-OFDM systems with user fairness," *IEEE Trans. Veh. Technol.*, vol. 59, no. 1, pp. 235–247, 2010.

[134] V. Jungnickel, K. Manolakis, L. Thiele, T. Wirth, and T. Haustein, "Handover sequences for interference-aware transmission in multicell MIMO networks," *Proc. WSA '09*, 2009.

[135] V. Jungnickel, M. Schellmann, A. Forck *et al.*, "Demonstration of virtual MIMO in the uplink," *Proc. IET Smart Ant. and Coop. Commun. Seminar*, 2007.

[136] V. Jungnickel, M. Schellmann, L. Thiele *et al.*, "Interference aware scheduling in the multiuser MIMO-OFDM downlink," *IEEE Commun. Mag.*, vol. 47, pp. 56–66, 2009.

[137] M. Zhu, F. Tufvesson, and J. Medbo, "Correlation properties of large scale parameters from 2.66 GHz multi-site macro cell measurements," *Proc. IEEE VTC '11 Spring*, 2011.

[138] T. Klingenbrunn and P. Mogensen, "Modelling cross-correlated shadowing in network simulations," *Proc. IEEE VTC '99 Fall*, vol. 3, pp. 1407–1411, 1999.

[139] X. Cai and G. B. Giannakis, "A two-dimensional channel simulation model for shadowing processes," *IEEE Trans. Veh. Technol.*, vol. 52, no. 6, pp. 1558–1567, 2003.

[140] S. Szyszkowicz, H. Yanikomeroglu, and J. Thompson, "On the feasibility of wireless shadowing correlation models," *IEEE Trans. Veh. Technol.*, vol. 59, pp. 4222–4236, 2010.

[141] V. Jungnickel, V. Pohl, and C. von Helmolt, "Capacity of MIMO systems with closely spaced antennas," *IEEE Commun. Lett.*, vol. 7, no. 9, pp. 361–363, 2003.

Erklärung

Ich versichere, dass ich die vorliegende Arbeit ohne unzulässige Hilfe Dritter und ohne Benutzung anderer als der angegebenen Hilfsmittel angefertigt habe. Die aus anderen Quellen direkt oder indirekt übernommenen Daten und Konzepte sind unter Angabe der Quelle gekennzeichnet.

Weitere Personen waren an der inhaltlich-materiellen Erstellung der vorliegenden Arbeit nicht beteiligt. Insbesondere habe ich hierfür nicht die entgeltliche Hilfe von Vermittlungs- bzw. Beratungsdiensten (Promotionsberater oder anderer Personen) in Anspruch genommen. Niemand hat von mir unmittelbar oder mittelbar geldwerte Leistungen für Arbeiten erhalten, die im Zusammenhang mit dem Inhalt der vorgelegten Dissertation stehen.

Die Arbeit wurde bisher weder im In- noch im Ausland in gleichere oder ähnlichen Form einer Prüfungsbehöorde vorgelegt.

Ich bin darauf hingewiesen worden, dass die Unrichtigkeit der vorstehenden Erklärung als Täuschungsversuch bewertet wird und gemäß § 7 Abs. 10 der Promotionsordnung den Abbruch des Promotionsverfahrens zur Folge hat.

Ort, Datum: _____

Unterschrift: _____